

AD-A160 420

JOINT AGENCY TURBULENCE EXPERIMENT(U) AIR FORCE
GEOPHYSICS LAB HANSCOM AFB MA A R BOHNE 21 JAN 85
AFGL-TR-85-0012

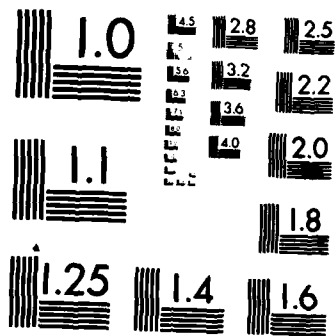
1/3

UNCLASSIFIED

F/G 17/9

NL

100



MICROCOPY RESOLUTION TEST CHART
NATIONAL BUREAU OF STANDARDS-1963-A

AD-A160 420

AFGL 85-0012
ENVIRONMENTAL RESEARCH PAPERS, NO. 905

Joint Agency Turbulence Experiment Final Report

ALAN R. BOHNE

21 January 1985

Approved for public release; distribution unlimited.

DTIC FILE COPY

DTIC
ELECTE
OCT 17 1985
S B D

ATMOSPHERIC SCIENCES DIVISION

PROJECT 6670

AIR FORCE GEOPHYSICS LABORATORY

HANSCOM AFB MA 01731

85 10 16 104

"This technical report has been reviewed and is approved for publication"

FOR THE COMMANDER



KENNETH M. GLOVER
Chief, Ground Based Remote Sensing Branch
Atmospheric Sciences Division



ROBERT A. McCLATCHEY
Director, Atmospheric Sciences Div.

This document has been reviewed by the ESD Public Affairs Office (PA) and is releasable to the National Technical Information Service (NTIS).

Qualified requestors may obtain additional copies from the Defense Technical Information Center. All others should apply to the National Technical Information Service.

If your address has changed, or if you wish to be removed from the mailing list, or if the addressee is no longer employed by your organization, please notify AFGL/DAA, Hanscom AFB, MA 01731. This will assist us in maintaining a current mailing list.

Unclassified

SECURITY CLASSIFICATION OF THIS PAGE

AD-A160 420

REPORT DOCUMENTATION PAGE				
1a. REPORT SECURITY CLASSIFICATION Unclassified		1b. RESTRICTIVE MARKINGS		
2a. SECURITY CLASSIFICATION AUTHORITY		3. DISTRIBUTION/AVAILABILITY OF REPORT Approved for public release; Distribution unlimited.		
2b. DECLASSIFICATION/DOWNGRADING SCHEDULE				
4. PERFORMING ORGANIZATION REPORT NUMBER(S) AFGL-TR-85-0012 ERP, No. 905		5. MONITORING ORGANIZATION REPORT NUMBER(S)		
6a. NAME OF PERFORMING ORGANIZATION Air Force Geophysics Laboratory	6b. OFFICE SYMBOL (If applicable) LYR	7a. NAME OF MONITORING ORGANIZATION		
6c. ADDRESS (City, State and ZIP Code) Hanscom AFB Massachusetts 01731		7b. ADDRESS (City, State and ZIP Code)		
8a. NAME OF FUNDING/SPONSORING ORGANIZATION	8b. OFFICE SYMBOL (If applicable)	9. PROCUREMENT INSTRUMENT IDENTIFICATION NUMBER		
8c. ADDRESS (City, State and ZIP Code)		10. SOURCE OF FUNDING NOS.		
		PROGRAM ELEMENT NO. 62101F	PROJECT NO. 6670	TASK NO. 15 WORK UNIT NO. 02
11. TITLE (Include Security Classification) Joint Agency Turbulence Experiment - Final Report				
12. PERSONAL AUTHOR(S) Alan R. Bohne				
13a. TYPE OF REPORT Scientific. Final.	13b. TIME COVERED FROM 1 Oct 81 to 30 Sep 84	14. DATE OF REPORT (Yr., Mo., Day) 1985 January 21	15. PAGE COUNT 220	
16. SUPPLEMENTARY NOTATION				
17. COSATI CODES			18. SUBJECT TERMS (Continue on reverse if necessary and identify by block number)	
FIELD	GROUP	SUB. GR.	Composite severity class Turbulence outer scale Doppler radar Eddy dissipation rate Turbulence Turbulence severity	
19. ABSTRACT (Continue on reverse if necessary and identify by block number) → Doppler radar and aircraft data acquired during the 1981 and 1982 Joint Agency Turbulence Experiment observation seasons are discussed. Time histories of Doppler radar mean velocity and spectrum variance data acquired while tracking an instrumented aircraft during 34 thunderstorm penetrations are presented. Time histories and analysis of turbulence severity, as determined from these radar and aircraft data, are also presented. Whereas use of radar mean velocity in structure function analysis results in underestimation of the actual turbulence severity, radar methods based upon Doppler spectrum variance successfully detect regions of turbulence hazardous to aircraft. The variance-based method, employing a modeled turbulence energy spectrum with a maximum finite eddy size, is found most effective when the turbulence outer scale lies in the range of 1-4 km. Classification of turbulence severity as light, moderate, heavy, or severe with a single outer scale value was found unreliable. However, classification into composite severity classes, where a composite class combined two or more individual (Contd)				
20. DISTRIBUTION/AVAILABILITY OF ABSTRACT UNCLASSIFIED/UNLIMITED <input checked="" type="checkbox"/> SAME AS RPT <input type="checkbox"/> DTIC USERS <input type="checkbox"/>			21. ABSTRACT SECURITY CLASSIFICATION Unclassified	
22a. NAME OF RESPONSIBLE INDIVIDUAL Alan R. Bohne			22b. TELEPHONE NUMBER (Include Area Code) (617) 861-4405	22c. OFFICE SYMBOL LYR

DD FORM 1473, 83 APR

EDITION OF 1 JAN 73 IS OBSOLETE.

Unclassified
SECURITY CLASSIFICATION

Unclassified

SECURITY CLASSIFICATION OF THIS PAGE(When Data Entered)

20. (Contd)

19. (Contd)

severity classes, was found to be a very successful approach for locating hazardous and nonhazardous turbulence regions. Data also show Doppler spectrum variance to be poorly correlated with shear of the radial wind. This shear, resulting from nonturbulence storm structure generally contributed less than 10 percent of the turbulence contribution to Doppler spectrum variance and could generally be neglected when estimating turbulence severity. Although the occurrence of lightning when the aircraft was in a region containing strong turbulence was a rare event, the limited lightning strike data acquired suggests that lightning events, when observed were well correlated with regions of strong turbulence.



Accession for	
NOIS	<input checked="checked" type="checkbox"/>
USCIB	<input type="checkbox"/>
Unpublished	<input type="checkbox"/>
Jury	
By	
Distribution	
Availability Codes	
Avail. and/or	
Dist	Special
A-1	

Unclassified

SECURITY CLASSIFICATION OF THIS PAGE(When Data Entered)

Preface

Successful completion of the Joint Agency Turbulence Experiment could not have been accomplished without the efforts of a number of agencies and individuals. The author wishes to thank the personnel at NASA Langley Research Center and NASA Wallops Flight Center for their assistance, enabling the Air Force Geophysics Laboratory to participate effectively in the NASA Storm Hazards Program. In particular, special thanks are given to Norman Crabill, Program Manager of the Storm Hazards Program, Bruce Fisher, Project Engineer, and Jim Usry, all of NASA Langley. Robert Carr, Project Manager, and Brooks Shaw, Project Coordinator at NASA Wallops are also acknowledged. The NASA Wallops SPANDAR radar group provided crucial support in the integration of AFGL equipment into the SPANDAR radar system and continual assistance during operations. Special consideration is given to John Howard and George Bishop, Branch Managers, and Norris Beasely and Richard Gagnon, all of the SPANDAR group. AFGL was well represented, with many individuals providing crucial support in directing operations and maintaining equipment. Thanks are given to Kenneth Glover, Chief of the Ground Based Remote Sensing Branch, and Kenneth Banis, Alexander Bishop, Major Carlton Bjerkaas, Major Douglas Forsythe, Pio Petrocchi, and in particular William Smith. Special thanks are given to Graham Armstrong for designing the tracking gate recording equipment as well as participating in operations. Typing of the manuscript by Donna Velardi is much appreciated. Finally, sincerest thanks are given to Albert Chmela, who helped in the analyses of the vast quantities of aircraft and radar data, and who also aided in the preparation of the data for publication. To all these individuals, and others who I unfortunately may not have accounted for, my sincerest thanks for making the Joint Agency Turbulence Experiment a successful effort.

Contents

1. INTRODUCTION	1
2. ESTIMATION OF TURBULENCE SEVERITY BY RADAR METHODS	2
3. STORM ENVIRONMENTS	9
4. COMPARISON OF RADAR AND AIRCRAFT ESTIMATES OF TURBULENCE SEVERITY	20
5. CONSIDERING ISOTROPY	30
6. STORM SHEAR AND LIGHTNING EFFECTS	35
7. SUMMARY AND CONCLUSIONS	38
REFERENCES	41
APPENDIX A: Data Reduction and Methodologies	43
APPENDIX B: Estimation of Effective Turbulence Outer Scale	49
APPENDIX C: Stability of Aircraft Turbulence Severity Estimates	59
APPENDIX D: Radar Pulse Volume Filtering Effects on Structure Function Estimates	65
APPENDIX E: Wallops Island Sounding Data	71
APPENDIX F: Tracking Gate Doppler Spectrum Mean and Variance Data	81
APPENDIX G: Estimates of Turbulence Severity Derived From Aircraft Gust Data	123
APPENDIX H: Estimates of Turbulence Severity Derived From Doppler Radar Data	175

Illustrations

1.	Time History of Turbulence Severity ($\epsilon^{1/3}$) as Estimated From Radar Data Using Structure Function (lower dash), and Doppler Spectrum Variance Methods With $\lambda_o = 0.5$ km (upper solid), $\lambda_o = 2.0$ km (upper dash), and $\lambda_o = \infty$ km (lower solid) for Penetration 5 on 31 July 1982	6
2.	Time History of Turbulence Severity ($\epsilon^{1/3}$) as Estimated From Aircraft Gust Data Using Structure Function Method	7
3.	Contours of Storm Reflectivity Factor (dBZ) for 1 July 1981 on Constant Height Surface at Aircraft Storm Penetration Altitude of 4.57 km	10
4.	Contours of Storm Reflectivity Factor (dBZ) for 3 July 1981 at Aircraft Penetration Altitude of 4.87 km at 20:02:11 GMT	11
5.	Contours of Storm Reflectivity Factor (dBZ) at Aircraft Penetration Altitude of 3.5 km for 16 July 1981 at 18:32:37 GMT	12
6.	Contours of Storm Reflectivity Factor (dBZ) at Aircraft Penetration Altitude of 3.35 km for 17 July 1981 at 18:35:00 GMT	13
7.	Contours of Storm Reflectivity Factor (dBZ) at 6.0 km Altitude for 17 July 1982 at 20:16:40 GMT	14
8.	Contours of Storm Reflectivity Factor (dBZ) at 6.0 km Altitude for 17 July 1982 at 20:40:35 GMT	15
9.	Contours of Storm Reflectivity Factor (dBZ) at 3.0 km Altitude for 28 July 1982 at 22:56:48 GMT	16
10.	Contours of Storm Reflectivity Factor (dBZ) Along an Azimuth Angle of 251 Degrees for 28 July 1982 at 22:33:53 GMT	17
11.	Contours of Storm Reflectivity Factor (dBZ) at Altitude of 7.2 km for 30 July 1982 at 19:45:20 GMT	18
12.	Contours of Storm Reflectivity Factor (dBZ) at Altitude of 7.19 km for 31 July 1982 at 19:20:02 GMT	19
13.	Contours of Storm Reflectivity Factor (dBZ) at Altitude of 7.19 km for 31 July 1982 at 20:14:52 GMT	20
14.	Ratio of Energies of Longitudinal to Transverse (solid), Longitudinal to Vertical (long dash), and Transverse to Vertical (short dash) Aircraft Gust Component Data as a Function of Data Segment Length	31
15.	Ratio of Energies of Longitudinal to Transverse (solid), Longitudinal to Vertical (long dash), and Transverse to Vertical (short dash) Aircraft Gust Component Data as a Function of Data Segment Length	32
16.	Ratio of Energies of Longitudinal to Transverse (solid), Longitudinal to Vertical (long dash), and Transverse to Vertical (short dash) Aircraft Gust Component Data as a Function of Data Segment Length	32
17.	Time Series of Aircraft Gust Component Data Along the North (Ug), East (Vg), and Vertical (Wg) Directions for the Period Shown in Figure 14	33

18.	Histogram of Storm Wind Shear Magnitude	36
19.	Histogram of Ratio of Storm Wind Shear to Turbulence Contribution to Doppler Spectrum Variance	37
B1.	Longitudinal Power Density Spectrum for Aircraft Gust Component Data From Penetration 1 on 3 July 1981	50
B2.	Longitudinal Power Density Spectrum for Model Turbulence Field	51
B3.	Autocorrelation Function for Longitudinal Aircraft Gust Data for Penetration 3 on 17 July 1981	52
B4.	Time History of Longitudinal Aircraft Gust Component Data for Penetration 3 on 17 July 1981	53
B5.	Autocorrelation Function After Removal of Large-scale Wave Feature	54
B6.	Autocorrelation Function With Exponential (dash) and Von Karman (solid) Representations Having a Longitudinal Integral Scale Length of 338 m	56
C1.	Behavior of Structure Function With Lag Distance of 18 m(A) and 108 m(B), Autocorrelation Function (C), and Estimate of Turbulence Severity (D), With Data Segment Length	62
C2.	Behavior of Structure Function With Lag Distance of 18 m(A) and 108 m(B), Autocorrelation Function (C), and Estimate of Turbulence Severity (D), With Data Segment Length	62
C3.	Behavior of Structure Function With Lag Distance of 18 m(A) and 108 m(B), Autocorrelation Function (C), and Estimate of Turbulence Severity (D), With Data Segment Length	63
C4.	Time Series of Aircraft Longitudinal Gust Data For Penetration 1 on 1 July 1981	63
C5.	Time Series of Turbulence Severity Estimates Derived From 400 m (solid), 800 m (long dash), and 1200 m (short dash) Local Data Segments	64
E1.	Wallops Island Sounding Data for 1 July 1981 at 1200 GMT	72
E2.	Wallops Island Sounding Data for 4 July 1981 at 00 GMT	73
E3.	Wallops Island Sounding Data for 17 July 1981 at 00 GMT	74
E4.	Wallops Island Sounding Data for 17 July 1981 at 1200 GMT	75
E5.	Wallops Island Sounding Data for 17 July 1981 at 00 GMT	76
E6.	Wallops Island Sounding Data for 28 July 1982 at 1200 GMT	77
E7.	Wallops Island Sounding Data for 30 July 1982 at 1200 GMT	78
E8.	Wallops Island Sounding Data for 31 July 1982 at 1200 GMT	79
F1.	Tracking Gate Doppler Spectrum Mean Data, Day 182, Penetration 1	82
F2.	Tracking Gate Doppler Spectrum Variance Data, Day 182, Penetration 1	82
F3.	Tracking Gate Doppler Spectrum Mean Data, Day 184, Penetration 1A	83
F4.	Tracking Gate Doppler Spectrum Variance Data, Day 184, Penetration 1A	83

F5.	Tracking Gate Doppler Spectrum Mean Data, Day 184, Penetration 1B	84
F6.	Tracking Gate Doppler Spectrum Variance Data, Day 184, Penetration 1B	84
F7.	Tracking Gate Doppler Spectrum Mean Data, Day 184, Penetration 2	85
F8.	Tracking Gate Doppler Spectrum Variance Data, Day 184, Penetration 2	85
F9.	Tracking Gate Doppler Spectrum Mean Data, Day 184, Penetration 3A	86
F10.	Tracking Gate Doppler Spectrum Variance Data, Day 184, Penetration 3A	86
F11.	Tracking Gate Doppler Spectrum Mean Data, Day 184, Penetration 3B	87
F12.	Tracking Gate Doppler Spectrum Variance Data, Day 184, Penetration 3B	87
F13.	Tracking Gate Doppler Spectrum Mean Data, Day 197, Penetration 1	88
F14.	Tracking Gate Doppler Spectrum Variance Data, Day 197, Penetration 1	88
F15.	Tracking Gate Doppler Spectrum Mean Data, Day 197, Penetration 2	89
F16.	Tracking Gate Doppler Spectrum Variance Data, Day 197, Penetration 2	89
F17.	Tracking Gate Doppler Spectrum Mean Data, Day 198, Penetration 1	90
F18.	Tracking Gate Doppler Spectrum Variance Data, Day 198, Penetration 1	90
F19.	Tracking Gate Doppler Spectrum Mean Data, Day 198, Penetration 2	91
F20.	Tracking Gate Doppler Spectrum Variance Data, Day 198, Penetration 2	91
F21.	Tracking Gate Doppler Spectrum Mean Data, Day 198, Penetration 3	92
F22.	Tracking Gate Doppler Spectrum Variance Data, Day 198, Penetration 3	92
F23.	Tracking Gate Doppler Spectrum Mean Data, Day 198, Penetration 1	93
F24.	Tracking Gate Doppler Spectrum Variance Data, Day 198, Penetration 1	93
F25.	Tracking Gate Doppler Spectrum Mean Data, Day 198, Penetration 2	94
F26.	Tracking Gate Doppler Spectrum Variance Data, Day 198, Penetration 2	94
F27.	Tracking Gate Doppler Spectrum Mean Data, Day 198, Penetration 3	95
F28.	Tracking Gate Doppler Spectrum Variance Data, Day 198, Penetration 3	95
F29.	Tracking Gate Doppler Spectrum Mean Data, Day 198, Penetration 4	96
F30.	Tracking Gate Doppler Spectrum Variance Data, Day 198, Penetration 4	96
F31.	Tracking Gate Doppler Spectrum Mean Data, Day 198, Penetration 5	97
F32.	Tracking Gate Doppler Spectrum Variance Data, Day 198, Penetration 5	97

F33.	Tracking Gate Doppler Spectrum Mean Data, Day 198, Penetration 6	98
F34.	Tracking Gate Doppler Spectrum Variance Data, Day 198, Penetration 6	98
F35.	Tracking Gate Doppler Spectrum Mean Data, Day 198, Penetration 7	99
F36.	Tracking Gate Doppler Spectrum Variance Data, Day 198, Penetration 7	99
F37.	Tracking Gate Doppler Spectrum Mean Data, Day 209, Penetration 1	100
F38.	Tracking Gate Doppler Spectrum Variance Data, Day 209, Penetration 1	100
F39.	Tracking Gate Doppler Spectrum Mean Data, Day 209, Penetration 2	101
F40.	Tracking Gate Doppler Spectrum Variance Data, Day 209, Penetration 2	101
F41.	Tracking Gate Doppler Spectrum Mean Data, Day 209, Penetration 3	102
F42.	Tracking Gate Doppler Spectrum Variance Data, Day 209, Penetration 3	102
F43.	Tracking Gate Doppler Spectrum Mean Data, Day 209, Penetration 4	103
F44.	Tracking Gate Doppler Spectrum Variance Data, Day 209, Penetration 4	103
F45.	Tracking Gate Doppler Spectrum Mean Data, Day 209, Penetration 5	104
F46.	Tracking Gate Doppler Spectrum Variance Data, Day 209, Penetration 5	104
F47.	Tracking Gate Doppler Spectrum Mean Data, Day 209, Penetration 6	105
F48.	Tracking Gate Doppler Spectrum Variance Data, Day 209, Penetration 6	105
F49.	Tracking Gate Doppler Spectrum Mean Data, Day 211, Penetration 1	106
F50.	Tracking Gate Doppler Spectrum Variance Data, Day 211, Penetration 1	106
F51.	Tracking Gate Doppler Spectrum Mean Data, Day 211, Penetration 2	107
F52.	Tracking Gate Doppler Spectrum Variance Data, Day 211, Penetration 2	107
F53.	Tracking Gate Doppler Spectrum Mean Data, Day 211, Penetration 3	108
F54.	Tracking Gate Doppler Spectrum Variance Data, Day 211, Penetration 3	108
F55.	Tracking Gate Doppler Spectrum Mean Data, Day 211, Penetration 4	109
F56.	Tracking Gate Doppler Spectrum Variance Data, Day 211, Penetration 4	109
F57.	Tracking Gate Doppler Spectrum Mean Data, Day 211, Penetration 5	110
F58.	Tracking Gate Doppler Spectrum Variance Data, Day 211, Penetration 5	110
F59.	Tracking Gate Doppler Spectrum Mean Data, Day 211, Day 6,	111
F60.	Tracking Gate Doppler Spectrum Variance Data, Day 211, Penetration 6	111

F61.	Tracking Gate Doppler Spectrum Mean Data, Day 211, Penetration 7	112
F62.	Tracking Gate Doppler Spectrum Variance Data, Day 211, Penetration 7	112
F63.	Tracking Gate Doppler Spectrum Mean Data, Day 211, Penetration 8	113
F64.	Tracking Gate Doppler Spectrum Variance Data, Day 211, Penetration 8	113
F65.	Tracking Gate Doppler Spectrum Mean Data, Day 212, Penetration 1	114
F66.	Tracking Gate Doppler Spectrum Variance Data, Day 212, Penetration 1	114
F67.	Tracking Gate Doppler Spectrum Mean Data, Day 212, Penetration 2	115
F68.	Tracking Gate Doppler Spectrum Variance Data, Day 212, Penetration 2	115
F69.	Tracking Gate Doppler Spectrum Mean Data, Day 212, Penetration 3	116
F70.	Tracking Gate Doppler Spectrum Variance Data, Day 212, Penetration 3	116
F71.	Tracking Gate Doppler Spectrum Mean Data, Day 212, Penetration 4	117
F72.	Tracking Gate Doppler Spectrum Variance Data, Day 212, Penetration 4	117
F73.	Tracking Gate Doppler Spectrum Mean Data, Day 212, Penetration 5	118
F74.	Tracking Gate Doppler Spectrum Variance Data, Day 212, Penetration 5	118
F75.	Tracking Gate Doppler Spectrum Mean Data, Day 212, Penetration 6	119
F76.	Tracking Gate Doppler Spectrum Variance Data, Day 212, Penetration 6	119
F77.	Tracking Gate Doppler Spectrum Mean Data, Day 212, Penetration 7	120
F78.	Tracking Gate Doppler Spectrum Variance Data, Day 212, Penetration 7	120
F79.	Tracking Gate Doppler Spectrum Mean Data, Day 212, Penetration 8	121
F80.	Tracking Gate Doppler Spectrum Variance Data, Day 212, Penetration 8	121
F81.	Tracking Gate Doppler Spectrum Mean Data, Day 212, Penetration 9	122
F82.	Tracking Gate Doppler Spectrum Variance Data, Day 212, Penetration 9	122
G1.	Estimates of Turbulence Severity Derived From Aircraft Gust Data, Day 182, Penetration 1	124
G2.	Estimates of Turbulence Severity Derived From Aircraft Gust Data, Day 184, Penetration 1	125
G3.	Estimates of Turbulence Severity Derived From Aircraft Gust Data, Day 184, Penetration 2	126
G4.	Estimates of Turbulence Severity Derived From Aircraft Gust Data, Day 184, Penetration 3	127

G5.	Estimates of Turbulence Severity Derived From Aircraft Gust Data, Day 197, Penetration 1	128
G6.	Estimates of Turbulence Severity Derived From Aircraft Gust Data, Day 197, Penetration 2	129
G7.	Estimates of Turbulence Severity Derived From Aircraft Gust Data, Day 198, Penetration 1	130
G8.	Estimates of Turbulence Severity Derived From Aircraft Gust Data, Day 198, Penetration 2	131
G9.	Estimates of Turbulence Severity Derived From Aircraft Gust Data, Day 198, Penetration 3	132
G10.	Estimates of Turbulence Severity Derived From Aircraft Gust Data, Day 198, Penetration 3	133
G11.	Estimates of Turbulence Severity Derived From Aircraft Gust Data, Day 198, Penetration 1	134
G12.	Estimates of Turbulence Severity Derived From Aircraft Gust Data, Day 198, Penetration 2	135
G13.	Estimates of Turbulence Severity Derived From Aircraft Gust Data, Day 198, Penetration 3	136
G14.	Estimates of Turbulence Severity Derived From Aircraft Gust Data, Day 198, Penetration 4	137
G15.	Estimates of Turbulence Severity Derived From Aircraft Gust Data, Day 198, Penetration 5	138
G16.	Estimates of Turbulence Severity Derived From Aircraft Gust Data, Day 198, Penetration 6	139
G17.	Estimates of Turbulence Severity Derived From Aircraft Gust Data, Day 198, Penetration 7	140
G18.	Estimates of Turbulence Severity Derived From Aircraft Gust Data, Day 209, Penetration 1	141
G19.	Estimates of Turbulence Severity Derived From Aircraft Gust Data, Day 209, Penetration 2A	142
G20.	Estimates of Turbulence Severity Derived From Aircraft Gust Data, Day 209, Penetration 2B	143
G21.	Estimates of Turbulence Severity Derived From Aircraft Gust Data, Day 209, Penetration 3A	144
G22.	Estimates of Turbulence Severity Derived From Aircraft Gust Data, Day 209, Penetration 3B	145
G23.	Estimates of Turbulence Severity Derived From Aircraft Gust Data, Day 209, Penetration 4A	146
G24.	Estimates of Turbulence Severity Derived From Aircraft Gust Data, Day 209, Penetration 4B	147
G25.	Estimates of Turbulence Severity Derived From Aircraft Gust Data, Day 209, Penetration 4C	148
G26.	Estimates of Turbulence Severity Derived From Aircraft Gust Data, Day 209, Penetration 5	149

G27.	Estimates of Turbulence Severity Derived From Aircraft Gust Data, Day 209, Penetration 6A	150
G28.	Estimates of Turbulence Severity Derived From Aircraft Gust Data, Day 209, Penetration 6B	151
G29.	Estimates of Turbulence Severity Derived From Aircraft Gust Data, Day 211, Penetration 1	152
G30.	Estimates of Turbulence Severity Derived From Aircraft Gust Data, Day 211, Penetration 2A	153
G31.	Estimates of Turbulence Severity Derived From Aircraft Gust Data, Day 211, Penetration 2B	154
G32.	Estimates of Turbulence Severity Derived From Aircraft Gust Data, Day 211, Penetration 3A	155
G33.	Estimates of Turbulence Severity Derived From Aircraft Gust Data, Day 211, Penetration 3B	156
G34.	Estimates of Turbulence Severity Derived From Aircraft Gust Data, Day 211, Penetration 4	157
G35.	Estimates of Turbulence Severity Derived From Aircraft Gust Data, Day 211, Penetration 5	158
G36.	Estimates of Turbulence Severity Derived From Aircraft Gust Data, Day 211, Penetration 6A	159
G37.	Estimates of Turbulence Severity Derived From Aircraft Gust Data, Day 211, Penetration 6B	160
G38.	Estimates of Turbulence Severity Derived From Aircraft Gust Data, Day 211, Penetration 7	161
G39.	Estimates of Turbulence Severity Derived From Aircraft Gust Data, Day 211, Penetration 8	162
G40.	Estimates of Turbulence Severity Derived From Aircraft Gust Data, Day 212, Penetration 1	163
G41.	Estimates of Turbulence Severity Derived From Aircraft Gust Data, Day 212, Penetration 2	164
G42.	Estimates of Turbulence Severity Derived From Aircraft Gust Data, Day 212, Penetration 3A	165
G43.	Estimates of Turbulence Severity Derived From Aircraft Gust Data, Day 212, Penetration 3B	166
G44.	Estimates of Turbulence Severity Derived From Aircraft Gust Data, Day 212, Penetration 4A	167
G45.	Estimates of Turbulence Severity Derived From Aircraft Gust Data, Day 212, Penetration 4B	168
G46.	Estimates of Turbulence Severity Derived From Aircraft Gust Data, Day 212, Penetration 5	169
G47.	Estimates of Turbulence Severity Derived From Aircraft Gust Data, Day 212, Penetration 6	170
G48.	Estimates of Turbulence Severity Derived From Aircraft Gust Data, Day 212, Penetration 7	171

G49.	Estimates of Turbulence Severity Derived From Aircraft Gust Data, Day 212, Penetration 8	172
G50.	Estimates of Turbulence Severity Derived From Aircraft Gust Data, Day 212, Penetration 9	173
H1.	Estimates of Turbulence Severity Derived From Doppler Radar Data, Day 182, Penetration 1	176
H2.	Estimates of Turbulence Severity Derived From Doppler Radar Data, Day 184, Penetration 1A	176
H3.	Estimates of Turbulence Severity Derived From Doppler Radar Data, Day 184, Penetration 1B	177
H4.	Estimates of Turbulence Severity Derived From Doppler Radar Data, Day 184, Penetration 2A	177
H5.	Estimates of Turbulence Severity Derived From Doppler Radar Data, Day 184, Penetration 2B	178
H6.	Estimates of Turbulence Severity Derived From Doppler Radar Data, Day 184, Penetration 3A	178
H7.	Estimates of Turbulence Severity Derived From Doppler Radar Data, Day 184, Penetration 3B	179
H8.	Estimates of Turbulence Severity Derived From Doppler Radar Data, Day 197, Penetration 1	179
H9.	Estimates of Turbulence Severity Derived From Doppler Radar Data, Day 197, Penetration 2	180
H10.	Estimates of Turbulence Severity Derived From Doppler Radar Data, Day 198, Penetration 1	180
H11.	Estimates of Turbulence Severity Derived From Doppler Radar Data, Day 198, Penetration 2	181
H12.	Estimates of Turbulence Severity Derived From Doppler Radar Data, Day 198, Penetration 3	181
H13.	Estimates of Turbulence Severity Derived From Doppler Radar Data, Day 198, Penetration 1	182
H14.	Estimates of Turbulence Severity Derived From Doppler Radar Data, Day 198, Penetration 2	182
H15.	Estimates of Turbulence Severity Derived From Doppler Radar Data, Day 198, Penetration 3	183
H16.	Estimates of Turbulence Severity Derived From Doppler Radar Data, Day 198, Penetration 4	183
H17.	Estimates of Turbulence Severity Derived From Doppler Radar Data, Day 198, Penetration 5	184
H18.	Estimates of Turbulence Severity Derived From Doppler Radar Data, Day 198, Penetration 6	184
H19.	Estimates of Turbulence Severity Derived From Doppler Radar Data, Day 198, Penetration 7	185
H20.	Estimates of Turbulence Severity Derived From Doppler Radar Data, Day 209, Penetration 1	185

H21.	Estimates of Turbulence Severity Derived From Doppler Radar Data, Day 209, Penetration 2A	186
H22.	Estimates of Turbulence Severity Derived From Doppler Radar Data, Day 209, Penetration 2B	186
H23.	Estimates of Turbulence Severity Derived From Doppler Radar Data, Day 209, Penetration 3A	187
H24.	Estimates of Turbulence Severity Derived From Doppler Radar Data, Day 209, Penetration 3B	187
H25.	Estimates of Turbulence Severity Derived From Doppler Radar Data, Day 209, Penetration 4A	188
H26.	Estimates of Turbulence Severity Derived From Doppler Radar Data, Day 209, Penetration 4B	188
H27.	Estimates of Turbulence Severity Derived From Doppler Radar Data, Day 209, Penetration 5A	189
H28.	Estimates of Turbulence Severity Derived From Doppler Radar Data, Day 209, Penetration 5B	189
H29.	Estimates of Turbulence Severity Derived From Doppler Radar Data, Day 209, Penetration 6A	190
H30.	Estimates of Turbulence Severity Derived From Doppler Radar Data, Day 209, Penetration 6B	190
H31.	Estimates of Turbulence Severity Derived From Doppler Radar Data, Day 211, Penetration 1	191
H32.	Estimates of Turbulence Severity Derived From Doppler Radar Data, Day 211, Penetration 2A	191
H33.	Estimates of Turbulence Severity Derived From Doppler Radar Data, Day 211, Penetration 2B	192
H34.	Estimates of Turbulence Severity Derived From Doppler Radar Data, Day 211, Penetration 3A	192
H35.	Estimates of Turbulence Severity Derived From Doppler Radar Data, Day 211, Penetration 3B	193
H36.	Estimates of Turbulence Severity Derived From Doppler Radar Data, Day 211, Penetration 4	193
H37.	Estimates of Turbulence Severity Derived From Doppler Radar Data, Day 211, Penetration 5	194
H38.	Estimates of Turbulence Severity Derived From Doppler Radar Data, Day 211, Penetration 6A	194
H39.	Estimates of Turbulence Severity Derived From Doppler Radar Data, Day 211, Penetration 6B	195
H40.	Estimates of Turbulence Severity Derived From Doppler Radar Data, Day 211, Penetration 7A	195
H41.	Estimates of Turbulence Severity Derived From Doppler Radar Data, Day 211, Penetration 7B	196
H42.	Estimates of Turbulence Severity Derived From Doppler Radar Data, Day 211, Penetration 8A	196

Illustrations

H43.	Estimates of Turbulence Severity Derived From Doppler Radar Data, Day 211, Penetration 8B	197
H44.	Estimates of Turbulence Severity Derived From Doppler Radar Data, Day 212, Penetration 1	197
H45.	Estimates of Turbulence Severity Derived From Doppler Radar Data, Day 212, Penetration 2	198
H46.	Estimates of Turbulence Severity Derived From Doppler Radar Data, Day 212, Penetration 3A	198
H47.	Estimates of Turbulence Severity Derived From Doppler Radar Data, Day 212, Penetration 3B	199
H48.	Estimates of Turbulence Severity Derived From Doppler Radar Data, Day 212, Penetration 4A	199
H49.	Estimates of Turbulence Severity Derived From Doppler Radar Data, Day 212, Penetration 4B	200
H50.	Estimates of Turbulence Severity Derived From Doppler Radar Data, Day 212, Penetration 5	200
H51.	Estimates of Turbulence Severity Derived From Doppler Radar Data, Day 212, Penetration 6	201
H52.	Estimates of Turbulence Severity Derived From Doppler Radar Data, Day 212, Penetration 7	201
H53.	Estimates of Turbulence Severity Derived From Doppler Radar Data, Day 212, Penetration 8	202
H54.	Estimates of Turbulence Severity Derived From Doppler Radar Data, Day 212, Penetration 9A	202
H55.	Estimates of Turbulence Severity Derived From Doppler Radar Data, Day 212, Penetration 9B	203

Tables

1.	Radar Probability of Detection and False Alarm Rate	22
2.	Radar Probability of Detection and False Alarm Rate	28
3.	Radar and Aircraft Observations During Lightning Events	38
B1.	Von Karman/Exponential Fit to Longitudinal Autocorrelation Function: Effective Turbulence Outer Scale λ_o (meters)	56
D1.	Radar Probability of Detection and False Alarm Rate: Variation With Range	67

Joint Agency Turbulence Experiment Final Report

1. INTRODUCTION

The Air Force Geophysics Laboratory (AFGL) is investigating the use of Doppler radar to detect turbulence in regions of precipitation. The purpose of this effort is to develop an airborne sensor which would enable pilots to identify and avoid regions of turbulence hazardous to aircraft. This effort is being directed in two phases. First, it is necessary to demonstrate the ability of radar to detect and quantify regions of hazardous turbulence, and secondly, to develop and test an on-board airborne sensor which could be used on aircraft. The theoretical foundations have been previously discussed (Bohne^{1, 2}). Preliminary aircraft and radar data analyses have also been presented (Bohne³). This report represents the completion of the data analysis phase.

To obtain the necessary highly coordinated aircraft and radar data to properly test the radar techniques, AFGL established the Joint Agency Turbulence Experiment and participated in the Storm Hazards Program directed by NASA Langley

(Received for publication 15 January 1985)

1. Bohne, A.R. (1981) Radar Detection of Turbulence in Thunderstorms, AFGL-TR-81-0102, AD A108679.
2. Bohne, A.R. (1982) Radar detection of turbulence in precipitation environments, J. Atmos. Sci. 39:1819-1837.
3. Bohne, A.R. (1983) Joint Agency Turbulence Experiment - Interim Report, AFGL-TR-83-0180, AD A137167.

Research Center and NASA Wallops Flight Center. The emphasis of the Storm Hazards Program was to study effects of lightning on aircraft systems and also to observe the meteorological phenomena associated with lightning events. To accomplish this the NASA Langley Research Center flew an F106B aircraft, instrumented with lightning strike, atmospheric chemical, optical, X-ray, microwave, and gust parameter measuring equipment through active thunderstorms. Direction of the aircraft to electrically active storm regions was aided by on-board electric field mills supplied by AFGL, and ground-based lightning detection equipment.

Of prime interest to AFGL was the ability of the aircraft to measure the three orthogonal gust component parameters, enabling AFGL to obtain ground-based radar and in situ aircraft data that were spatially and temporally coincident. To accomplish this AFGL incorporated Doppler Pulse Pair Processing and display equipment into the NASA Wallops Spandar radar. With the Spandar radar operating in an aircraft tracking mode during storm penetration, AFGL was able to obtain the desired coordinated aircraft gust data and ground-based Doppler pulse-to-pulse in-phase and quadrature return data. The correlation of the turbulence severity estimates, as determined from these aircraft and radar data, have been used to more accurately determine useful radar methodologies for remote turbulence detection.

For the sake of brevity much of the material is presented in the appendices. This includes discussions of methods for estimating effective turbulence outer scale, the stability of the aircraft turbulence severity estimates, and radar pulse volume filtering effects upon radar structure function estimates. The basic radar time history data, along with the time histories of turbulence severity estimates are presented in Appendices F-H. Also, a discussion of the operational mode and methodologies for basic data reduction and analyses were presented in the Joint Agency Turbulence Experiment - Interim Report. This material, along with supplemental information concerning additional data reduction and analysis procedures are presented in Appendix A. The main body of the report will present only the necessary background material and a discussion of the results of the analyses.

2. ESTIMATION OF TURBULENCE SEVERITY BY RADAR METHODS

The parameter of interest for determining the degree of hazard of turbulence is the turbulence severity, where turbulence severity is here defined as the cube root of the eddy dissipation rate (ϵ). Estimates of turbulence severity are obtained through use of in situ aircraft gust component data and ground-based radar time series in-phase and quadrature sample return data. Here we will consider only the relationship of the radar measurements to the environmental turbulence

field. The radar data were obtained from a radar pulse volume located generally within 300 m of the aircraft position by slaving the NASA Wallops SPANDAR radar (parallax corrected) to a tracking radar. The radar time series data were analyzed using objective thresholding, Pulse Pair Processing, and constant threshold below Doppler spectrum peak, methods to observe the performance of the various Doppler techniques currently in use. In the final comparisons only the objectively thresholded data were used in the turbulence analyses, since the Doppler spectra data were found to be contaminated, requiring full Doppler spectrum data at hand to employ objective image spectrum removal techniques. The resulting radar data were used with three different techniques for estimating the turbulence severity.

First, the Doppler spectrum variance is employed in a technique discussed by Bohne³ which assumes that the environmental turbulence field may be modeled as inertial in form (Kolmogorov 5/3 law) with a finite effective turbulence outer scale. The term effective outer scale implies that the energy contained in the environmental turbulence field, distributed over a range of scales including permanent, energy containing, and inertial subrange eddy (Kolmogorov) regimes, may be set equal to that found in the modeled field by adjustment of the turbulence outer scale. Numerical tests, using a Von Karman relation to model the true turbulent environment and the Kolmogorov model field with an effective outer scale length set such that the energy of the Kolmogorov field was equal to that contained in a Von Karman field which included eddy scales from the non-isotropic energy containing scales and smaller, showed differences of less than 3 percent in the derived estimates of turbulence severity. Thus, use of the Kolmogorov (inertial) model for the environmental turbulence field, with a properly adjusted effective outer scale, is adequate.

The second method employed the Doppler spectrum variance with a relation derived by Frisch and Clifford.⁴ Here, once again, it is assumed that the energy contained in the environment turbulence field is Kolmogorov distributed, but the effective turbulence outer scale is assumed infinite in size.

The third technique employed the Doppler spectrum mean radial velocity in a structure function analysis. Here the general relation which include both the longitudinal and transverse terms was used. This was necessitated by the aircraft penetration tracks usually not lying along, or transverse to, the radial from the radar to the aircraft. The structure function data were analyzed at scale lengths where the turbulence field is assumed inertial in form.

4. Frisch, A. S., and Clifford, S. P. (1974) A study of convection capped by a stable layer using Doppler radar and acoustic echo sounders, J. Atmos. Sci. 31:1622-1628.

The success of all three techniques is dependent not only upon the environmental turbulence field being successfully modeled by a Kolmogorov type energy distribution scheme, but also upon the turbulence field being homogeneous and isotropic. Consideration of the apparent degree of isotropy in the environmental turbulence field is presented in Section 5.

The applicability of these techniques under various turbulence conditions is easily understood when one considers the mechanics by which the turbulent gusts are mapped into the Doppler spectrum variance or the fluctuation of the Doppler mean velocity. This mapping is a result of the spatial filtering effects of the radar pulse volume upon the spectral distribution of energy in the environmental turbulence field. The general relationship between the Doppler spectrum parameters and the turbulence field is given by

$$\langle \text{VAR} \rangle = \int_{\vec{k}} \phi_{11}(\vec{k}) (R_2(k_z) - R_1(k_z)) \phi_I^*(\vec{k}) d\vec{k} \quad (1)$$

where $\langle \text{VAR} \rangle$ is the ensemble estimate of Doppler spectrum variance, \vec{k} is the three-dimensional turbulence wavevector, and

$$\phi_I(\vec{k}) = (2\pi)^6 F_I(\vec{k}) F_I^*(\vec{k}) \quad (2)$$

is the radar pulse volume filter function in wavevector space. Note that $F_I(\vec{k})$ is the Fourier transform of the two-way radar beam filter function $I(\vec{r}, \vec{R})$, where

$$I(\vec{r}, \vec{R}) = e^{-\left[\alpha \left(\frac{\theta^2}{\theta_o^2} + \frac{\phi^2}{\phi_o^2} \right) + \beta \left(\frac{x^2}{h^2} \right) \right]} \quad (3)$$

θ_o , ϕ_o are the one way full half-power beamwidths, and h the pulse volume length. The terms $R_2(k_z)$, $R_1(k_z)$ are the precipitation turbulent motion variance, and velocity, weighting factors respectively. These terms may be written as

$$R_z(k_z) = \frac{\int \frac{e^{-\Lambda D} D^6 dD}{(1 + k_z^2 (a D^b)^4 / g^2)}}{\int e^{-\Lambda D} D^6 dD} \quad (4)$$

$$R_1(k_z) = \left[\frac{\int \frac{e^{-\Lambda D} D^6 dD}{(1 + k_z^2 (a D^b)^4 / g^2)^{1/2}}}{\int e^{-\Lambda D} D^6 dD} \right]^2 \quad (5)$$

where the precipitation size distribution is assumed to follow an exponential form

$$N(D) dD = N_0 e^{-\lambda D} \quad (6)$$

and where $N(D) dD$ is the number of precipitation particles having diameter D to $D + dD$. The terms $(a D^b)^4$ and k_z represent the terminal velocity

$$V_T = a D^b \quad (7)$$

and z component of turbulence wavevector, respectively. $\phi_{||}(\vec{k})$ is the turbulence power density spectrum function of the radial [Eq. (1)] air velocity component. When looking along the z direction, the precipitation weighting functions [Eqs. (4, 5)] should be multiplied by 0.25. Now Eq. (1) may also be written as

$$\langle \text{VAR} \rangle = \overline{V_{\text{Prec}}^2} - \overline{V_{\text{Dop}}^2} \quad (8)$$

where the first term on the right represents the total measurable one dimensional precipitation motion variance contained by the precipitation in the environmental turbulence field. The second term represents the portion of this total measurable energy which is mapped into the fluctuation of the Doppler mean velocity. Thus the Doppler spectrum variance is simply the difference between the maximum one-dimensional radar measurable precipitation motion variance and the average variance of the turbulence induced fluctuation of the Doppler mean velocity.

The general performance of the two radar techniques (structure function and variance) may now be considered. When the radar pulse volume is small in size compared to the largest turbulence eddies, the radar pulse volume may effectively be considered a point size pulse volume interrogating the larger scale eddy structures. In wave vector space the beam filter function $\phi_1(\vec{k})$ is effectively unity over all \vec{k} , resulting in most turbulent motion energy being mapped into fluctuation of the mean Doppler velocity, and results in a very small measured Doppler spectrum variance. Here, the structure function method which relies upon the fluctuation of the Doppler mean velocity

$$D(r) = \langle (V_{\text{Dop}}(x) - V_{\text{Dop}}(x+r))^2 \rangle \quad (9)$$

where r is the separation distance between the two velocity measurements, has potential to accurately represent the true environmental structure function. Alternatively, when the radar pulse volume is larger than the largest turbulence scale, the beam filter function in wavevector space is close to zero except for \vec{k} near zero. In this instance the measurable turbulent precipitation motion is mapped primarily

into Doppler spectrum variance. Now the radar structure function is a poor representation and severely underestimates the true environmental value.

The Doppler spectrum variance-based methods, on the other hand, take into account the radar beam filtering effects, and if the variance estimates are not contaminated, then these methods have potential to estimate well the turbulence severity over a wide range of pulse volume sizes (distance from the radar) as long as the true environmental turbulence field has been modeled properly and the proper choice of effective outer scale has been made. If the outer scale chosen is too large (small), then the resulting turbulence severity estimate will underestimate (overestimate) the true environmental value.

A demonstration of the typical performance of the two different techniques may be observed in Figures 1 and 2. Figure 1 displays the turbulence severity estimates for the structure function, and variance ($\lambda_o = 0.5, 2.0, \infty$ km) methods. The corresponding estimates derived from the in situ aircraft data are shown in Figure 2.

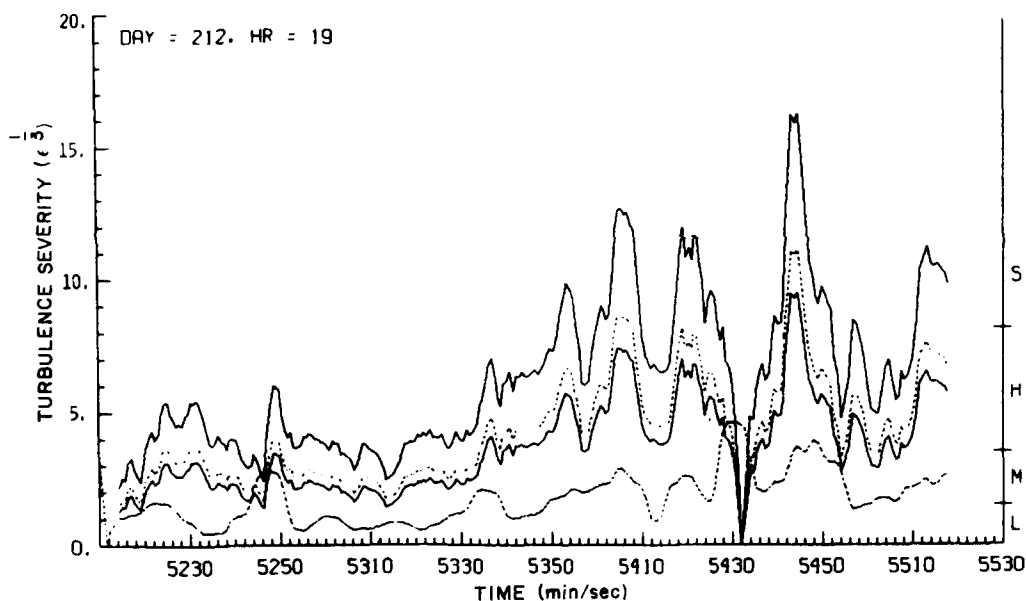


Figure 1. Time History of Turbulence Severity ($\epsilon^{1/3}$) as Estimated From Radar Data Using Structure Function (lower dash), and Doppler Spectrum Variance Methods With $\lambda_o = 0.5$ km (upper solid), $\lambda_o = 2.0$ km (upper dash), and $\lambda_o = \infty$ km (lower solid) for Penetration 5 on 31 July 1982. Light, moderate, heavy, and severe severity regimes are noted on right ordinate

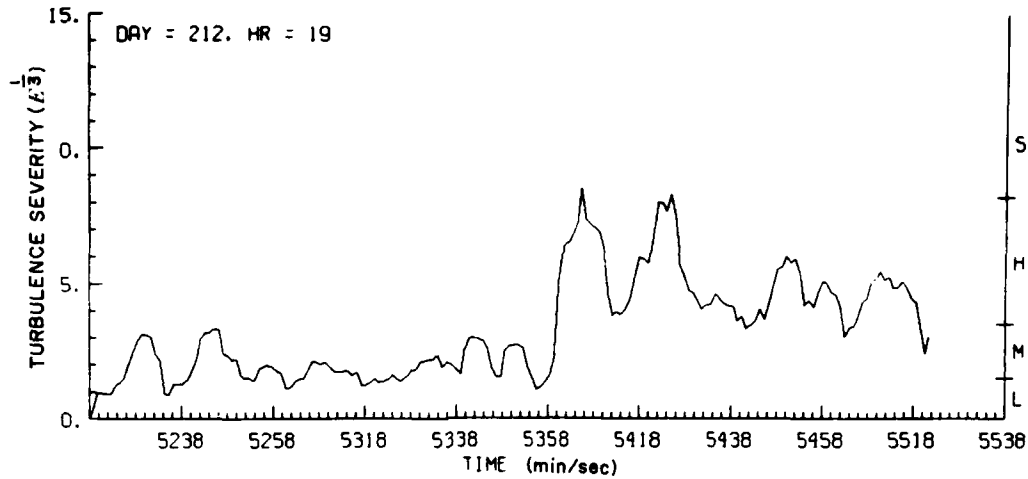


Figure 2. Time History of Turbulence Severity ($\epsilon^{1/3}$) as Estimated From Aircraft Gust Data Using Structure Function Method

These results are typical and demonstrate that the turbulence severity estimates determined from the radar structure function method are, in practice, almost always smaller in magnitude than those derived from the radar variance methods. As stated above, this results mainly from reduction of the fluctuation of the Doppler mean velocity due to radar beam filtering. Also note, however, that the variance techniques appear to consistently overestimate the severity in truly light turbulence regions. This results from contamination of the Doppler spectrum variance estimates. Finally, note the reduction in the magnitude of the turbulence severity estimate with increasing effective turbulence scale.

The inability of the structure function method to detect moderate to severe levels of turbulence, combined with the inability of the variance methods to detect light levels of turbulence while demonstrating good potential to detect moderate to severe classes, suggests additional factors are influencing the radar estimates. We may estimate a minimum bias in the two estimators by considering the measured radial velocity V_{Dop} to be a sum of a storm V_S , turbulence V_T , and error eRR component as shown by

$$V_{Dop} = V_S + V_T + eRR. \quad (10)$$

The resulting structure function estimate is now expanded to

$$D(r) = \left\langle \left[(V_S(x) + V_T(x) + eRR(x)) - (V_S(x+r) + V_T(x+r) + eRR(x+r)) \right]^2 \right\rangle \quad (11)$$

Now experience has shown that the dominant storm scales, those which contain the major portion of storm wind field energy, appear to be in the range of 5 to 8 km (Bohne¹). Observed effective turbulence outer scale values consistently appear to lie in the range of 0.5 to 3 km. To a first approximation, the storm wind field may be considered quasi-stationary relative to the turbulence and error components, and the turbulence field quasi-stationary relative to the error component. Each component may also be considered uncorrelated with the others. Under this assumption the structure function is approximately represented by

$$D(r) = \langle (V_S(x) - V_S(x+r))^2 \rangle + \langle (V_T(x) - V_T(x+r))^2 \rangle + 2 \overline{eRR^2} . \quad (12)$$

Any constant bias component of eRR has been removed and only the random component remains. To a first level of approximation we may assume its minimum value results from the natural statistical fluctuation of the Doppler mean velocity. This is given by

$$eRR^2 = L \sigma_D / (8\sqrt{\pi} T) \quad (13)$$

where T is the radar dwell time, σ_D is Doppler spectrum standard deviation, and L is radar wavelength. For typical observations, T = 0.25 sec, L = 0.1 m. Thus for a Doppler spectrum variance of 4 (m/sec)² we have a value of $eRR^2 = 0.06$ (m/sec)². The resulting contribution to the structure function estimate of turbulence severity is about 0.14 cm^{2/3}/sec. For a nominal storm wind shear of the radar radial velocity of 1.0 m/sec/km, a typical contribution to D(r) from the storm component would be about 0.25(m/sec)², contributing about 0.21 cm^{2/3}/sec to the turbulence severity estimate. So a typical minimum turbulence severity estimate via the radar structure function method may be of the order of 0.25 cm^{2/3}/sec. This value is small when compared against the observed deficit in severity estimates in regions of strong turbulence and shows that pulse volume filtering may be the dominant influence in determining the applicability of the structure function method for estimation of turbulence severity by radar.

Alternatively, at a range of 100 km, the contribution to Doppler spectrum variance from this same level of storm shear is only 0.05(m/sec)² and the corresponding minimum severity value is only 0.75 cm^{2/3}/sec. This value is small when compared to the observed severity overestimate. Although the variance data here were corrected for storm shear, antenna rotation, and spectrum averaging effects, there is obviously some contribution not yet accounted for. Thus the limiting factor which determines the ability of the variance-based method to detect light

turbulence regions is the degree to which we can remove contaminant effects. This topic will be discussed further in Section 4.

3. STORM ENVIRONMENTS

A brief discussion of the storm environments encountered by the NASA Langley aircraft will be presented. Since the 1981 data have already been reported (Bohne³), only a brief discussion of the 1981 data will be given here. The methods of obtaining the sounding data and the storm reflectivity factor on Cartesian surfaces are detailed in Appendix A. In the following discussion all reference to radar radial velocity and spectrum variance refer to data acquired in the tracking gate while the SPANDAR radar was slaved to the aircraft. These data are presented in Appendix F. Also, analysis has shown that large spectrum variance is almost always an indicator of strong turbulence, thus these two terms may be used interchangeably in following discussions.

During the 1981 season, four storm periods were chosen for analysis. The first data set was obtained on 1 July 1981 (Day 182). The environmental sounding (Figure E1) shows the wind to vary slowly from about 170 degrees near the surface to 120 degrees at 6 km, with the speed increasing gradually from about 14 m/sec to 20 m/sec over the same layer. At the penetration altitude of 4.57 km (Figure 3) the storm appears as a simple, single cell storm of very limited spatial extent, with the radar observed storm boundary occupying only 200 km² in area. The maximum observed reflectivity factor at penetration altitude is slightly more than 35 dBZ. The aircraft penetrates the northern portion of the storm in a region of low reflectivity factor and light radial velocity and light to moderate shear. The time history of Doppler spectrum variance data (Figure F2) shows reasonably good correlation with the periods of strongest shear of the radial wind (Figure F1), but no distinct correlation with storm reflectivity structure.

The second analysis period, 3 July 1981 (Day 184), represents a case where the aircraft penetrated a storm complex consisting of two dominant reflectivity factor cells having maximum values near 45 dBZ at penetration level (Figure 4). The radial velocity (Figures F3, F5, F7 and F9) and Doppler spectrum Figures F4, F6, F8 and F10) variance data exhibit regions of large variance with generally little correlation to periods of strong shear of the radial wind. There is some notable correlation of regions of strong turbulence with storm structure, however. For example, locations where the aircraft penetrated the storm cells or passed along the cell boundaries (19:58:00 GMT, Figures F3-F6; 20:04:35 GMT, and 20:05:40 GMT, Figures F7, F8, and 20:11:50 GMT, Figures F11 and F12). Other regions of strong turbulence are encountered in between the two storm cells (Pen 2) in the benign

appearing 25 dBZ region northeast of the northern storm cell, and in the low reflectivity factor region downwind of the southern storm cell.

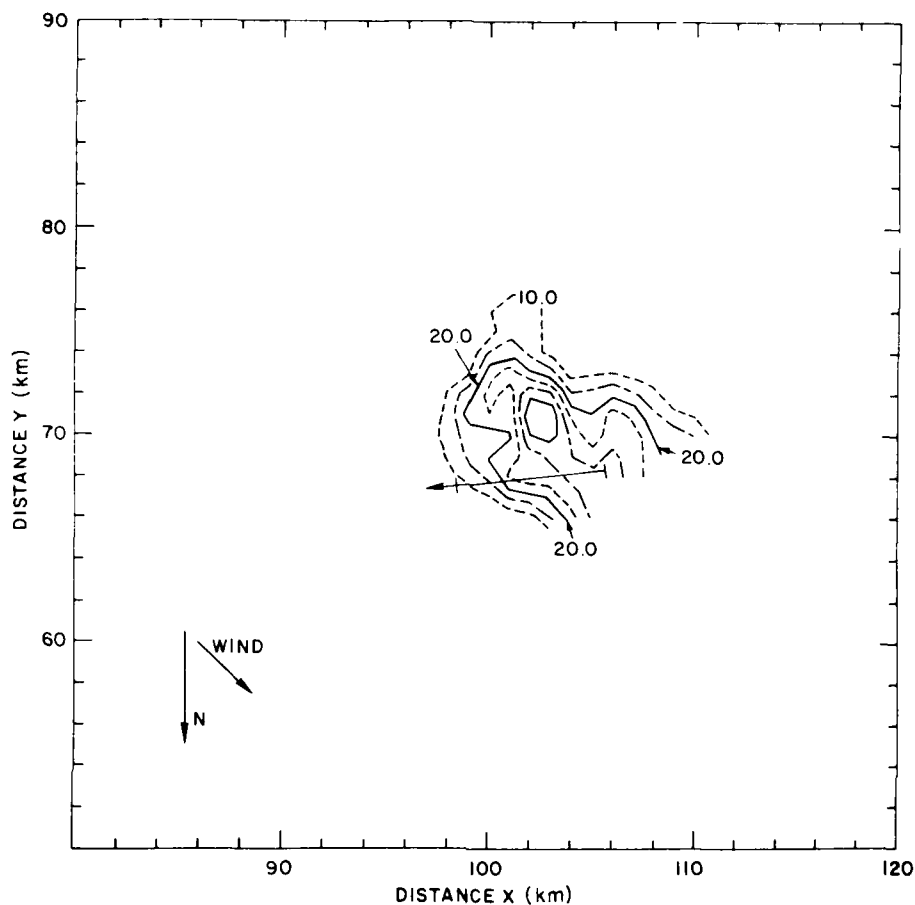


Figure 3. Contours of Storm Reflectivity Factor (dBZ) for 1 July 1981 on Constant Height Surface at Aircraft Storm Penetration Altitude of 4.57 km. Contours are in 5 dBZ increments with a recycling dot, dash, and solid pattern. Minimum plot contour value is 10 dBZ. Time-adjusted aircraft track is shown. Distances are relative to SPANDAR radar. Plot time is 18:17:00 GMT

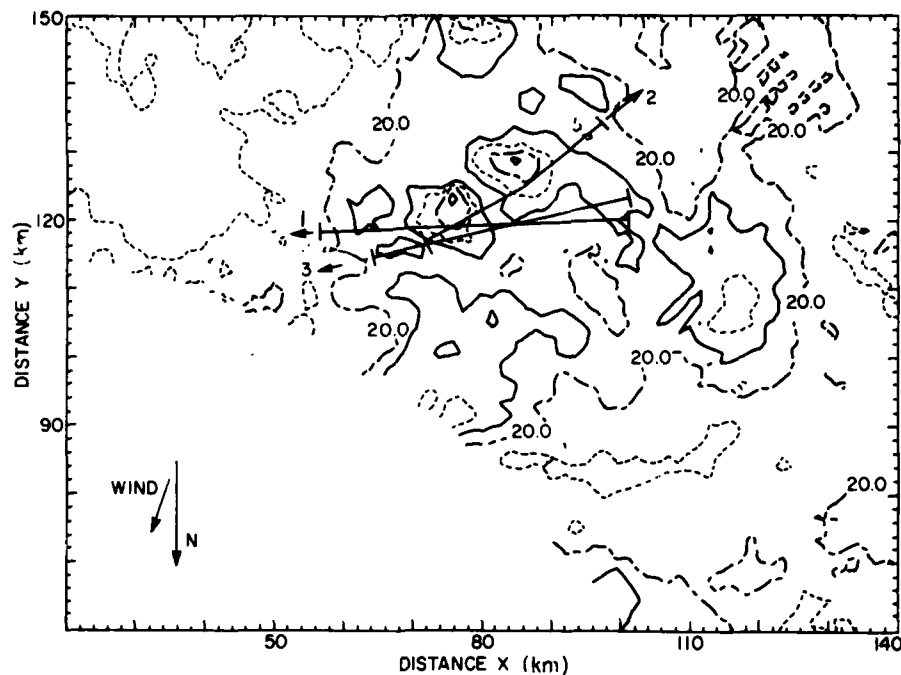


Figure 4. Contours of Storm Reflectivity Factor (dBZ) for 3 July 1981 at Aircraft Penetration Altitude of 4.87 km at 20:02:11 GMT. Contours are in 5 dBZ increments with a recycling dot, dash, and solid pattern. Minimum plot contour value is 15 dBZ. Time-adjusted aircraft tracks are shown. Distances are relative to SPANDAR radar

16 July (Day 197) represents a case of widespread precipitation containing a few localized cells of maximum reflectivity factor near 35 dBZ at the penetration altitude of 3.5 km (Figure 5). For both penetrations, one passing through a small reflectivity factor cell and the other near the radar detectable storm boundary, variance values are small, being in the range of $1-2.5 \text{ (m/sec)}^2$. The shear of the radial wind is small, and except for a minor correlation of increased shear with increased variance at 18:48:23 GMT (Figures F15 and F16), there is negligible correlation between the variation of variance and radial velocity shear.

The last analysis period for 1981, 17 July (Day 198) represents an unusual occurrence where the storm complex (Figure 6) is relatively close to the SPANDAR radar. This complex is dominated by a single cell storm having a maximum reflectivity factor near 50 dBZ. The time-adjusted aircraft tracks show the penetration paths to reside on the periphery of this dominant storm. The radar Doppler spectrum variance and velocity data show significant fluctuations. However, except for the period near 18:39:40 GMT (Figures F19 and F20), there is very little correlation of increased variance with increased shear of the radial wind.

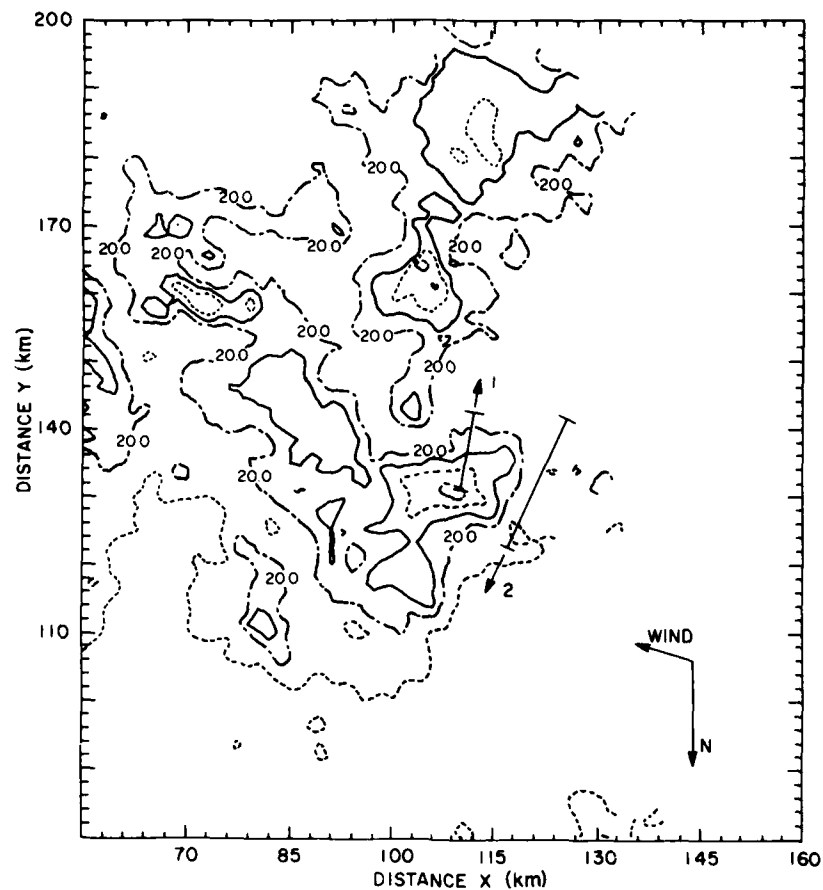


Figure 5. Contours of Storm Reflectivity Factor (dBZ) at Aircraft Penetration Altitude of 3.5 km for 16 July 1981 at 18:32:37 GMT. Contours are in 5 dBZ increments with a recycling dot, dash, and solid pattern. Minimum plot contour value is 15 dBZ. Time-adjusted aircraft tracks are shown. Distances are relative to SPANDAR radar

It is observed that for the 1981 season most of the storm relative aircraft penetration tracks were in peripheral regions of the storms under investigation. Thus, incomplete information concerning the occurrence of significant Doppler spectrum variance, usually indicating significant turbulence severity, with dominant reflectivity features of the storms was obtained. Episodes of significant turbulence were found throughout the general storm environments. This small 1981 data set shows that strong turbulence may generally be expected in close proximity to the active storm cells, but may also be found in benign appearing regions exhibiting low reflectivity factor. Finally, periods of strong turbulence do not appear well-correlated with strong storm wind shear.

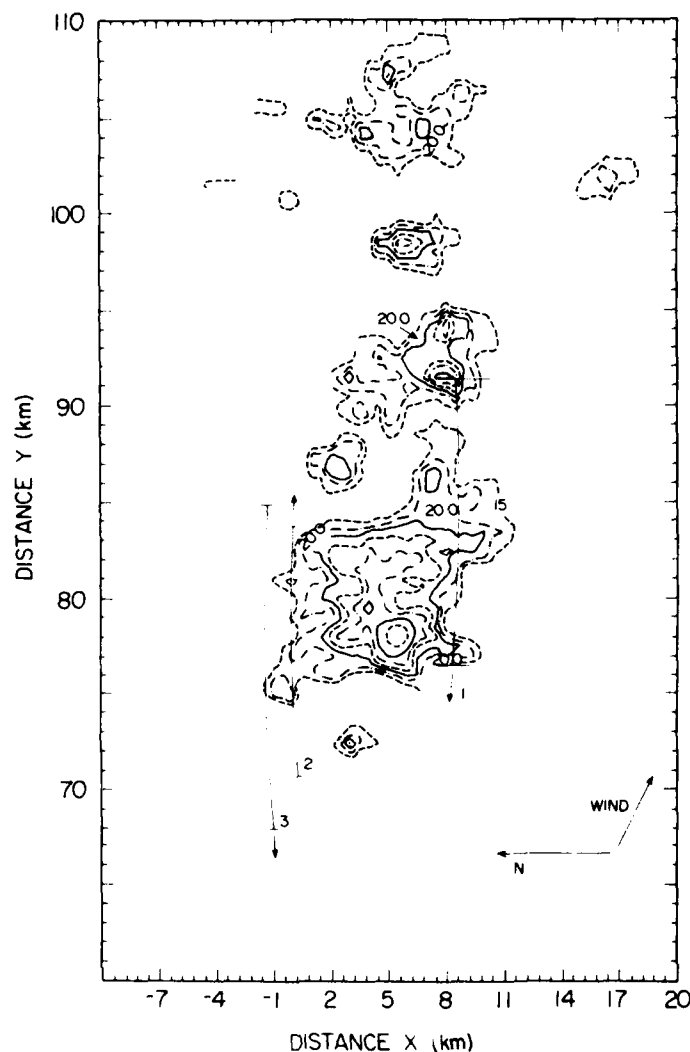


Figure 6. Contours of Storm Reflectivity Factor (dBZ) at Aircraft Penetration Altitude of 3.35 km for 17 July 1981 at 18:35:00 GMT. Contours are in 5 dBZ increments with a recycling dot, dash, and solid pattern. Minimum plot contour value is 15 dBZ. Time-adjusted aircraft tracks are shown. Distances are relative to SPANDAR radar

During the 1982 field program a large number of data sets were acquired. However, in an attempt to attract a greater number of lightning strikes, the aircraft penetrations were frequently made near storm top where storm reflectivity factor was often low. This factor, in combination with the extreme range of some of the storms penetrated, resulted in only four data sets actually being analyzed. Also, the aircraft turn around interval, the time between the end of the last storm penetration and the start of the next penetration was significantly less than in 1981. This, in addition to other scan requirements resulted in few radar volume sector scans being obtained during aircraft turn around periods. Thus relatively few

reflectivity factor plots are available to portray the changing character of the penetrated storms during the observation periods. As for 1981 data, the aircraft tracks are advected, as determined by storm motion, to more accurately display the placement of the penetrations relative to the prominent storm features at plot time. On several occasions, insufficient data exist to develop a useful plot at the aircraft penetration altitude. In this instance a storm reflectivity factor profile for a lower altitude is chosen in an attempt to display the prominent storm features. Finally, on several occasions, very long penetrations were broken into two separate components for ease of data analysis. These exceptions will be noted.

The first analysis period, 17 July (Day 198), studied a relatively small storm approximately 160 km to the southwest of the radar (Figures 7 and 8). The aircraft altitude, as determined by radar, increases from roughly 8.3 to 9.3 km over the duration of the penetrations. The reflectivity factor plot depicts the nature of the storm at a lower altitude of 6.0 km. Figures 7 and 8 may be considered roughly coincident in time with the second and sixth penetrations. As shown, the aircraft is basically skirting two small cells exhibiting maximum reflectivity factors in the neighborhood of 45 dBZ. During the observation period, these two storms dissipate and advect northeastward as shown by the region exhibiting 25 dBZ near 40 km west and 140 km south (Figure 8). The last two tracks (Pen 6 and 7), pass through a new cell which develops on the upwind side of the initial storm complex. As shown, all penetrations occur in weak storm reflectivity factor environments having values in the range of 15 to 25 dBZ, except for penetration 2 which passes through a small cell of 35 dBZ.

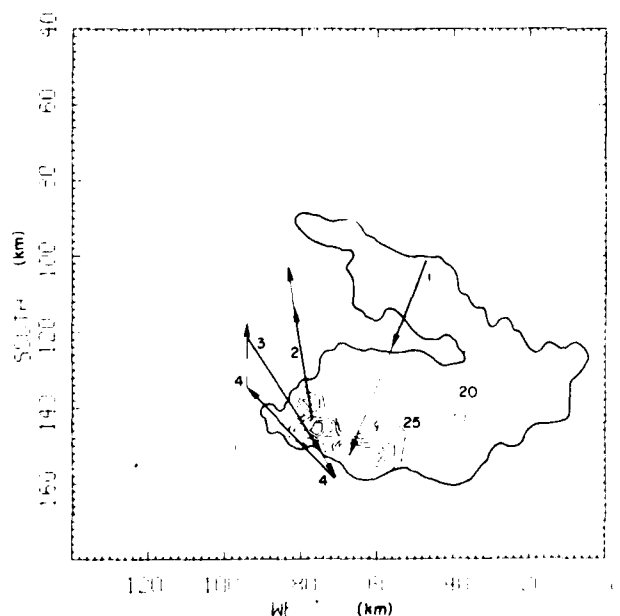


Figure 7. Contours of Storm Reflectivity Factor (dBZ) at 6.0 km Altitude for 17 July 1982 at 20:16:40 GMT. Time-adjusted aircraft tracks shown as arrows. Periods of coincident radar data shown as thick arrows. Minimum plot contour value is 20 dBZ. Contours are in 5 dBZ increments with a recycling dot, dash, and solid pattern. Distances are relative to SPANDAR radar

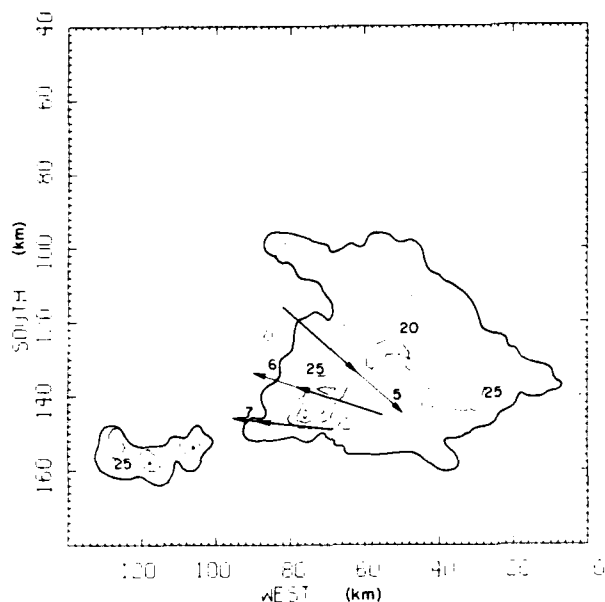


Figure 8. Contours of Storm Reflectivity Factor (dBZ) at 6.0 km Altitude for 17 July 1982 at 20:40:35 GMT. Minimum plot contour value is 20 dBZ. Contours are in 5 dBZ increments with a recycling dot, dash, and solid pattern. Distances are relative to SPANDAR radar

The seven penetration tracks shown in Figures 7 and 8 indicate that useful radar data were acquired generally in the vicinity of the storm cells. Observation of the radar radial velocity and variance data show only very minor fluctuations in radial velocity and Doppler spectrum variance along penetrations 1 (Figures F23 and F24) and 5 (Figures F31 and F32). Penetrations 2 (Figures F25 and F26), 3 (Figures F27 and 28), and 4 (Figures F29 and F30) display moderate shear at the outer 25 dBZ boundary (Pen 2, 19:42:42 GMT) of the smallest cell, upwind of the center cell (Pen 3 19:52:01 GMT, Pen 4 19:58:36 - 19:59:20 GMT), and between the two larger cells (Pen 3 19:52:21 GMT). The most significant variance periods are found within the smallest cell (Pen 2 19:42:12 GMT) and near the radar detectable boundary (Pen 2 19:42:42 GMT). Significant variance values are also found upwind of the center cell, but diminish in the region between the two larger cells. During penetration of the later cell development, the only notable shear is found within and adjacent to the 30 dBZ contour, but very large variance is found on the upwind edge of the 25 dBZ contour in this set of observations. The presence of significant shear of the radial velocity and heightened Doppler spectrum variance appear to be fairly well correlated with those periods where the aircraft track is within about 10 km of an active cell.

28 July (Day 209), represents an atypical case where an extensive and very active storm complex is close to the SPANDAR radar. The radar determined penetration altitude for penetrations 2 through 4 varies from 8-9 km, however, only Figure 9, showing the reflectivity factor at 3 km is available to show the active storm environment. The environmental wind is roughly 20 m/sec from 240 degrees (Figure E6) with the line advecting from 265 degrees at about 20 m/sec.

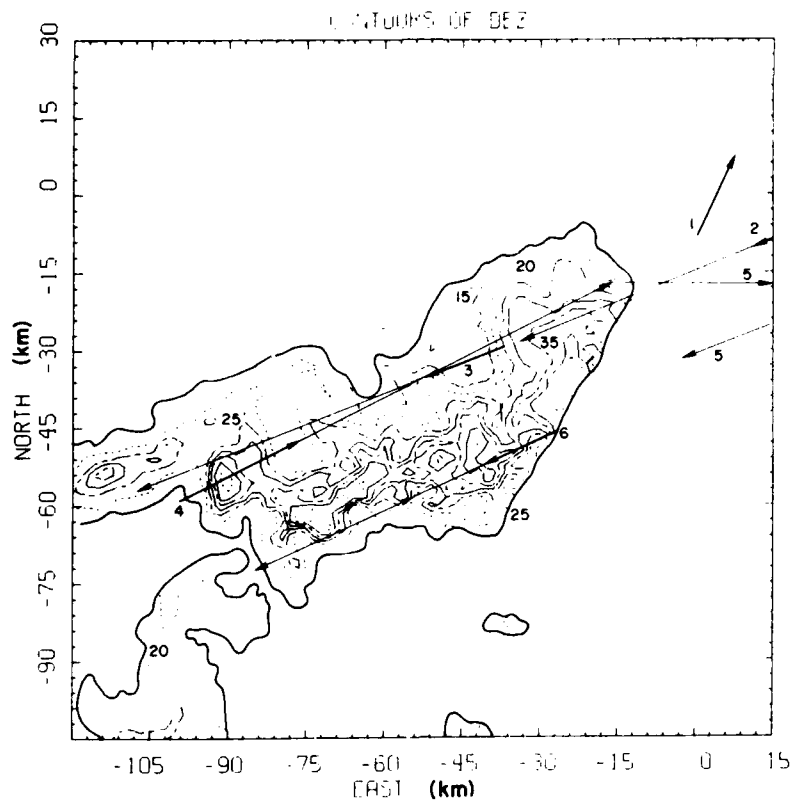


Figure 9. Contours of Storm Reflectivity Factor (dBZ) at 3.0 km Altitude for 28 July 1982 at 22:56:48 GMT. Contours are in 5 dBZ increments with a recycling dot, dash, and solid pattern. Minimum plot contour value is 15 dBZ. Time-adjusted aircraft tracks are shown. Distances are relative to SPANDAR radar

The storm advected aircraft tracks indicate that only penetration 4 passes near any active storm cells. The line actually extends another 90 km to the northeast, but this area was not the main region of interest. Figure 10, an RHI looking along an azimuth of 251 degrees may be considered to roughly approximate the storm environment along the third penetration. With storm tops near 12 km the aircraft was generally flying through regions exhibiting low reflectivity factor, resulting in those portions of aircraft penetrations where useful radar data were found to be extremely limited. Beyond the appearance of periods of large fluctuating variance being accompanied by minor shear of the radial wind during the last flight period (Pen 6), little correlation of storm features with radar kinematic features can be noted.

The third analysis period, 30 July (Day 211) shows an isolated storm of small extent ($< 900 \text{ km}^2$) with maximum reflectivity factor near 40 dBZ advecting rapidly towards the northeast at approximately 20 m/sec. The radar estimated aircraft

penetration altitude decreased from 8 km to 6 km during observations. Figure 11 portrays the storm reflectivity factor environment for a mean radar determined altitude of 7.2 km, and may be considered nearly coincident in time with penetration 2. This run approaches to within 6 km of the region of highest reflectivity factor (40 dBZ). The other penetrations essentially flirt with the radar determined storm boundary.

The time histories of radar radial velocity and spectrum variance are shown in Figures F49-F64. Note that penetration 8 occurred where a small new cell was developing, but the radar scan geometry does not include it in the present plot. Penetration 1 (Figures F49 and F50) exhibits some significant shear of the radial wind and large Doppler spectrum variance in the blowoff region downwind of the storm, while penetration 2 (Figures F51 and F52) shows no strong kinematic structure. Penetrations 3 (Figures F53 and F54), 5 (Figures F57 and F58) and 6 (Figures F59 and F60) show strong shear of the radial velocity as the aircraft passes along and through the 25 dBZ contour, and strong shear is also found outside the

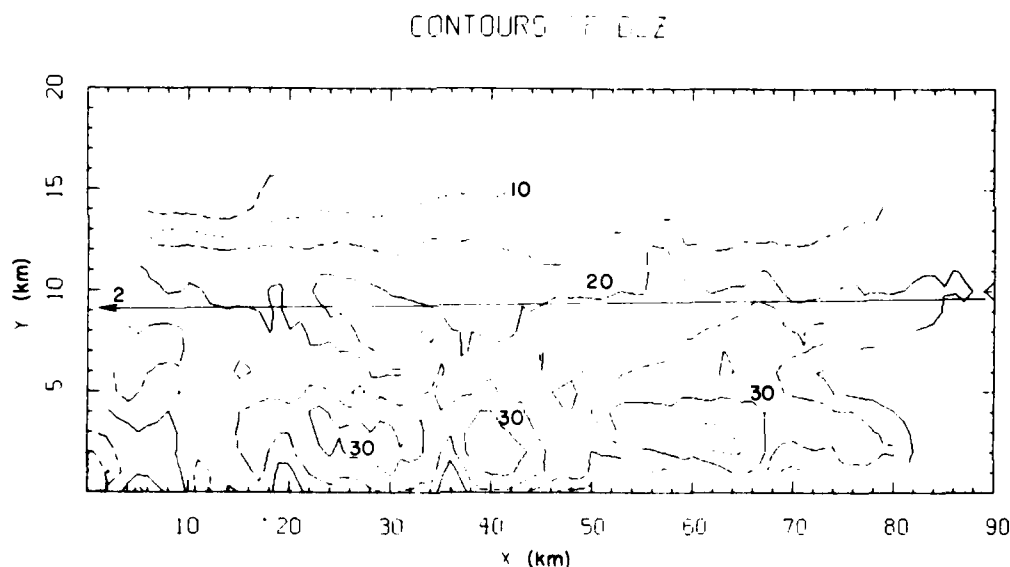


Figure 10. Contours of Storm Reflectivity Factor (dBZ) Along an Azimuth Angle of 251 Degrees for 28 July 1982 at 22:56:48 GMT. Contours are in 5 dBZ increments with a recycling dot, dash, and solid pattern. Minimum plot contour value is 5 dBZ. Time-adjusted aircraft track is shown. Distances are relative to SPANDAR radar

central storm region (Pen 5 20:02:29 GMT). Significant spectrum variance, however, is distributed throughout the 25 dBZ region (Pen 5), during exit from the 25 dBZ region (Pen 3 19:38:55 GMT) and passage along the 25 dBZ contour (Pen 6). Strong shear and large variance are also observed upwind of the storm and in low (< 20 dBZ) reflectivity factor regions. In general, we note that strong shear and variance are found well distributed throughout the storm.

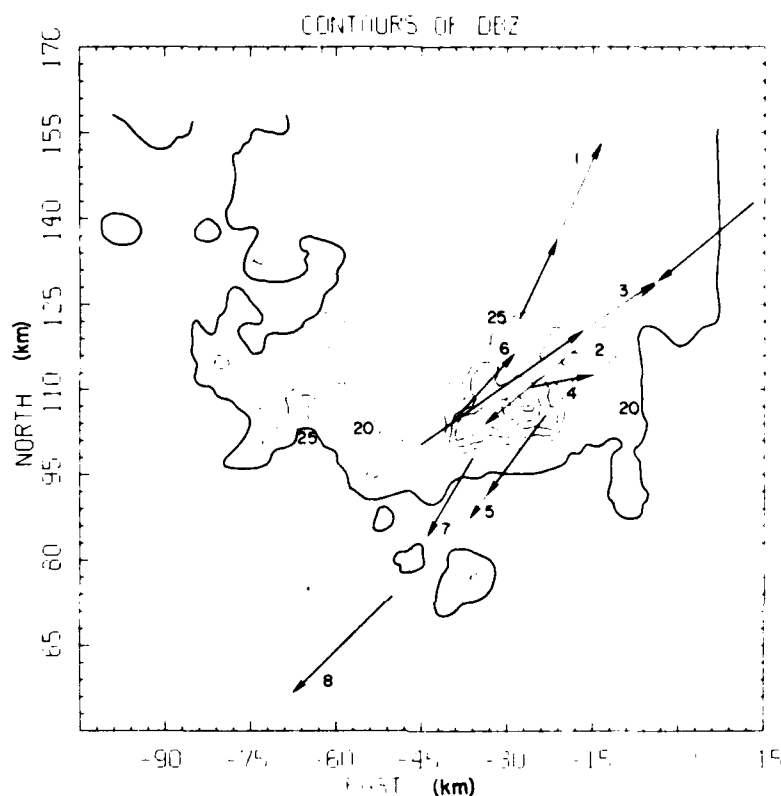


Figure 11. Contours of Storm Reflectivity Factor (dBZ) at Altitude of 7.2 km for 30 July 1982 at 19:45:20 GMT. Contours are in 5 dBZ increments with a recycling dot, dash, and solid pattern. Minimum plot contour value is 20 dBZ. Time-adjusted aircraft tracks are shown. Distances are relative to SPANDAR radar

The final observation period 31 July (Day 212), represents a second period where an extensive complex of storms was penetrated. The three primary storms are located near (110 km, 114 km), (40 km, 128 km), and (6 km, 132 km) west and south, respectively. The line is advecting with a speed of about 14 m/sec from 250 degrees. The plots portray the environment at the radar determined

mean penetration altitude of 7.19 km. Penetrations 1 through 5 lie just downwind of the storms, while penetrations 6 through 9 pass through the storms during dissipation stage. Track No. 's 2, 3, and 5, 6 represent the beginning and latter portions of actual penetrations 2 and 4, respectively. Figures 12 and 13 may be considered coincident with penetrations 1 and 6.

On this final day of analysis the most dramatic occurrence of strong shear of radial velocity and large spectrum variance occur during passage through the 30 dBZ cell near 30 km west and 120 km south (Figure 12). Here the shear and variance values are consistently high during passage through the entire cell. There are to be noted, however, areas far removed from any active storm regions which also exhibit significant shear and variance. Examples would be penetrations 2 (19:25:10 GMT) and 3 (19:27:56 GMT). This is shown in Figures F67 and F68 and Figures F69 and F70, respectively. The magnitude of shear and variance observed during penetration of the small cells during penetrations 8, 9 (Figures F79, F80 and Figures F81, F82) are no greater than, nor offer any more significance than, those observed in the low reflectivity factor regions. Observations this day further demonstrate that regions of large radial velocity shear and spectrum variance are not necessarily concentrated within the general confines of the storm cells, but may also be found in peripheral areas as well.

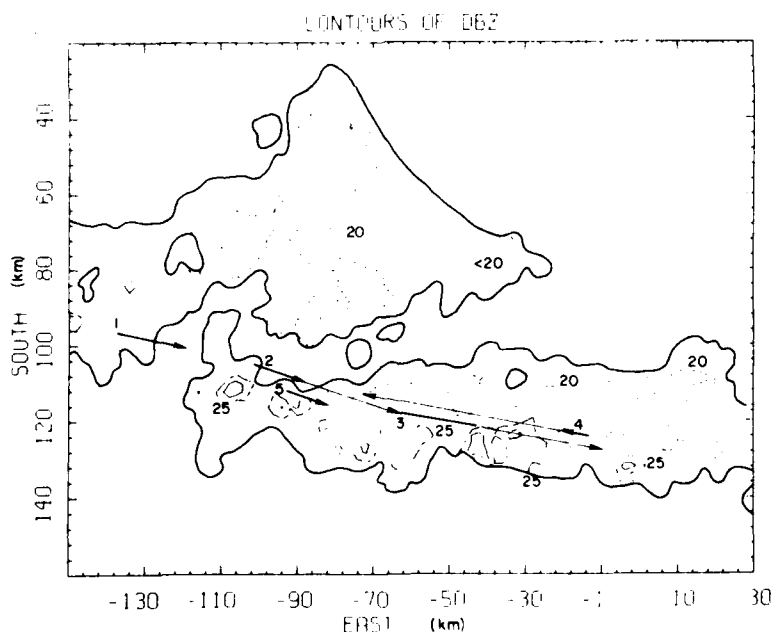


Figure 12. Contours of Storm Reflectivity Factor (dBZ) at Altitude of 7.19 km for 31 July 1982 at 19:20:02 GMT. Contours are in 5 dBZ increments with a recycling dot, dash, and solid pattern. Minimum plot contour value is 20 dBZ. Time-adjusted aircraft tracks are shown. Distances are relative to SPANDAR radar

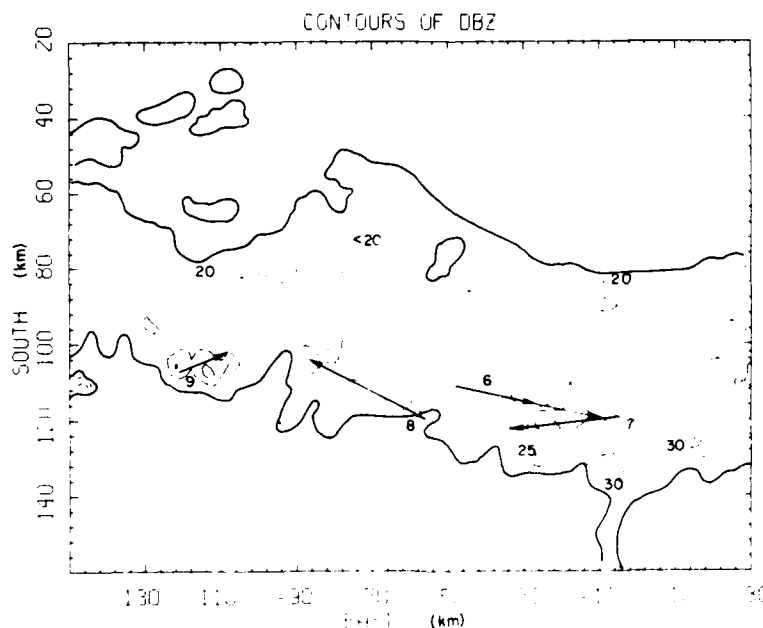


Figure 13. Contours of Storm Reflectivity Factor (dBZ) at Altitude of 7.19 km for 31 July 1982 at 20:14:52 GMT. Contours are in 5 dBZ increments with a recycling dot, dash, and solid pattern. Minimum plot contour value is 20 dBZ. Time-adjusted aircraft tracks are shown. Distances are relative to SPANDAR radar

4. COMPARISON OF RADAR AND AIRCRAFT ESTIMATES OF TURBULENCE SEVERITY

Perhaps the simplest measure of applicability of the various radar based techniques for estimating turbulence severity is the rate of success and failure of each method. The probability of detection (POD) and false alarm rate (FAR) values for the various techniques were determined over four separate ranges of turbulence severity (0-1.5, 1.5-3.5, 3.5-8.2, > 8.2 $\text{cm}^{2/3}/\text{sec}$). The technique of Bohne² employed four different estimates of the effective turbulence outer scale. The values used were $\lambda_o = 0.5, 1.0, 2.0, \text{ and } 4.0 \text{ km}$. Time series plots of radar turbulence severity estimates for these four values of λ_o will obviously be identical in form. However, use of such a field of values may provide some insight into a single effective outer scale value which may be used in general storm environments, or at least those values which will emphasize light or heavy turbulence regimes. The assignment of the values of turbulence severity for these light, moderate, heavy,

and severe ranges are the same as described by MacCready.⁵ This in no way suggests that these levels are the standard to be used by all aircraft in all situations, since they are somewhat a function of aircraft type and speed. They do, however, provide a useful means of comparing the various techniques. It is felt that any adjustment of the demarcation of the various turbulence severity levels would most likely be upward, so that any techniques which better emphasize the heavier turbulence regimes would be more successful in any new turbulence severity scale.

The aircraft estimates of turbulence severity are serving as ground truth data against which the radar estimates are compared. The aircraft structure function estimates of eddy dissipation rate from the separate gust component data are used to form a weighted average value. The weights are proportional to the degree of alignment of the gust component directions along the radar viewing direction at the location in question. Thus along a nearly radial aircraft penetration greatest weight is given to the estimate derived from the longitudinal gust component data. For a penetration nearly perpendicular to the radar viewing direction, the greatest weight is given to the transverse component estimate. The detection and failure rates of radar estimates of turbulence severity as determined from comparison with this "merged" aircraft data set are presented in Table 1.

Since the aircraft penetration tracks were generally not aligned along, or transverse to, the radar viewing direction, the radar tracking gate was frequently stepping in range as the radar scanned in azimuth. This, in combination with selection of a subset of radar data (Appendix A) where the radar estimates are spaced roughly uniformly apart, results in a radar data set where the estimates are essentially independent. On the other hand, the radar data spacing is much smaller than the 1200-m length of the segments of aircraft data used to form each aircraft estimate. Thus the aircraft estimates used are not completely independent. To increase the number of aircraft estimates and account for orientation and statistical biases a second method was also employed. Here the radar estimates of turbulence severity are compared separately with estimates derived from the individual gust components. This approach is reasonable if the turbulence is isotropic. Note that the merged data set attempts to compare the radar estimate of turbulence severity with an aircraft data derived estimate approximating the value obtained along the radar viewing direction. The second method relies upon isotropocity and may be useful for removing errors due to small data sample statistics. If the turbulence field is isotropic, at least when measured in terms of turbulence severity, and the aircraft and radar estimates reasonably well represent ensemble values, then the comparisons should yield similar results. The separate

5. MacCready, P. (1964) Standardization of gustiness values from aircraft, J. Appl. Meteorol. 13:439-449.

analyses were performed. The POD and FAR results for the non-merged aircraft data were in fact nearly identical for all techniques and all ranges of turbulence severity. Thus they need not be discussed separately. This agreement, however, does suggest that at least when measured in terms of turbulence severity, the turbulence regions encountered may be considered effectively isotropic.

Table 1. Radar Probability of Detection and False Alarm Rate

1981 Merged Data												
Turbulence Severity ($\text{cm}^{2/3}$ /sec)	STRFN		$\lambda_o = 0.5$ km		$\lambda_o = 1.0$ km		$\lambda_o = 2.0$ km		$\lambda_o = 4.0$ km		$\lambda_o = \infty$ km	
	POD	FAR	POD	FAR	POD	FAR	POD	FAR	POD	FAR	POD	FAR
Light 0 - 1.5	38	54	1	0	1	0	2	0	6	0	10	0
Moderate 1.5 - 3.5	38	80	2	88	10	72	22	66	28	64	34	64
Heavy 3.5 - 8.2	26	22	38	54	65	40	77	34	81	30	84	27
Severe >8.2	0	100	75	83	46	84	9	92	10	87	10	80
1982 Merged Data												
Turbulence Severity ($\text{cm}^{2/3}$ /sec)	STRFN km		$\lambda_o = 0.5$ km		$\lambda_o = 1.0$ km		$\lambda_o = 2.0$ km		$\lambda_o = 4.0$ km		$\lambda_o = \infty$	
	POD	FAR	POD	FAR	POD	FAR	POD	FAR	POD	FAR	POD	FAR
Light 0 - 1.5	67	70	12	60	14	59	17	59	19	58	22	58
Moderate 1.5 - 3.5	37	66	22	46	33	45	46	45	47	46	55	45
Heavy 3.5 - 8.2	26	40	59	56	68	49	72	41	69	40	68	35
Severe >8.2	7	92	78	81	54	76	29	74	27	72	16	69

The POD and FAR estimates are determined from the standard relations

$$\text{POD} = X / Z$$

$$\text{FAR} = Y / (X + Y)$$

where Z is the total number of occurrences of aircraft severity in the desired range, X is the number of simultaneous radar estimates in the same severity range, and Y the number of radar estimates in the desired range when the aircraft value is not. Note that comparisons here are made between simultaneous aircraft and radar data. This is a stringent condition, in that it assumes that the radar and aircraft data are ideally co-located. Relaxation of this condition to allow for comparison of a radar value with nearby adjacent aircraft data could also be considered a reasonable approach, and would return higher POD and smaller FAR values than those reported here. Therefore the POD and FAR values presented here may be considered conservative. Because of different equipment configurations during the two seasons and the vast difference in the number of input data, results for the 1981 and 1982 seasons will be presented separately. First, the POD and FAR results for detection of turbulence severity within an individual severity level will be presented. Later, results for detection of turbulence within a range of severity levels will be presented. Finally, note that the probability values presented are multiplied by 100.

The distribution of the POD estimates for 1981 for the light turbulence range shows that of all six estimators used (structure function, and variance method with effective turbulence outer scale values of $\lambda_o = 0.5, 1.0, 2.0, 4.0, \infty$ km) only the structure function method displays any degree of success. Its mean value of detectability is 37 percent, indicating that 37 percent of the time the radar structure function estimate is in the same light turbulence range when the aircraft estimate is also in that same range. The variance-based methods are all totally inadequate, each having a POD under 10 percent. The aircraft measured 160 events while the total number of radar events (X + Y) in this severity regime for the various variance methods ranged only from 16 to 1 for the $\lambda_o = \infty$ to 0.5 km cases, respectively. Thus the variance methods all overestimate the turbulence severity when the aircraft measured turbulence in this light range. Since the solution ($\lambda_o = \infty$ km) generally underestimates the strength of turbulence when the measured variance accurately represents the turbulence contribution to Doppler spectrum variance, this result suggests the Doppler spectrum variance data contain significant non-turbulence conditions. It should be noted that although the structure function method offered greatest success, roughly 50 percent of the time it produced a false alarm.

Also, the variance-based methods yield deceptively low false alarm rates due to the extremely small data samples in this range.

The distribution of POD for the moderate range once again shows the structure function method is most successful in this low energy range of turbulence. The variance-based methods now begin to display some success in detecting this regime of turbulence with the $\lambda_o = \infty$ km estimator being most successful. The POD values are 38 percent and 34 percent for the structure function and $\lambda_o = \infty$ km variance method, respectively. The slightly greater success of the structure function method over the $\lambda_o = \infty$ km variance method is somewhat offset by its significantly greater false alarm rate. Thus the two techniques may be considered roughly equivalent. Once again the variance-based methods which use a finite outer scale length have overestimated the turbulence severity values, lifting many of them into the adjacent higher severity range. This is noted when comparing the number of aircraft events (210) with the total (X + Y) number of radar events (193 to 31) for λ_o ranging from ∞ to 0.5 km.

There are significant changes in the distributions of POD and FAR for the various techniques in the more hazardous turbulence regimes. Over the heavy range of turbulence severity the structure function method enjoys little success. The various-based methods with $\lambda_o = \infty$, and 4 km are quite reliable with POD and FAR values of 84 and 81, and 27 and 30 percent, respectively. Even the $\lambda_o = 1$ and 2 km methods enjoy greater success here than that realized by any technique in the two lowest severity regimes. Thus it would appear that the variance method with λ_o within the range 2 - ∞ km would be acceptable for detecting turbulence in this severity range.

Finally, for the severe turbulence range ($> 8.2 \text{ cm}^{2/3}/\text{sec}$) another dramatic shift in performance has occurred. The structure function, $\lambda_o = \infty$, 4, 2 km variance-based methods are all essentially useless in this severity regime. The $\lambda_o = 0.5$ km method enjoys the greatest success with a POD of 75 percent. With the number of aircraft and total radar events being 68 and 273 respectively, it is observed that much of this success results perhaps from mapping more radar estimates into the severe range than necessary, thus enabling the radar to capture an increased number of aircraft events. The number of false alarms for the $\lambda_o = 0.5$ and 1 km methods is 242 and 159 and drops to 10 for $\lambda_o = 4.0$ km. Thus, although the false alarm rates are all somewhat comparable, the actual number of false alarms resulting from use of $\lambda_o = 0.5$ km may be unacceptable. Realizing that heavy severity regions are themselves significant indicators of hazardous turbulence, one may prefer to use $\lambda_o = 1.0$ km with the knowledge that some borderline severe events may occasionally be dropped into the heavy severity range.

Although the quantity of data for 1981 is small, definite patterns of behavior for the various techniques are easily observed. The structure function method, where pulse volume effects have not been incorporated into the radar method, generally underestimates the true turbulence severity and fails miserably in the more hazardous regions of turbulence. The Doppler spectrum variance-based techniques, on the other hand, are always overestimating the severity in those areas where environmental turbulence is truly light. In more severe turbulence regimes an outer scale near 1 - 4 km in length appears to be a reasonable compromise. The trends noted here will also be observed in the 1982 data to be discussed next.

Consider first the light range of turbulence severity. One notices immediately that none of the techniques which are based upon radar Doppler spectrum variance are successful in detecting this light turbulence range. Only the structure function method exhibits any success with a POD of 67 percent. Once again, however, the false alarm rate of 70 percent indicates that other effects, such as storm shear and sample statistics, strongly influence severity estimates in this light range.

Over the moderate turbulence severity range the spread of POD values of the various techniques has decreased. Here the infinite outer scale method is most successful, with a POD of 55 percent. The variance methods using $\lambda_o = 4$ and 2 km are nearly comparable, with detection rates of 47 and 46 percent. With false alarm rates among the three techniques essentially equal, the choice of effective outer scale length would be $\lambda_o = \infty$ km. The variance method using $\lambda_o = 0.5$ km fails most often as it continuously inflates radar severity estimates, some of which have been mapped into a higher range. This can be observed from comparison of the number of aircraft events within the moderate, heavy, and severe regimes (2940, 3209, and 418), with those (X + Y) of this radar ($\lambda_o = 0.5$ km) method (1172, 4466, and 1689). It is interesting to observe how the structure function POD has slipped downward, while the variance based methods, useless for detection of light turbulence, have broken out and now show varying success in this moderate range.

The behavior for the heavy range of turbulence severity displays the same trends noted in the lower two ranges. The structure function method, grossly underestimating the turbulence severity has become essentially useless, with a POD value of 26 percent. A wide range of variance-based methods ($\lambda_o = \infty$, 4, and 2 km) enjoy comparable success with probability of detection values between 68 - 72 percent and false alarm rates between 35 - 49 percent.

Finally, consider the results for the extreme severity level. The variance methods with $\lambda_o = \infty$, 4, and 2 km severely underestimate the aircraft derived value and are of little use. Only the variance-based methods employing $\lambda_o = 0.5$ and 1.0 enjoy any real success in detecting the presence of environmental turbulence

in this severe range. Their POD values are 78 and 54 percent. Again, with the number of aircraft events at this level being 418 and the total $(X + Y)$ radar observed events being 1689 for $\lambda_0 = 0.5$ km, it is again observed that the success of this (0.5 km) technique can be partially attributed to inflation of borderline radar estimates from the heavy range into the severe range, thus enabling the radar to capture more of the aircraft estimates found at this level. This is also reflected in the relative number of radar estimates found at this level for the $\lambda_0 = 0.5$ km (1689) and $\lambda_0 = 1.0$ km (922) cases.

Observations of the behavior of the POD and FAR values dramatically display some inherent characteristics in methodologies and equipment. It has been shown that the structure function technique should in most cases, due to pulse volume filtering effects, show very limited success in estimating turbulence severity except for cases where radar pulse volume size is very small, that is, at very close range (for example 0 - 10 km). The question that must be asked is why the method appears somewhat successful in regions of light to moderate turbulence, but behaves as expected in the more severe turbulence regions. It is felt that this results from contributions from the natural statistical fluctuation of Doppler mean velocity, storm shear, and equipment introduced biases which, although perhaps small, combine with the measured, diminished, turbulence fluctuations to produce an estimate which in many cases approaches the true turbulence value. In regions of greater turbulence severity, where these additional non-turbulence contributing factors are not sufficient to significantly inflate the structure function underestimate, its true behavior is unmasked. Thus the structure functions method appears successful in the lightest regimes of environmental turbulence, but only because it is partially aided by storm, statistical, and equipment introduced biases.

The variance-based methods, on the other hand, are plagued with the opposite problem. Here the measured Doppler spectrum variance, even with estimates of storm shear and other standard radar measurement contributions removed, may still result in an overestimate of the true turbulence contribution. That is, there are yet some biases which have not been properly accounted for. However, from Table 1 the behavior of the POD and FAR estimates show that this bias is significant only in the lower turbulence severity regimes and is a minor contributor when large turbulence induced variance occurs. Thus in the light turbulence regimes, because of this overestimate of turbulence induced variance, we may be forced to use a turbulence outer scale length which normally would yield an underestimate of turbulence severity if the true turbulence induced variance alone had been measured. In regions of greater severity, the bias effects become smaller and we approach the more reasonable outer scale lengths which more accurately represent the true environmental field.

If the measurements obtained here may be considered representative of most radars, then the results suggest much care must be taken to ensure that the non-turbulence factors contributing to Doppler spectrum variance are accounted for. In this instance one may consider it possible for the variance method with a single outer scale length to be used over all severity ranges. However, much care was exercised in the present data analyses. Thus it is perhaps doubtful that all such contributions can be properly accounted for, and success in the lightest regimes of turbulence severity is questionable. Also, the results presented here show that no single outer scale length will provide the most reliable estimation of turbulence severity for all individual turbulence regimes. Considering the reliability of the variance-based techniques and the desire to emphasize detection of the more hazardous turbulence fields, concentration on the detection of heavy and severe levels seems most reasonable. It would appear that $\lambda_o = 1 - \infty$ km is most useful for detection of these levels of turbulence. However, choice of outer scale length and correct classification of turbulence severity into individual severity levels is still difficult, and the utility of this classification scheme must be questioned.

An alternative method for quantization of the strength of turbulence into hazardous and non-hazardous classes may be possible. The previous discussions clearly show that no single radar technique is optimal for detection of all individual severity classes and that FAR values become unacceptably high when attempting to detect the higher severity classes. In light of this, a separate analysis was performed to determine the feasibility of detecting composite classes of turbulence, where a composite class combines all classes including and above a defined severity level. In particular two regimes, equal to and greater than moderate, and equal to and greater than heavy, were studied. It should be mentioned that the composite class, including light and greater turbulence severity, is meaningless since this includes detection of all possible values and will necessarily return a POD of 100 and FAR of 0 percent. Likewise, detection of a severe composite class has already been presented in Table 1. Classification of turbulence into these two composite classes may offer a method for locating regions of significant turbulence and allow for more reasonable discrimination between hazardous and non-hazardous regions. The POD and FAR results for these analyses are presented in Table 2. Consider first the 1981 data.

Comparison of the simultaneous occurrence of turbulence severity within the moderate composite (equal to and greater than moderate severity) class for the radar and aircraft data indicate effectively complete detection of aircraft observed events by all radar variance-based methods. The structure function technique yields a POD of 90 percent. The FAR values for all these methods are quite reasonable, all lying in the range of 17 to 20 percent.

Table 2. Radar Probability of Detection and False Alarm Rate

1981								
Turbulence Severity ($\text{cm}^{2/3}/\text{sec}$)	STRFN		$\lambda_o = 0.5$ km	$\lambda_o = 1.0$ km	$\lambda_o = 2.0$ km	$\lambda_o = 4.0$ km	$\lambda_o = \infty$ km	
	POD	FAR	POD	FAR	POD	FAR	POD	FAR
\geq Moderate ≥ 1.5	90	16	100	20	100	20	100	19
\geq Heavy ≥ 3.5	43	32	100	39	99	36	96	29
1982								
Turbulence Severity ($\text{cm}^{2/3}/\text{sec}$)	STRFN		$\lambda_o = 0.5$ km	$\lambda_o = 1.0$ km	$\lambda_o = 2.0$ km	$\lambda_o = 4.0$ km	$\lambda_o = \infty$ km	
	POD	FAR	POD	FAR	POD	FAR	POD	FAR
\geq Moderate ≥ 1.5	70	9	96	16	96	15	95	15
\geq Heavy ≥ 3.5	33	36	95	47	92	44	83	37

Results are somewhat similar when attempting to determine those regions containing turbulence of the heavy composite (equal to and greater than heavy) class. The POD values have remained quite high, ranging from 100 to 93 percent for the radar variance-based methods using effective outer scale lengths of 0.5 to ∞ km, respectively. The structure function POD has dropped to 43 percent. The FAR values have increased over the moderate composite class values and range from 39 to 27 percent for $\lambda_o = 0.5$ to ∞ km, with the structure function FAR being 32 percent. The behavior of the various techniques in detecting these composite classes, when compared to that observed for radar detection of individual severity levels is only vaguely noted here, except for the relatively poor performance of the structure function method in detecting regions of very strong turbulence.

The POD and FAR results for 1982 are very similar to those presented for 1981. For radar detection of turbulence severity within the moderate composite class, the variance-based POD values have slipped to a range of 96 to 94 percent with the FAR values being 16 to 15 percent. The corresponding structure function values are 70 and 9 percent respectively. For the heavy composite class the variance-based methods return to POD values of 95 to 78 percent for $\lambda_o = 0.5$ to ∞ km. The structure function POD has dropped dramatically to 33 percent. The FAR values have increased over the 1981 counterparts to 47 to 35 percent for 0.5 to ∞ km outer scale lengths, and the structure function FAR is 36 percent.

The apparent success in detecting turbulence lying in the moderate composite severity class reflects the fact that the aircraft observed turbulence severity was only infrequently below the moderate level. Thus with most aircraft, and certainly radar, turbulence severity estimates at or above this level, great success is ensured. With radar severity estimates rarely below the moderate level, the FAR values essentially reflect the roughly 15 percent occurrence of aircraft determined severity estimates in the light regime. Successful detection of turbulence severity in the heavy composite class is also well assured. The increased FAR values observed here, however, do reflect the occasional overestimation of turbulence severity by the radar variance-based methods, as least as determined by comparison with the "ground truth" aircraft estimates.

In previous discussions concerning detection of individual severity classes, it was demonstrated that the variance-based techniques were superior to the structure function method, but that no single outer scale value produced optimum results for all turbulence severity classes. The results here, for detection of composite severity classes, again demonstrate that the structure function method is least successful but there now exists a broad range of effective outer scale values which will work quite successfully with the variance-based method. These results suggest a more reliable method for discriminating between hazardous and non-hazardous turbulence. It seems reasonable to use a single outer scale to detect both composite classes discussed here. Observation of the POD and FAR results suggest that an outer scale of 2 km is perhaps a good compromise. One would then first locate regions of turbulence of the moderate composite class. This will outline well all regions where meaningful turbulence exists. Within this data there will exist imbedded areas of turbulence which fall into the heavy composite class. Where the appearance of this class is random and speckled, one may attribute this occurrence to the 1/3 false alarm rate suggested by the results presented here. These regions most likely contain turbulence with values in the high end of the single moderate level, to low end of the single heavy level, of turbulence severity. Where the appearance of the heavy composite class is not random, but is continuous in nature and forms a solid areal region, then this truly signifies the presence of heavy, or greater, turbulence. Thus, when both classifications are overlayed, those regions where turbulence severity classification indicates the moderate composite class one notes the presence of non-hazardous turbulence. Where a random, speckled appearance of the heavy composite signature is observed, this may be considered a region where a transition zone between hazardous and non-hazardous turbulence exists. In those areas where a solid heavy composite signature exists, one may consider that hazardous turbulence is present. This approach, utilizing the detection of composite classes of turbulence, appears to be clearly superior to detection of individual classes, and the results above suggest that an effective turbulence outer

scale of 2 km would be most appropriate for the current turbulence severity classification as suggested by MacCready.⁵

5. CONSIDERING ISOTROPY

Casual observation of the aircraft data derived estimates of turbulence severity (Appendix G) at any given instant show occasional marked differences in the severity estimates among the three components. It may be argued that the differences between the gust component estimates result from not incorporating all the necessary turbulence scales. The method for estimating turbulence severity from the aircraft data, however, has been shown (Appendix C) to yield reasonably stable values which may well be considered local ensemble estimates. The other obvious suggestion would be that the turbulence fields penetrated are not characterized by the ideal homogeneous, isotropic behavior assumed in the theoretical models used in the estimation techniques. Finally, measurement biases introduced through the measurement equipment could also be present.

To investigate this behavior a brief study was performed to compare the relative strength of the measured gust energy of the three components over various segment lengths. A single aircraft time history of the three gust components was broken into series of non-overlapping segments. For each segment, and for each gust component, the mean and the trend were estimated. These were separately subtracted from gust component data of each segment, and the mean gust energy ($\langle V^2 \rangle$) determined. Ratios of the energies of the components were then estimated for each segment and then these ratios were averaged along the entire data series. Next a larger segment size was chosen and the process repeated until the last ratios formed were produced from one segment alone, that comprising the entire data set. A simple relation describing this ratio value is

$$\text{Ratio} = \left\langle \frac{\langle V_{Lo}^2 \rangle L}{\langle V_{La}^2 \rangle L} \right\rangle \quad (14)$$

where $\langle V_{Lo}^2 \rangle$, $\langle V_{La}^2 \rangle$ are the mean energy for the longitudinal and lateral components for a segment of length L . Figures 14-16 are typical plots. In Figure 14, the trend was removed from each segment before mean gust energy was determined. The ratios indicate that the measured energy in the longitudinal and lateral components are roughly equal for all segment sizes all along the aircraft track. However, the energies of the longitudinal and lateral components are greater than that contained in the vertical gust component. Observations of Figure 17, the corresponding time series of aircraft data show that there is only minor storm wind structure and

turbulence along this track. Figures 15 and 16 on the other hand show marked differences in the track averaged gust component energies for a different run. In Figure 15 we see that for segment sizes less than about 2 km in length the longitudinal component energy is greater than that contained in the lateral component. However, for segment lengths greater than about 5 km, the lateral component contains the greatest energy. Such behavior most likely results from a large-scale storm structure, which in the horizontal plane, exhibits greater fluctuation and energy along the lateral than longitudinal directions. As larger segment sizes are used this feature begins to dominate the gust velocity deviations. A simple analogy would be the measurement of the oscillation components of a wave feature while moving along a path aligned nearly parallel to the wavefronts. This suggests that as larger data segment lengths are used to estimate the turbulence parameters storm wind structure becomes increasingly important and may strongly bias turbulence measurements. Once again the vertical component is least energetic. Figure 16 represents analysis of the same data set as shown in Figure 15, however, here the deviation from the mean of each segment rather than from the segment trend was utilized. It is presented to further show the effects of large-scale features as segment size is increased. This is noted by the significantly greater range of ratio values with increasing segment size as the trend begins to dominate the gust measurements.

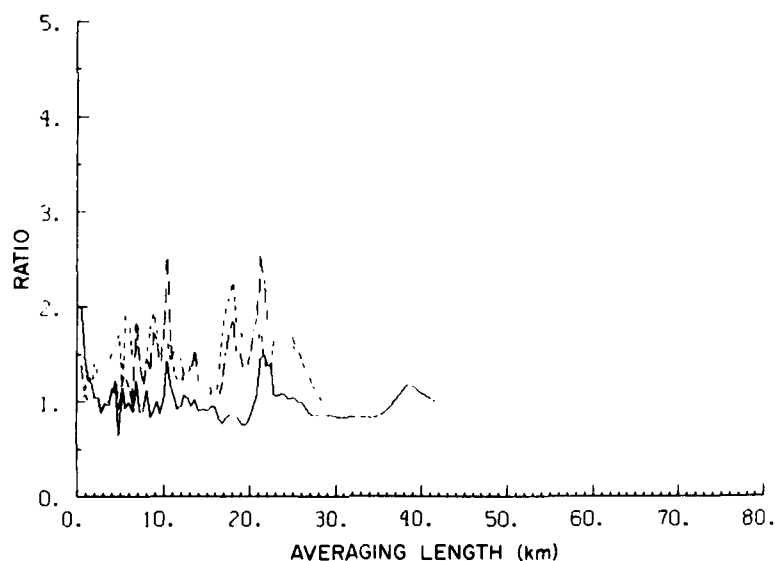


Figure 14. Ratio of Energies of Longitudinal to Transverse (solid), Longitudinal to Vertical (long dash), and Transverse to Vertical (short dash) Aircraft Gust Component Data as a Function of Data Segment Length. The trend has been removed from each data segment. Data is from penetration 1 on 31 July 1982

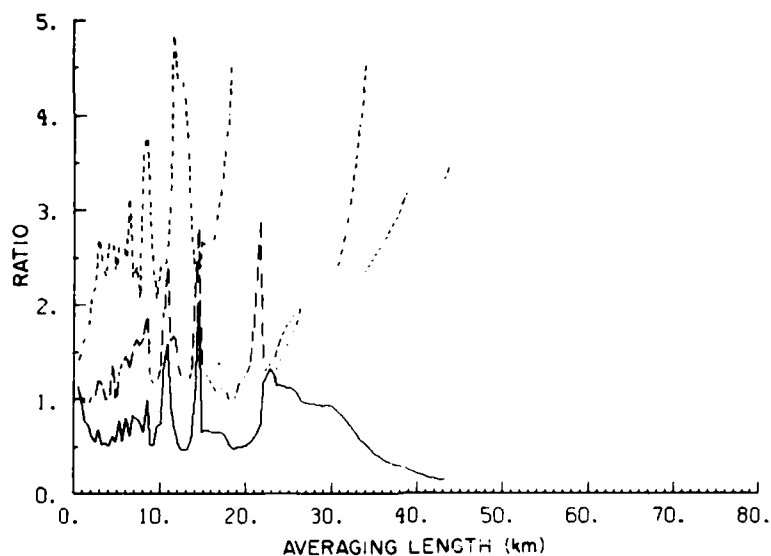


Figure 15. Ratio of Energies of Longitudinal to Transverse (solid), Longitudinal to Vertical (long dash), and Transverse to Vertical (short dash) Aircraft Gust Component Data as a Function of Data Segment Length. The trend has been removed from each data segment. Data is from penetration 5 on 31 July 1982

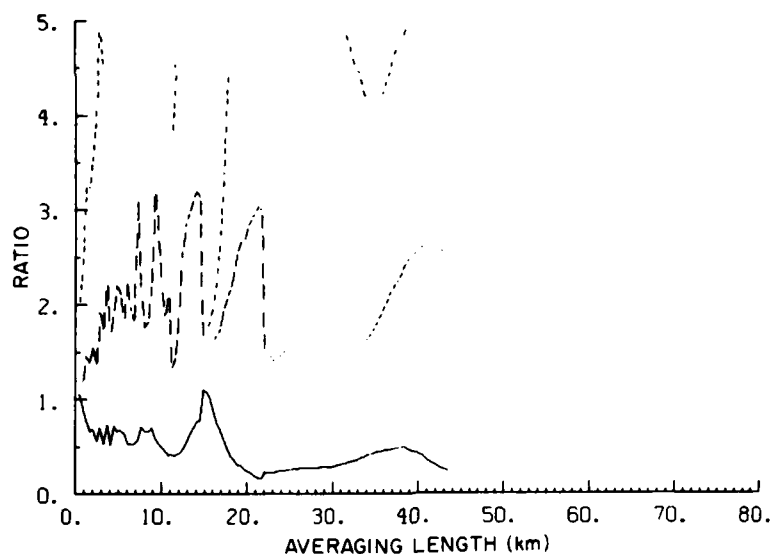


Figure 16. Ratio of Energies of Longitudinal to Transverse (solid), Longitudinal to Vertical (long dash), and Transverse to Vertical (short dash) Aircraft Gust Component Data as a Function of Data Segment Length. The mean has been removed from each data segment. Data is from penetration 5 on 31 July 1982

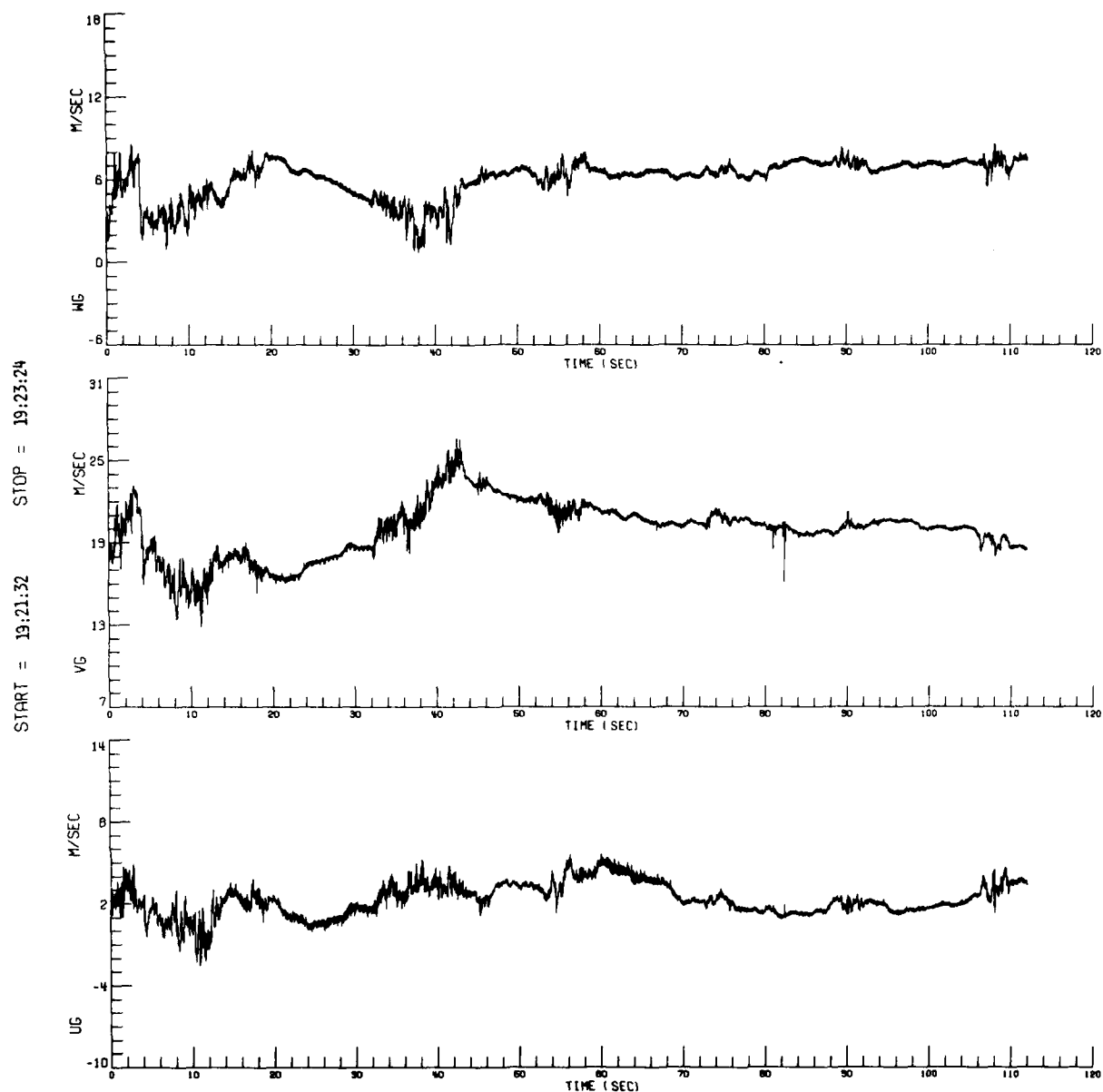


Figure 17. Time Series of Aircraft Gust Component Data Along the North (Ug), East (Vg), and Vertical (Wg) Directions for the Period Shown in Figure 14

Similar analyses were performed on the bulk of the 1982 gust data. The results show that the vertical gust component almost always contains the least energy, while the longitudinal and lateral components are roughly comparable in terms of frequency of dominance at large-scale lengths. However, at short segment lengths, the apparent energy in the longitudinal component is consistently greater than that of the lateral component. It is somewhat of a curious result that the vertical component remains the least energetic since, on the small scale, buoyancy effects, and

on the large-scale, updrafts and downdrafts, often result in the vertical winds having the greatest fluctuation energy. This observation suggests there may be damping effects in equipment measuring the vertical gust component which are greater than those which measure the horizontal components.

Some care must be exercised in the interpretation of these data. If the actual turbulence field consisted of a weakly to uncorrelated storm wind field structure with an isotropic turbulence field imbedded within it, as has been assumed in the conceptual model to derive the radar turbulence relations, and if extractions of the storm wind component was properly performed, then the ratios of energy in the various gust components should be equal if all turbulence wave numbers were incorporated. If, however, only a small range of scales were well incorporated, whose scale lengths were less than the effective outer scale length and in the inertial subrange regime, then the vertical and lateral energies measured should be nearly equal, but $4/3$ the longitudinal component. Now in the true environment, where the turbulence is generated by strong shear of the environmental flow, the largest permanent eddies, having a scale comparable to the local generation region, and the energy containing eddies from which energy is transferred down into the inertial subrange, are generally anisotropic. If these scales are only partially included, then the components need not be equal, and no single component should be favored. For 1982 data no consistent behavior which follows any of the above mentioned patterns was observed.

In conclusion, observations suggest that the vertical component measurements are most highly damped at all scales, while the lateral component measurements are more highly damped at short scale lengths (few km) than the longitudinal. It is difficult to prove the existence, or lack of, local isotropy given the apparent influences of storm scale wind structure, turbulence transition zone, equipment, and natural statistical biases. The dominance of the horizontal gust components do, however, suggest the turbulence field may be more two-dimensional in character, with the greater component of turbulence eddy motion mapped into the horizontal plane and somewhat damped in the vertical. However, agreement between the three component estimates of turbulence severity is reasonably good. Certainly when comparison is made on the basis of severity classes, agreement is very good except for those occasional regions when non-turbulence storm structure winds dominate over the true turbulence contributions in the gust measurements. It must be noted, however, that this greater degree of apparent isotropy is somewhat artificial and results from the severity value being proportional to the square root of the gust energy. Thus, at least in terms of turbulence severity, the field may be considered isotropic.

6. STORM SHEAR AND LIGHTNING EFFECTS

When estimating turbulence parameters through Doppler spectrum variance methods, contamination of the variance estimate must always be considered. Radar noise, and imbalances in the amplitudes or phases of the in-phase and quadrature channels are always possible contributors and can most easily be dealt with in the frequency domain. There are also contributing environmental factors, such as storm wind shear, where the storm wind field here is considered a relatively stationary background feature upon which is embedded turbulent wind fluctuations. Storm shear is generally considered to be the greatest environmental contributor to Doppler spectrum variance other than turbulence. This contribution was estimated for all Doppler spectrum variance measurements and its effects removed. In the 1981 data the storm shear was determined by interpolating Doppler radial velocity data, typically 768 contiguous range gates along the radial, onto a 3-D Cartesian grid from which the shear of the radial velocity along the radial and transverse directions could be estimated.

During the 1982 season, as a result of the decreased turn around time from the end of one penetration to the start of the next penetration, and other recording requirements, insufficient time was generally available to perform volume scans from which the 3-D data base could be determined. Thus for 1982, the shear contribution was determined by a combination of methods. When possible, the radar velocity data were placed onto a 2-D grid surface. This surface was a plane which contained the aircraft track and a parallel line lying at the ground passing through the radar location. Use of such a surface required that the aircraft tracks remained at constant altitude and that the tracks were relatively straight. In regions where a track surface technique was not applicable the tracking gate radial velocities themselves were used to estimate shear. These auxiliary methods generally allowed for an estimate of two components of the shear. As will be discussed shortly, the relatively small shear contribution to Doppler spectrum variance observed in the 1981 data suggests the missing shear component is not expected to be influential in the final results.

Figures 18 and 19 show the distribution of estimated storm shear values and their contribution to Doppler spectrum variance. In these data the three components of shear of the radial velocity are considered separate events. Figure 18 displays the percentage occurrence of observed shear component values in increments of 0.2 m/sec/km. The trend is very striking and shows grid point estimated shear with a magnitude greater than $3 \times 10^{-3} \text{ sec}^{-1}$ is relatively rare. The mean measured shear value is about $7.5 \times 10^{-4} \text{ sec}^{-1}$. Figure 19 shows the frequency of occurrence of the ratio of the shear and turbulence contributions to Doppler spectrum variance. It is quite obvious that at least for the shear estimates

determined by the methods described here the shear contribution to Doppler spectrum variance is generally very small. Figure 19 does not show the 6.4 percent occurrence where the shear contribution was greater than that from turbulence. Generally these events occurred in regions of very light precipitation, exhibiting low signal to noise ratio values, and it is expected that nearly 50 percent of these events resulted from poor estimates of Doppler spectrum mean and variance. Thus there appears to be a 3 percent occurrence rate where the shear contribution to Doppler spectrum variance is greater than the turbulence contribution.

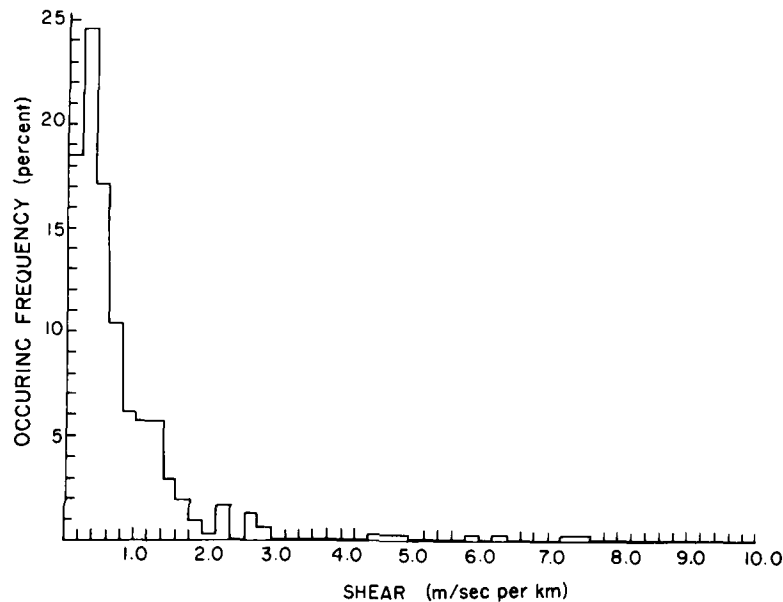


Figure 18. Histogram of Storm Wind Shear Magnitude

It may be argued that even if the Doppler spectrum mean and variance values well represent true ensemble estimates, then the grid point method for estimating storm shear of the radial velocity may underestimate the true environmental value which may be influencing Doppler spectrum variance. The grid point separation distances used here were between 0.5 - 1.5 km, and allow for good estimates of the shear for storm scales greater than about 2.0 - 6.0 km, respectively. A typical range of scales for dominant storm wind field features has been observed (Bohne¹) to lie generally in the range of 4.0 - 8.0 km. Thus the shear estimates obtained here are probably quite reasonable. These results thus demonstrate that storm shear contributions to Doppler spectrum variance are in most instances very small in comparison to the turbulence contribution. As a first approximation then, when

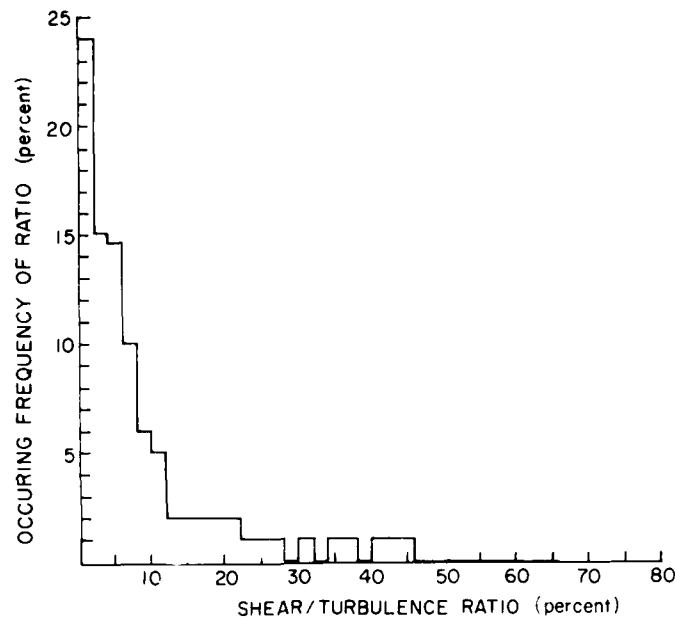


Figure 19. Histogram of Ratio of Storm Wind Shear to Turbulence Contribution to Doppler Spectrum Variance

estimating turbulence severity by radar variance methods, it may in most cases be ignored.

Finally, it is of interest to note the occurrence of lightning strike events upon the aircraft in relation to radar and aircraft observations. Very few simultaneous observations are available for comparison, with only three for radar and nine for aircraft, respectively. The behavior of the shear of the radar radial velocity and Doppler spectrum variance, and turbulence severity estimates derived from aircraft gust data during lightning strike episodes, are shown in Table 3. Although little statistical significance can be attributed to these results, some patterns are noted. First, the radar shear and variance data exhibit relative minima at the lightning event times. The aircraft turbulence severity estimates, however, are at periods of relative maxima at lightning event times. It is unclear why the two sets of observations exhibit different effects. The radar tracking gate is offset about 150 - 300 m from the aircraft position. Perhaps it is this offset which enabled the radar pulse volume environment to be unaffected by the lightning events. The consistent behavior of the aircraft data correlations do suggest that lightning events when they occur, are found in regions of heightened turbulence severity. One should not, however, consider lightning location a reliable method for locating hazardous turbulence within storms, since the overwhelming majority of hazardous turbulence regions encountered by the aircraft exhibited no lightning events.

Table 3. Radar and Aircraft Observations During Lightning Events

	<u>Lightning Event</u>	<u>Radar</u>	<u>Aircraft</u>
1981 JUL 1	18:17:14 18:17:36	negligible RVS/DSV min	indeterm TC max
1982 JUL 17	19:36:55 19:58:56 20:06:19	negligible RVS/DSV min	TC max TC max TC max
1982 JUL 28	22:26:48		TC max
1982 JUL 30	19:30:24 19:30:34		TC max indeterm
1982 JUL 31	20:02:19	negligible RVS/DSV min	TC max

DSV Doppler Spectrum Variance

TC Turbulence Severity

RVS Radial Velocity Shear

7. SUMMARY AND CONCLUSIONS

The results presented here describe the observations and analyses of coordinated Doppler radar and instrumented aircraft gust data obtained during the 1981 and 1982 seasons of the Joint Agency Turbulence Experiment, a participation of the Air Force Geophysics Laboratory in the Storm Hazards Program of NASA Langley Research Center. A total of eight storm penetration days, comprising 34 actual storm penetrations, were analyzed. While the aircraft storm penetration altitude during the 1981 seasons was near 3 km, an attempt to attract more lightning strike events in the 1982 season resulted in storm penetrations being closer to mid- to high-levels in the storms, about 7 - 9 km altitude. Storm environments ranged from simple, single cell systems to extended line complexes containing many cells.

Shear of the radar radial velocity resulting from nonturbulent storm structure contributed generally less than 10 percent of the turbulence contribution to Doppler spectrum variance, and at least for the cases observed here, to a first approximation, could generally be neglected. Radar signatures of lightning events were not detected, however about 80 percent of the lightning strike episodes occurred when aircraft measured turbulence was near a local maximum value. The data sample here however is extremely small, and the significance of these results must be questioned. The probability of encountering a lightning event when in a region of strong turbulence was found to be extremely low, thus use of lightning location methods to determine the distribution of hazardous turbulence within storms must

be considered unreliable. Simple analysis of the energy contained in the three gust components suggest the turbulence field to have greater energy content in the horizontal plane than in the vertical direction. This anisotropy, however, is not very significant when comparisons are made in terms of aircraft turbulence severity estimates. Thus, except for obvious cases where storm structure dominates the gust component measurements, the turbulence field may be reasonably well approximated as isotropic when one is concerned only with turbulence severity levels. Almost all measurements were made at large radar range, resulting in precipitation effects to be small. It is believed that the dominant source of error in use of radar for turbulence severity detection will result from improper choice of outer scale length.

The aircraft gust data were analyzed by use of the structure function method. It was demonstrated that the estimated turbulence parameters well represent local ensemble values when a local data segment length of about 1200 m was utilized. When measured relative to the turbulence severity scale suggested by MacCready⁵ the observed environments were well distributed over light to severe turbulence regimes.

Estimates of turbulence severity by radar were obtained through use of three methods. The Doppler mean velocity data were employed in structure function analysis, and the Doppler spectrum variance data were used with relationships presented by Frisch and Clifford⁴ and Bohne.¹ The variance-based methods assumed the turbulence field may be modeled as inertial subrange in form (Kolmogorov 5/3 law) where the largest eddy size in the model is infinite (Frisch and Clifford⁴) or finite (Bohne¹). Comparison of the turbulence severity estimates from the radar and aircraft data demonstrate that use of the radar structure function method strongly underestimated the true strength of the turbulence field, except in light severity regimes. This apparent success, however, is believed to result as much from equipment and storm biases as well as the measured turbulence contributions. The dominant feature of the structure function technique was the limitation placed upon it by radar pulse volume filtering. Reduction in the rate of success at all turbulence severity levels with increasing range from the radar, hence increasing radar pulse volume size, was well demonstrated. These analyses indicate that use of radar structure function methods, when radar pulse volume filtering is not accounted for, are inappropriate except for very short radar ranges (perhaps < 10 km).

The Doppler spectrum variance-based methods, on the other hand, demonstrated very well their capacity to detect moderate to severe turbulence severity regions. However, contaminant contributions to Doppler spectrum variance severely limit the usefulness of this method in light severity environments, at least at the large radar ranges occurring here. Classification of turbulence into individual turbulence severity levels through use of these radar methods with any significant degree of

confidence was found difficult. In addition, no single effective outer scale length provided optical detection capability for two or more individual severity levels. The uncertainty in this form of turbulence classification makes use of this classification scheme unreasonable. However, classifications of turbulence severity into composite classes was very successful, and resulted in both high probability of detection and relatively low false alarm rates. In particular, use of two composite classes, moderate and greater (moderate composite) and heavy and greater (heavy composite), appears to offer good potential for discriminating between non-hazardous and hazardous turbulence. Use of the variance-based method with a single effective outer scale between 1 - 4 km works well with this classification scheme. Thus, if nonturbulent contributions are removed successfully from the Doppler spectrum variance, then the variance-based radar method with a single effective outer scale length, with perhaps 2 km being a reasonable compromise, provides a successful means for detecting atmospheric turbulence of moderate to severe intensity.

References

1. Bohne, A. R. (1981) Radar Detection of Turbulence in Thunderstorms, AFGL-TR-81-0102, AD A108679.
2. Bohne, A. R. (1982) Radar detection of turbulence in precipitation environments, J. Atmos. Sci. 39:1819-1837.
3. Bohne, A. R. (1983) Joint Agency Turbulence Experiment - Interim Report, AFGL-TR-83-0180, AD A137167.
4. Frisch, A. S., and Clifford, S. P. (1974) A study of convection capped by a stable layer using Doppler radar and acoustic echo sounders, J. Atmos. Sci. 31:1622-1628.
5. MacCready, P. (1964) Standardizations of gustiness values from aircraft, J. Appl. Meteorol. 13:439-449.

Appendix A

Data Reduction and Methodologies

A1. SOUNDING DATA

The environmental soundings are an attempt to represent the structure at the time and location of observations. Generally, the observation periods occurred in between standard sounding locations and times. To obtain a representative sounding, the Wallops Island and other nearest sounding station data from the earlier and later sounding periods were used to construct a best-fit sounding for the time and location desired. Due to the close proximity of the storms to Wallops Island, however, these best-fit soundings were nearly identical to the Wallops Island soundings alone. Thus, the use of interpolated soundings was abandoned and only Wallops Island data are used here. Although the accuracy of the temperature data are of some concern, the environmental wind structure, as observed from the storm radial velocity data, generally agree well with the Wallops Island sounding wind structure. These data are presented in Appendix E.

A2. CARTESIAN REPRESENTATION OF SECTOR SCAN DATA

During the 1981 season the rate of storm penetration was low and frequent volume sector scan sequences were recorded. The 1982 season saw a marked increase in the time rate of storm penetration. Subsequently few storm volume scan sequences were obtained during these aircraft operations. Thus more than

one storm reflectivity factor plot will be occasionally shown to portray the features of the storm complexes during the 1982 penetration periods. The data acquired during the radar sector scan portion of storm observations are interpolated to a Cartesian grid system. The data shown are the equivalent reflectivity factor at radar determined storm penetration altitude. This level was determined from the radar computed tracking altitude, rather than from the aircraft determined altitude, to ensure proper accounting for Earth curvature and index of refraction effects. The reflectivity factor structures were observed over a few sector scans where possible to determine an advection velocity for each storm during the observation period. This advection velocity was then applied to all scan data to ensure that the data were interpolated to the proper grid-point locations. In all cases this advection velocity is in good agreement with the estimated sounding velocity for the observational period.

As stated, a number of aircraft storm penetrations were generally performed before a complete sector scan update could be obtained. Thus, a single representative Cartesian data set, with the aircraft penetration tracks advected to the proper storm locations as determined by the storm advection velocity, is used. Now, however, comparisons between aircraft and radar scan data do require a relatively stationary storm structure. Those cases where significant evolution was observed between the time of aircraft storm penetrations and the sector scan period are noted. The grid-point separations in these plots range from 0.5 to 1.5 km in the horizontal and 0.5 to 1.0 km in the vertical. The occasional coarse resolution is a result of the limited number of sector scans performed between penetrations and the large range of the storms from the SPANDAR radar. Finally, since a 15-dBZ (10 dBZ for 1982) threshold is used in the plotting of the reflectivity data, the plots do not represent the entire spatial extent of the storms.

A3. TRACKING DATA

The tracking gate Doppler data displayed are the Doppler spectrum mean velocity and variance. The data shown are not the original fine scale time series of tracking gate velocity and variance. The mode of movement of the tracking gates combined uniform scanning and a 1 μ sec range jump as the plane moved in or out in range. Thus, the tracking gate data comprising the continuous time histories are not uniformly spaced. To obtain a more spatially uniform data set for use in the structure function analyses, a subset of Doppler spectrum mean velocity and variance data are chosen from the continuous data set. This results in a basic data set where successive data values are about 150 to 240 m apart.

A4. RADAR TURBULENCE SEVERITY ESTIMATES

The parameter of interest here is the eddy dissipation rate (ϵ), which represents the rate of transfer of turbulence kinetic energy from larger to smaller scales of motion, or eddies. The turbulence severity index, simply the cube root ($\epsilon^{1/3}$), has been offered (MacCready)⁵ as a means of quantifying the degree of hazard to aircraft penetrating a given region of turbulence. Radar estimates of eddy dissipation rate (ϵ) along the aircraft penetration tracks are determined using two different methods. First, the tracking gate Doppler velocity data are used in a structure function analysis, which essentially measures the degree of correlation of radar radial velocity data with distance. Second, the tracking gate Doppler spectrum variance data are related to the eddy dissipation rate via a relation founded on the concept that the turbulent air and precipitation motions, particularly at scales primarily less than the maximum pulse volume dimension, are mapped into Doppler spectrum variance. In these variance methods, the turbulence field is assumed to obey the Kolmogorov law and can be characterized as having an energy distribution totally similar in form to the inertial subrange regime of atmospheric turbulence. Two methods, that of Frisch and Clifford,⁴ where the maximum eddy size is assumed to be infinite, and Bonne,^{1, 2} where there is a finite effective turbulence outer scale, are used. The following material briefly outlines the manner in which the two methods, structure function and spectrum variance-based methods are employed.

The form of the one-dimensional structure function used is

$$D(\vec{r}) = (D_L(r) - D_T(r)) \frac{X^2}{r^2} + D_T(r) \quad (A1)$$

where $D_L(r)$ and $D_T(r)$ are the one-dimensional longitudinal and transverse structure functions, respectively, and are given by

$$D_L(r) = C \epsilon^{2/3} r^{2/3} \quad (A2)$$

$$D_T(r) = \frac{4}{3} C \epsilon^{2/3} r^{2/3} \quad (A3)$$

for the inertial subrange region of a homogeneous isotropic turbulence field. This relation is required since the aircraft penetration tracks were generally neither parallel nor orthogonal to the radar viewing direction. In these relations C is a universal constant (1.77), r is the distance interval between successive radar velocity measurements used to form the estimate, and X is the component of this distance along the radar viewing direction.

As written, this relation portrays the behavior for an ensemble of observations derived from point velocity measurements in the turbulence field. However, when using radar radial velocity values, the random fluctuation in Doppler velocity arising from turbulence scales less than the maximum pulse volume dimension may be strongly filtered out. Thus, the radar structure function estimates, at least for the case of an ensemble of measurements, will be diminished in magnitude and contain proportionately greater amounts of energy from the larger scales of motion.

The estimates of $D(r)$ determined by this method will exhibit some error. First, the structure function estimates are derived from a limited number of observations that may only loosely approximate an ensemble of observations. Second, the magnitude of $D(r)$ is diminished due to pulse volume filtering action. Third, the estimates are biased through incorporation of nonturbulent storm structure wind shear. Fourth, each velocity value naturally includes a random error component related to Doppler spectrum breadth and sample dwell time. This may add from 0.1 to 0.4 (m/sec)^2 to the structure function magnitude.

In an attempt to account for these effects, the local data sets are first linearly detrended and eddy dissipation rate estimates are determined at the smallest length scales where the $r^{2/3}$ behavior is reasonably well observed, typically at length scales of 150 through 450 meters. Note that a local data set is represented by a segment of data, centered around the desired location. These segments varied in length from 3 to 6 km.

The second method employed to estimate $(\epsilon^{1/3})$ relies upon the relationship between Doppler spectrum variance and the turbulent air motions. This method assumes some knowledge of the effective size of the largest turbulence eddies within the inertial subrange model. The term effective is used since we are replacing the actual turbulence energy spectrum that contains energy-containing eddies, in addition to the inertial subrange, with a fully Kolmogorov energy spectrum form. As discussed in Section 4, this approximation is quite reasonable.

First consider the solution of Frisch and Clifford,⁴ whereby the inertial subrange is assumed to extend to eddies of infinite size. The relationship used is

$$\text{var} = 1.354 C (\epsilon \alpha)^{2/3} \left(1 - \frac{z}{15} - \frac{z^2}{105} - \dots\right) \quad (\text{A4})$$

where C is a universal constant of value near 1.35, and z , α , β are related to effective pulse volume width (R) and length (L) by

$$z = (1 - \frac{\beta^2}{\alpha^2}) \quad (A5)$$

$$\alpha = \frac{R}{(8 \ln 4)^{1/2}} \quad \beta = \frac{L}{(8 \ln 4)^{1/2}} \quad (A6)$$

Next consider the solution of Bohne¹ where the effective turbulence outer scale is assumed finite. Unfortunately the integral relations do not reduce to simple analytic form as shown in Eq. (A4) for the case of an infinite outer scale length. However, they have been modeled by a series of expressions which closely approximate the theoretical relationship over all useful ranges for these SPANDAR radar data sets. The relation developed for the SPANDAR radar is given by

$$\langle \text{VAR} \rangle / (C \epsilon^{2/3}) = (\text{INT} + \text{SLOPE} (\text{EEE}) (\text{RANGE})) \text{EEE} + \text{ASYM}(1 - \text{EEE}) \quad (A7)$$

where INT is the value of $\langle \text{VAR} \rangle / (C \epsilon^{2/3})$ at zero range, SLOPE is the slope of the $\langle \text{VAR} \rangle / (C \epsilon^{2/3})$ curve between 0 and 5 km, RANGE is radar range, and EEE is a beam filter function. The variance data used in these analyses are the companion data to the Doppler velocity data employed in the radar structure function analyses.

It is important to note that the structure function and spectrum variance techniques rely upon different effects of the turbulent air (precipitation) motions on the radar Doppler spectrum parameters. First, the structure function relies upon the turbulent air motions being mapped into fluctuation of the Doppler velocity, and then relates this fluctuation to intensity of the turbulence field. In the form used here [Eq. (A1)], no accounting for the pulse volume filtering effects, that is, transference of some of this fluctuation energy into Doppler spectrum breadth is performed. The variance methods, on the other hand, rely upon the spectrum broadening effects, and do account for the transfer of energy between the Doppler spectrum variance and the fluctuating mean velocity. If the outer scale length is considerably larger than twice the maximum pulse volume dimension, then Eq. (A4) is quite good. In theory, use of Eq. (A4) should be limited to short ranges (Bohne^{1,2}), perhaps < 40 km for typical weather radars. However, as shown in Section 2, other factors such as storm scale structure and equipment biases may alter the restrictions on its applicability. Experience (Section 4 and Appendix B) has shown that a length λ_o of 1 - 4 km is a reasonable choice of effective outer scale to ensure detection of heavy to severe turbulence regions.

Appendix B

Estimation of Effective Turbulence Outer Scale

The determination of an outer scale of turbulence is of interest for a variety of reasons. First, it is a necessary input when a finite outer scale variance technique is employed. Second, it is useful in determining what length of local segment is to be used in analysis of the aircraft data for the estimation of eddy dissipation rate. Third, it is of purely meteorological interest to compare the larger turbulence scales with the dominant quasi-stationary storm scales observed in thunderstorms. Analysis of patterns of radial velocity and shear of the radial wind (Bohne¹) show this storm scale length to be about 4 - 8 km.

A variety of methods were employed to determine an effective outer scale length. First to be used was simple observation of the character of the power spectral density curves, in particular, the location where the curves change from an approximate $-5/3$ slope to a slope near zero. Second, the autocorrelation function is observed to determine the lag distance at which it first becomes zero. Third, the longitudinal autocorrelation function is integrated to obtain an estimate of the longitudinal integral scale. From this quantity an effective outer scale estimate is derived. Fourth, the longitudinal autocorrelation function is fitted to exponential and Von Karman forms. Only 1981 aircraft data were subjected to these analyses owing to the somewhat variable results obtained. However, the various methods were useful in isolating a range of most probable values for the effective outer scale. The range of probable values does support the conclusions obtained from direct comparison of the radar and aircraft derived estimates of turbulence severity

(Section 4). An entire aircraft penetration series of gust data was used in each analysis. The data were detrended and lowpass filtered to remove bias from non-turbulent long and short scale features.

A typical power spectral density plot, obtained from power spectral analysis of aircraft longitudinal gust data is shown in Figure B1. Figure B2 shows a modeled turbulence field. The model displays the expected behavior of a longitudinal power density spectrum where the turbulence field is of the inertial subrange (Kolmogorov) form with a finite maximum scale of length of 1 km. In this Kolmogorov representation the curve (Figure B2) is given by

$$S(K) = \frac{3}{5} (C\epsilon^{2/3}) K_o^{-5/3} (1 - 5/11 (K_1/K_o)^2) \quad K_1 < K_o \quad (B1)$$

$$= 18/55 (C\epsilon^{2/3}) K_1^{-5/3} . \quad (B2)$$

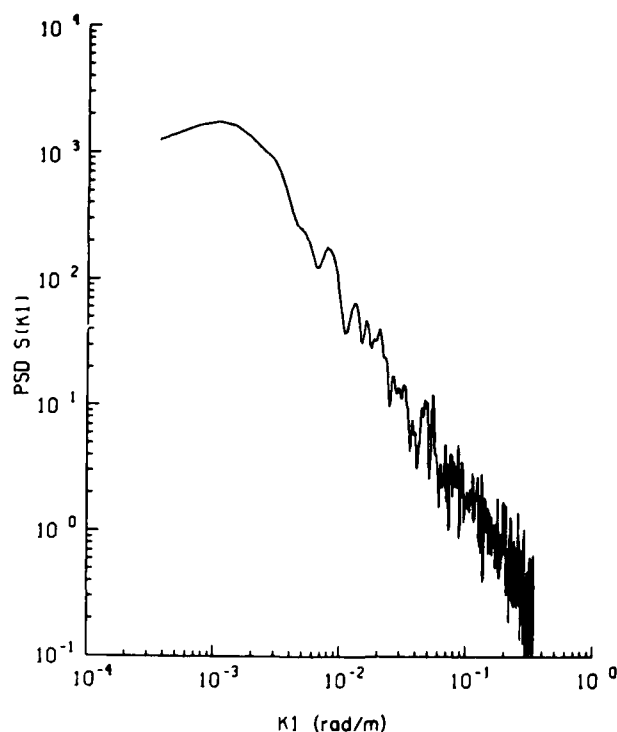


Figure B1. Longitudinal Power Density Spectrum for Aircraft Gust Component Data From Penetration 1 on 3 July 1981

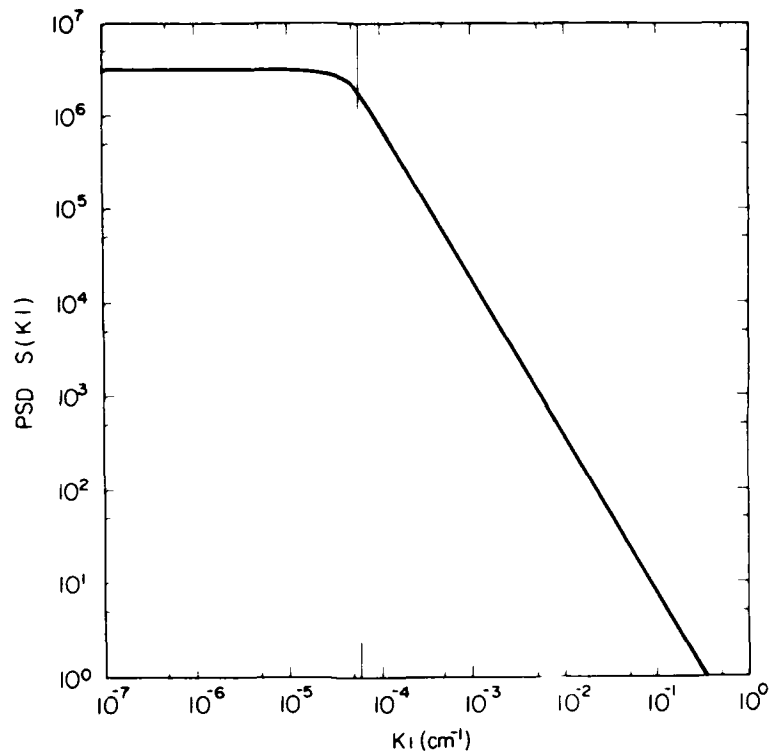


Figure B2. Longitudinal Power Density Spectrum for Model Turbulence Field

Observation of the behavior of this curve suggests that under ideal conditions, that is the turbulence field is homogeneous and isotropic and has a distinct maximum eddy scale length, a reasonable estimate of the outer scale value can be obtained from the shape of the power density spectrum curve.

The real data (Figure B1) were obtained from penetration 1 on 3 July 1981 and may be considered representative of the 1981 aircraft data. Figure B1 exhibits a slope somewhat greater than $(-5/3)$ in what one would loosely call the inertial subrange region and a reasonably distinct change in slope near $k = 0.002 \text{ m}^{-1}$. Comparison with theoretical behavior (Figure B2), suggests that the effective outer scale is roughly 3.14 km. However it is readily apparent that the change in slope occurs at a scale length where very few independent estimates are available, making accurate estimation of outer scale perhaps questionable. Also, detrending of the entire data set removes energy from large-scale (small k) regions. Thus this technique may allow for a reasonable approximation only when the effective outer scale is much less than the data segment length so that the knee of the curve reflects the true behavior and has not been artificially induced. Comparisons between detrended and non-detrended 1981 gust data show that the power reduction at those scales where the power spectrum density curve exhibited the abrupt change in slope

is usually minor. Finally, it must be remembered that use of a large local data segment occasionally forces one to incorporate storm regions exhibiting different turbulence and storm wind field regimes. Thus this simplistic approach may at best give only a range of probable values for effective outer scale length.

Power spectral density plots were developed for each aircraft penetration for year 1981. These were analyzed and estimates of the turbulence outer scale determined for each penetration. Considering the difficulties in interpretation discussed earlier, it is understandable that no truly consistent set of estimates were obtained. However, it is significant that the outer scale estimates generally fell within the range of 0.5 - 4 km, with values most frequently occurring in the interval of 1.0 - 2.0 km.

B1. AUTOCORRELATION ANALYSIS

In the autocorrelation analyses, the results were similar to those obtained from analysis of power spectral density plots, particularly in the determination of the most probable range of outer scale length. A typical plot of a longitudinal ACF is shown in Figure B3. It is noted that the curve exhibits a somewhat decreasing exponential behavior for short lag lengths and then a large-scale oscillation around zero as lag length increases. At very large lag values the curve becomes very erratic. This longwave feature may be seen in the corresponding original time series of data shown in Figure B4. It is quite clear that this nonturbulent artifact strongly biases the autocorrelation function and may corrupt any outer scale estimates. This nonturbulent feature was removed in the following way.

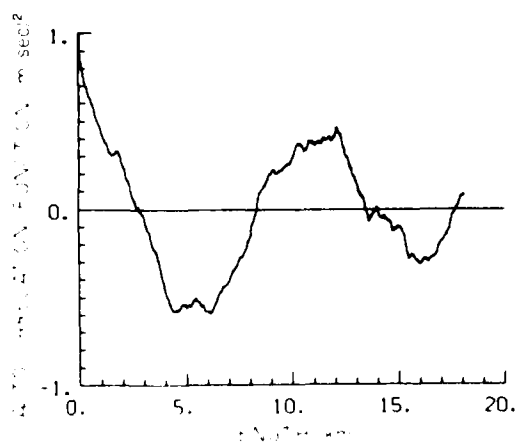


Figure B3. Autocorrelation Function for Longitudinal Aircraft Gust Data From Penetration 3 on 17 July 1981

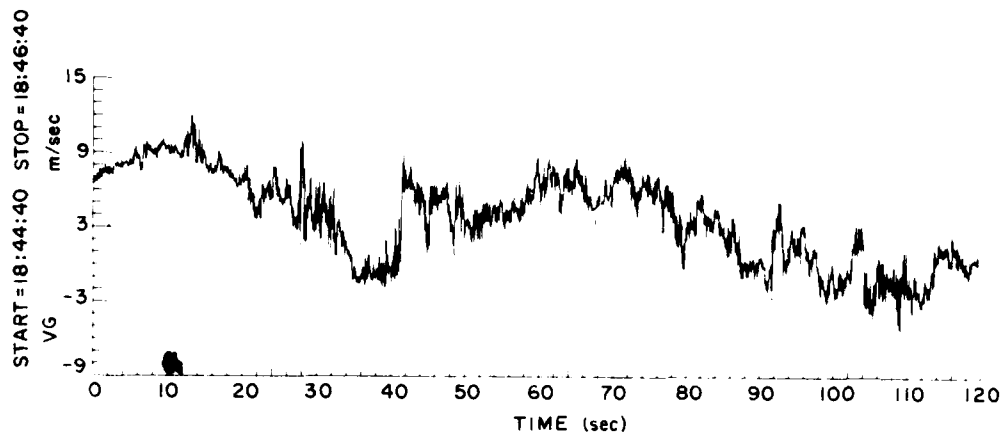


Figure B4. Time History of Longitudinal Aircraft Gust Component Data for Penetration 3 on 17 July 1981

If one assumes the gust velocity data to be composed of turbulent fluctuations and a storm scale periodic component, the resulting autocorrelation function may be considered a sum of the two autocorrelations independently since the large-scale and turbulence components may be considered as independent. Under this assumption the aircraft gust data contain a true turbulence component V_T and a large-scale wave component V_W as given by

$$V = V_T + V_W. \quad (B3)$$

Assuming that the two components are independent

$$B(r) = B_T(r) + B_W(r), \quad (B4)$$

showing the resultant autocorrelation function $B(r)$ is a linear sum of the two individual autocorrelation terms.

Consider the wave component. If the wave has wavelength L and the total original segment length is T , then for a wave component of the form

$$V_W(x) = A \cos(2\pi x/L) \quad (B5)$$

the autocorrelation for a distance τ is

$$R(\tau) = \frac{A^2}{T} \left[\cos\left(\frac{2\pi\tau}{L}\right) \frac{1}{2} \left(T - \tau + \frac{L}{4\pi} \sin\left(\frac{4\pi(T-\tau)}{L}\right) - \frac{L}{4\pi} \sin\left(\frac{2\pi\tau}{L}\right) \sin^2\left(\frac{2\pi(T-\tau)}{L}\right) \right] \quad (B6)$$

The value at $\tau = 0$ is

$$R(0) = \frac{A^2}{T} \left[\frac{T}{2} + \frac{L}{8\pi} \sin\left(\frac{4\pi T}{L}\right) \right] \quad (B7)$$

and if $T = mL$ where m is an integer then we obtain the usual $R(0) = A^2/2$. Observation of Eq. (B6) displays the characteristic nature of this function. In the special case $\tau = nL$ and $T = mL$

$$R(\tau) = \frac{A^2}{2} \left(1 - \frac{n}{m}\right) \quad (B8)$$

which is a periodic function of amplitude $A^2/2$, having wavelength L and an amplitude modulation factor of $(1 - n/m)$. This modulation factor is equivalent to normalizing the autocorrelation by $T - x$, and then applying a filter $(1 - \frac{x}{T})$ on the autocorrelation function. Thus the amplitude of $R(\tau)$ in this instance decreases linearly from $A^2/2$ to zero.

To remove this sinusoidal contamination one may either remove the periodic term from the sum correlation function a posteriori or apply a notch filter to the input time series data. Limited attempts with a notch filter yielded results that were not as satisfying as the manual removal method. Thus the original autocorrelation function was used to determine the wavelength and magnitude of the large-scale feature by observing the maximum upward and downward amplitudes beyond the first $R(\tau) = 0$ crossing and the placement of the minima and maxima. This approach is reasonable if the turbulence outer scale is much less than the scale of the storm feature, allowing the turbulence autocorrelation to approach zero rapidly and enabling the periodic feature to be easily detected. Figure B5 shows the result after removal of the wave component from the function in Figure B3. It should be noted that all four methods which employed the autocorrelation function were run both with and without large-scale wave removal. Results clearly demonstrated greater consistency when removal was employed. Thus the final analyses employed wave removal when the storm scale appeared to strongly influence the original autocorrelation function.

The first method, observation of the lag distance where the autocorrelation function equals zero, yielded values ranging from 0.25 - 4 km. The resulting values were quite inconsistent and because of the possibility of incomplete removal of any large-scale periodic effect, these results are expected to be useful only as establishing a general range of possible values of turbulence outer scale.

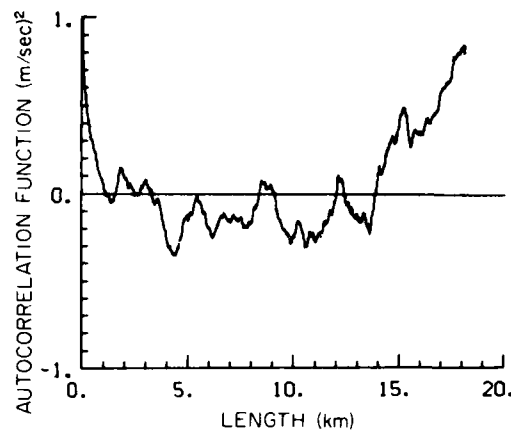


Figure B5. Autocorrelation Function After Removal of Large-scale Wave Feature

The second method employed integration of the autocorrelation function to estimate the longitudinal integral scale. From this value the effective outer scale was derived from

$$\lambda_o = 4.189 L . \quad (B9)$$

The results obtained here were once again scattered about in the range 0.4 - 4 km. These first two simple procedures provide a range of probable values for the effective turbulence outer scale length.

The final two methods, fitting the normalized autocorrelation function to a Von Karman and decreasing exponential form provided somewhat more stable results and are shown in Table B1. The exponential relation is given by

$$f(x) = e^{-x/L} \quad (B10)$$

where $f(x)$ is the longitudinal autocorrelation function, x is the lag distance, and L is the longitudinal integral scale. The Von Karman representation is given by

$$R(x) = 2^{7/2} \left(\frac{9}{55}\right) \frac{\sqrt{\pi}}{\Gamma(5/6)} K_e E(K_e) x^{1/3} K_e^{1/3} K_{1/3}(xK_e) \quad (B11)$$

where $K_{1/3}(x)$ is the modified Bessel function of order 1/3, and K_e is the wave-vector magnitude where the turbulence energy spectrum is a maximum. It should be noted that these methods are applied only over lag distances less than about 2 km. Estimates of effective turbulence outer scale derived from these two methods were very similar in almost every case and results for the exponential fitting procedure only are shown. Figure B6 shows the curves for a longitudinal integral scale length of 338 m. Table B1 lists the estimates of effective turbulence outer scale as determined from analyses of the longitudinal autocorrelation both with and

without wave removal. With the wave factor included the effective turbulence outer scale values lie in the range of 2 - 6 km. However, with wave removal the estimates are more consistent and exhibit a range of roughly 0.5 - 3 km. These values lie within the bounds established by the previous methods and are in better agreement with those derived from comparison of aircraft and radar derived turbulence severity estimates (Section 4).

Table B1. Von Karman/Exponential Fit to Longitudinal Autocorrelation Function Effective Turbulence Outer Scale λ_0 (meters)

Day	Penetration	λ_0 (meters) Without Sinusoidal Removal	λ_0 (meters) With Sinusoidal Removal
182	1	3920	2737
184	1	2324	1986
	2	2685	2523
	3	3130	2853
197	1	4863	1345
	2	3881	3104
198	1	5144	3047
	2	6111	648
	3	2898	1259
		4494	1416

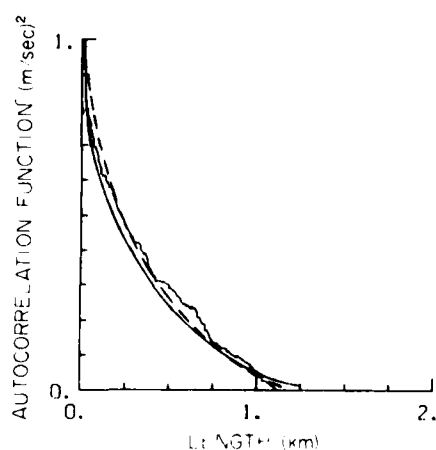


Figure B6. Autocorrelation Function With Exponential (dash) and Von Karman (solid) Representations Having a Longitudinal Integral Scale Length of 338 m

The final conclusion of these particular efforts is that estimation of a single well defined turbulence outer scale value from a time series of aircraft gust data is a difficult task. This result should not be unexpected if we consider the meteorological environment that we are interrogating. The aircraft penetration track typically began on the periphery of the radar detectable storm boundary, traced through the storm, frequently passing near interior storm cells, and exited through the opposite storm boundary. Thus, each penetration incorporates regions of widely varying environmental shear, updraft-downdraft complexes, and varying turbulence regimes. One should not expect the resultant aircraft gust time series data to well represent a homogeneous isotropic turbulence field embedded within a slowly varying quasi-stationary storm environmental wind field. In fact, what is encountered can best be described as an amalgum of a series of relatively localized zones within which each displays a resultant wind field structure which may only roughly approximate a stationary storm environment and uniform turbulence field. Each local region responds to the local forcing dynamic field, and displays dominant scales and energy content corresponding to that local forcing influence. It may be possible to reduce the entire penetration into a series of segments, with each segment capable of being decomposed into large scale storm and small scale turbulence components (Bohne¹). From this it can easily be demonstrated that analysis of various combinations of such segments yields results which do not describe the behavior of any one segment, but are dominated more by features which have scales comparable to the segment sizes. Thus use of autocorrelation and power spectral analyses as commonly performed and described above may not be useful in determining a single effective outer scale length. However, these techniques may be useful in establishing bounds for the effective turbulence scale. It is certainly enlightning to observe that the range of probable values agrees well with the conclusions derived from direct comparison of radar and aircraft estimates of turbulence severity.

Appendix C

Stability of Aircraft Turbulence Severity Estimates

There are numerous methods for estimating the turbulence eddy dissipation rate from the time series of aircraft gust data. Primary candidates usually make use of the power spectral density, autocorrelation, or structure function methods. In the analyses performed here the structure function has been utilized, due to its ability to remove storm structure bias from the estimate when the storm structure scales are significantly greater than the energy-containing eddy scales. This feature may be easily demonstrated by assuming a measured gust component V as composed of a true turbulence component V_T and a storm scale component V_S .

$$V = V_T + V_S . \quad (C1)$$

For this example the storm scale is sufficiently large to approximate it by a straight line trend over the data segment to be analyzed, giving

$$V_S = a + bx . \quad (C2)$$

The autocorrelation of the fluctuating gust velocity deviations is

$$B(\tau) = \frac{1}{L} \int_L (V(x) - \bar{V}(x)) (V(x+\tau) - \bar{V}(x+\tau)) dx \quad (C3)$$

$$= \frac{b^2 L \tau}{4} + \frac{b^2 L^2}{12} + \rho(\tau) V_T^2 \quad (C4)$$

where $\rho(\tau) V_T^2$ is the true turbulence autocorrelation function.

We see that the autocorrelation function incorporates two trend terms. The minimum bias in the autocorrelation is $b^2 L^2 / 12$. The bias contribution will remain close to this value as long as the lag distance $\tau \ll L/3$. Alternatively, the structure function estimate for the same segment L is

$$D(\tau) = \frac{1}{L} \int_L (V(x) - V(x+\tau))^2 dx \quad (C5)$$

$$= 2 \overline{V_T^2} (1 - \rho(\tau)) + b^2 \tau^2. \quad (C6)$$

Assuming the storm field gradient is not excessively large, the resultant structure function estimate at short lags is dominated by the actual turbulence structure function estimate, with the storm field term a minor contributor. Thus, if the largest turbulence scale is small relative to the dominant storm scale, the structure function estimate will effectively correspond to the turbulence contribution. As r is increased the storm bias term may become significant. In the case where there is no distinct separation in scale between the turbulence and storm wind fields, then the resultant structure function estimate will not approach a stable value with increasing separation size, but will be continually influenced by storm structure effects.

The relative significance of storm bias may be obtained by forming the ratio of the storm scale bias for the two methods. The ratio is

$$D(\tau)/B(\tau) = b^2 \tau^2 / \left(\frac{b L^2}{12} + \frac{b^2 L \tau}{4} \right) \quad (D7)$$

$$\approx 12 \tau^2 / L^2.$$

It is observed that as long as the lag distance τ is less than $L/3$ the bias in the structure function will be less than in the autocorrelation function. In the analyses performed here lag distances of the order of 100 m were used while the segment length L was approximately 1200 m. Thus here the structure function method will exhibit less bias than the autocorrelation (and power spectrum) method. It may be stated that one can always remove the trend from the data segment before analysis. However, here a local and stable estimate of eddy dissipation rate is desired, and the segment lengths over which the analyses are performed may be comparable to the larger eddy scales. Detrending these short data segments could have the

undesirable effect of severely reducing the energy contributions from the moderate to large turbulence scales and is therefore unacceptable. Thus the aircraft data were analyzed through use of the structure function technique, at lag distances small (about 100 m) in comparison to the expected turbulence outer scale, and certainly significantly smaller than the dominant storm structure scale.

To establish the proper data segment length to be used in forming the structure function at any desired location, a series of data segments, with each segment centered about the desired location, but greater in length than the preceeding, is used. Successive estimates of the structure function, when made at short lag distances will eventually approach an asymptotic value which remains relatively constant, even as the data segment lengths are increased. This is true as long as the segment length is much smaller than the dominant storm scale. This behavior may be interpreted as allowing the data segment to incorporate sufficient turbulence scales so that the estimate is effectively a local ensemble estimate.

A demonstration of the behavior of the autocorrelation function, structure function, and turbulence severity estimate as a function of data segment length is shown in Figures C1 - C3. The corresponding longitudinal gust component is shown in Figure C4. With an aircraft speed of about 200 m/sec, a 1200-m data segment is about 6 sec wide. The time series plot shows a definite large-scale feature upon which lies the turbulent fluctuations. Location A lies within a feature having a scale which may be that of either large-scale turbulence or small scale storm environment. Location B lies on a peak where no significant storm scale trend exists, and location C lies imbedded within a definite large-scale storm feature.

At location A (Figure C1) the autocorrelation function shows an initial strong increase in magnitude with increasing lag distance, but then levels off at a data segment length of about 1300 meters. This indicates that with a 1300-m segment all necessary turbulence scales have apparently been incorporated into the local estimate and it resembles a good local ensemble value. Location B, however, displays a nearly constant value of 0.5 up to a data segment length of 1200 meters. At larger lag distances the storm scale bias becomes influential and the magnitude increases. Location C displays a continual increase in the autocorrelation function as the storm scale feature biases the estimate through all data segment lengths. These results show that observation of the behavior of the autocorrelation function would not give any clear indication of what data segment length, in general, could be used to form a stable estimate of turbulence severity.

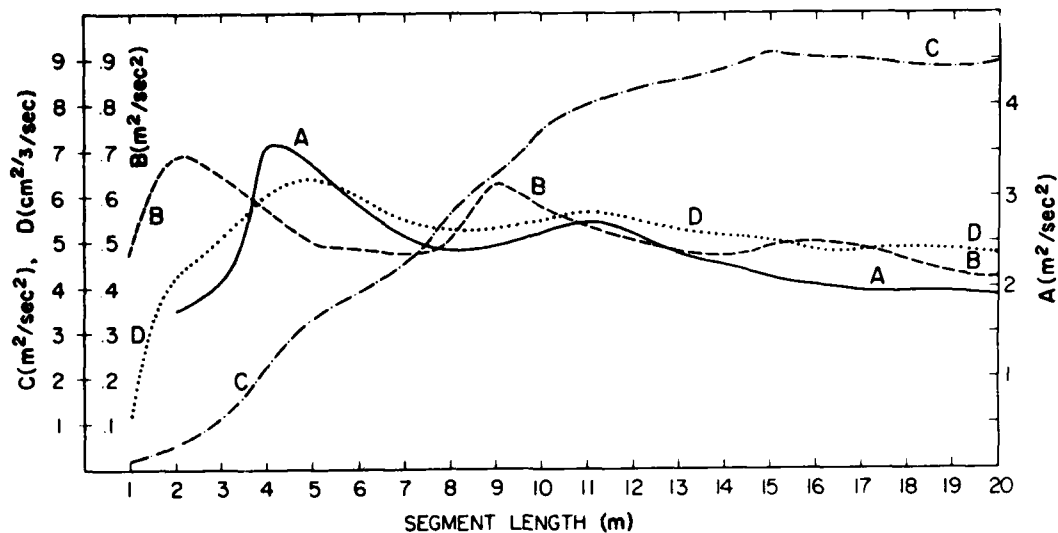


Figure C1. Behavior of Structure Function With Lag Distance of 18 m (A) and 108 m (B), Autocorrelation Function (C) and Estimate of Turbulence Severity (D) With Data Segment Length. Data segments are centered about location A

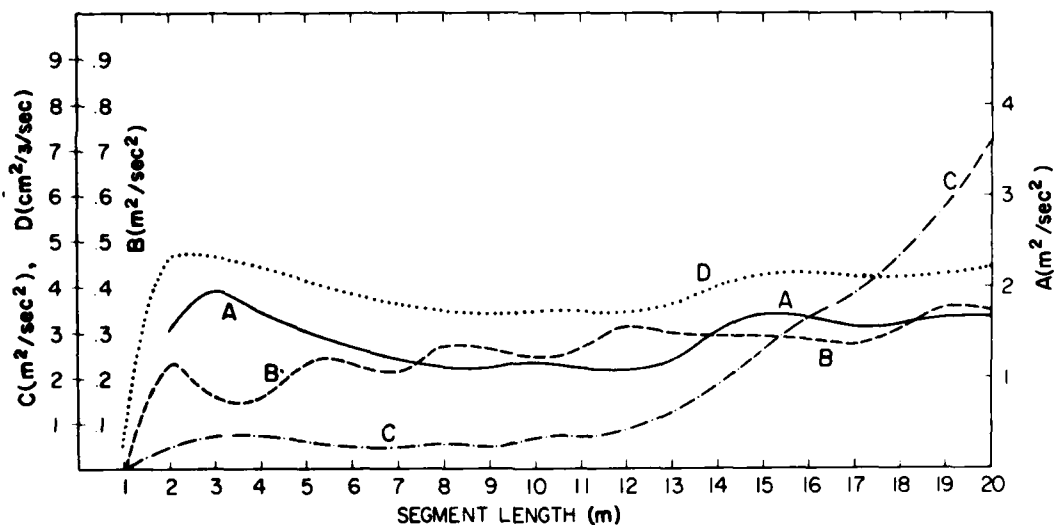


Figure C2. Behavior of Structure Function With Lag Distance of 18 m (A) and 108 m (B), Autocorrelation Function (C) and Estimate of Turbulence Severity (D) With Data Segment Length. Data segments are centered about location B

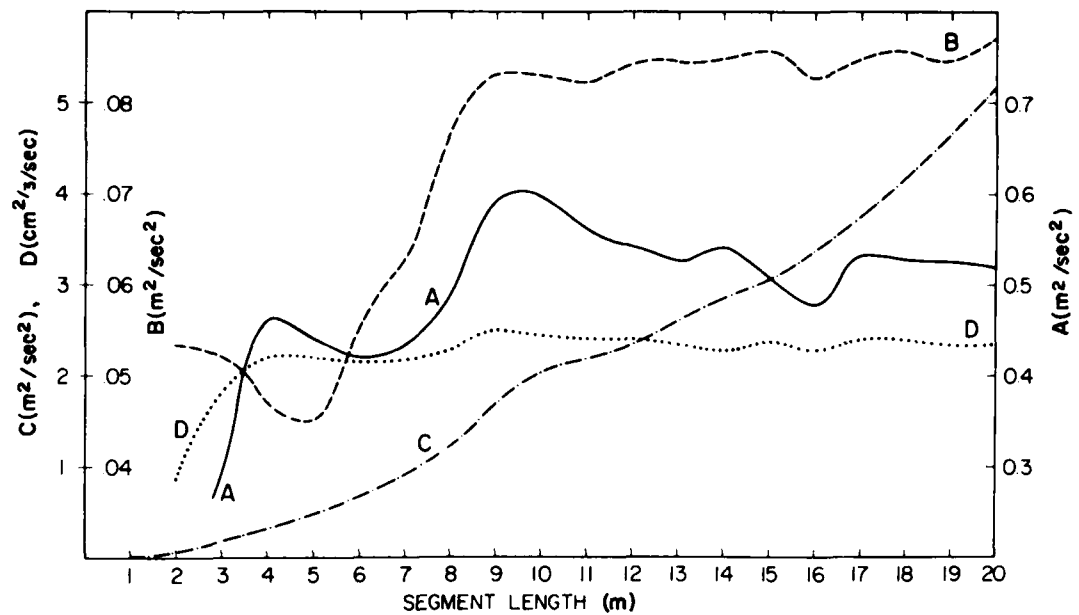


Figure C3. Behavior of Structure Function With Lag Distance of 18 m (A) and 108 m (B), Autocorrelation Function (C) and Estimate of Turbulence Severity (D) With Data Segment Length. Data segments are centered about Location C

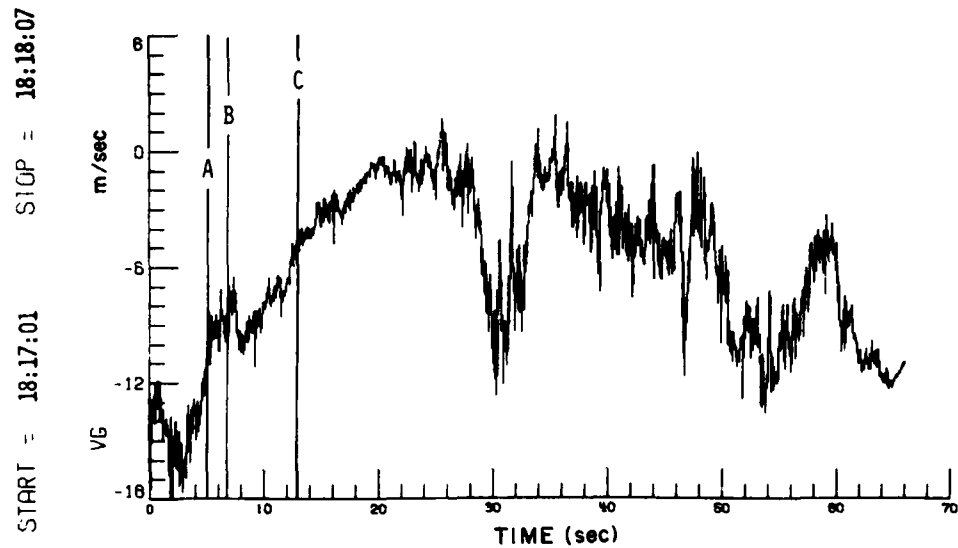


Figure C4. Time Series of Aircraft Longitudinal Gust Data From Penetration 1 on 1 July 1981

Now if one follows the behavior of the structure function estimates at these same locations over the same data segment lengths one immediately is impressed with the rapidity at which they reach a nearly stable value. In all cases a data segment length of about 1100 m is sufficient to determine a stable estimate of the structure function. The corresponding turbulence severity estimates are also shown. These were determined from the structure function estimates and are seen to become relatively constant in value more rapidly than the structure function estimates. This more rapid rise to a stable value is simply a result of the turbulence severity being proportional to the square root of the structure function estimate.

An additional demonstration of the variability of the turbulence severity estimate with data segment size is presented in Figure C5. The three curves represent estimates of turbulence severity using data segment lengths of roughly 400, 800, and 1200 m, respectively. Quick observation shows that the 800 m and 1200 m segment length estimates are consistently very close in value. This suggests that for a reasonable estimate of turbulence severity, one incorporating the major portion of large turbulence scales, either length may be used on this data set. Analyses of aircraft data were generally performed with multiple data segment lengths to ensure that a reasonably stable estimate of the local turbulence severity was obtained. In the final analyses, owing to the reliable behavior of estimates at the 1200 m segment length, only these values were used in the correlation analyses with the radar results. The turbulence severity estimates derived from the aircraft data by this method are shown in Appendix G.

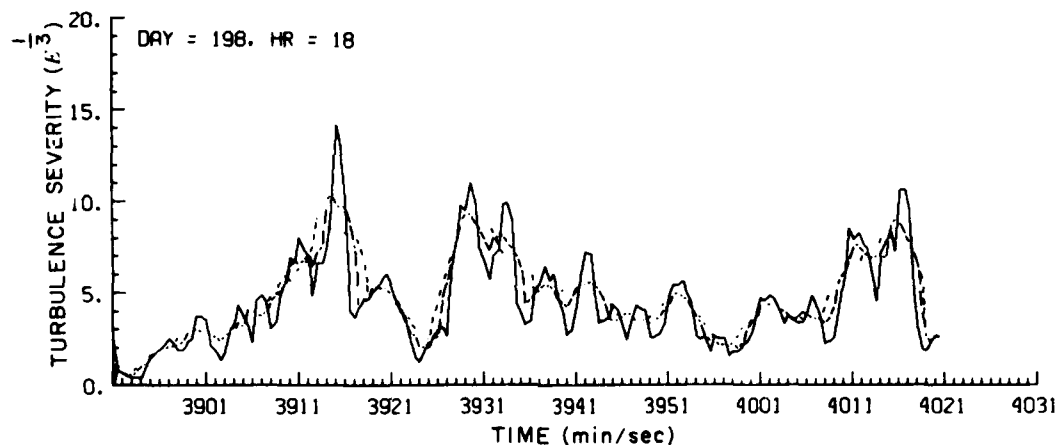


Figure C5. Time Series of Turbulence Severity Estimates Derived From 400 m (solid), 800 m (long dash), and 1200 m (short dash) Local Data Segments. Data is from penetration 2 on 17 July 1981

Appendix D

Radar Pulse Volume Filtering Effects on Structure Function Estimates

It was shown (Section 4) that use of the structure function method with real data for estimation of the eddy dissipation rate produces results which greatly underestimate the true environmental values. This results from the pulse volume filtering effects on the mapping of the normal fluctuating environmental gust velocity into Doppler mean velocity. In addition to the comparison of POD and FAR values for the various methods (structure function and variance-based methods), an additional analysis was performed to further demonstrate the pulse volume filtering effects.

28 July and 31 July 1982 represent observation periods when the useful aircraft penetration periods were close to, and far removed, from the SPANDAR radar. Comparison of the probability of detection (POD) and false alarm rates (FAR) (Section 4) for these two periods well demonstrate the radar pulse volume effects. The tracks also happen to be aligned nearly parallel and perpendicular to the radar viewing direction. Thus for these data, one is effectively estimating the longitudinal and transverse structure functions, respectively.

Consider for a moment that we shrink the radar pulse volume to a point size and that the turbulence field is homogeneous and isotropic. The general relation for point measurements made in the inertial subrange of the field is

$$D_{ij}(r) = 2 (B_{ij}(0) - B_{ij}(r)) \quad (D1)$$

where we will call (X_1 , X_2 , and X_3) the radial, horizontal and vertical transverse, directions respectively. Since the radar measures the radial wind component {1} Eq. (D1) becomes

$$D_{||}(r) = 2(B_{||}(0) - B_{||}(r)) . \quad (D2)$$

Now, for measurements made along the radial and azimuthal directions we obtain

$$D_{||}(X_1) = 2(B_{||}(0) - B_{||}(X_1)) = C \epsilon^{2/3} X_1^{2/3} \quad (D3)$$

$$D_{||}(X_2) = 2(B_{||}(0) - B_{||}(X_2)) = \frac{4}{3} C \epsilon^{2/3} X_2^{2/3} \quad (D4)$$

for the longitudinal and transverse structure function relations, respectively. To consider the pulse volume effects we first transfer to wavevector space, noting that

$$B_{||}(\vec{r}) = \int \phi_{||}(\vec{k}) \cos(\vec{k} \cdot \vec{r}) d\vec{k} \quad (D5)$$

where $\phi_{||}(\vec{k})$ is the power spectral density for the radial wind velocity component. Inserting this relation into Eqs. (D3) and (D4) we obtain

$$D_{||}(X_1) = 2 \int_{\vec{k}} \phi_{||}(\vec{k}) (1 - \cos(k_1 X_1)) d\vec{k} \quad (D6)$$

$$D_{||}(X_2) = 2 \int_{\vec{k}} \phi_{||}(\vec{k}) (1 - \cos(k_2 X_2)) d\vec{k} . \quad (D7)$$

The power spectral density $\phi_{||}(\vec{k})$ simply details how the environmental turbulence energy is distributed throughout wavevector space \vec{k} ($|\vec{k}| = 2\pi/\lambda$) where λ is the wavelength representation of an eddy pair of size $L/2$. Note further that

$$\phi_{||}(\vec{k}) = \left(\frac{k_2^2 + k_3^2}{k^2} \right) \frac{E(k)}{4\pi k^2} \quad (D8)$$

where $E(k)$ may, in general, represent the effective Kolmogorov energy spectrum or the Von Karman spectrum. From these point measurement relations we see that the $(1 - \cos(\vec{k} \cdot \vec{r}))$ term is a sort of filter acting upon the total energy spectrum $\phi_{||}(\vec{k})$. From Eqs. (1), (D7), and (D8) we see that the energy reduction from this effective filtering in the transverse direction is smaller (bracket closer to unity) than for the longitudinal direction. This effect is demonstrated by the increased fluctuation energy (the 4/3 multiplier) measured in the transverse mode.

Now with use of radar, we are no longer making point measurements, but rather each radar radial velocity estimate is a spatial average of the environmental gust velocity components throughout the radar pulse volume. In this case we must replace $\phi_{||}(\vec{k})$ by

$$\phi_{||}(\vec{k}) = \phi_{||}(\vec{k}) \phi_I(\vec{k}) \quad (D9)$$

where

$$\phi_I(\vec{k}) = (\sin(k_1 H/2)/(k_1 H/2))^2 e^{-\sigma_2^2 k_2^2} e^{-\sigma_3^2 k_3^2} \quad (D10)$$

is the two way pulse volume filter representation in wavevector space, H is the pulse volume length, and

$$\sigma_2 = \sigma_3 = R\theta/(8 \ln 4)^{1/2} \quad (D11)$$

where R is the range from the radar to the pulse volume location and θ is the full half-power beam width. With this modification, Eqs. (D6) and (D7) become

$$D_{||}(X_1) = 2 \int_{\vec{k}} \phi_I(\vec{k}) \phi_{||}(\vec{k}) (1 - \cos(k_1 X_1)) d\vec{k} \quad (D12)$$

$$D_{||}(X_2) = 2 \int_{\vec{k}} \phi_I(\vec{k}) \phi_{||}(\vec{k}) (1 - \cos(k_2 X_2)) d\vec{k} . \quad (D13)$$

Thus inclusion of radar beam effects simply requires multiplying the original environmental energy distribution by the beam filter function.

Table D1. presents the probability of detection (POD) and false alarm rates (FAR) for the suggested composite severity levels for these two periods. These values were obtained from comparison of the merged (Section 4) aircraft estimates of turbulence severity with those from the radar structure function method. The corresponding results for the variance-based method with effective outer scale length of 2 km are also included for comparison. On 28 July the average distance from the radar to the observed aircraft penetration regions is about 60 km, while on 31 July the distance is closer to 110 km. First consider the moderate composite class. The results show that in going from the near to more distant storm the structure function POD has decreased 6 percent while the FAR has increased by 7 percent. The variance-based method shows virtually no change in POD and FAR for the two observation periods. For the heavy composite class the structure function POD has been cut in half from 47 to 21 percent, while the FAR value has more

than doubled from 21 to 49 percent. Meanwhile the variance-based FAR remains constant, while the POD has decreased by 10 percent. This decrease, however, is much smaller than that observed for the structure function method. Indeed, when the combined behavior of the POD and FAR results are considered, it is clear that the success of the structure function method, particularly in detection of hazardous turbulence, is strongly range dependent. The variance-based method which includes beam filtering effects is comparatively unaffected by range. Experience with these radar data indicate that effects of large-scale wind shear, inability to properly obtain an equivalent ensemble of observations, and radar induced biases are minor influences on the range dependent behavior noted here. Thus the range effects observed here are considered to result mainly from pulse volume filtering. One may account for the filtering effects through inversion methods (Sychra^{D1}). However, due to nonturbulent influences in the Doppler measurements discussed above, it is often difficult to obtain satisfying results. Certainly, this method would not generally be applicable for real time analysis.

Table D1. Radar Probability of Detection and False Alarm Rate Variation With Range

Turbulence Severity (cm^2/sec)	Structure Function				Variance $\lambda_o = 2 \text{ km}$			
	July 28 (near)		July 31 (far)		July 28 (near)		July 31 (far)	
	POD	FAR	POD	FAR	POD	FAR	POD	FAR
\geq Moderate ≥ 1.5	75	7	69	13	95	16	96	15
\geq Heavy ≥ 3.5	47	21	23	49	90	40	80	40

These observations force one to consider the possible range at which useful radar structure function techniques could be employed. The SPANDAR pulse volume widths at ranges of 60 and 120 km are about 0.4 and 0.8 km, respectively. Typical ground based and airborne radars have full half-power beamwidths of about 1 and 4 degrees. Thus the pulse volume effects observed here would be comparable to a ground based radar observing regions roughly 23 and 46 km away.

D1. Sychra, J. (1972) On the Theory of Pulse Volume Filtering of Turbulent Reflectivity and Velocity Fields, Technical Report 29, LAP, University of Chicago, Chicago, Illinois.

For the airborne radar the ranges would be 6 and 12 km respectively. Unless radar beam filtering is accounted for, an effective range from the airborne radar to produce truly representative estimates of environmental turbulence severity may actually be so small as to render them useless to the pilot. Thus, it appears that use of simple structure function methods with radar mean velocity data as a means of detecting hazardous turbulence regions are constrained to use with ground based radars at short range.

Appendix E

Wallops Island Sounding Data

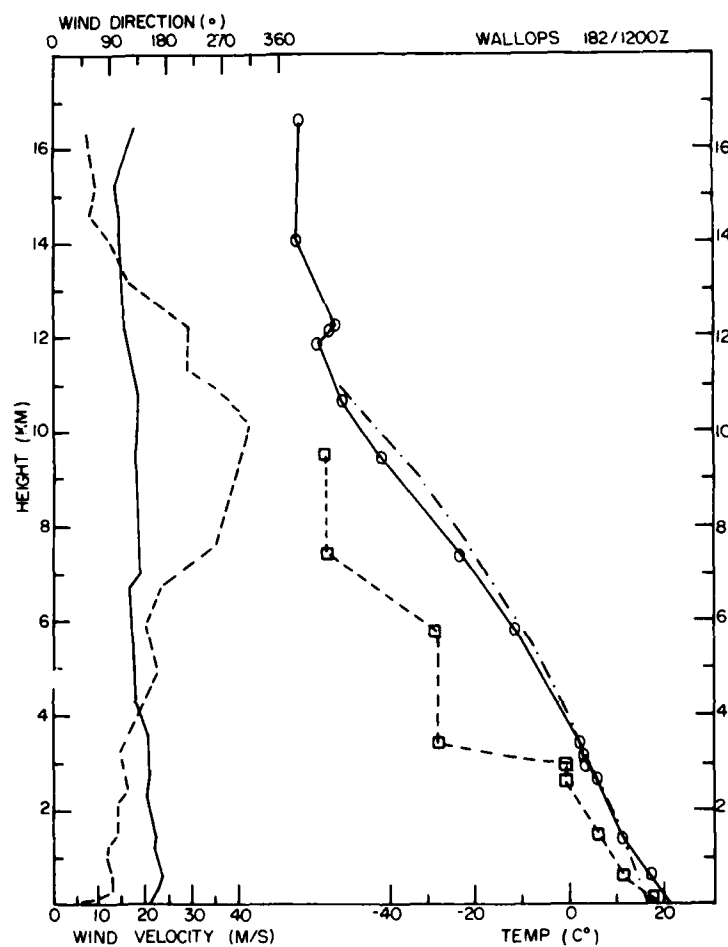


Figure E1. Wallops Island Sounding Data for 1 July 1981 at 1200 GMT. Wind data; speed (dash) and direction (solid); temperature; temperature (solid), dew point (dash), and pseudoadiabat (dash-dot)

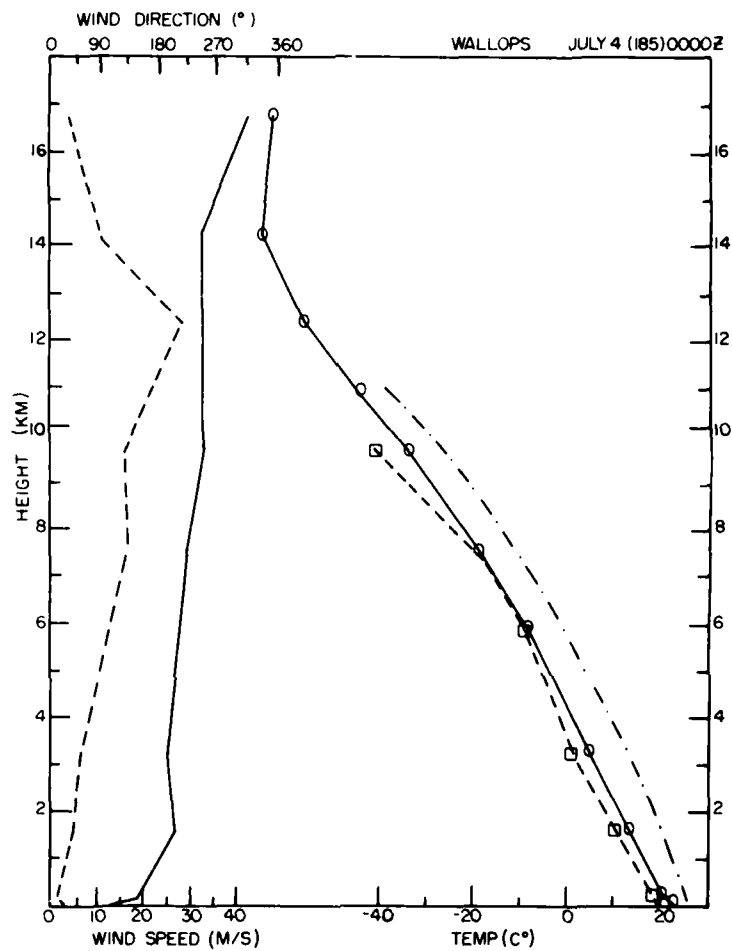


Figure E2. Wallops Island Sounding Data for 4 July 1981 at 00 GMT. Wind data; speed (dash) and direction (solid); temperature; temperature (solid), dew point (dash), and pseudoadiabats (dash-dot)

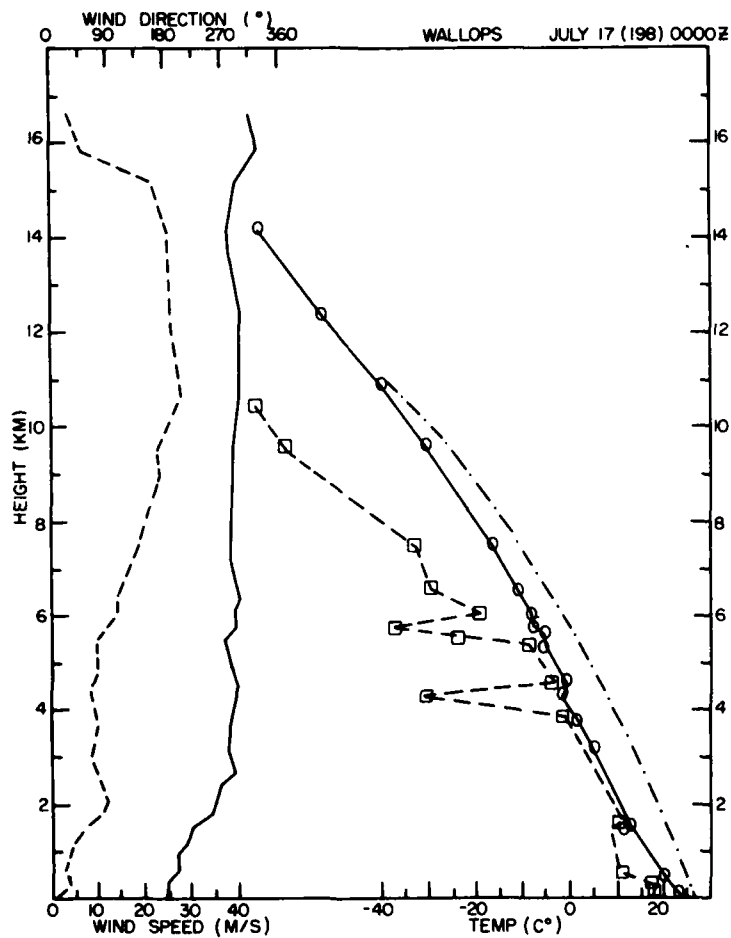


Figure E3. Wallops Island Sounding Data for 17 July 1981 at 00 GMT. Wind data; speed (dash) and direction (solid); temperature; temperature (solid), dew point (dash), and pseudoadiabats (dash-dot)

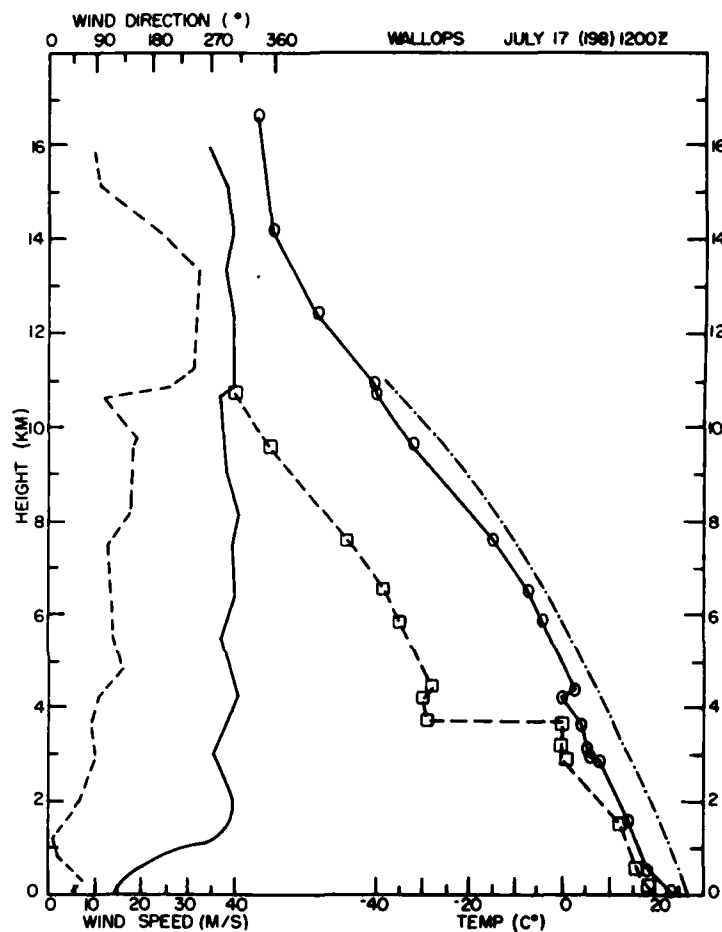


Figure E4. Wallops Island Sounding Data for 17 July 1981 at 1200 GMT. Wind data; speed (dash) and direction (solid); temperature; temperature (solid), dew point (dash), and pseudoadiabats (dash-dot)

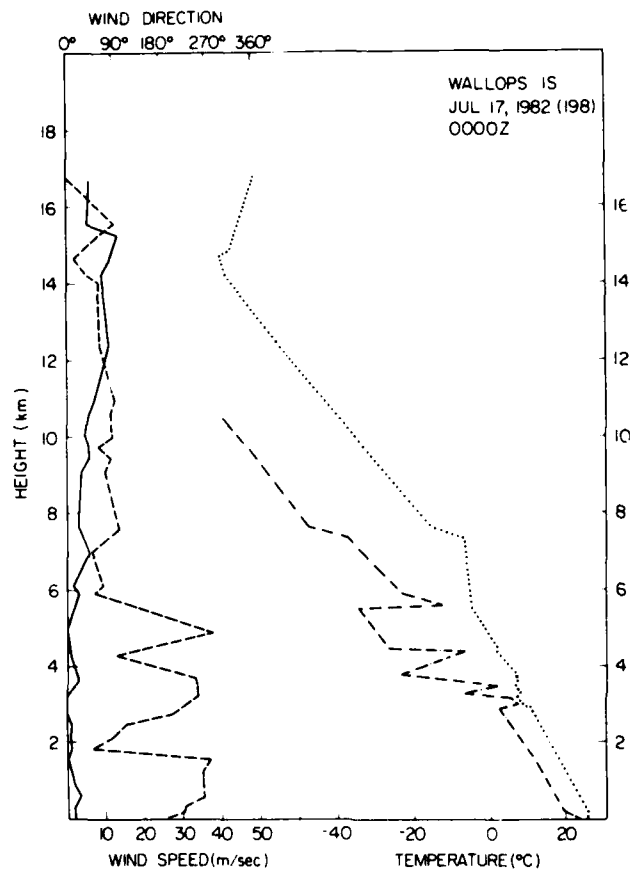


Figure E5. Wallops Island Sounding Data for 17 July 1982 at 00 GMT. Wind data; speed (dash) and direction (solid); temperature; temperature (solid), dew point (dash), and pseudoadiabats (dash-dot)

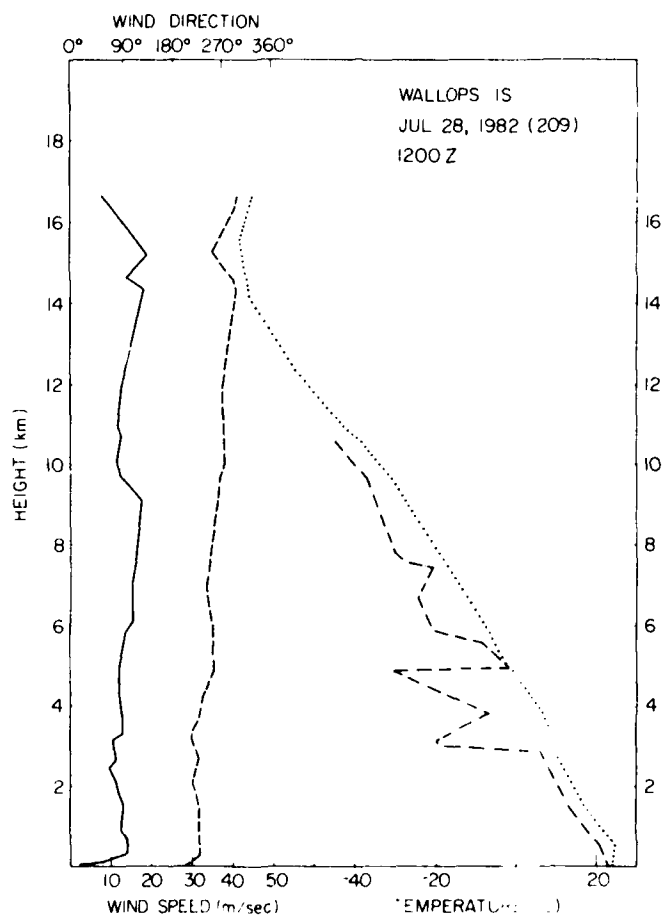


Figure E6. Wallops Island Sounding Data for 28 July 1982 at 1200 GMT. Wind data; speed (dash) and direction (solid) temperature; temperature (solid), dew point (dash), and pseudoadiabat (dash-dot)

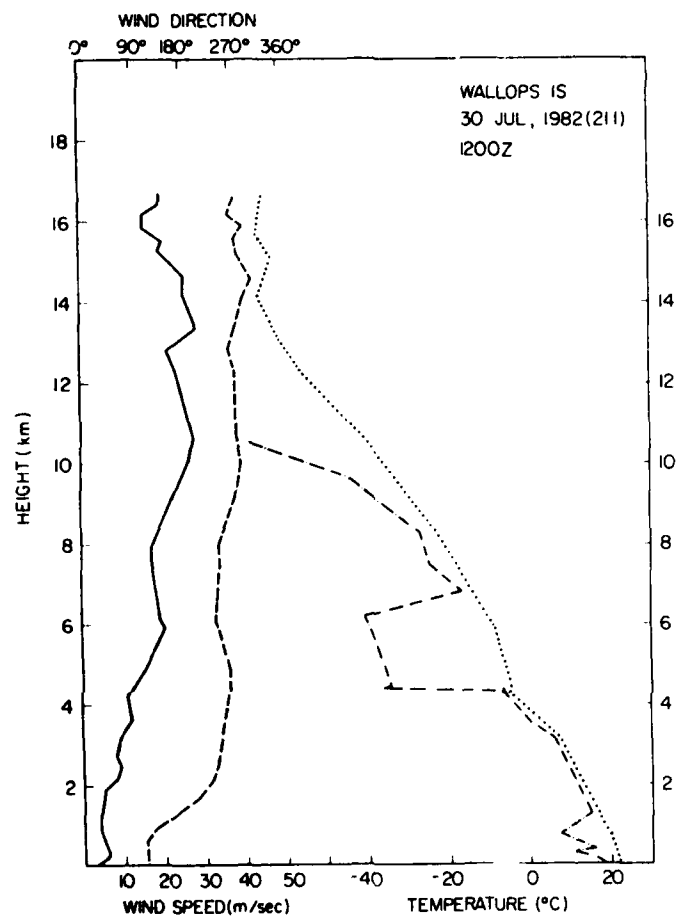


Figure E7. Wallops Island Sounding Data for 30 July 1982 at 1200 GMT. Wind data; speed (dash) and direction (solid) temperature; temperature (solid), dew point (dash), and pseudoadiabats (dash-dot)

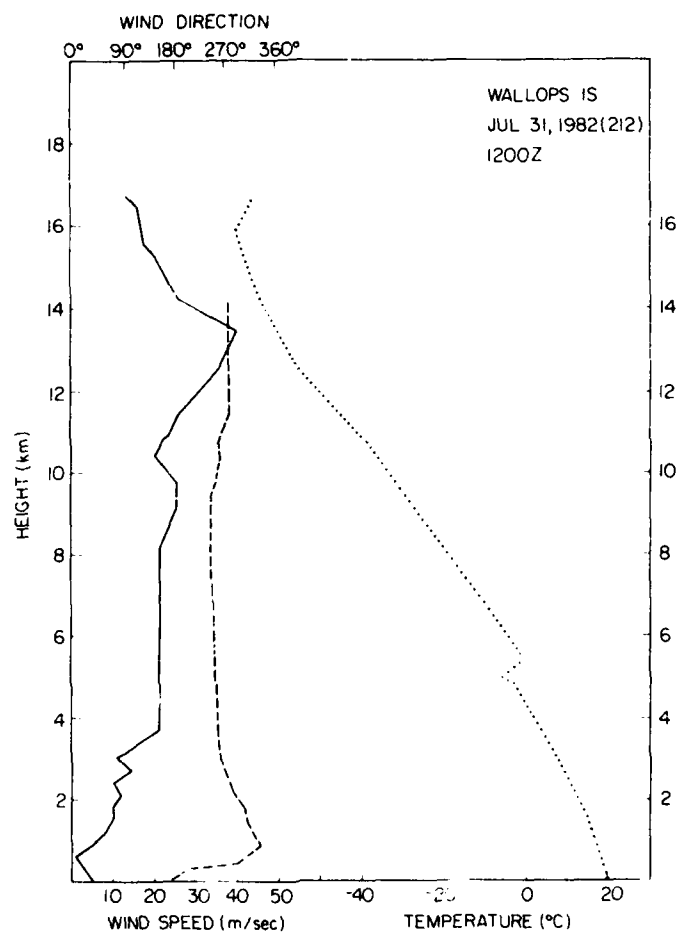


Figure E8. Wallops Island Sounding Data for 31 July 1982 at 1200 GMT. Wind data; speed (dash) and direction (solid) temperature; temperature (solid), dew point (dash), and pseudoadiabatic (dash-dot)

Appendix F

Tracking Gate Doppler Spectrum Mean and Variance Data

Data for Figures F1 through F22 were acquired in 1981 and for Figures 23 through F82, in 1982.

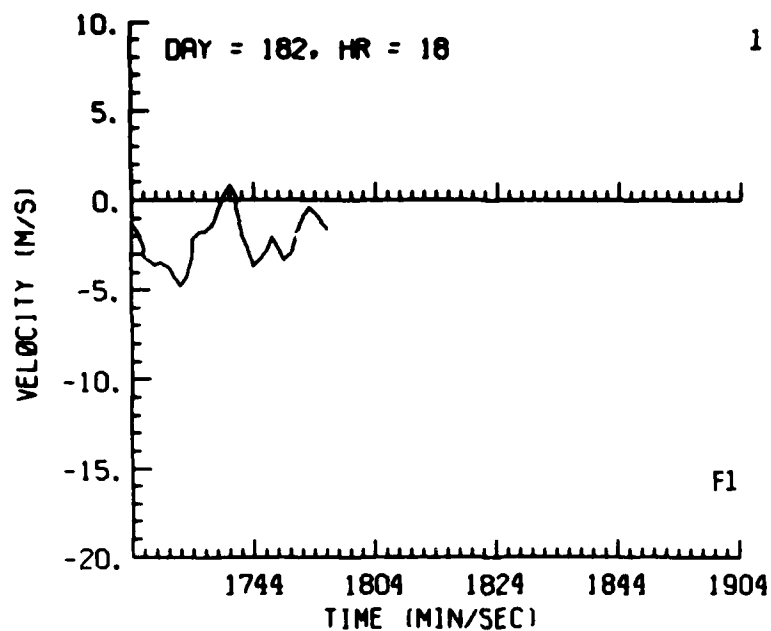


Figure F1. Tracking Gate Doppler Spectrum
Mean Data, Day 182, Penetration 1

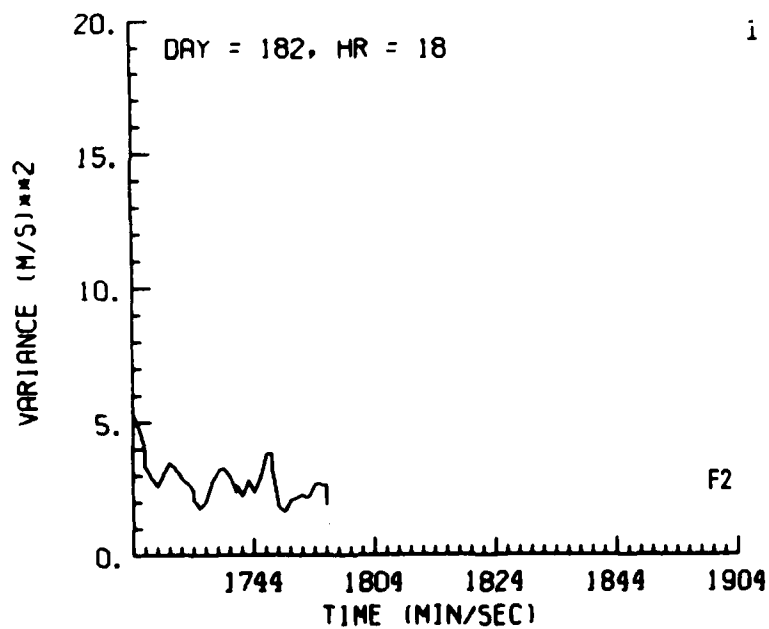


Figure F2. Tracking Gate Doppler Spectrum
Variance Data, Day 182, Penetration 1

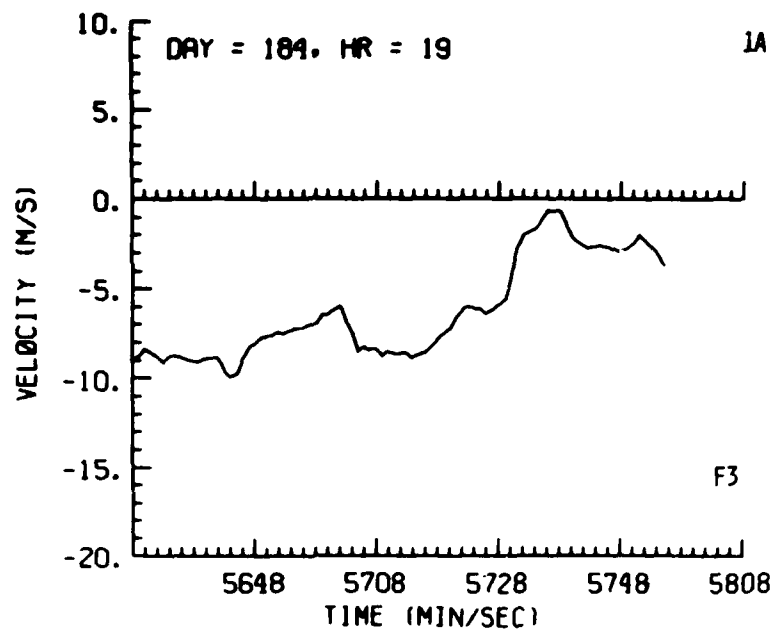


Figure F3. Tracking Gate Doppler Spectrum Mean Data, Day 184, Penetration 1A

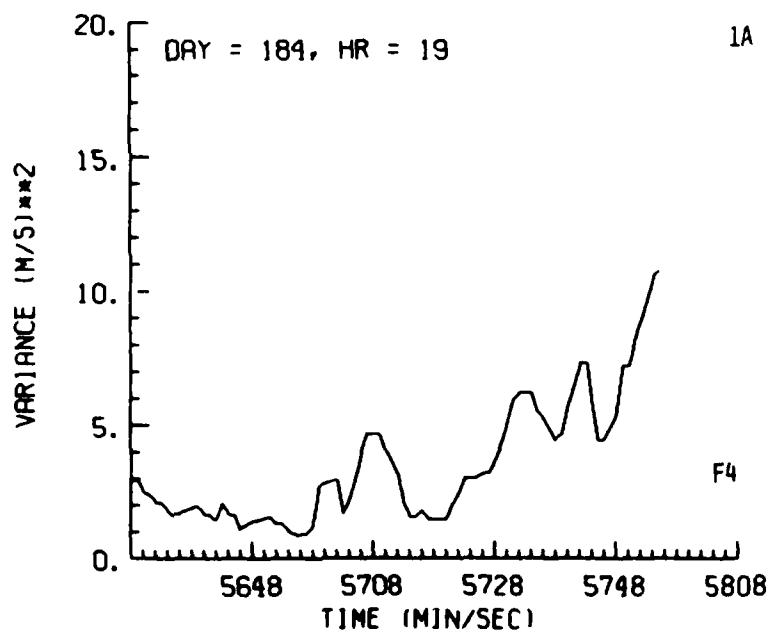


Figure F4. Tracking Gate Doppler Spectrum Variance Data, Day 184, Penetration 1A

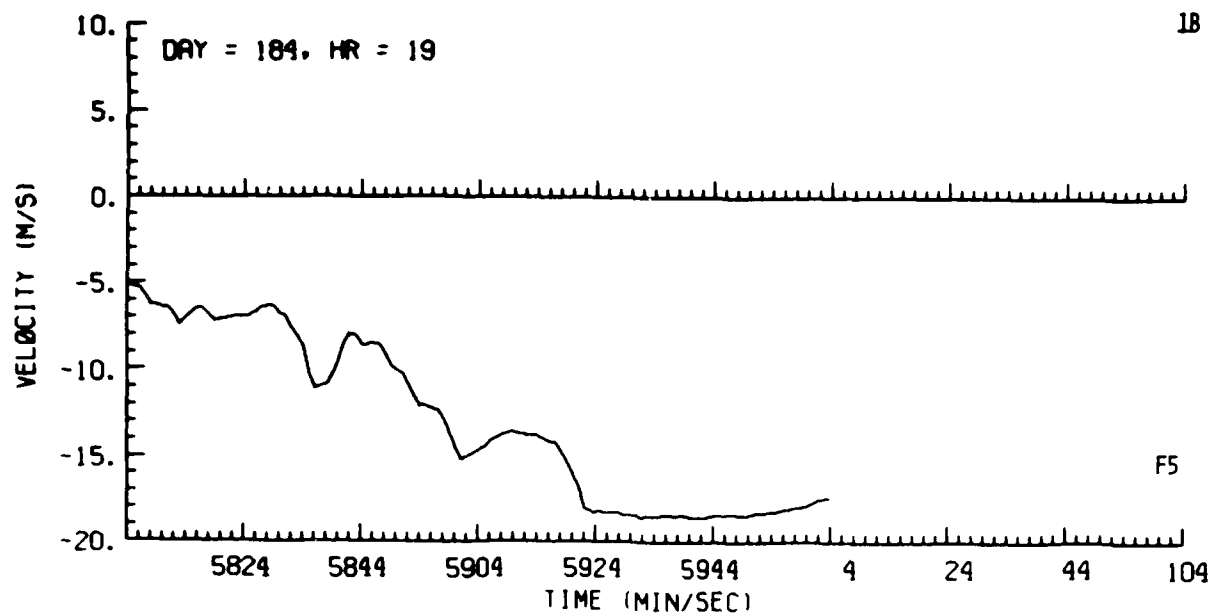


Figure F5. Tracking Gate Doppler Spectrum Mean Data, Day 184, Penetration 1B

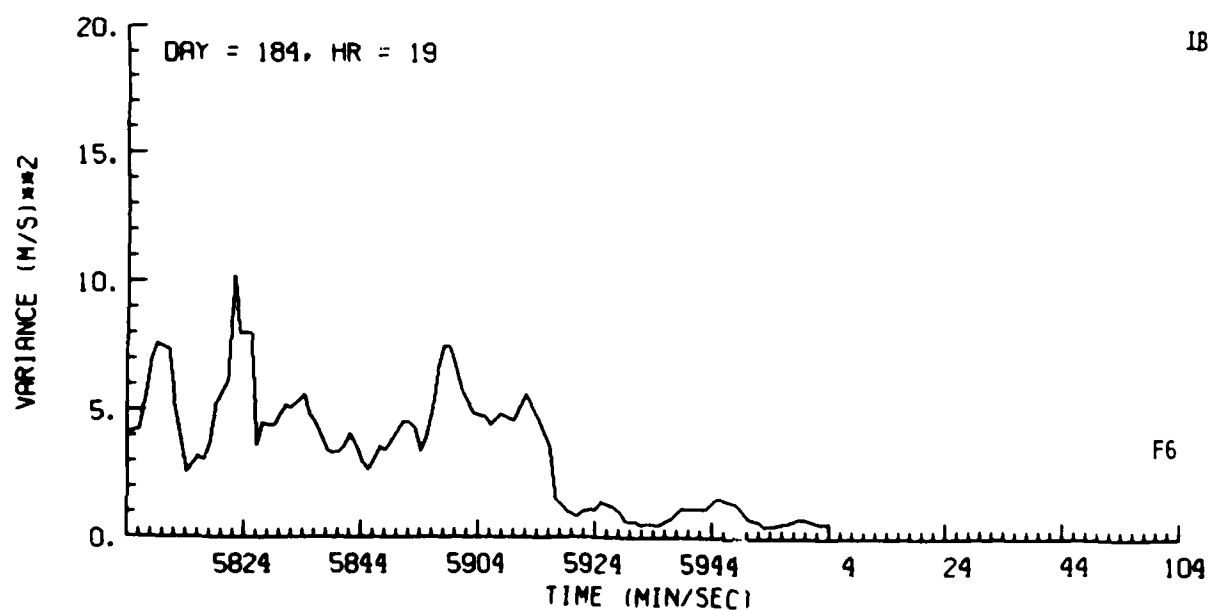


Figure F6. Tracking Gate Doppler Spectrum Variance Data, Day 184, Penetration 1B

AD-A160 420

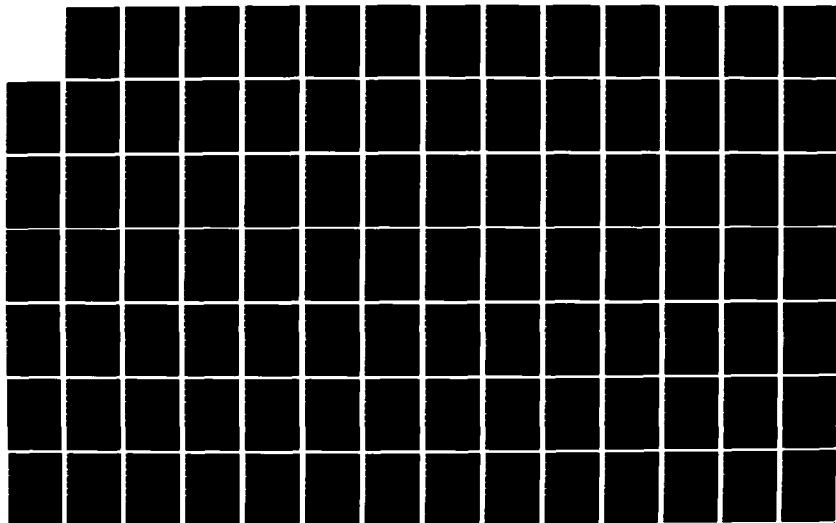
JOINT AGENCY TURBULENCE EXPERIMENT(U) AIR FORCE
GEOPHYSICS LAB HANSCOM AFB MA A R BOHNE 21 JAN 85
AFGL-TR-85-0012

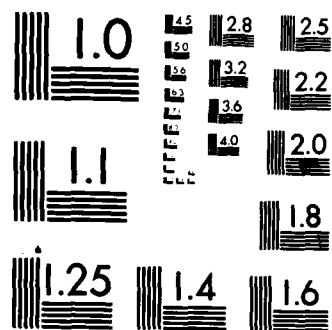
2/3

UNCLASSIFIED

F/G 17/9

NL





MICROCOPY RESOLUTION TEST CHART
NATIONAL BUREAU OF STANDARDS-1963-A

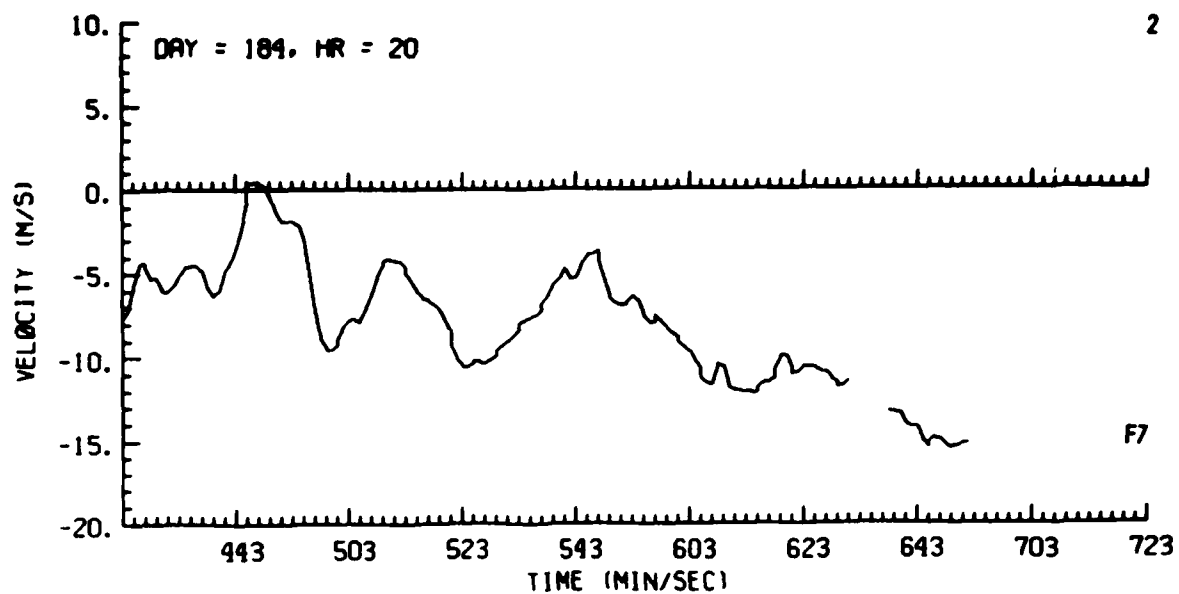


Figure F7. Tracking Gate Doppler Spectrum Mean Data, Day 184, Penetration 2

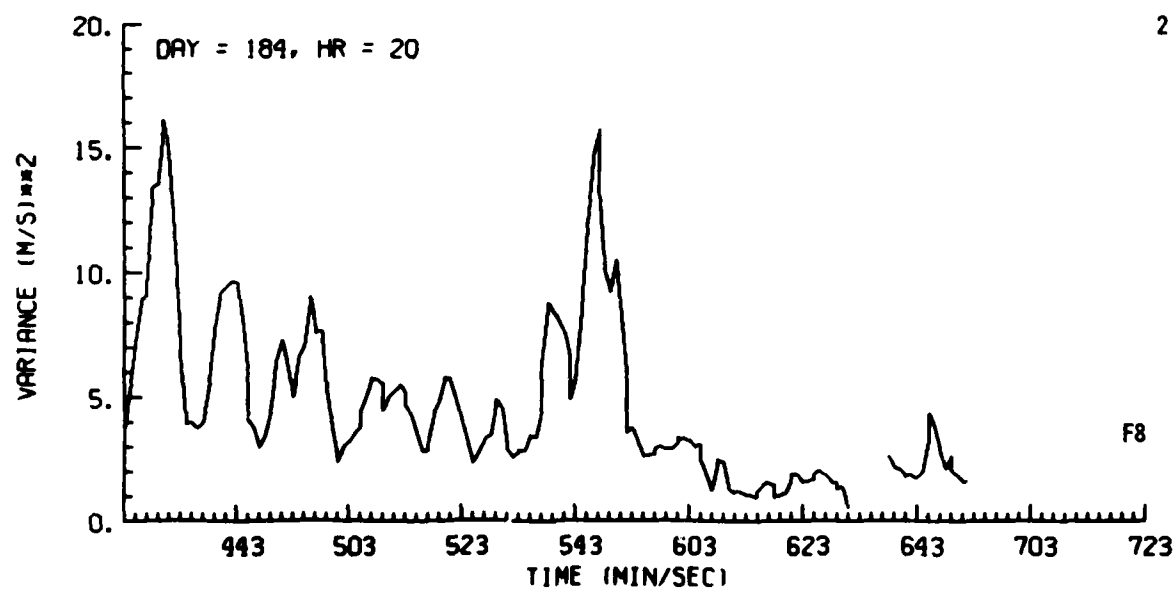


Figure F8. Tracking Gate Doppler Spectrum Variance Data, Day 184, Penetration 2

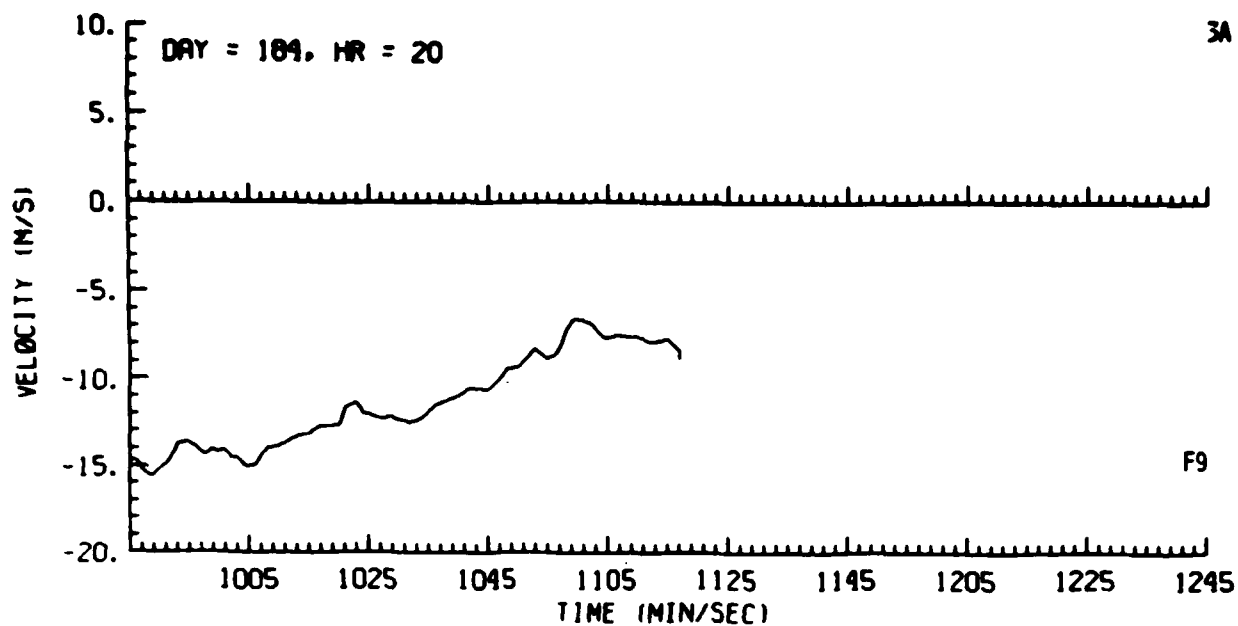


Figure F9. Tracking Gate Doppler Spectrum Mean Data, Day 184, Penetration 3A

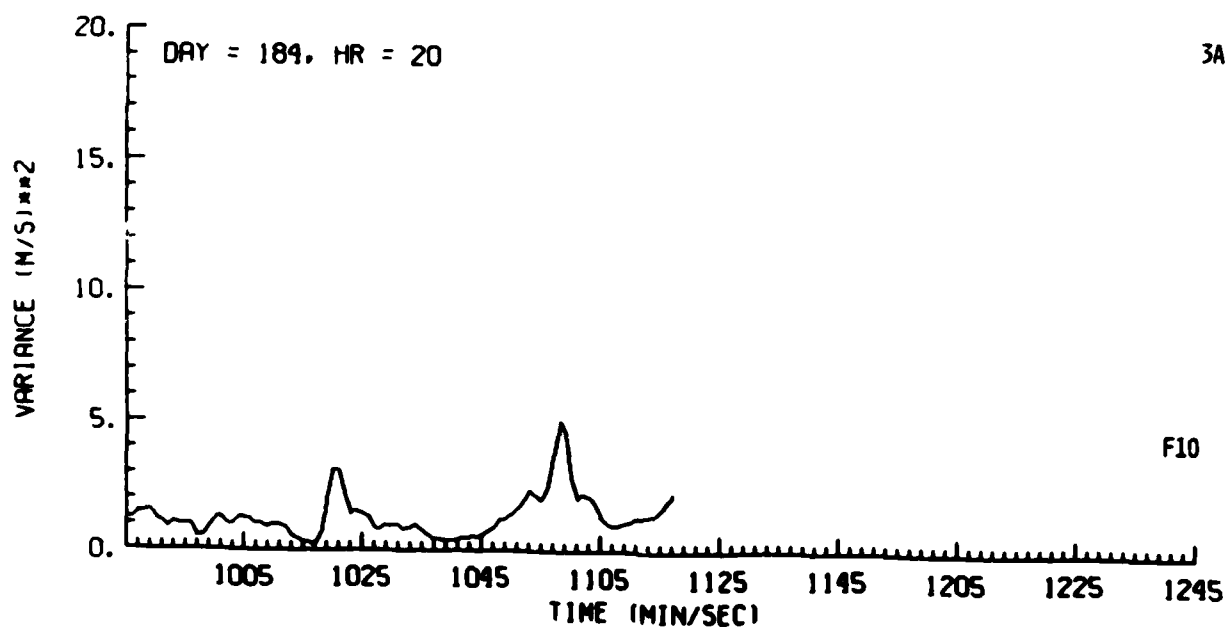


Figure F10. Tracking Gate Doppler Spectrum Variance Data, Day 184, Penetration 3A

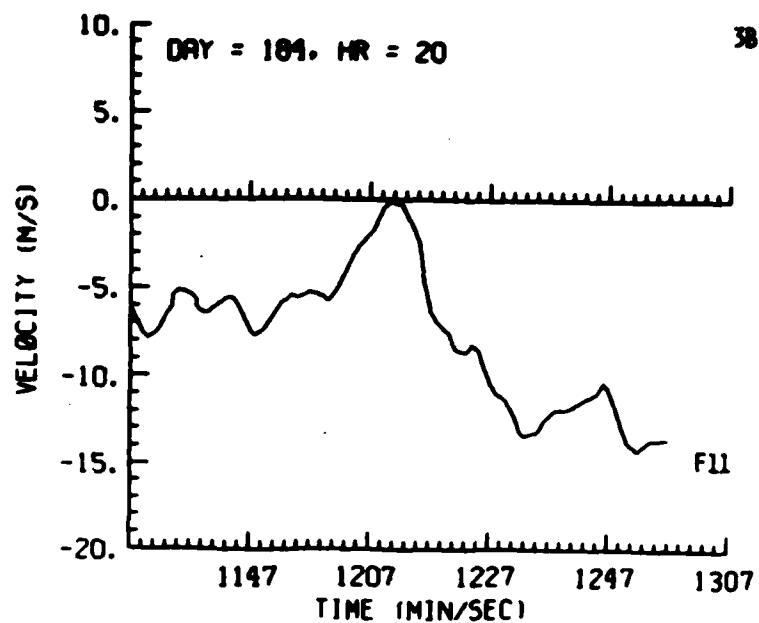


Figure F11. Tracking Gate Doppler Spectrum Mean Data, Day 184, Penetration 3B

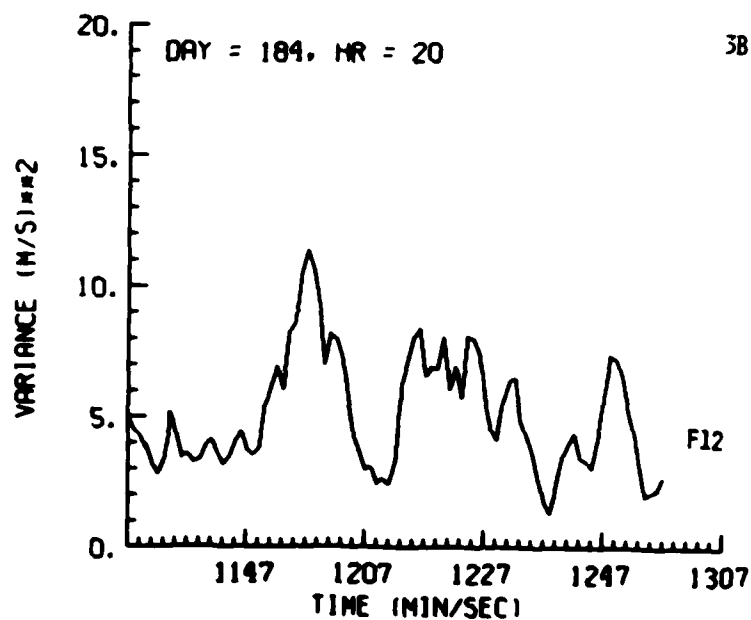


Figure F12. Tracking Gate Doppler Spectrum Variance Data, Day 184, Penetration 3B

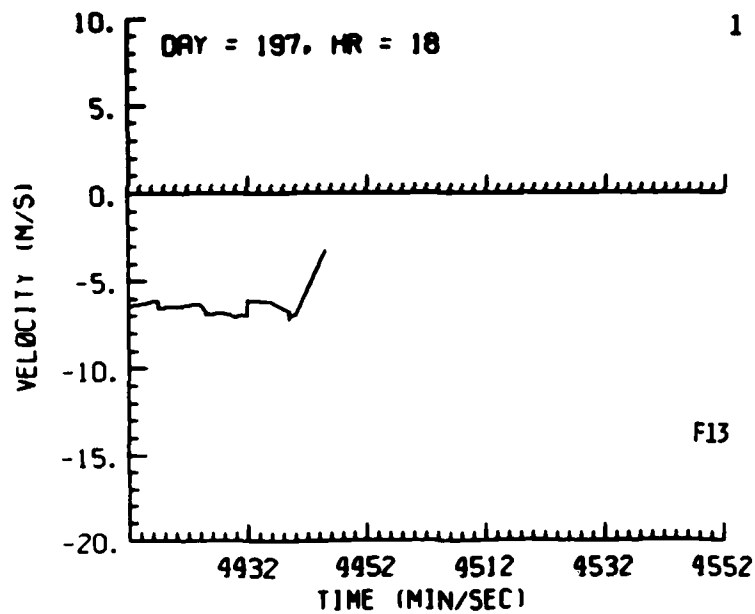


Figure F13. Tracking Gate Doppler Spectrum Mean Data, Day 197, Penetration 1

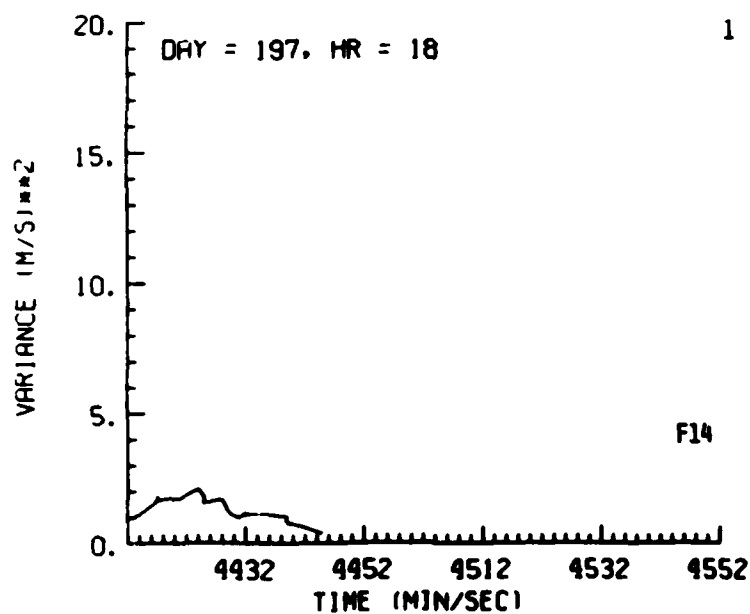


Figure F14. Tracking Gate Doppler Spectrum Variance Data, Day 197, Penetration 1

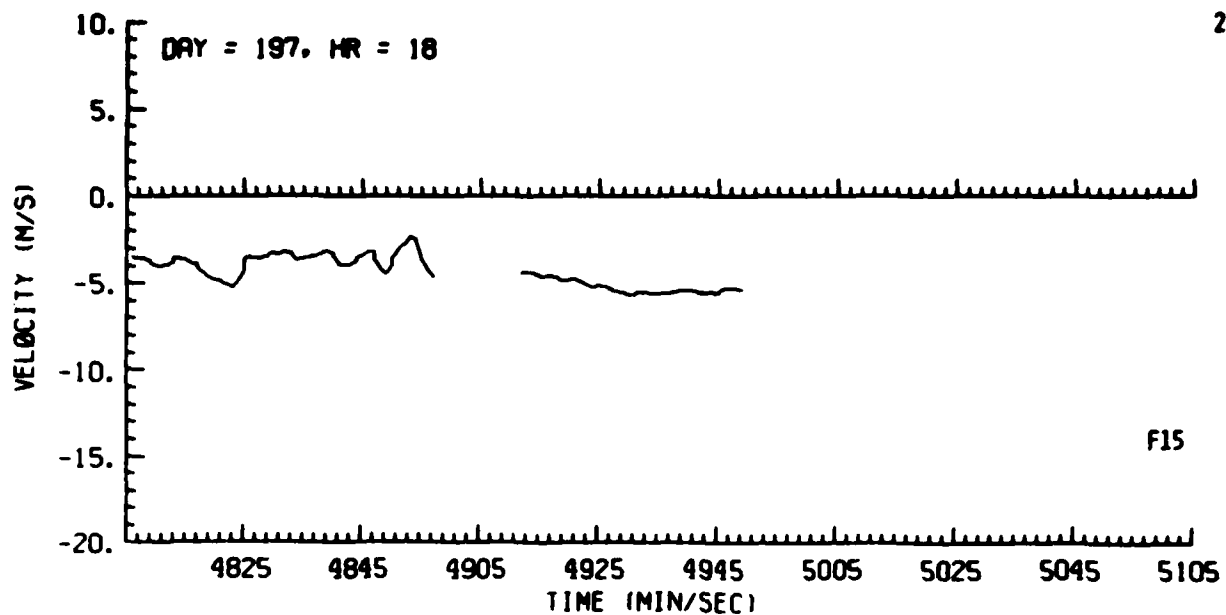


Figure F15. Tracking Gate Doppler Spectrum Mean Data, Day 197, Penetration 2

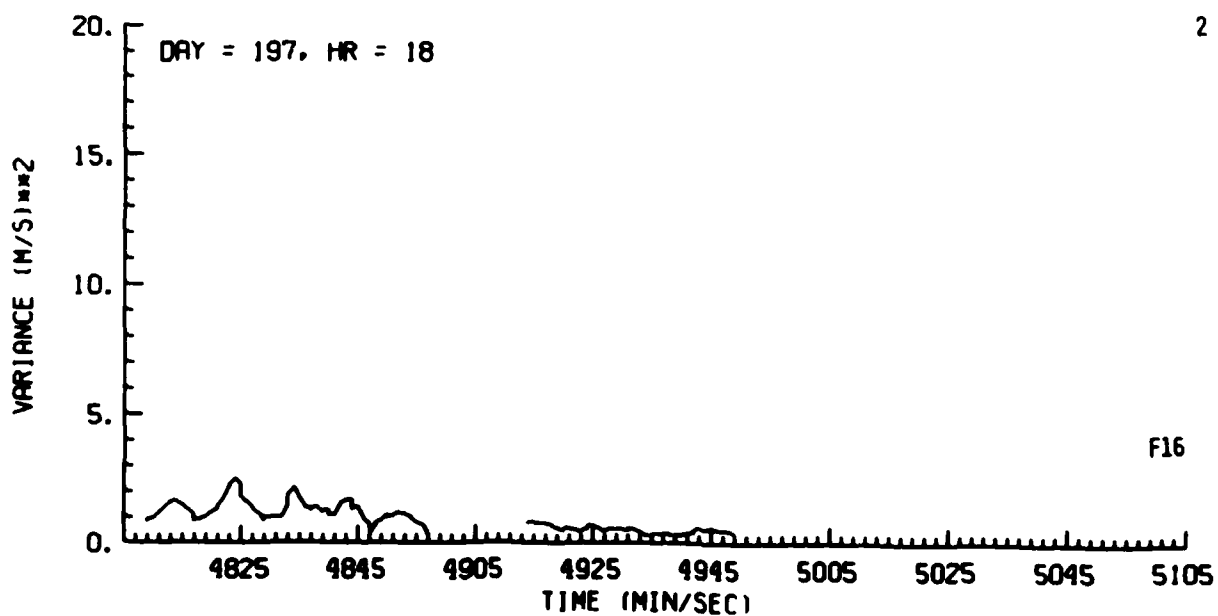


Figure F16. Tracking Gate Doppler Spectrum Variance Data, Day 197, Penetration 2

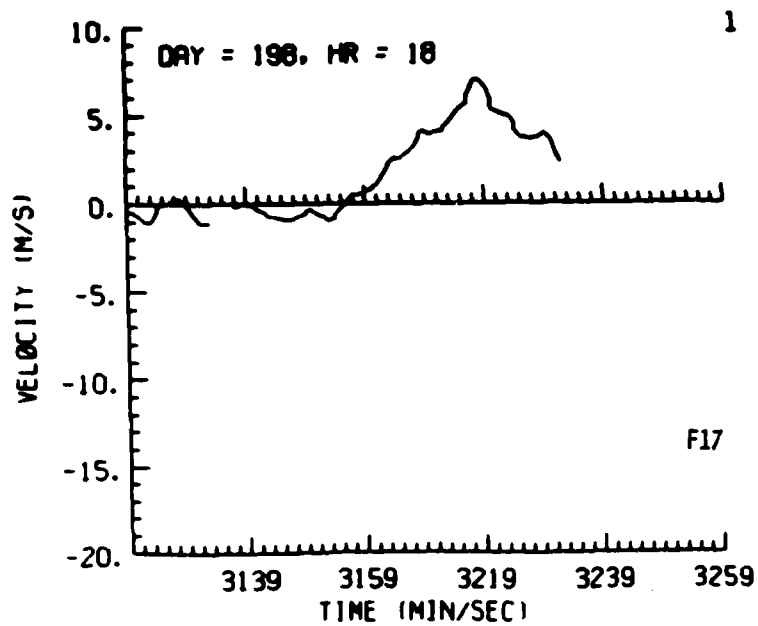


Figure F17. Tracking Gate Doppler Spectrum
Mean Data, Day 198, Penetration 1

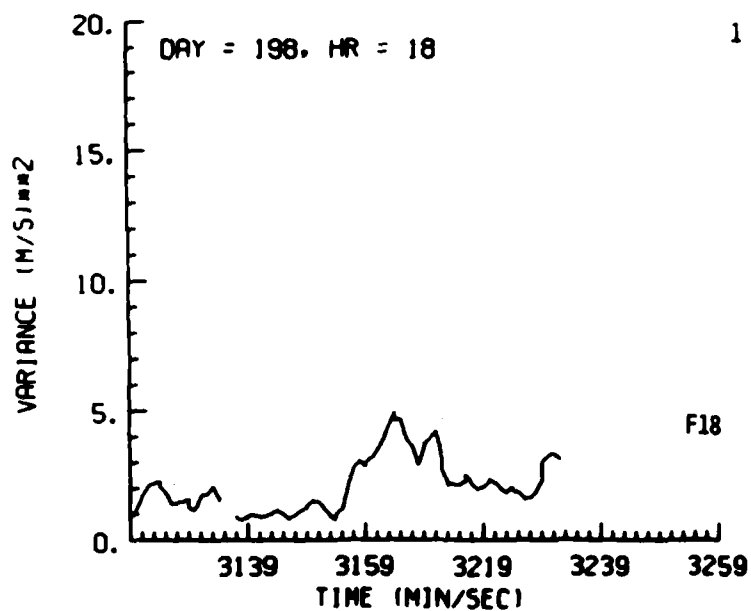


Figure F18. Tracking Gate Doppler Spectrum
Variance Data, Day 198, Penetration 1

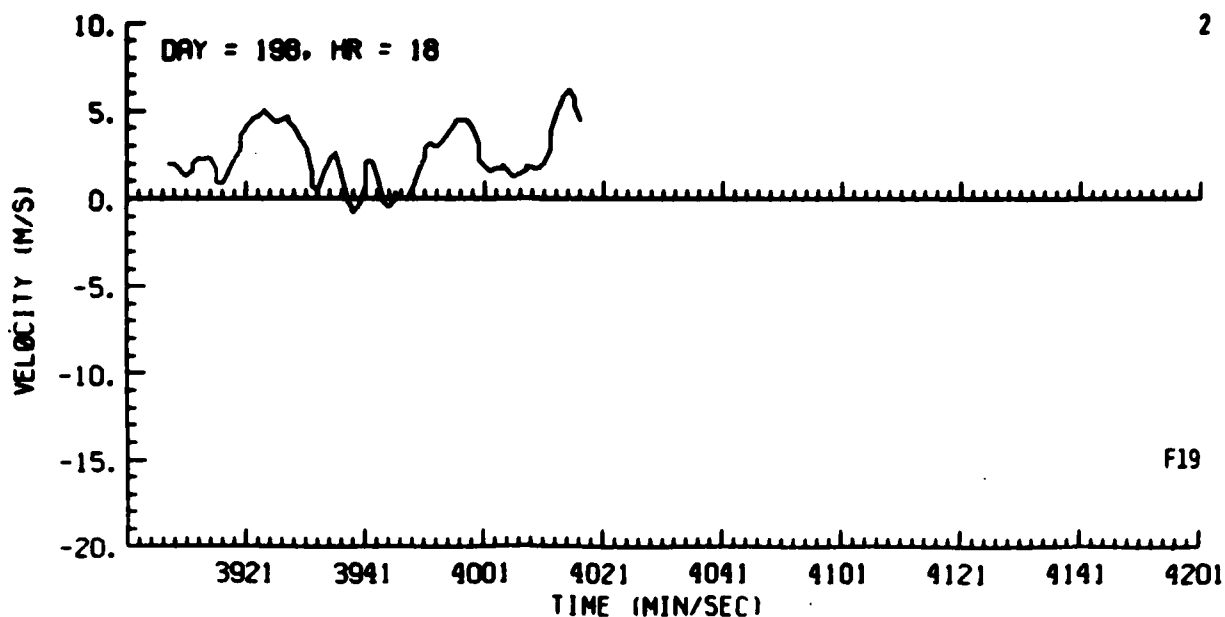


Figure F19. Tracking Gate Doppler Spectrum Mean Data, Day 198, Penetration 2

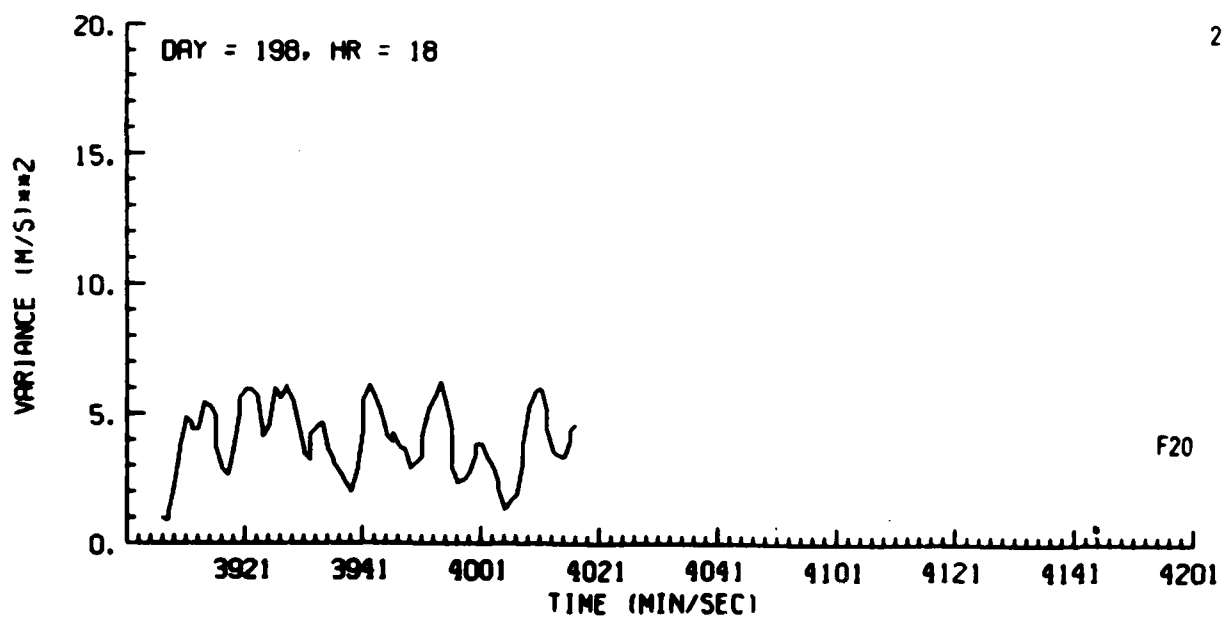


Figure F20. Tracking Gate Doppler Spectrum Variance Data, Day 198, Penetration 2

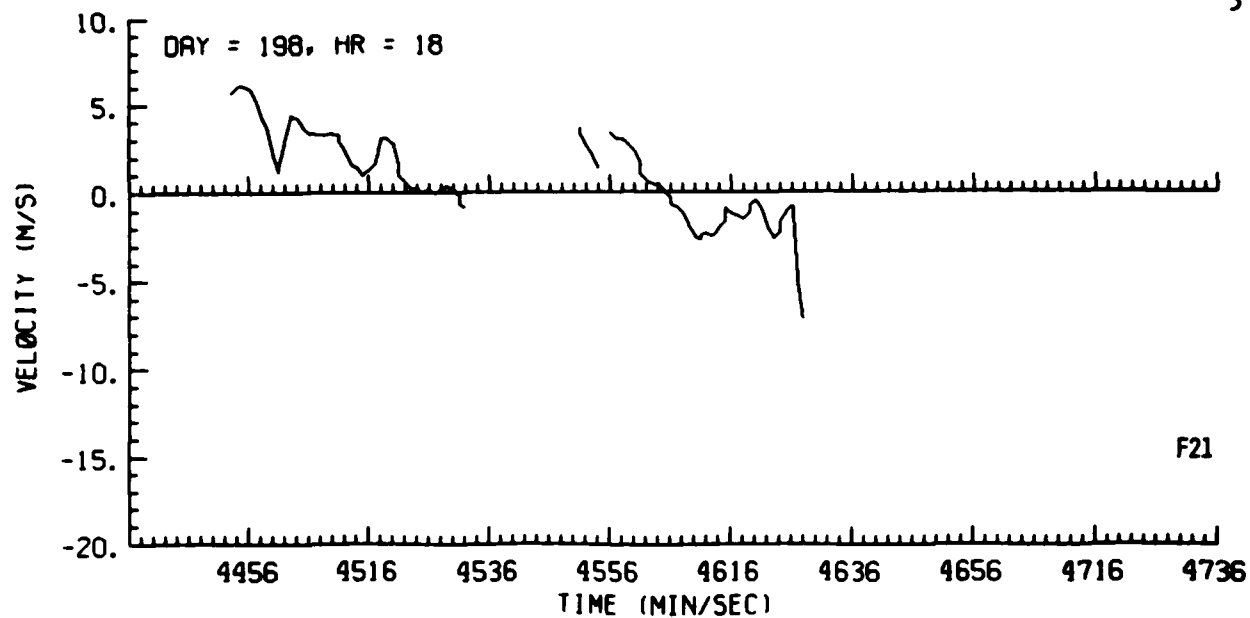


Figure F21. Tracking Gate Doppler Spectrum Mean Data, Day 198, Penetration 3

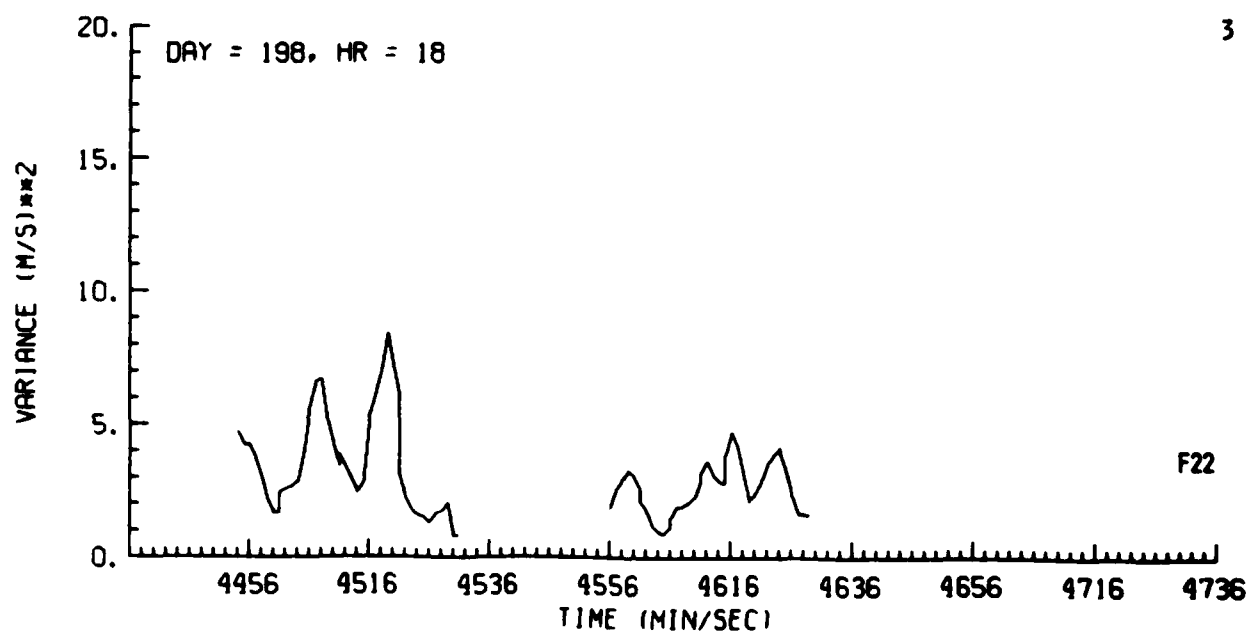


Figure F22. Tracking Gate Doppler Spectrum Variance Data, Day 198, Penetration 3

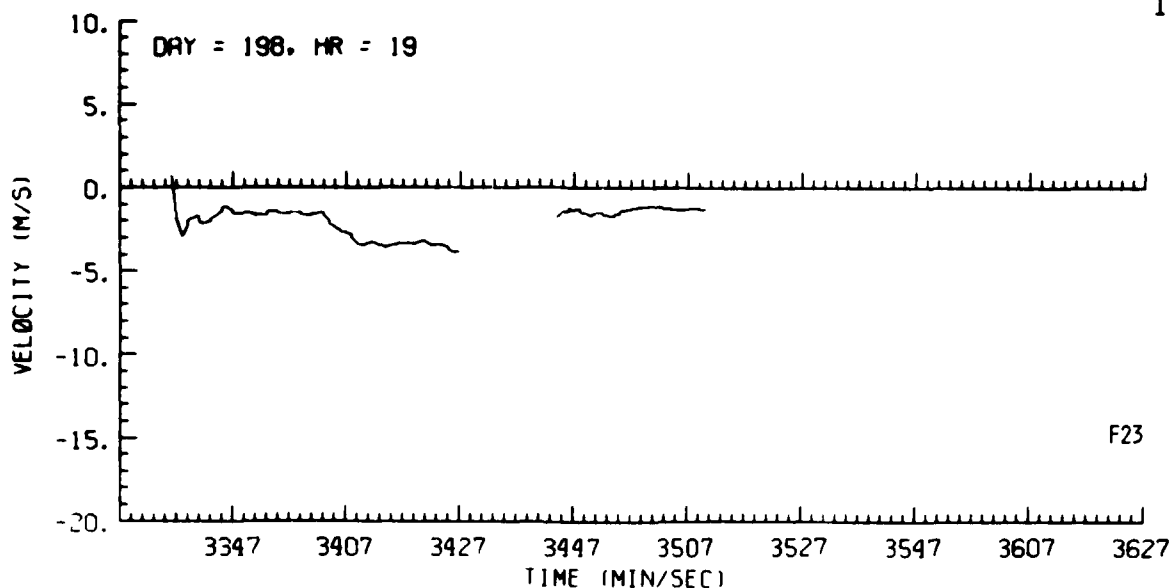


Figure F23. Tracking Gate Doppler Spectrum Mean Data, Day 198, Penetration 1

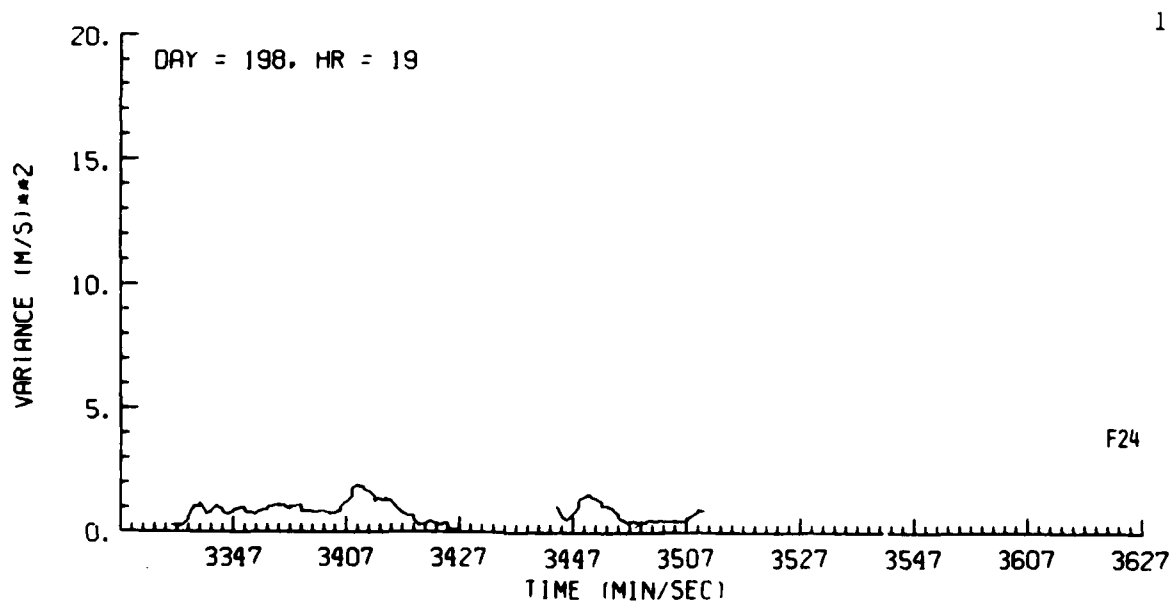


Figure F24. Tracking Gate Doppler Spectrum Variance Data, Day 198, Penetration 1

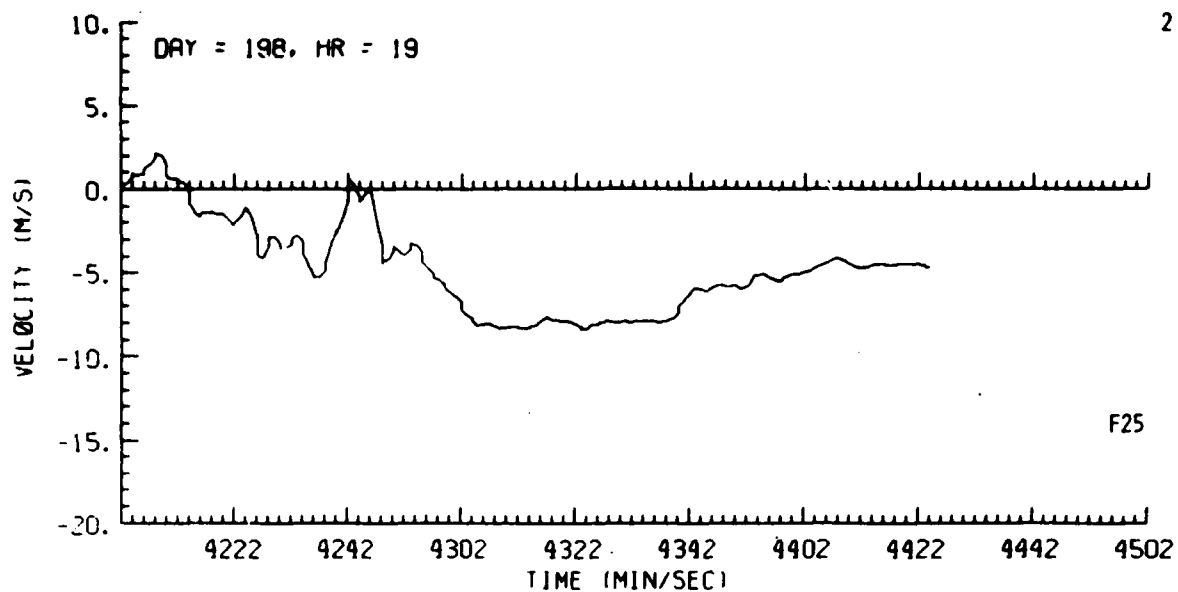


Figure F25. Tracking Gate Doppler Spectrum Mean Data, Day 198, Penetration 2

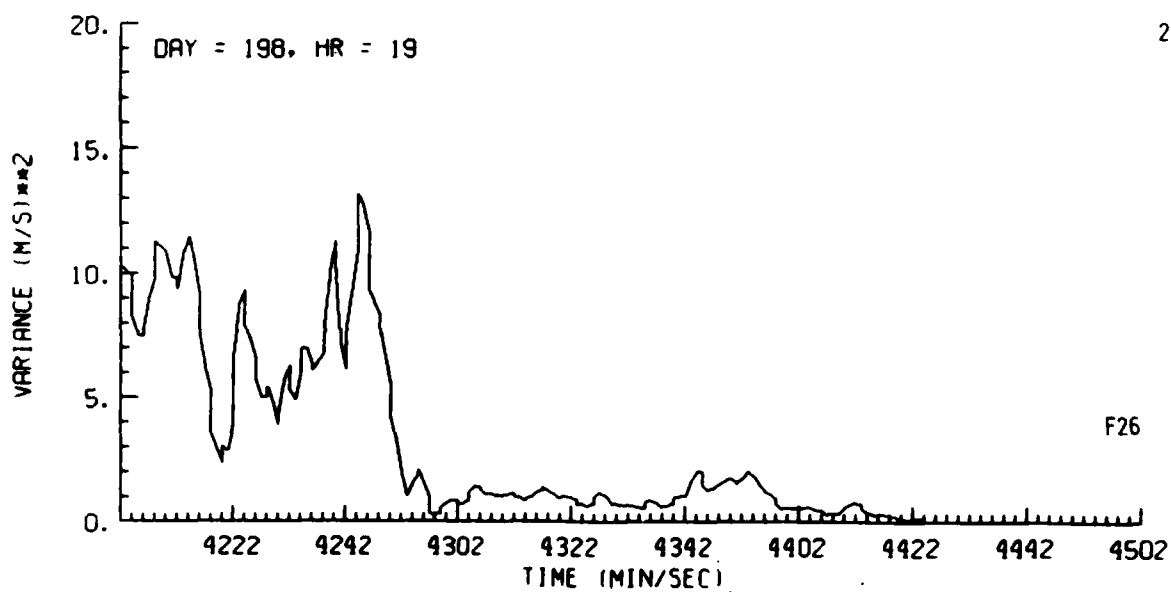


Figure F26. Tracking Gate Doppler Spectrum Variance Data, Day 198, Penetration 2

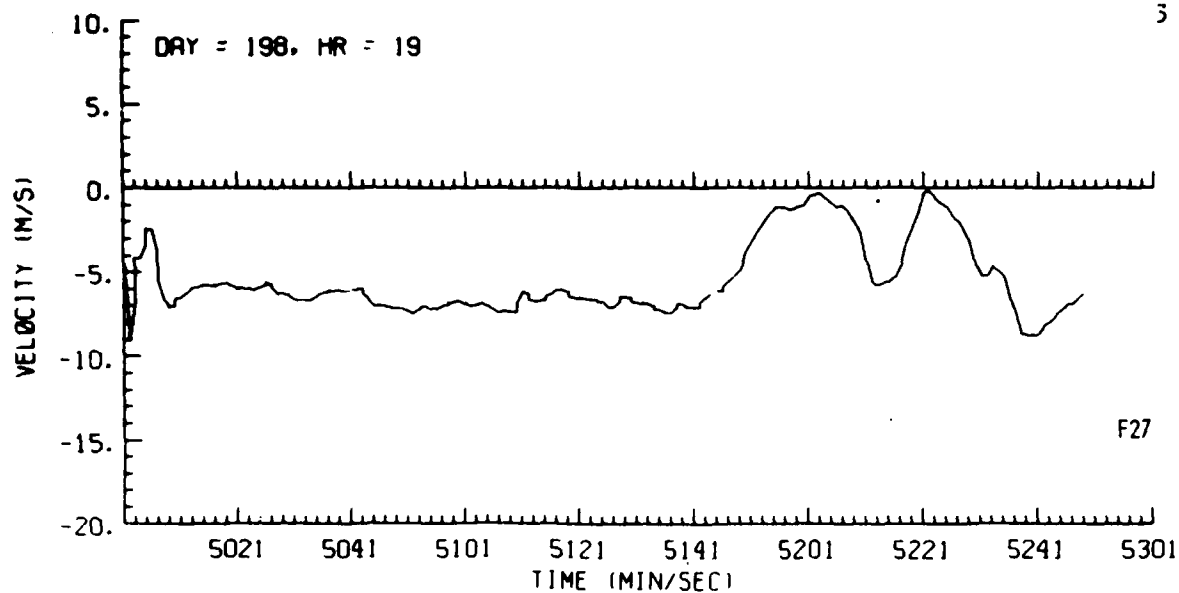


Figure F27. Tracking Gate Doppler Spectrum Mean Data, Day 198, Penetration 3

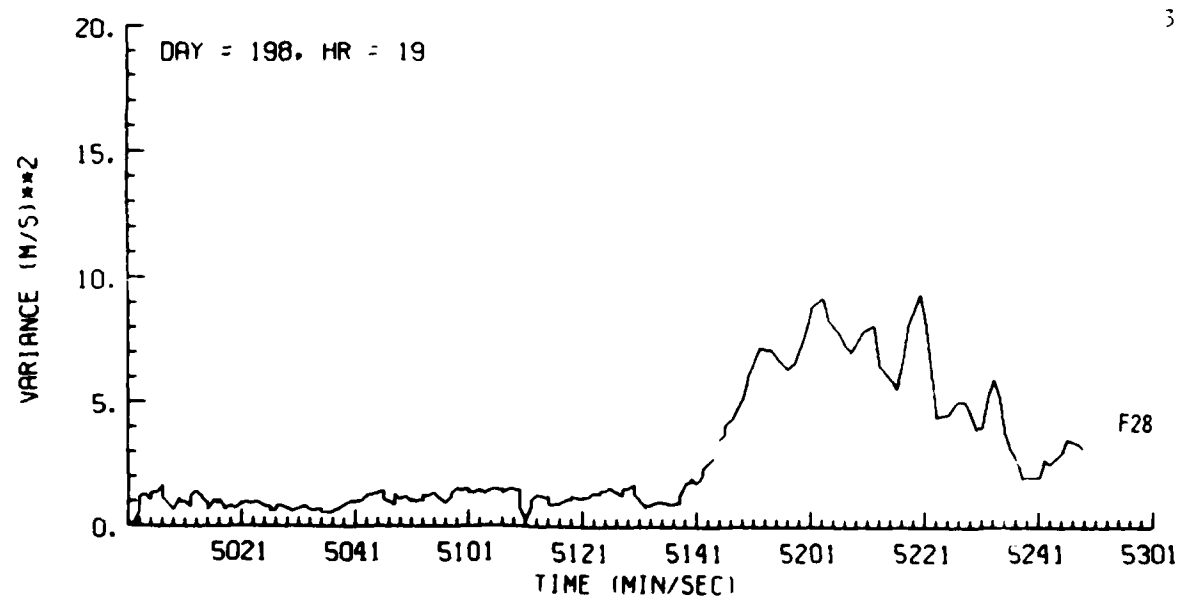


Figure F28. Tracking Gate Doppler Spectrum Variance Data, Day 198, Penetration 3

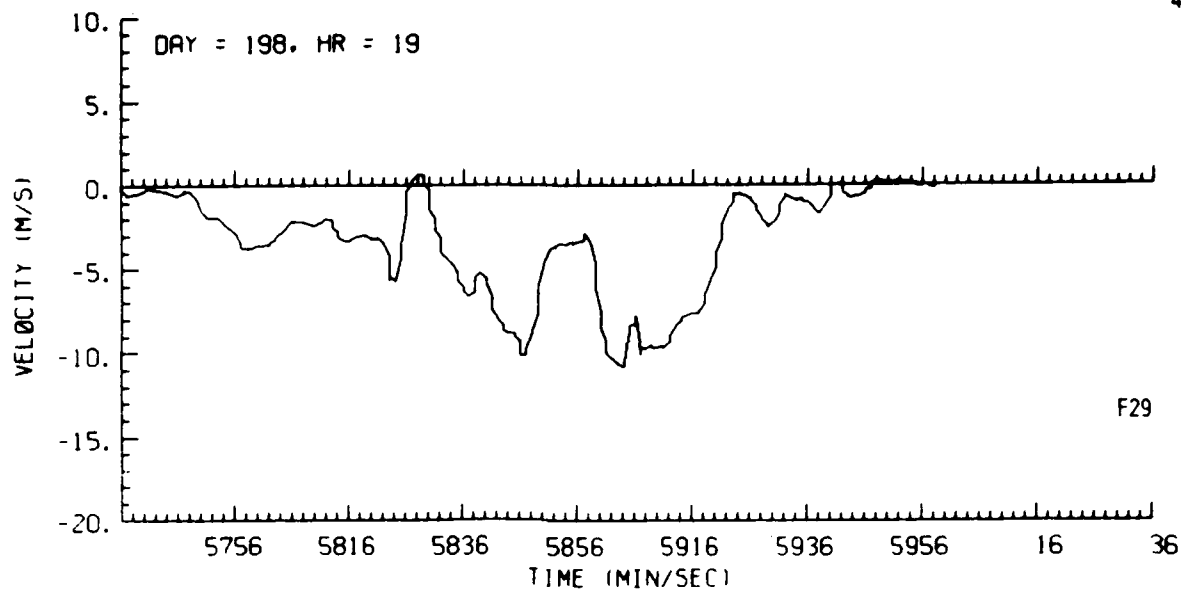


Figure F29. Tracking Gate Doppler Spectrum Mean Data, Day 198, Penetration 4

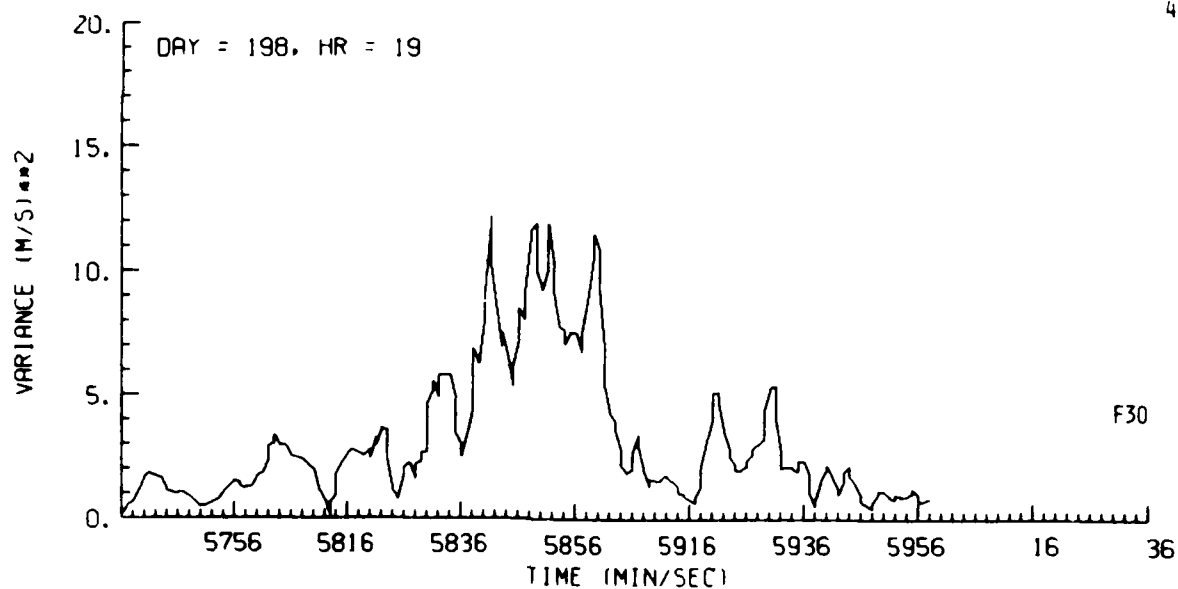


Figure F30. Tracking Gate Doppler Spectrum Variance Data, Day 198, Penetration 4

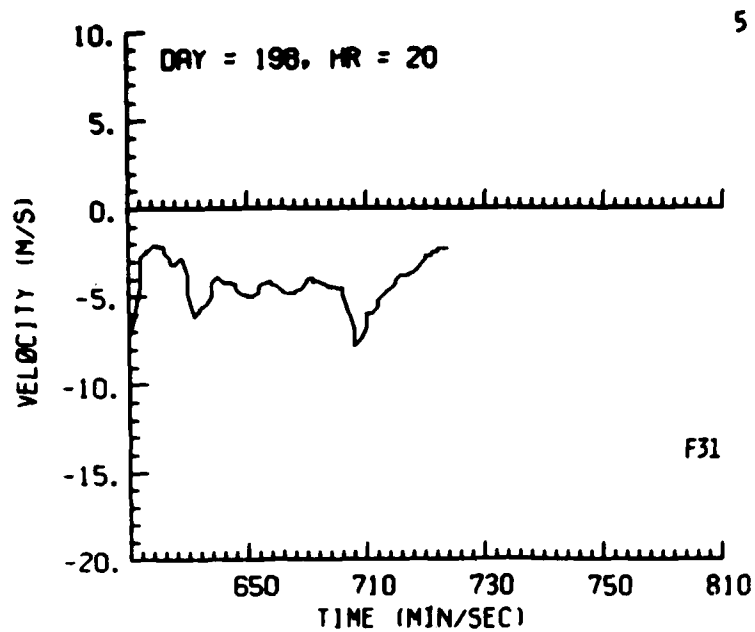


Figure F31. Tracking Gate Doppler Spectrum
Mean Data, Day 198, Penetration 5

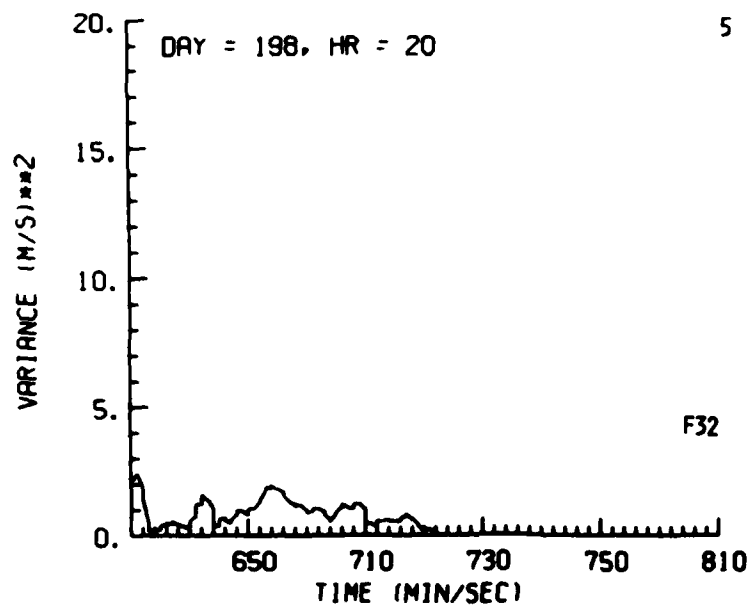


Figure F32. Tracking Gate Doppler Spectrum
Variance Data, Day 198, Penetration 5

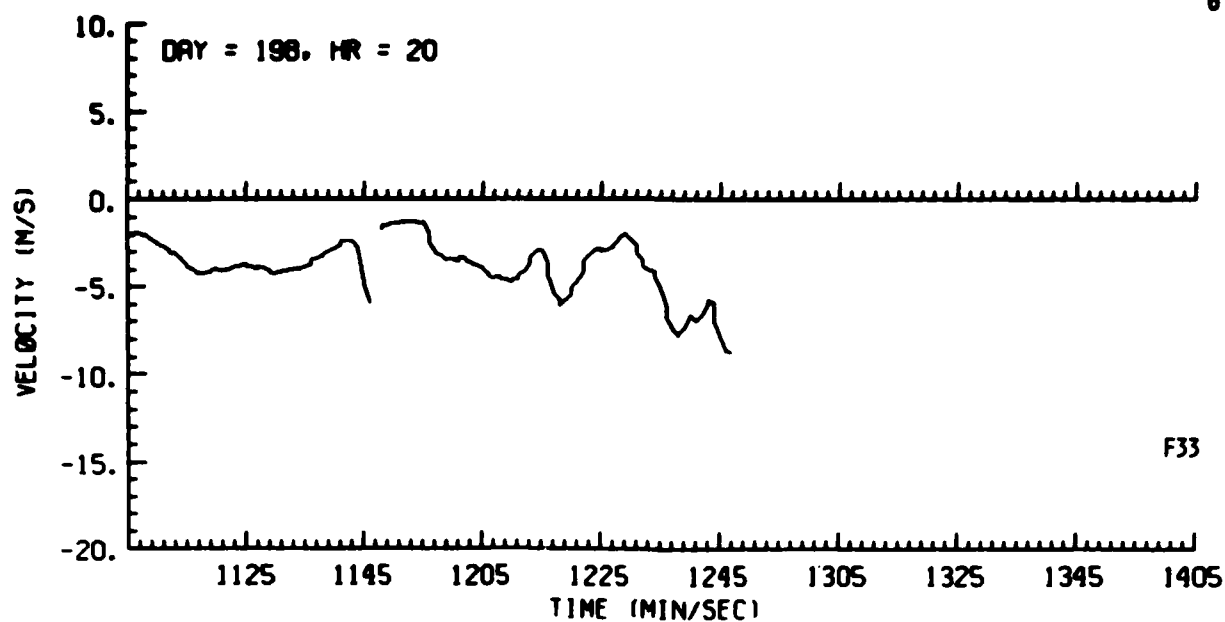


Figure F33. Tracking Gate Doppler Spectrum Mean Data, Day 198, Penetration 6

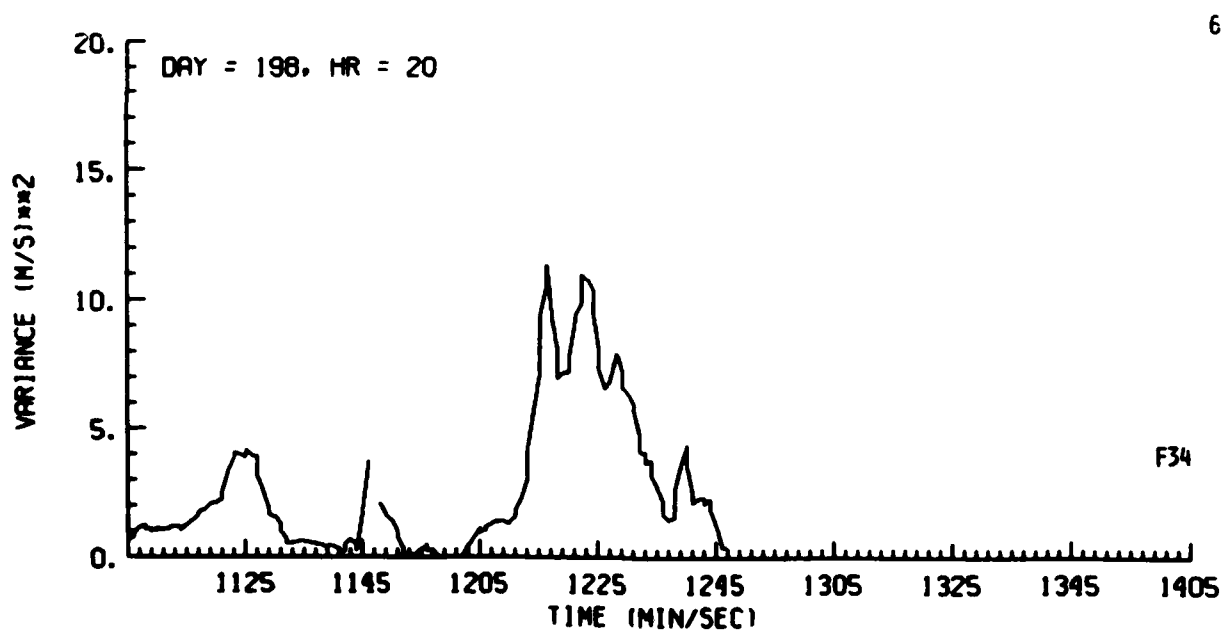


Figure F34. Tracking Gate Doppler Spectrum Variance Data, Day 198, Penetration 6

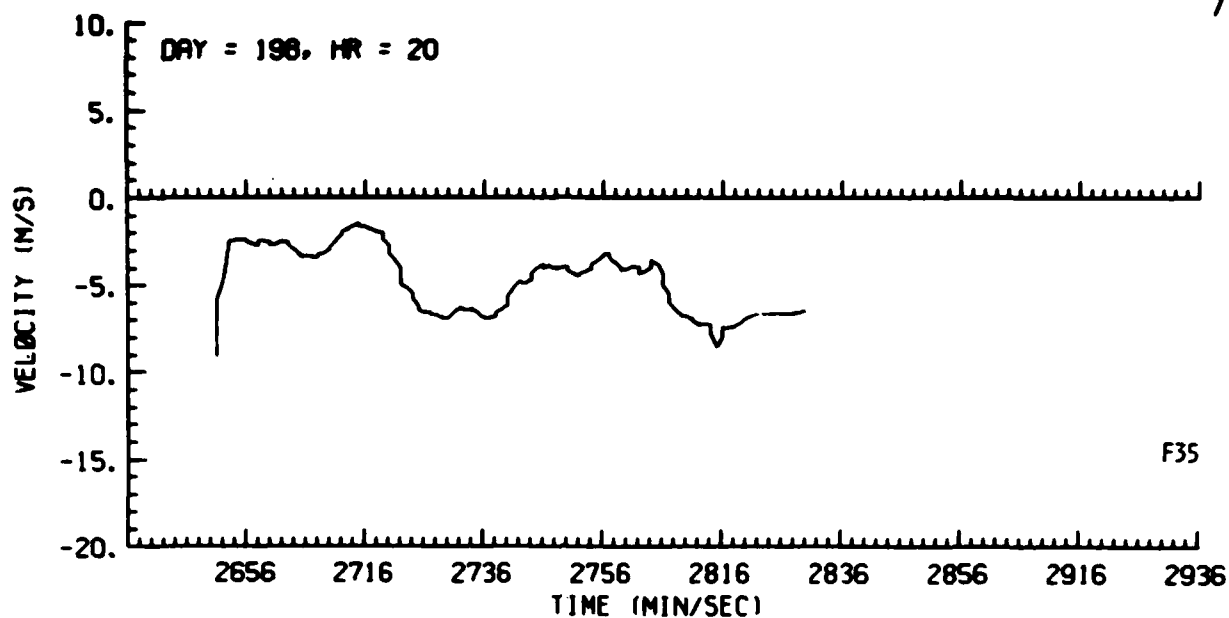


Figure F35. Tracking Gate Doppler Spectrum Mean Data, Day 198, Penetration 7

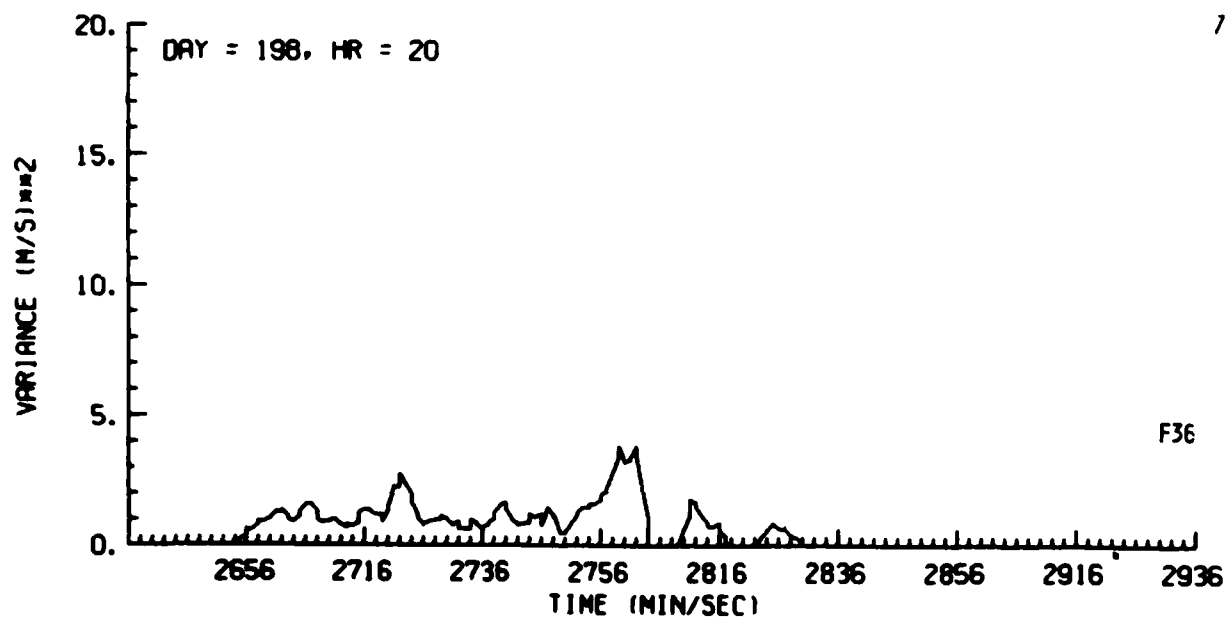


Figure F36. Tracking Gate Doppler Spectrum Variance Data, Day 198, Penetration 7

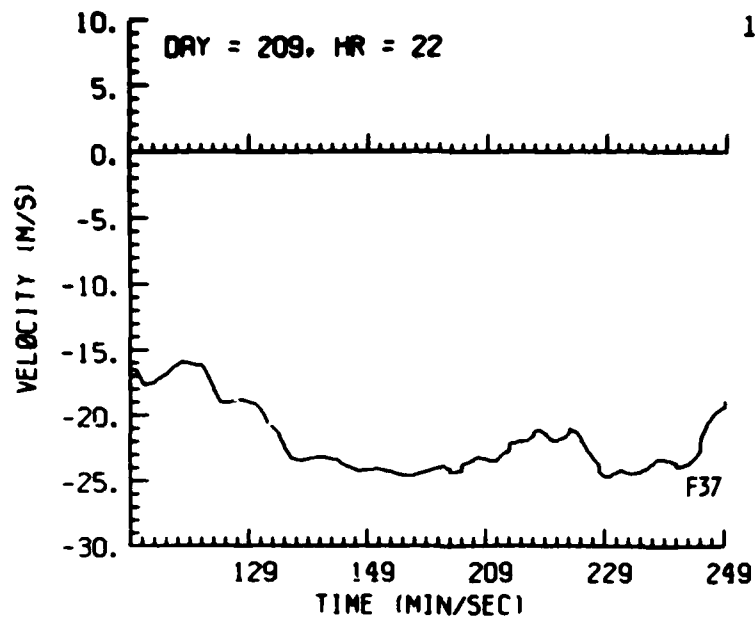


Figure F37. Tracking Gate Doppler Spectrum Mean Data, Day 209, Penetration 1

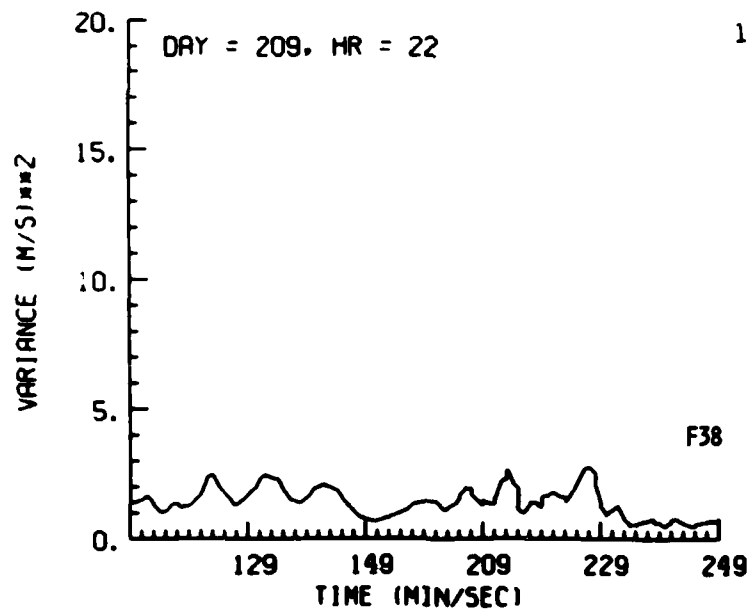


Figure F38. Tracking Gate Doppler Spectrum Variance Data, Day 209, Penetration 1

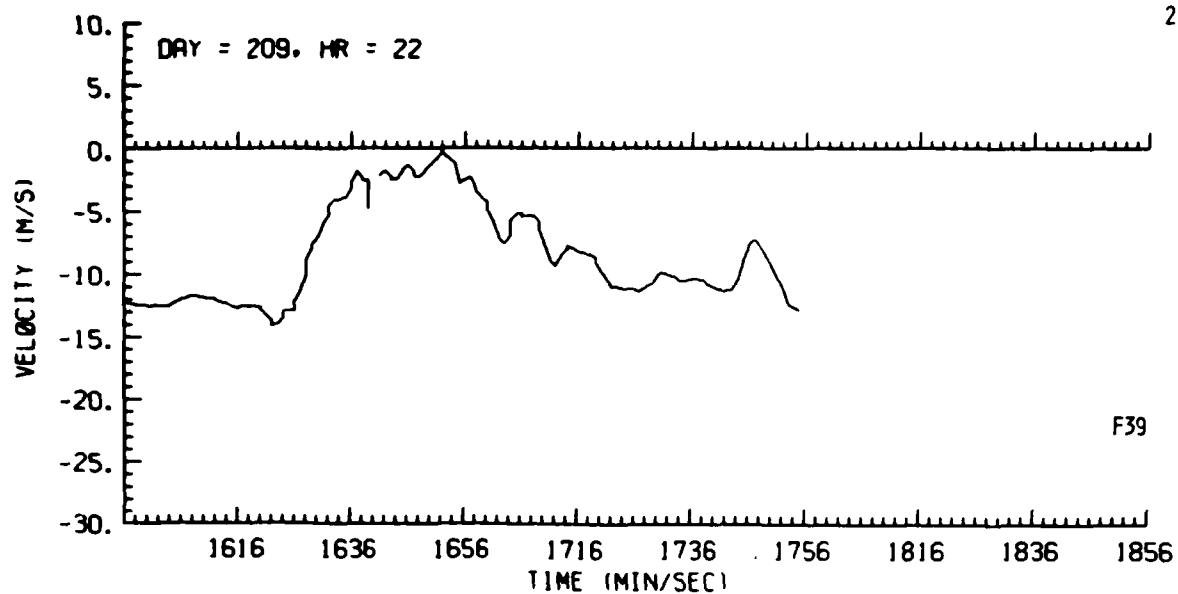


Figure F39. Tracking Gate Doppler Spectrum Mean Data, Day 209, Penetration 2

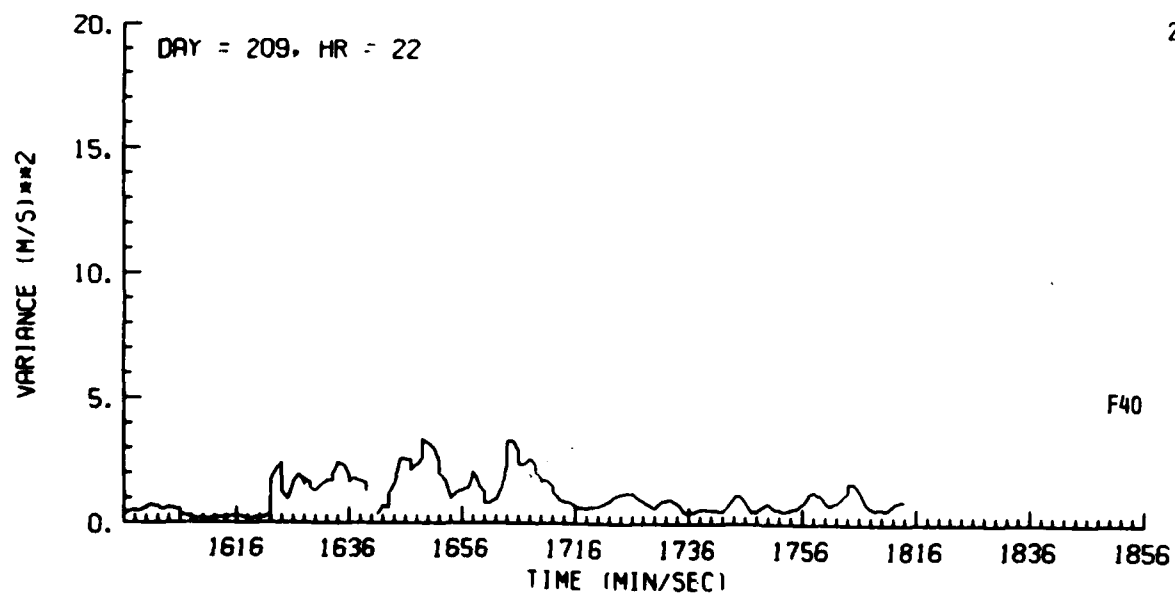


Figure F40. Tracking Gate Doppler Spectrum Variance Data, Day 209, Penetration 2

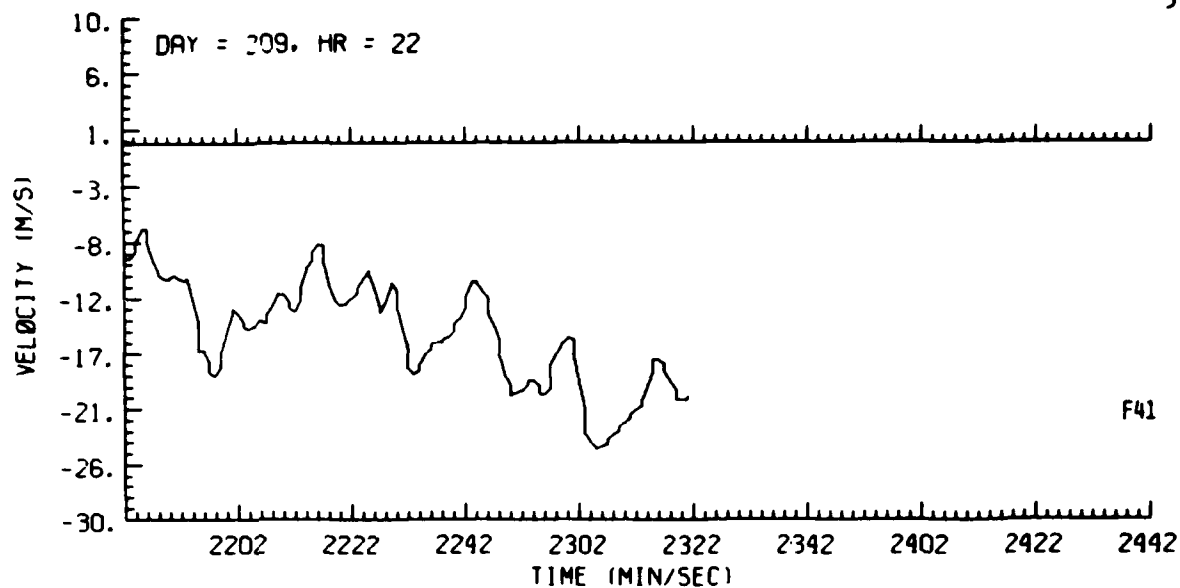


Figure F41. Tracking Gate Doppler Spectrum Mean Data, Day 209, Penetration 3

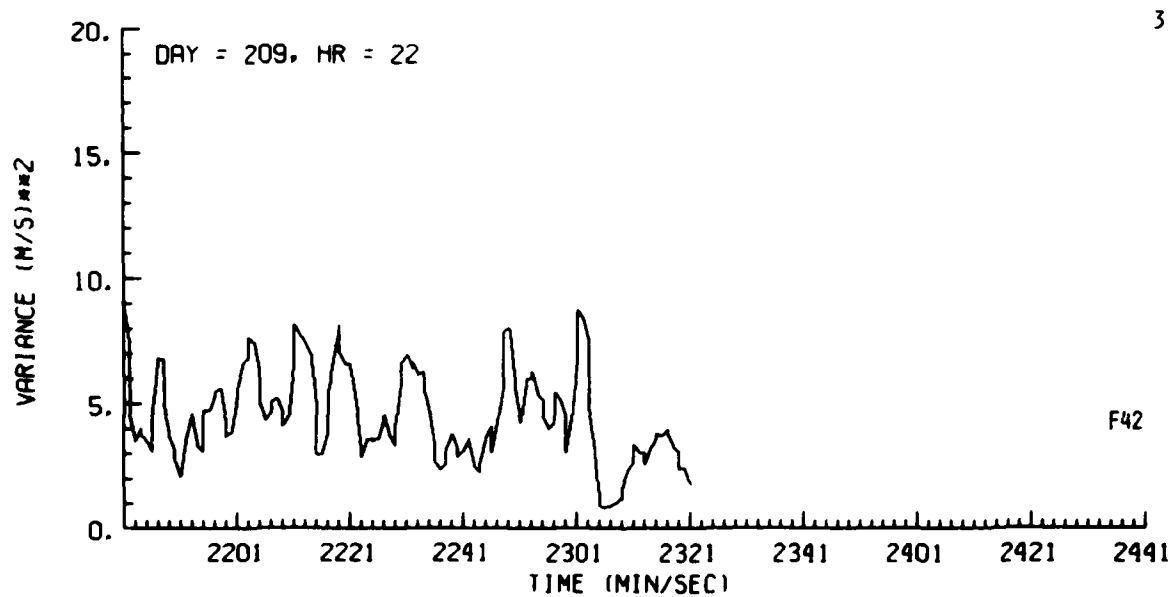


Figure F42. Tracking Gate Doppler Spectrum Variance Data, Day 209, Penetration 3

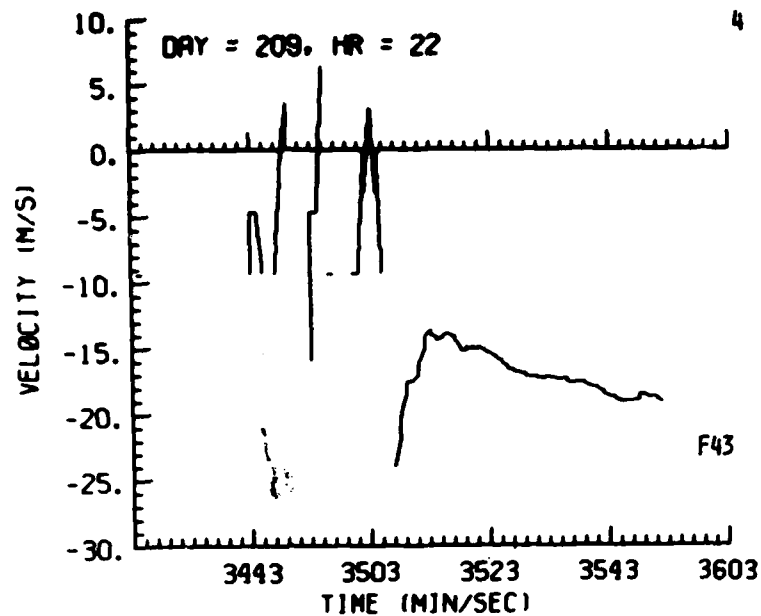


Figure F43. Tracking Gate Doppler Spectrum
Mean Data, Day 209, Penetration 4

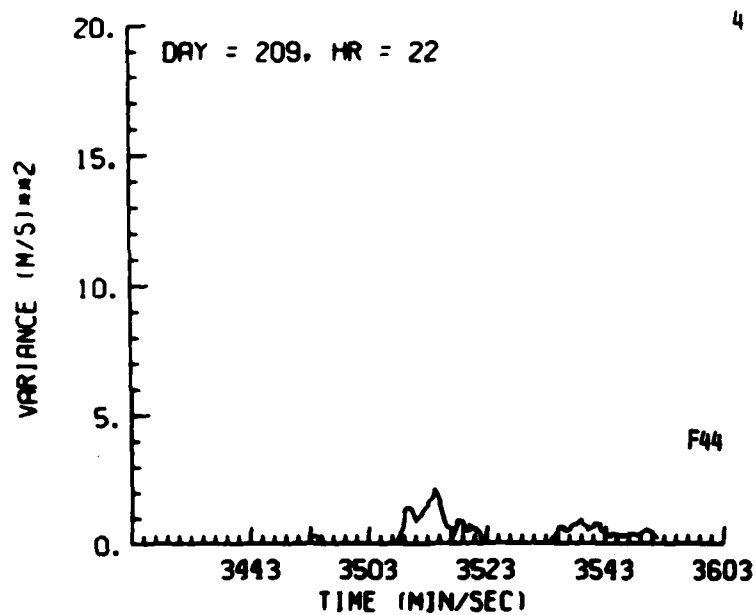


Figure F44. Tracking Gate Doppler Spectrum
Variance Data, Day 209, Penetration 4

5

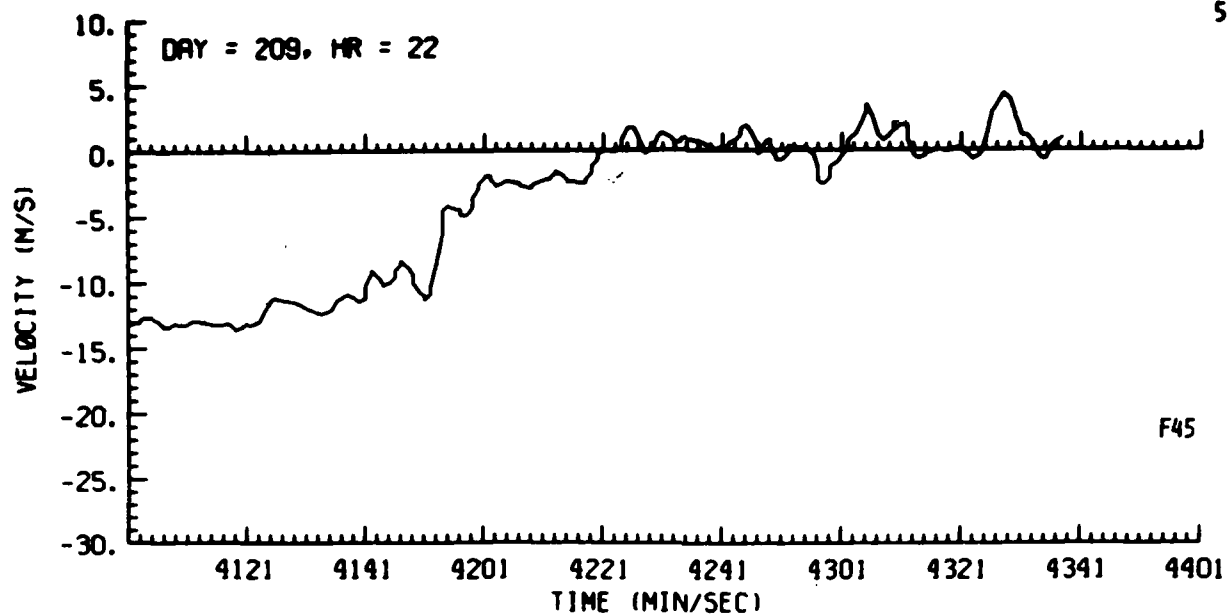


Figure F45. Tracking Gate Doppler Spectrum Mean Data, Day 209, Penetration 5

5

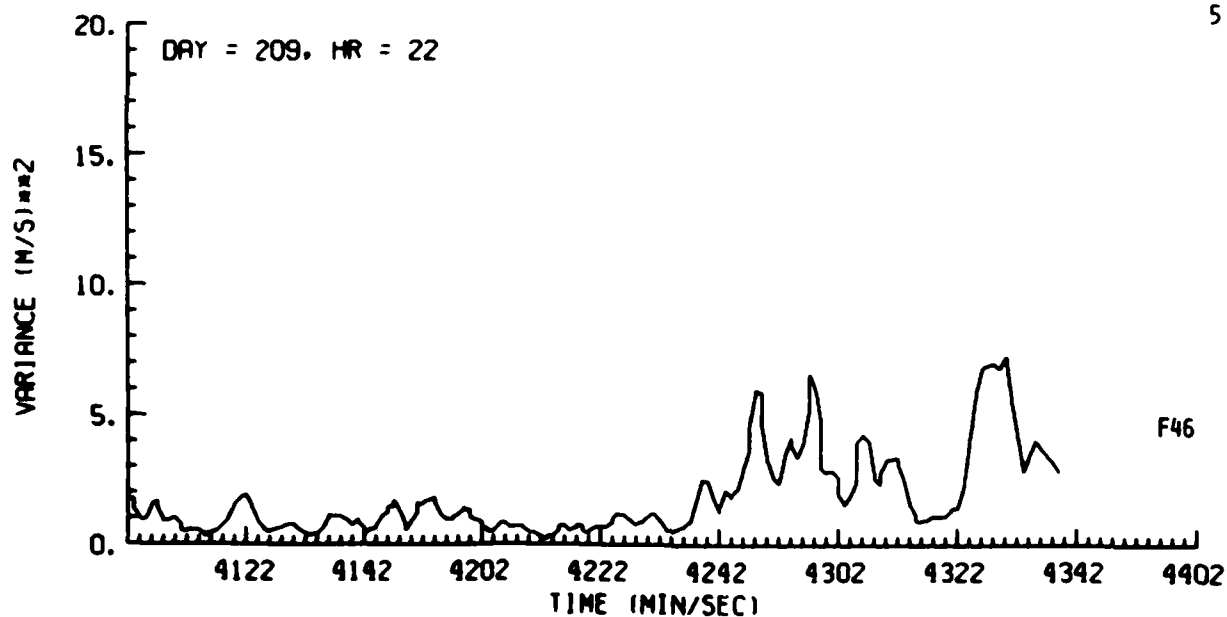


Figure F46. Tracking Gate Doppler Spectrum Variance Data, Day 209, Penetration 5

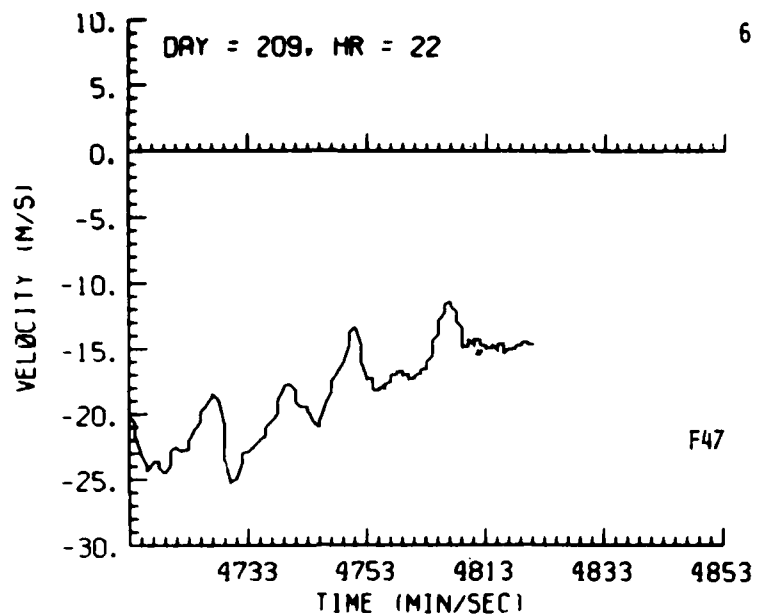


Figure F47. Tracking Gate Doppler Spectrum Mean Data, Day 209, Penetration 6

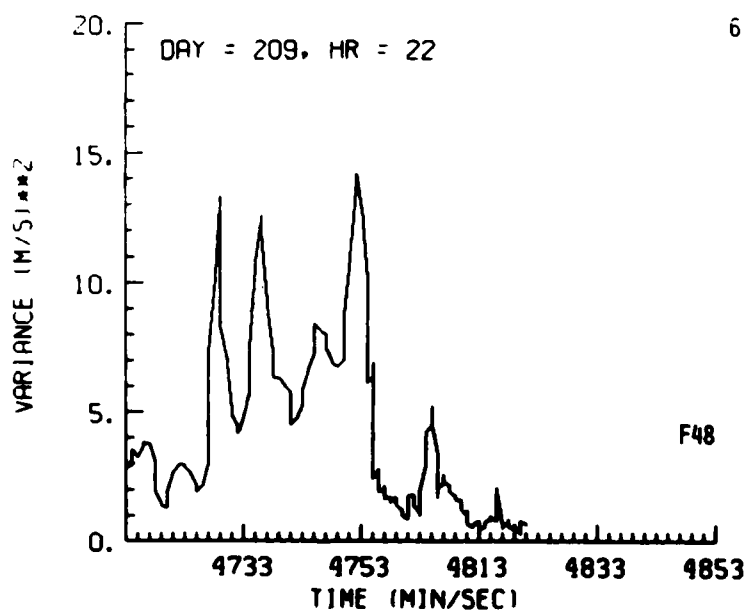


Figure F48. Tracking Gate Doppler Spectrum Variance Data, Day 209, Penetration 6

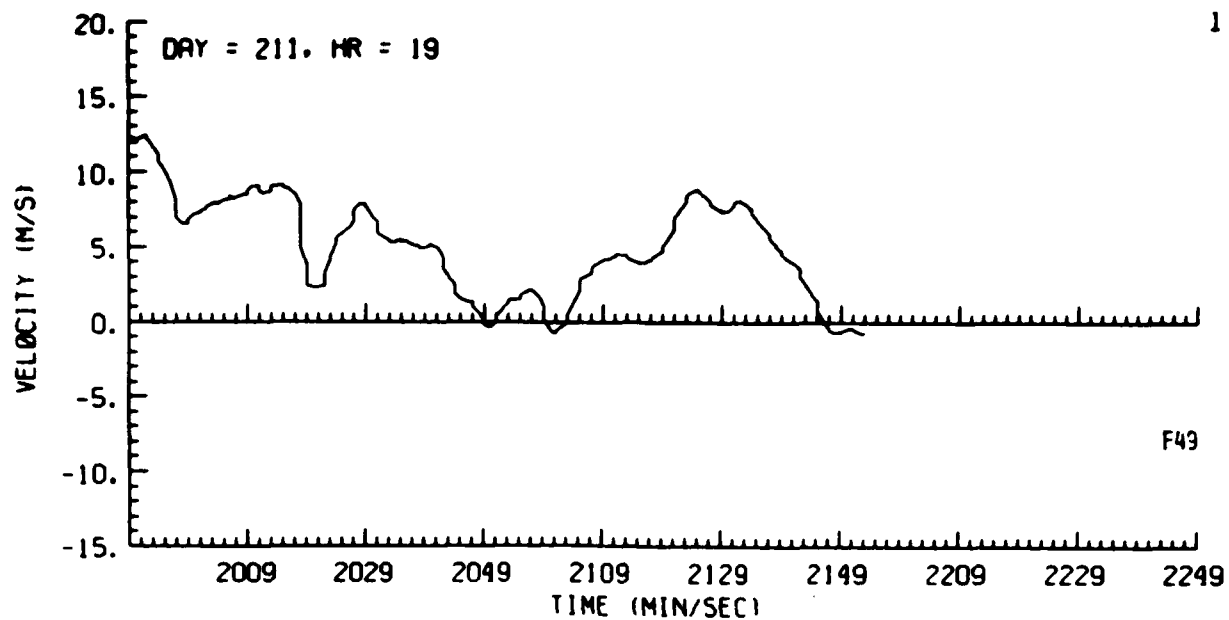


Figure F49. Tracking Gate Doppler Spectrum Mean Data, Day 211, Penetration 1

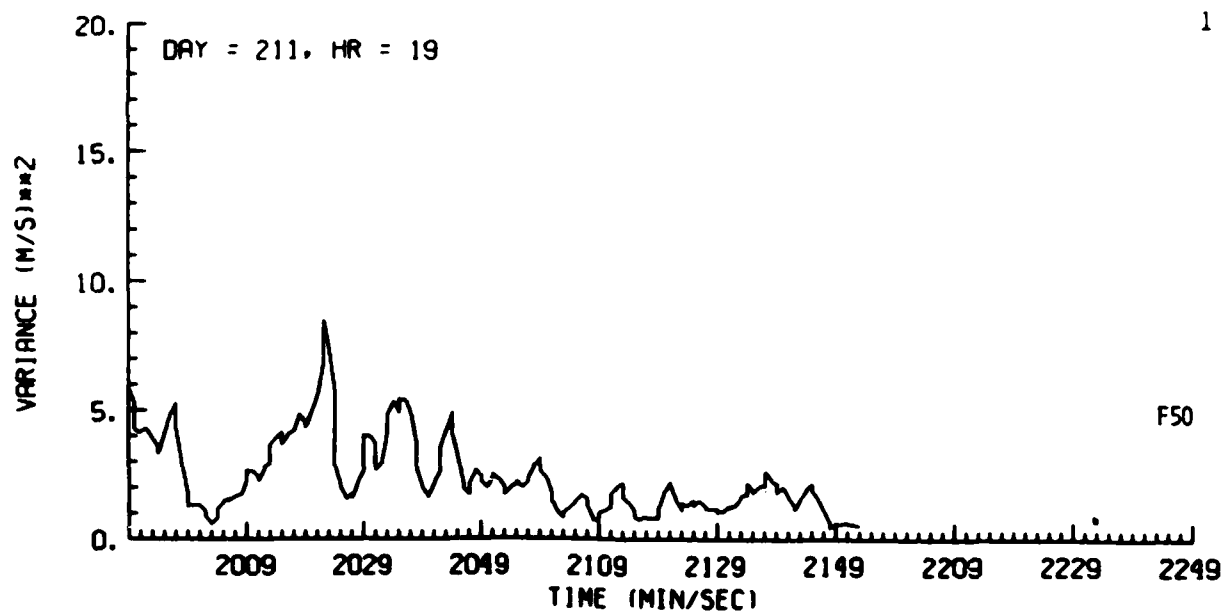


Figure F50. Tracking Gate Doppler Spectrum Variance Data, Day 211, Penetration 1

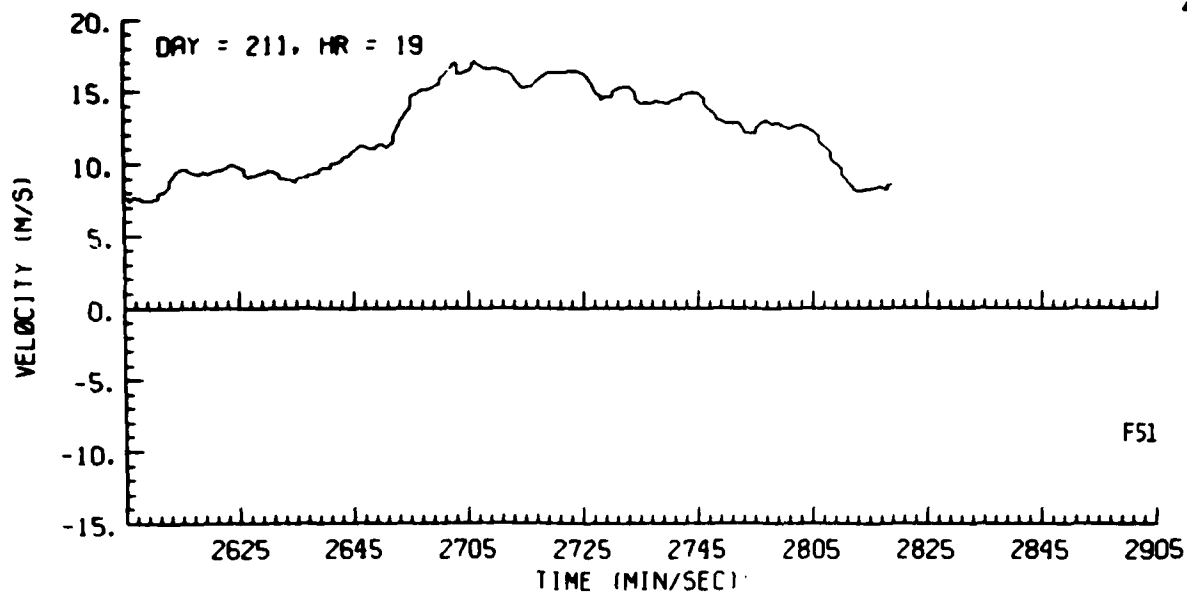


Figure F51. Tracking Gate Doppler Spectrum Mean Data, Day 211, Penetration 2

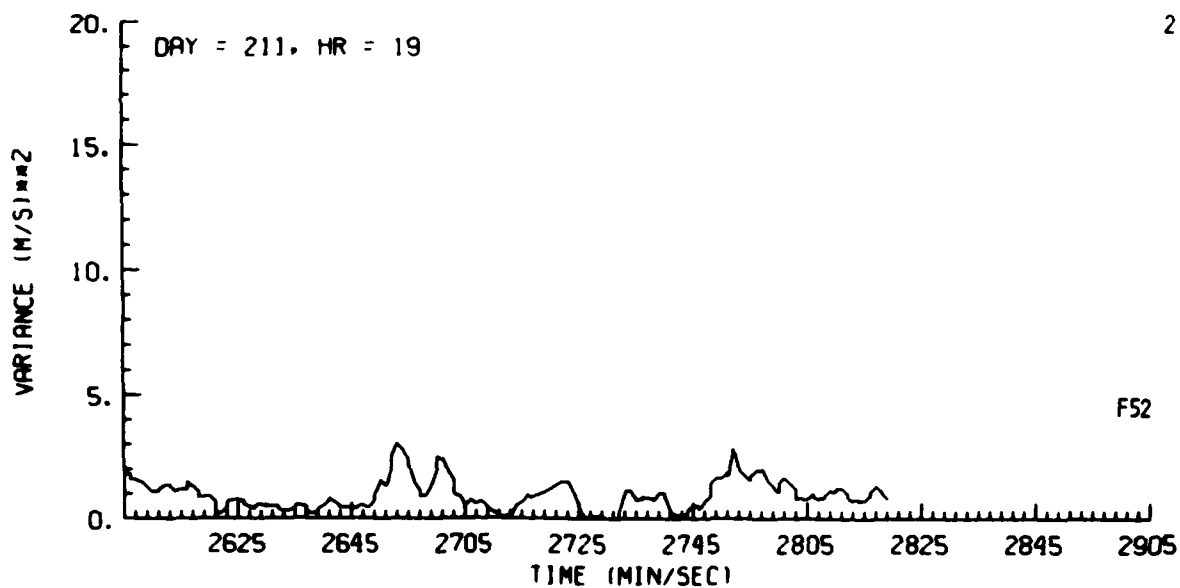


Figure F52. Tracking Gate Doppler Spectrum Variance Data, Day 211, Penetration 2

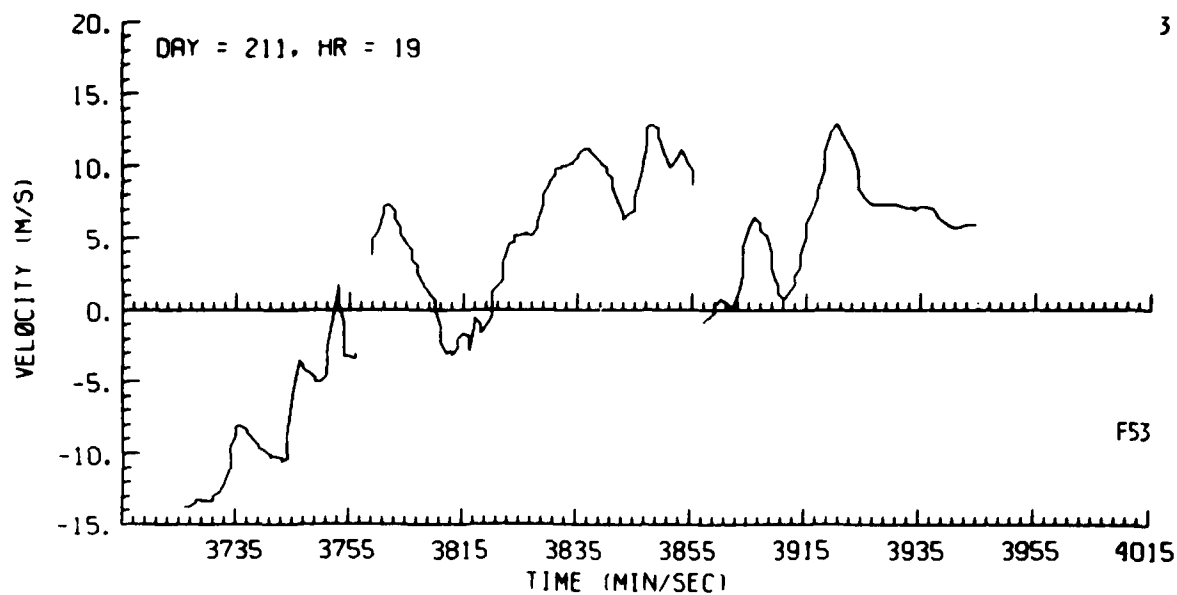


Figure F53. Tracking Gate Doppler Spectrum Mean Data, Day 211, Penetration 3

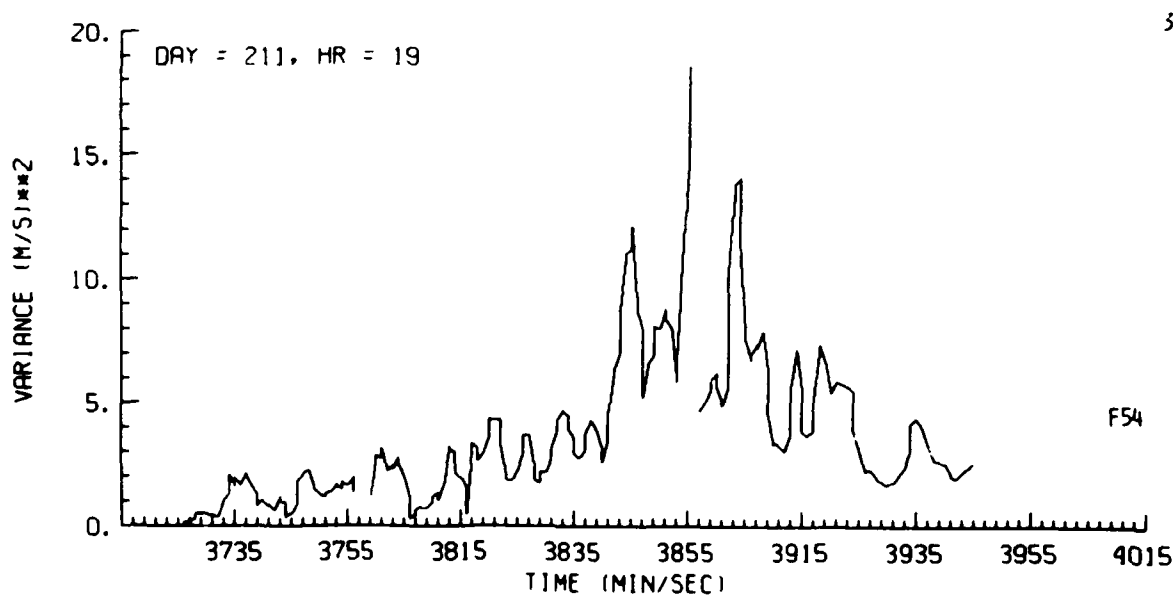


Figure F54. Tracking Gate Doppler Spectrum Variance Data, Day 211, Penetration 3

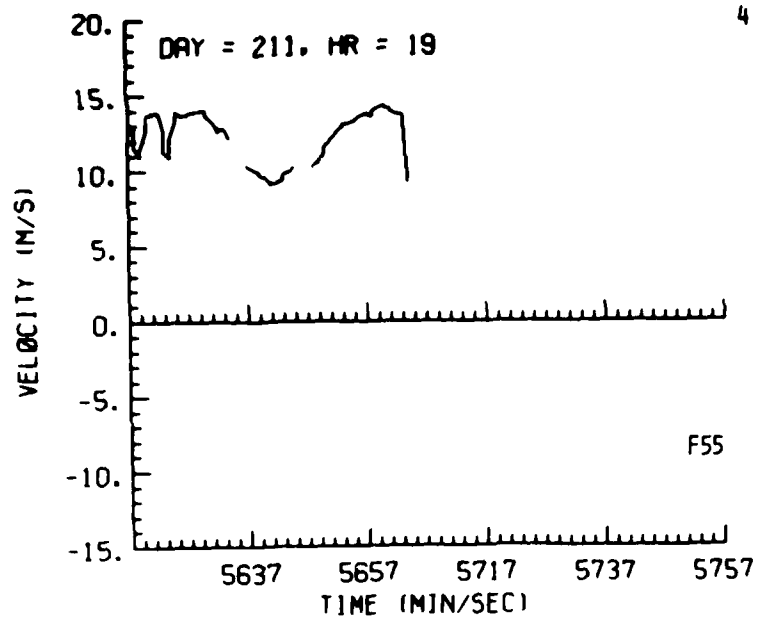


Figure F55. Tracking Gate Doppler Spectrum
Mean Data, Day 211, Penetration 4

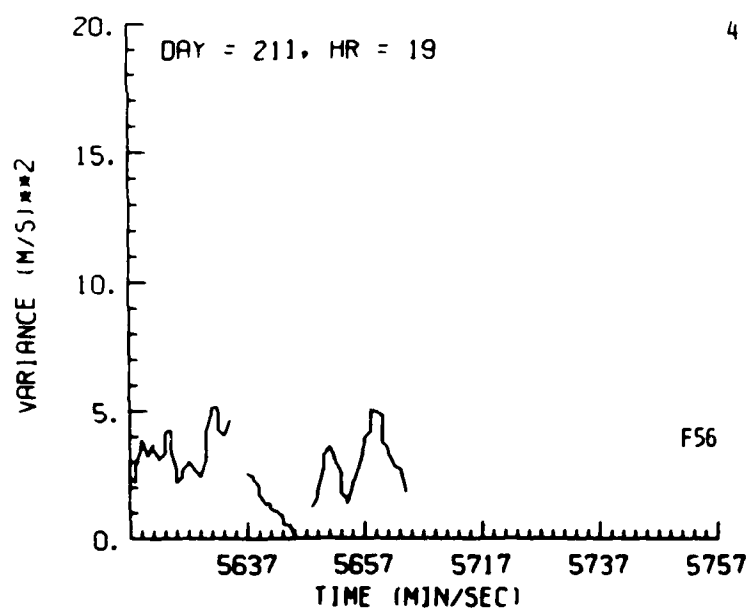


Figure F56. Tracking Gate Doppler Spectrum
Variance Data, Day 211, Penetration 4

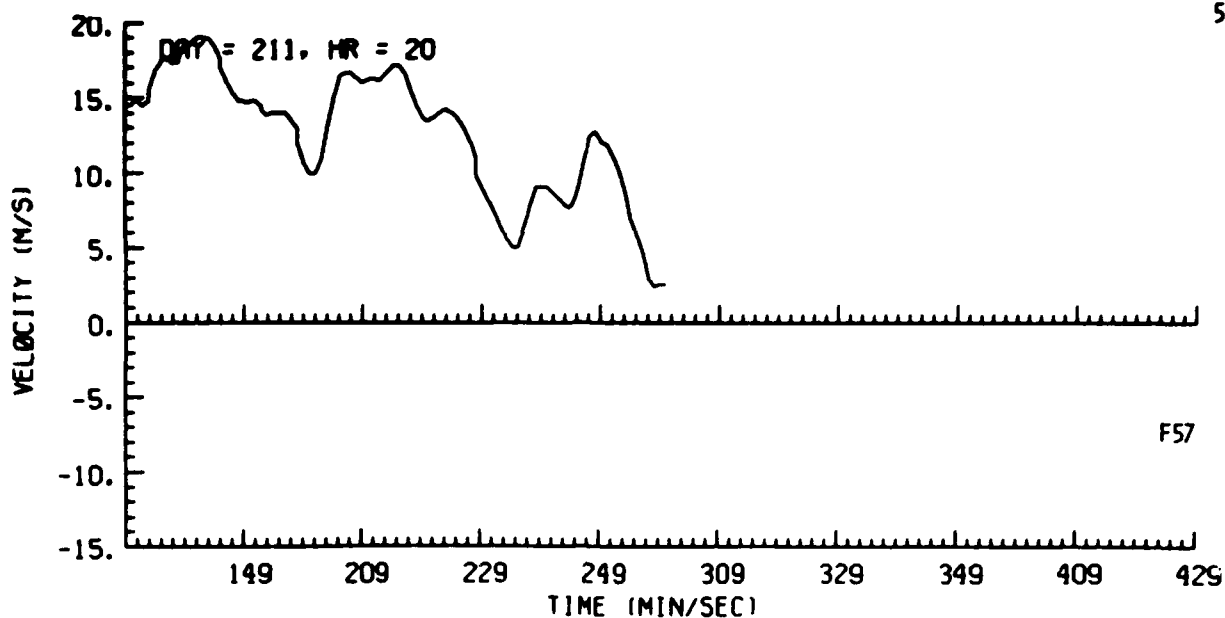


Figure F57. Tracking Gate Doppler Spectrum Mean Data, Day 211, Penetration 5

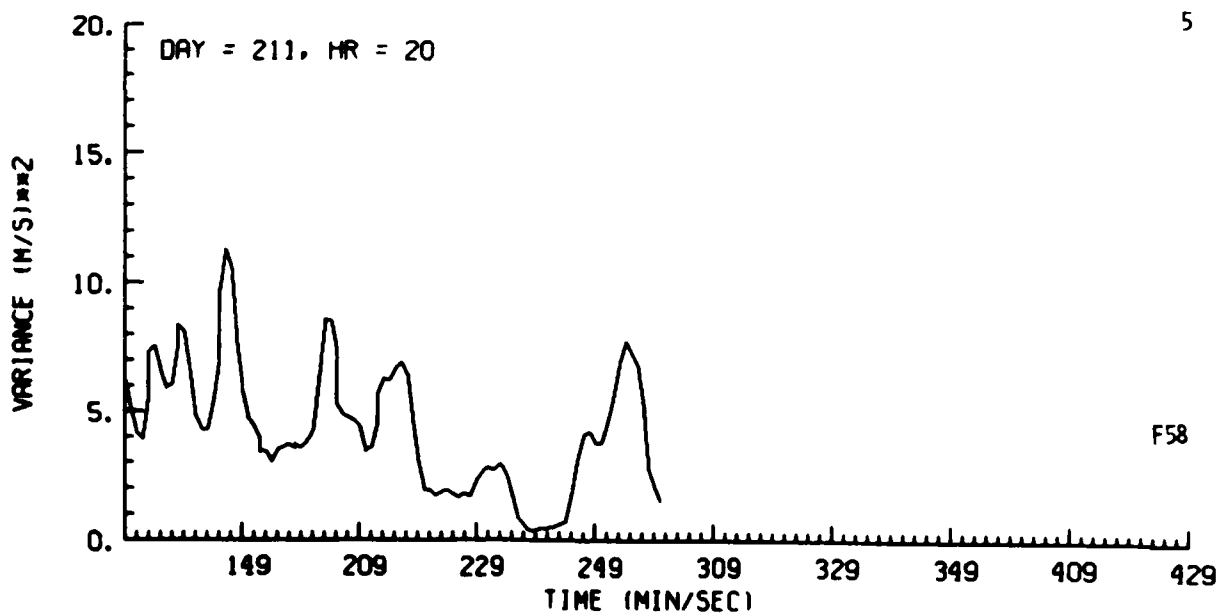


Figure F58. Tracking Gate Doppler Spectrum Variance Data, Day 211, Penetration 5

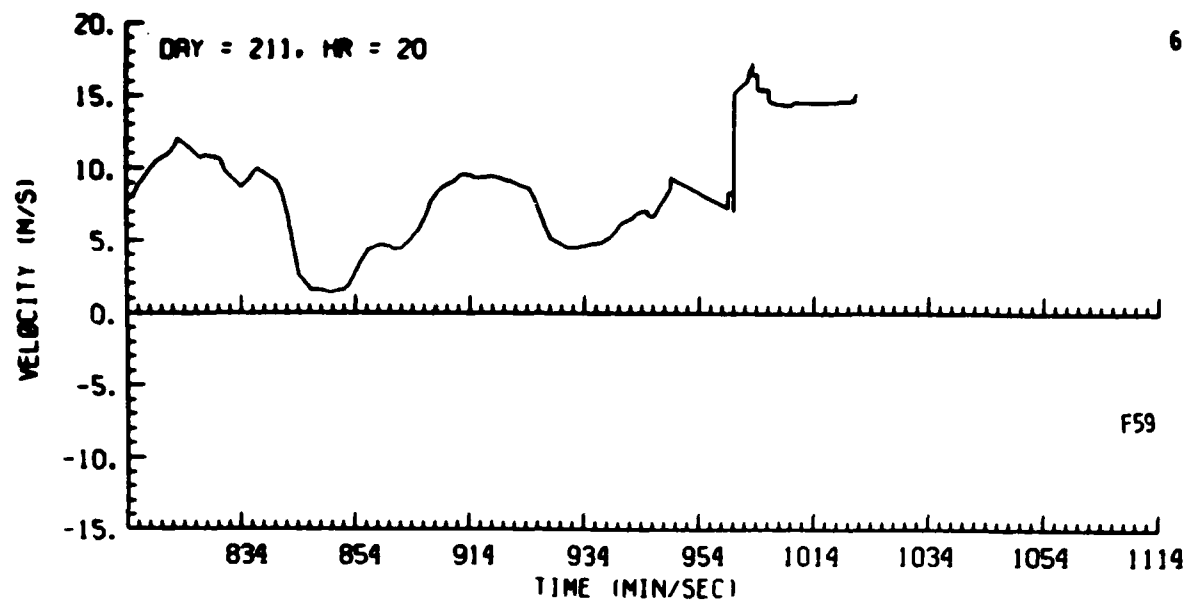


Figure F59. Tracking Gate Doppler Spectrum Mean Data, Day 211, Penetration 6

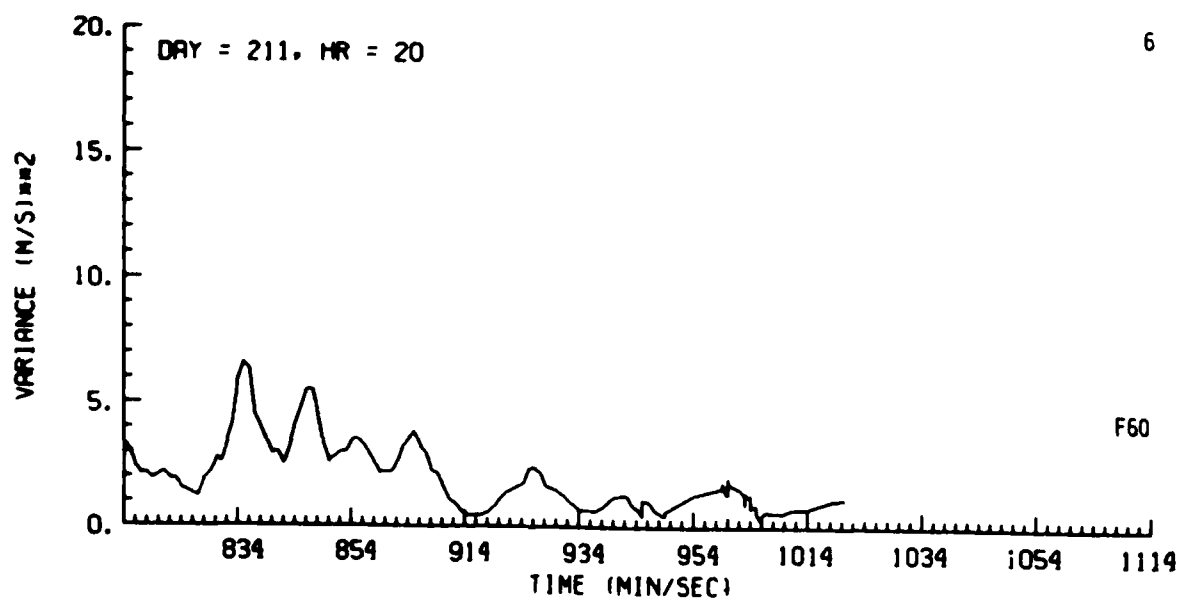


Figure F60. Tracking Gate Doppler Spectrum Variance Data, Day 211, Penetration 6

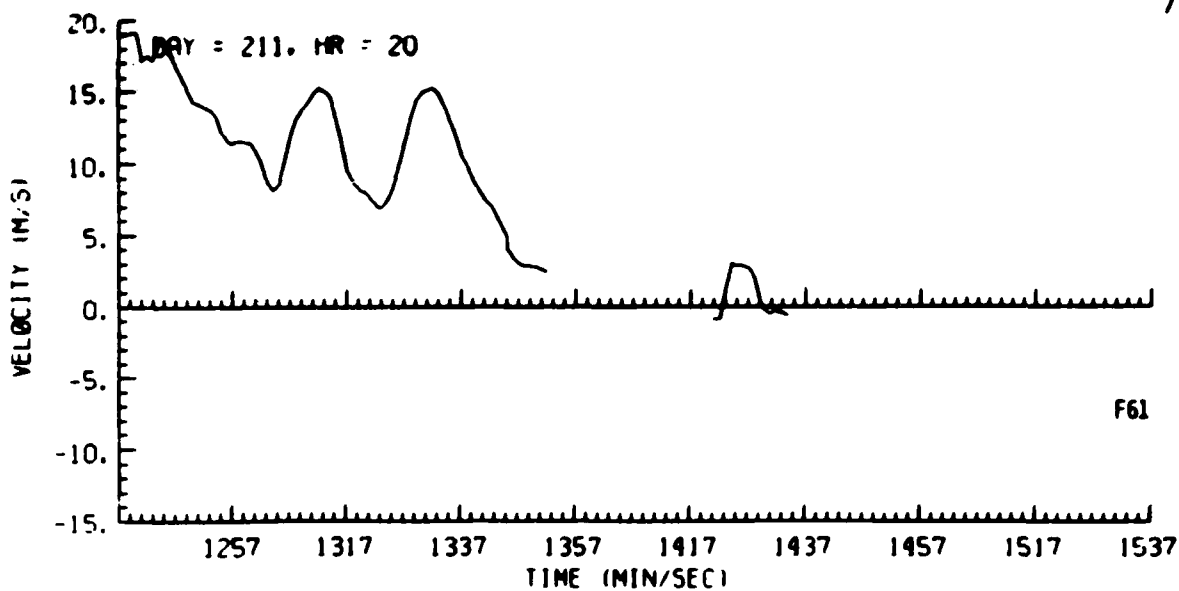


Figure F61. Tracking Gate Doppler Spectrum Mean Data, Day 211, Penetration 7

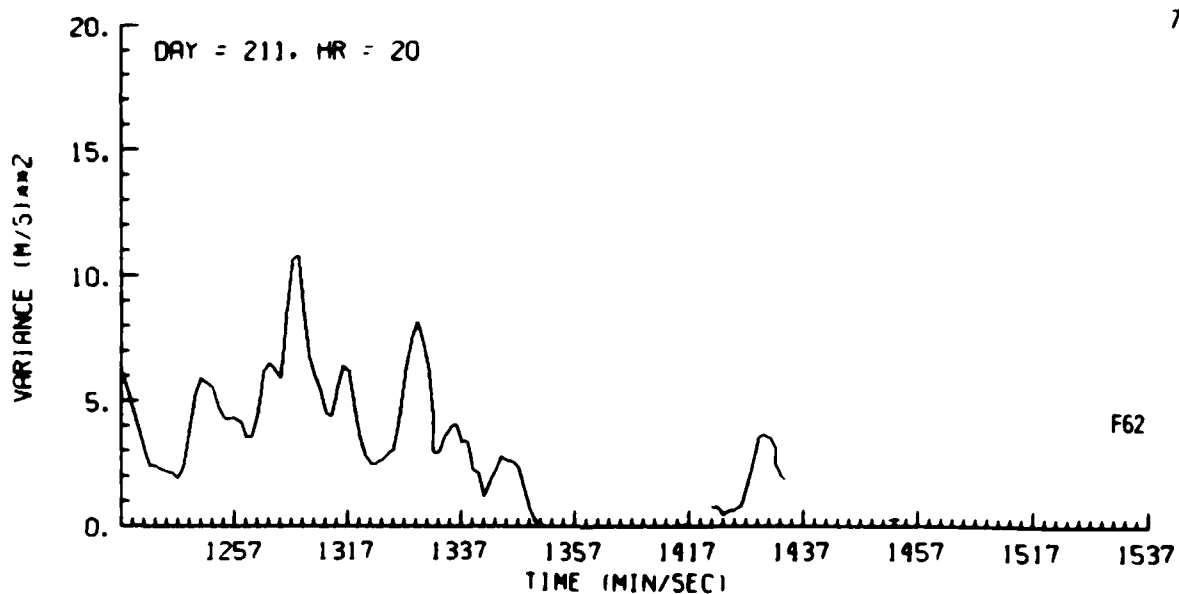


Figure F62. Tracking Gate Doppler Spectrum Variance Data, Day 211, Penetration 7

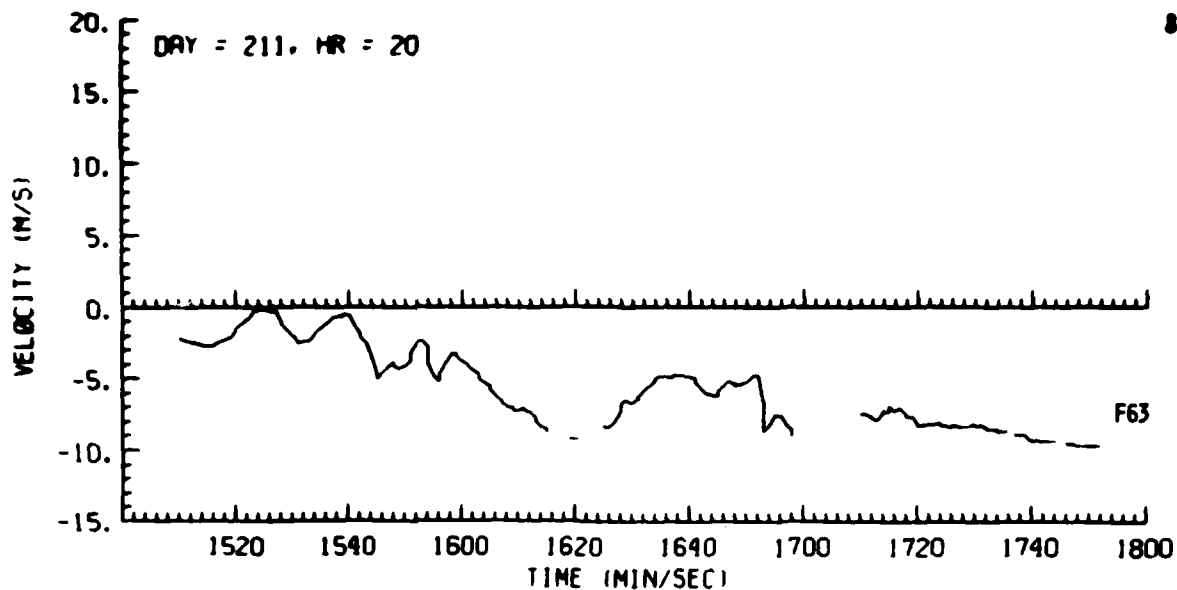


Figure F63. Tracking Gate Doppler Spectrum Mean Data, Day 211, Penetration 8

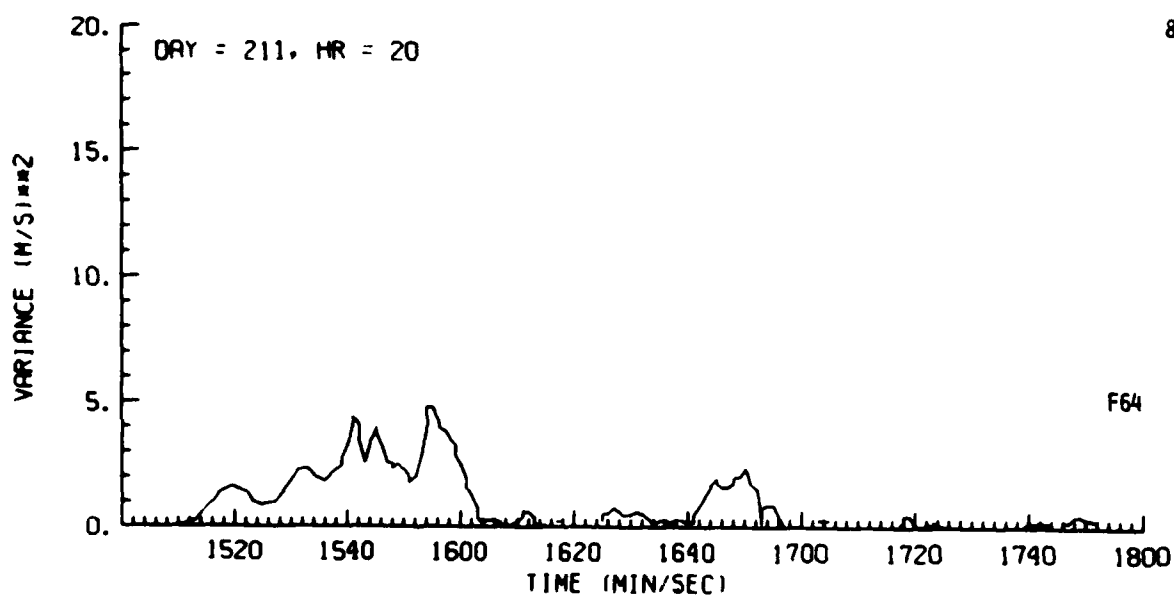


Figure F64. Tracking Gate Doppler Spectrum Variance Data, Day 211, Penetration 8

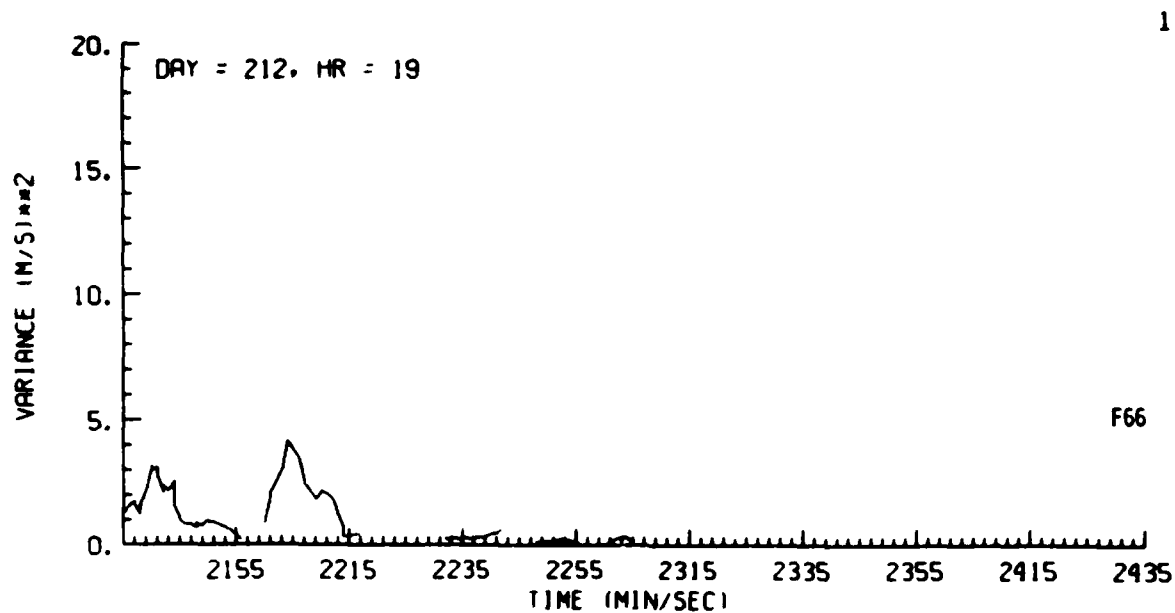


Figure F65. Tracking Gate Doppler Spectrum Mean Data, Day 212, Penetration 1

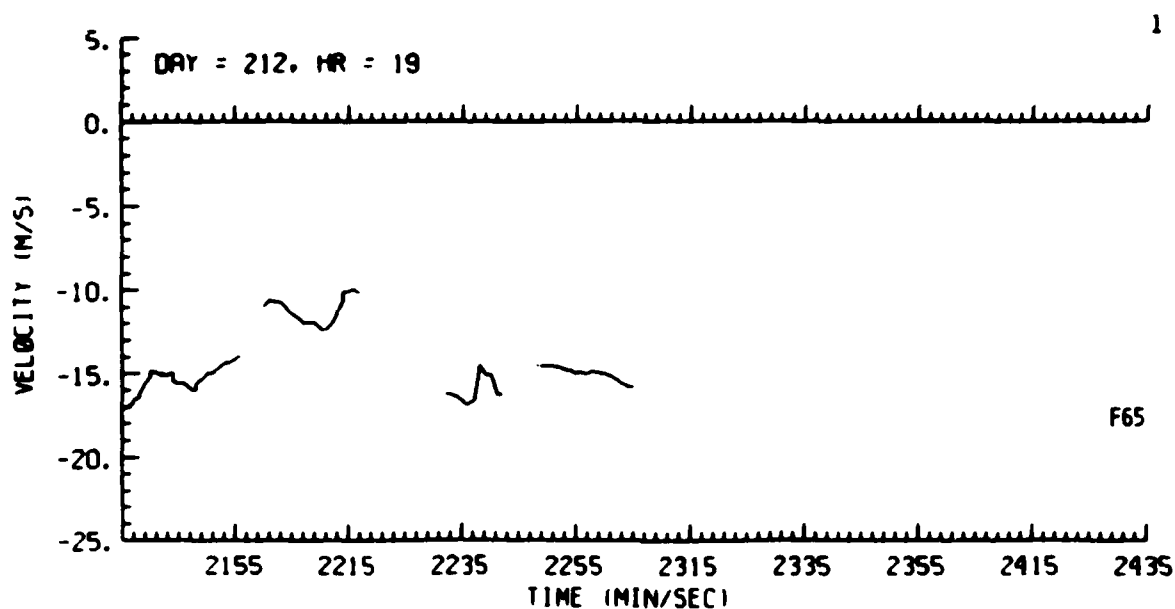


Figure F66. Tracking Gate Doppler Spectrum Variance Data, Day 212, Penetration 1

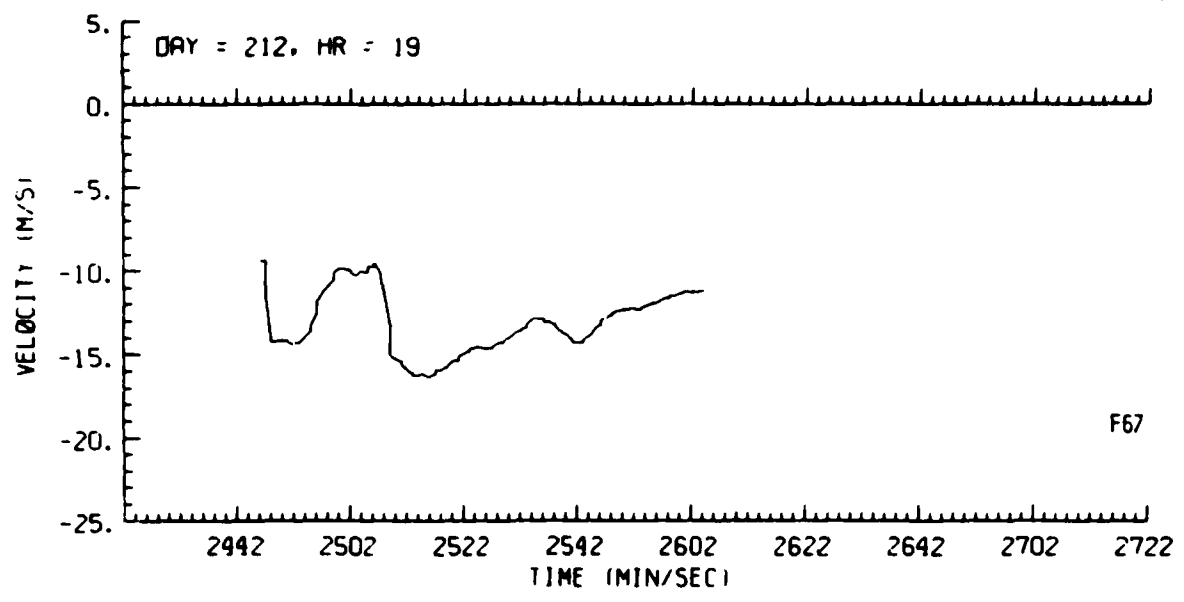


Figure F67. Tracking Gate Doppler Spectrum Mean Data, Day 212, Penetration 3

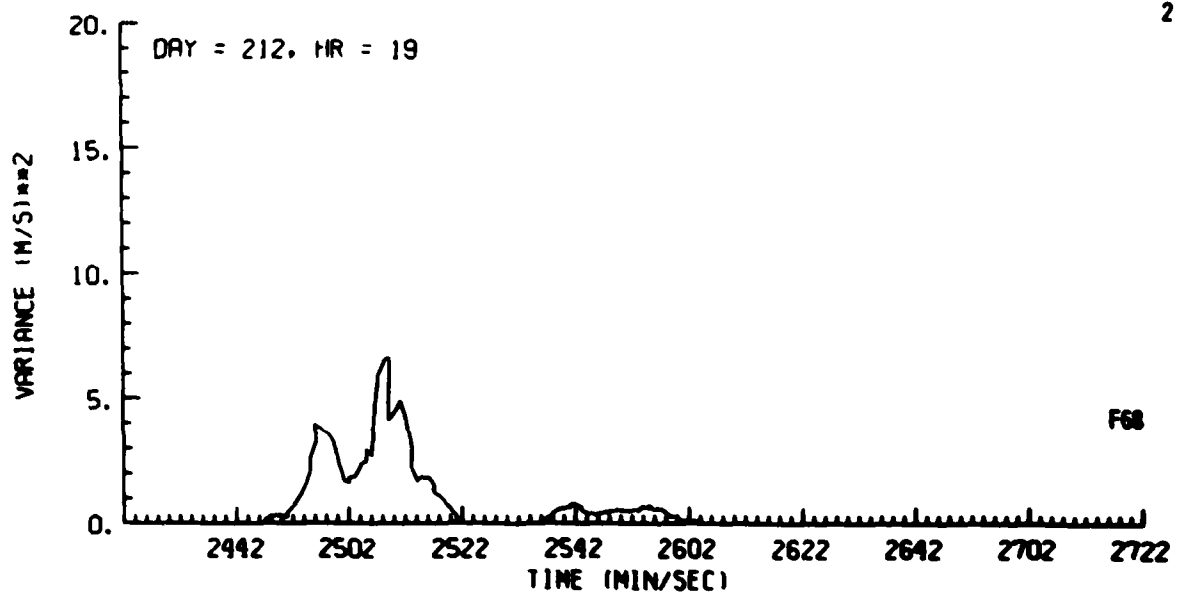


Figure F68. Tracking Gate Doppler Spectrum Variance Data, Day 212, Penetration 2

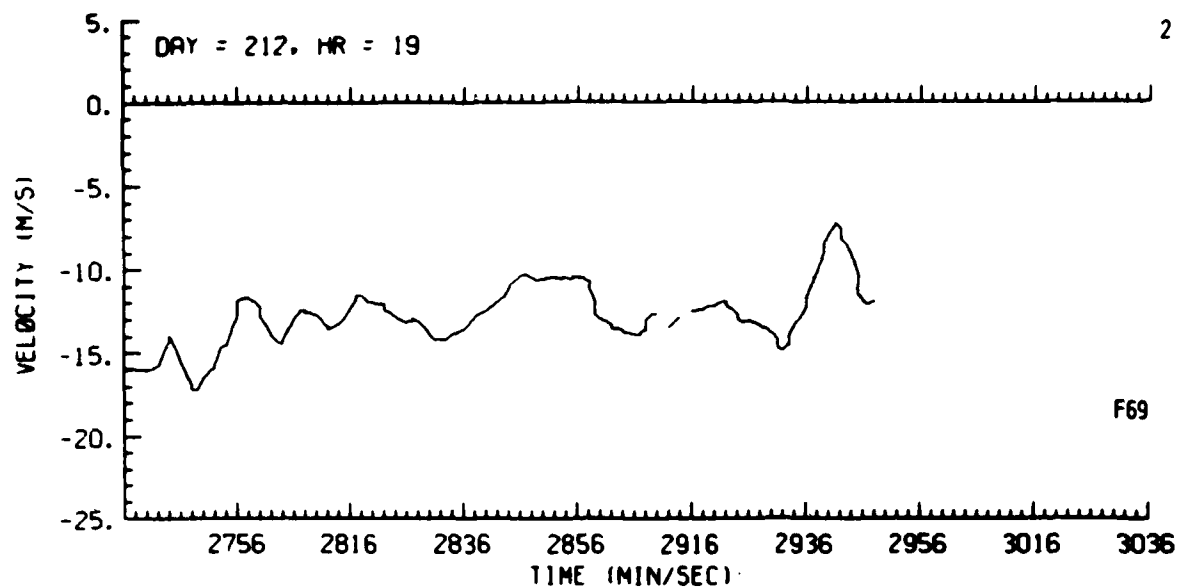


Figure F69. Tracking Gate Doppler Spectrum Mean Data, Day 212, Penetration 2

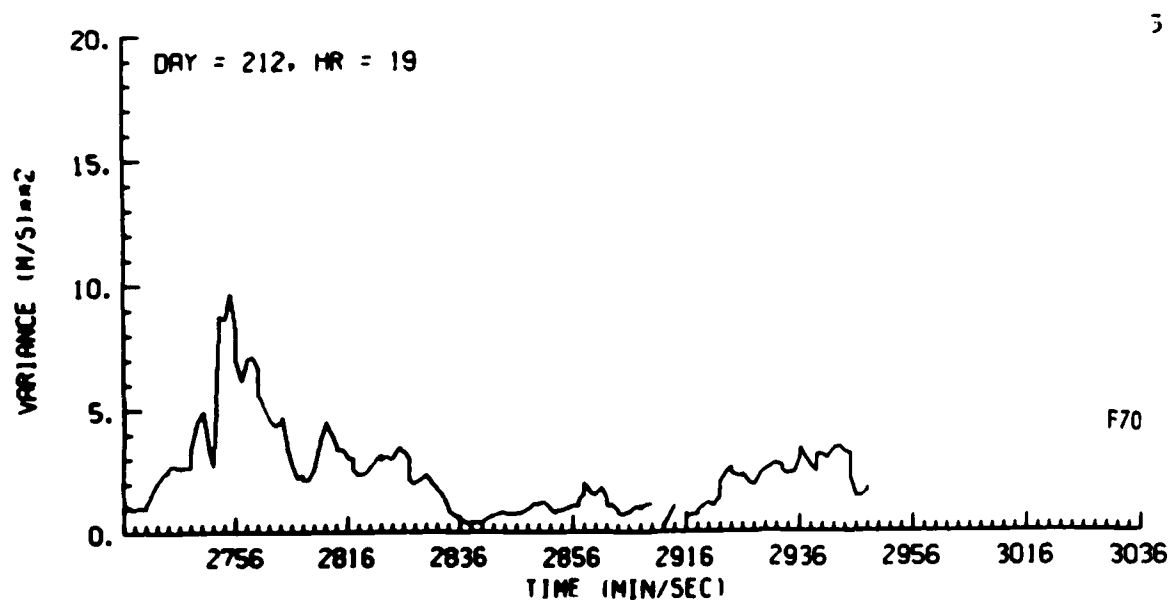


Figure F70. Tracking Gate Doppler Spectrum Variance Data, Day 212, Penetration 3

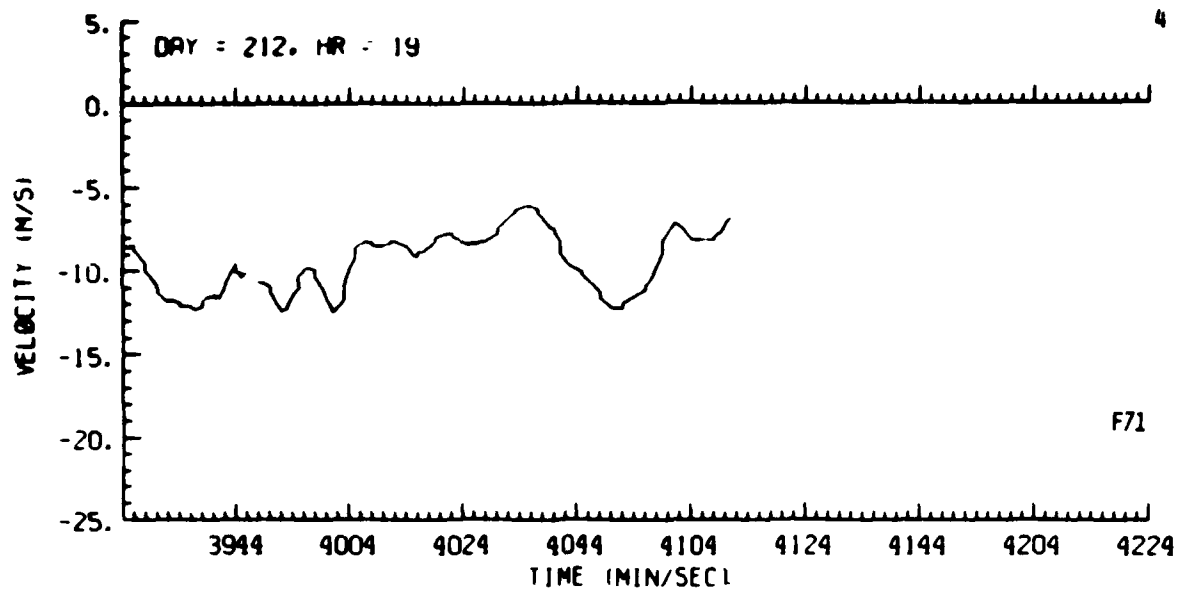


Figure F71. Tracking Gate Doppler Spectrum Mean Data, Day 212, Penetration 4

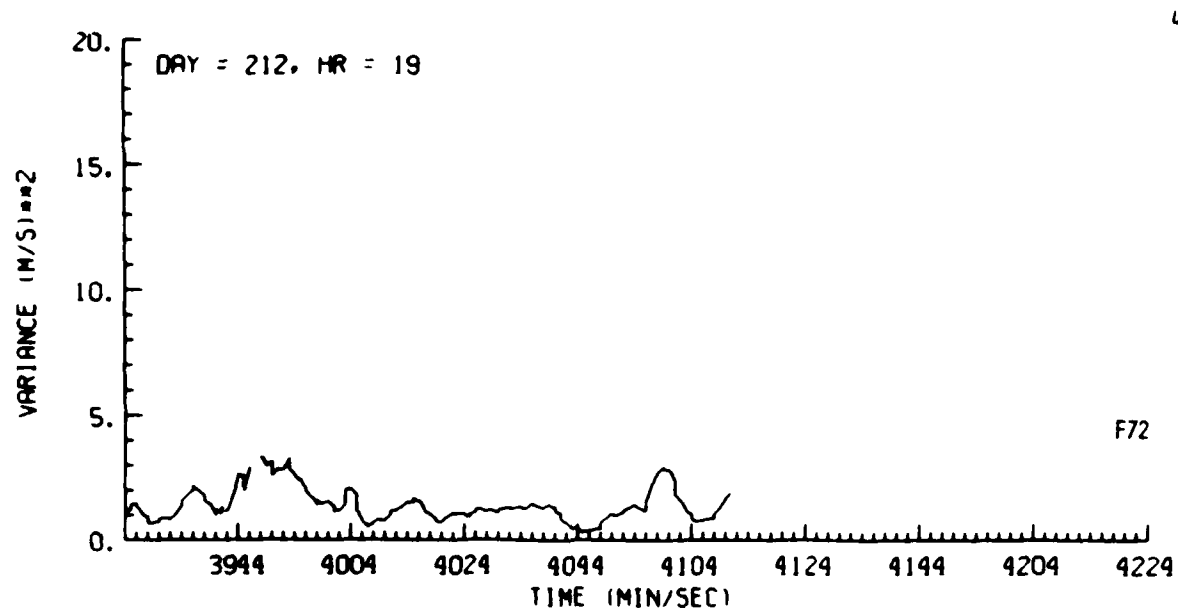


Figure F72. Tracking Gate Doppler Spectrum Variance Data, Day 212, Penetration 4

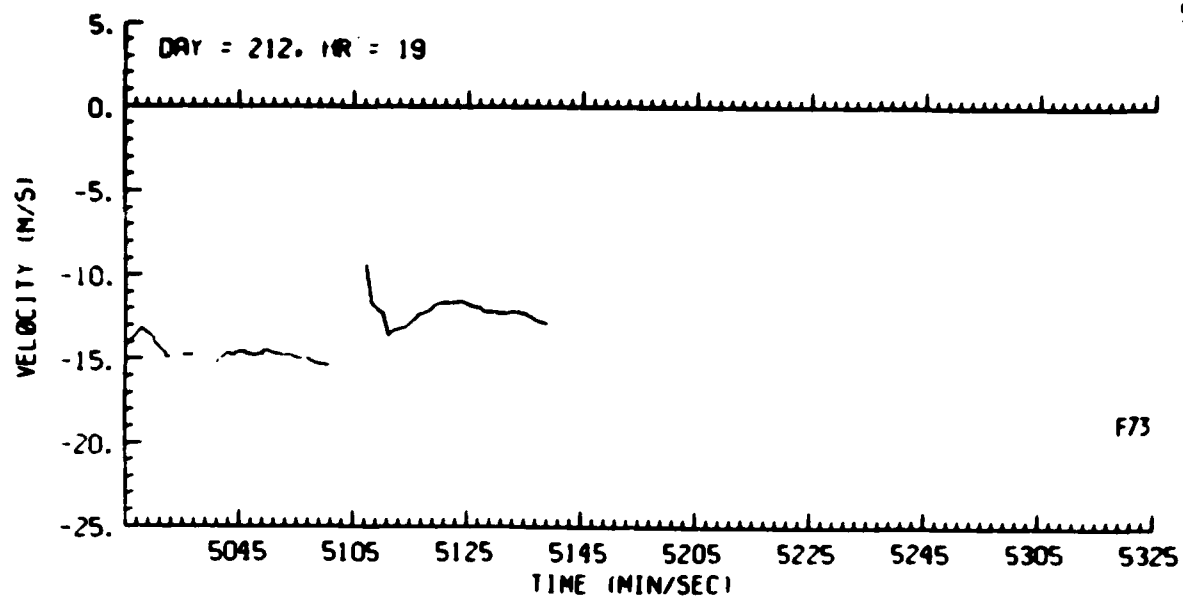


Figure F73. Tracking Gate Doppler Spectrum Mean Data, Day 212, Penetration 5

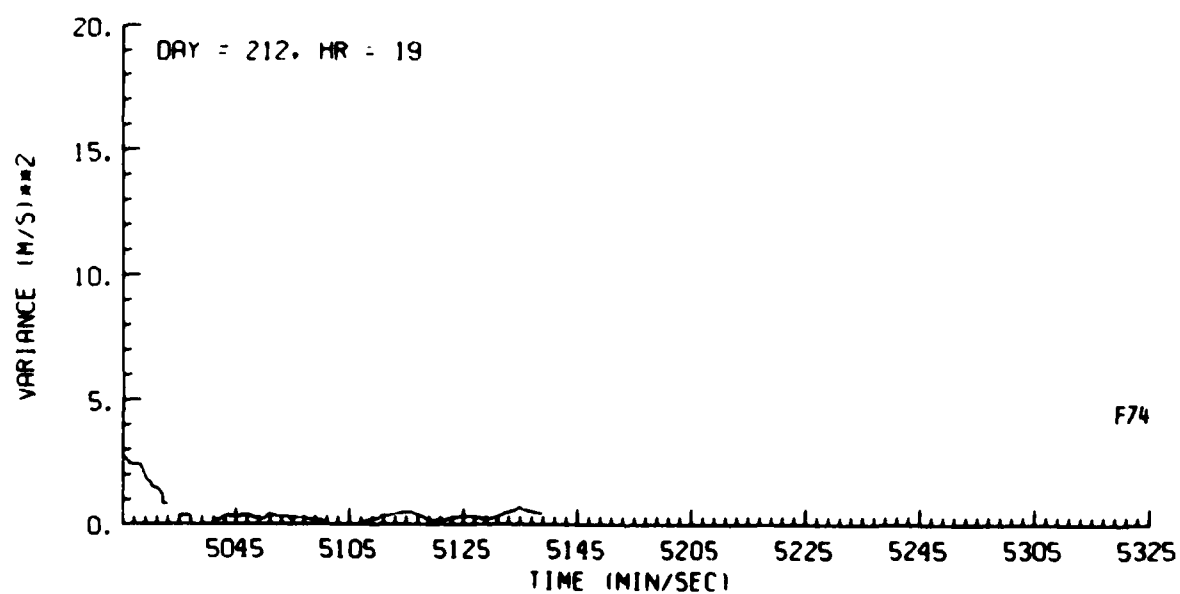


Figure F74. Tracking Gate Doppler Spectrum Variance Data, Day 212, Penetration 5

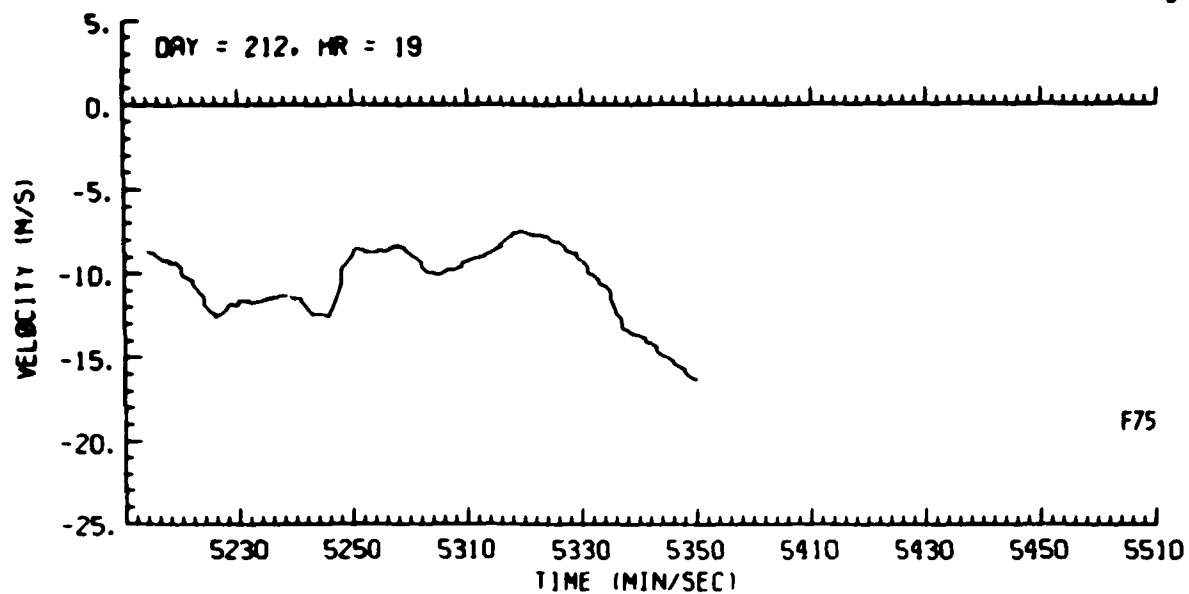


Figure F75. Tracking Gate Doppler Spectrum Mean Data, Day 212, Penetration 6

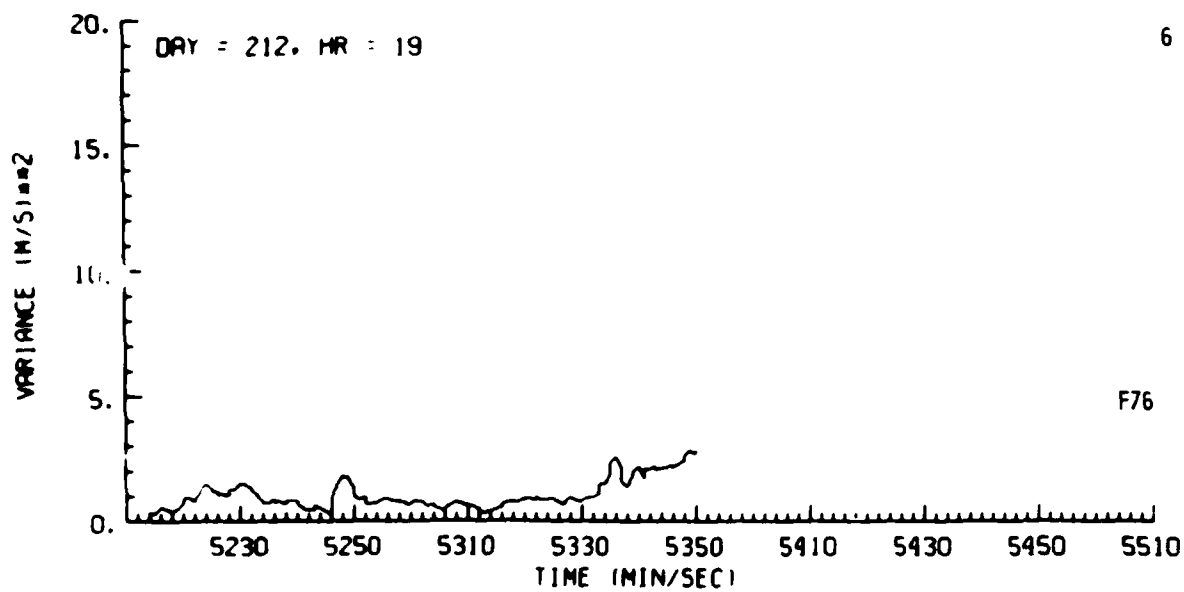


Figure F76. Tracking Gate Doppler Spectrum Variance Data, Day 212, Penetration 6

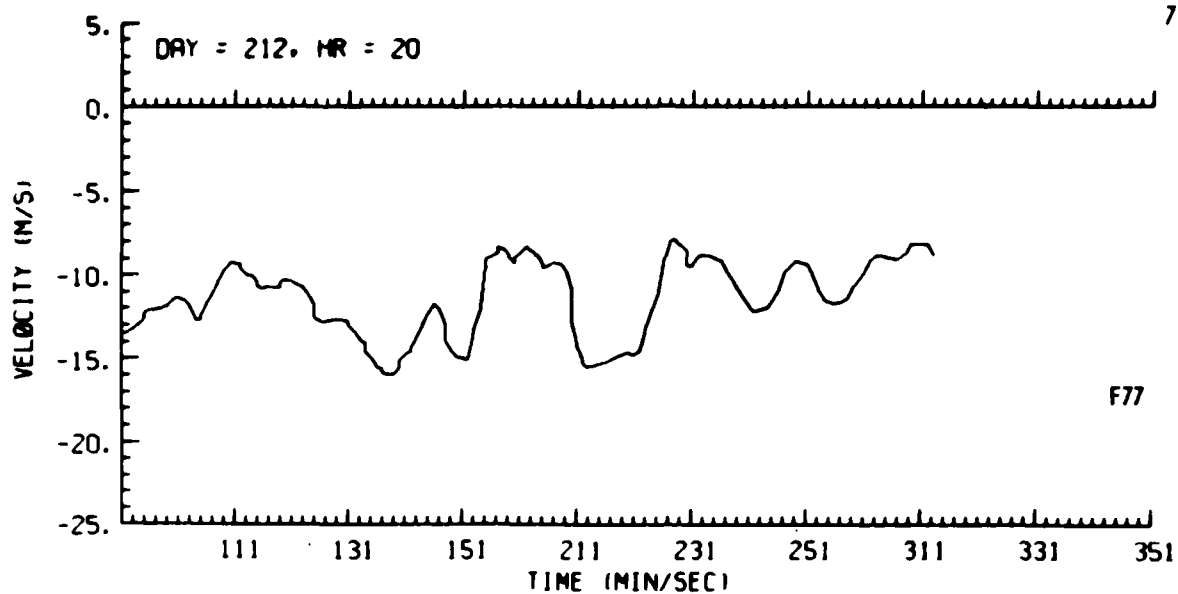


Figure F77. Tracking Gate Doppler Spectrum Mean Data, Day 212, Penetration 7

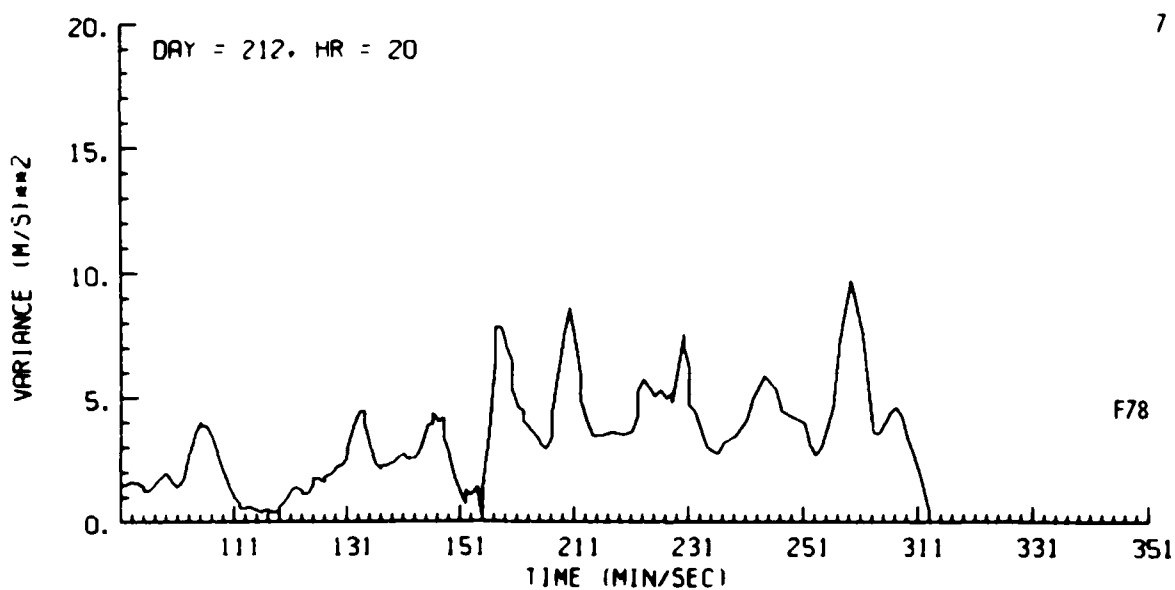


Figure F78. Tracking Gate Doppler Spectrum Variance Data, Day 212, Penetration 7

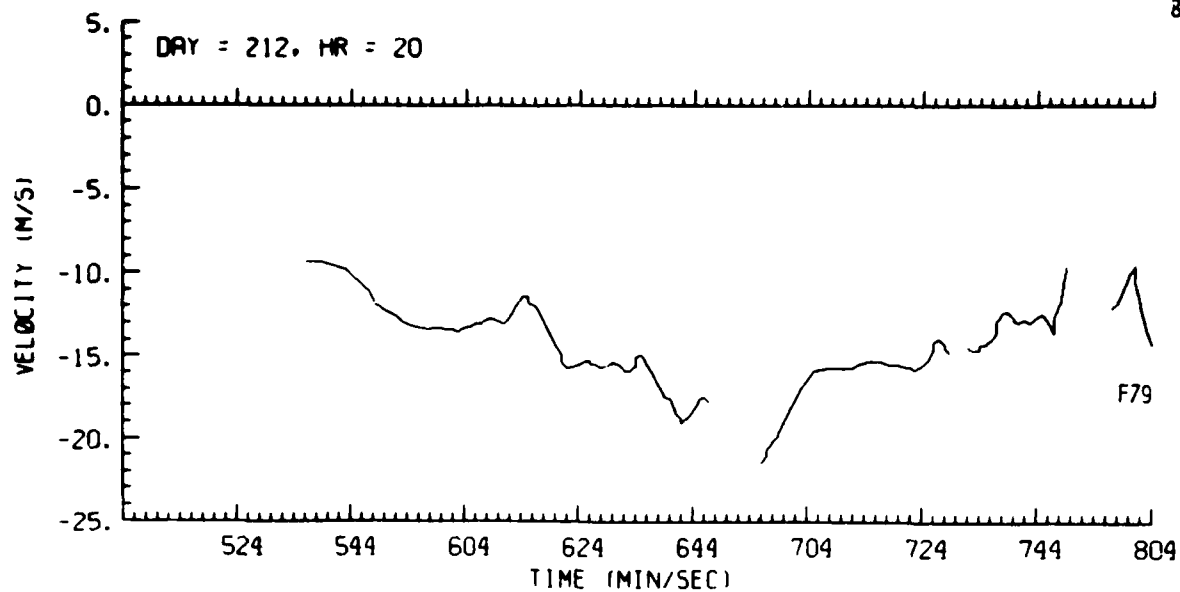


Figure F79. Tracking Gate Doppler Spectrum Mean Data, Day 212, Penetration 8

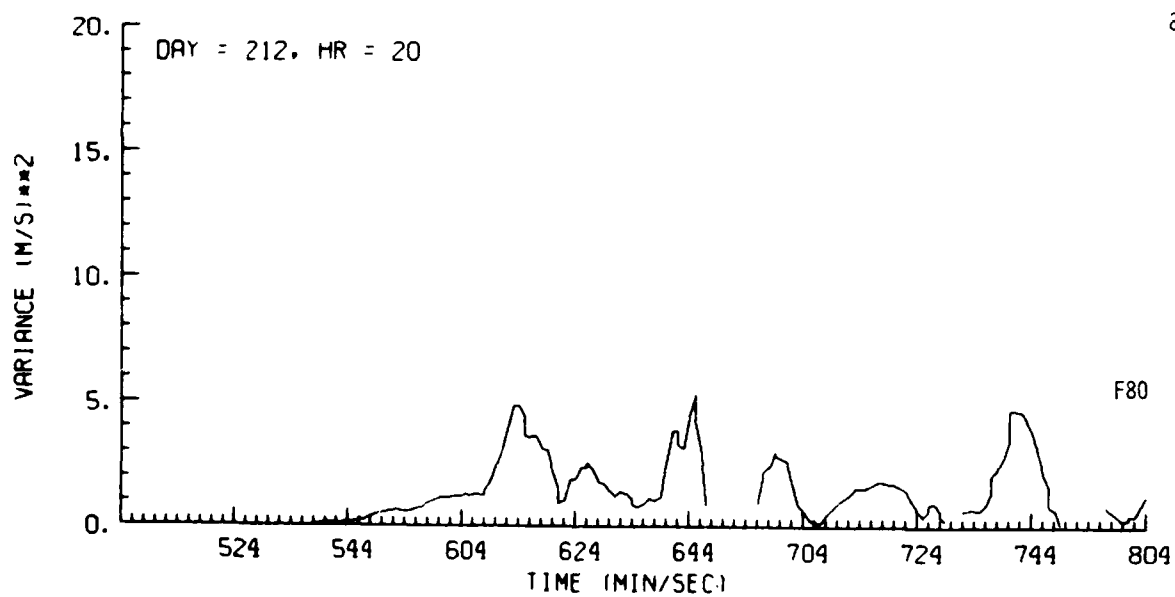


Figure F80. Tracking Gate Doppler Spectrum Variance Data, Day 212, Penetration 8

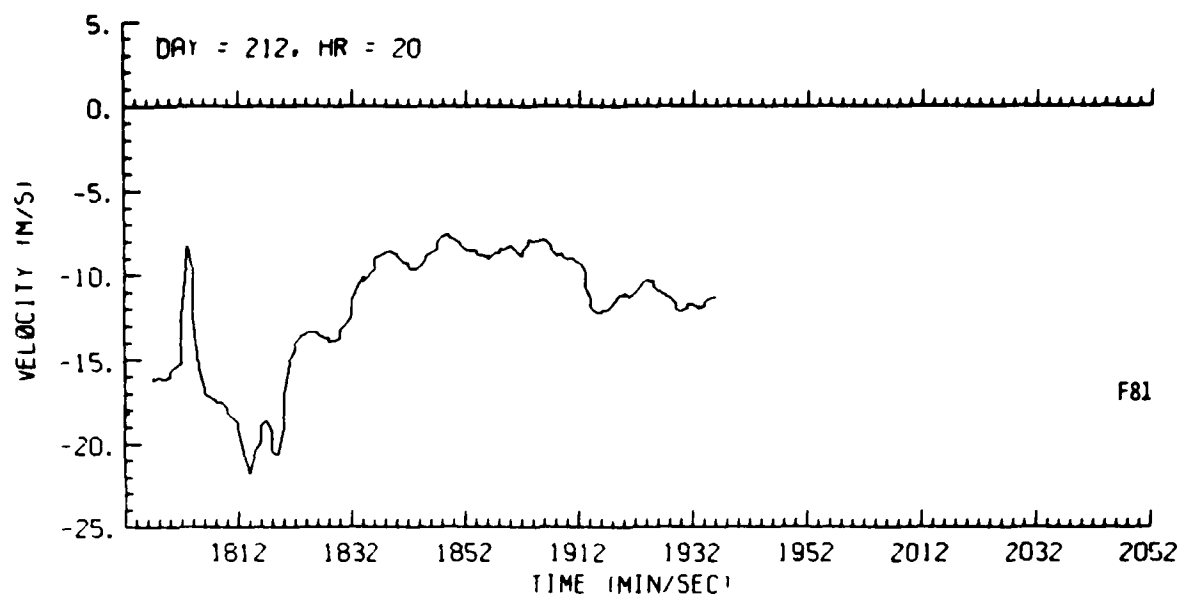


Figure F81. Tracking Gate Doppler Spectrum Mean Data, Day 212, Penetration 9

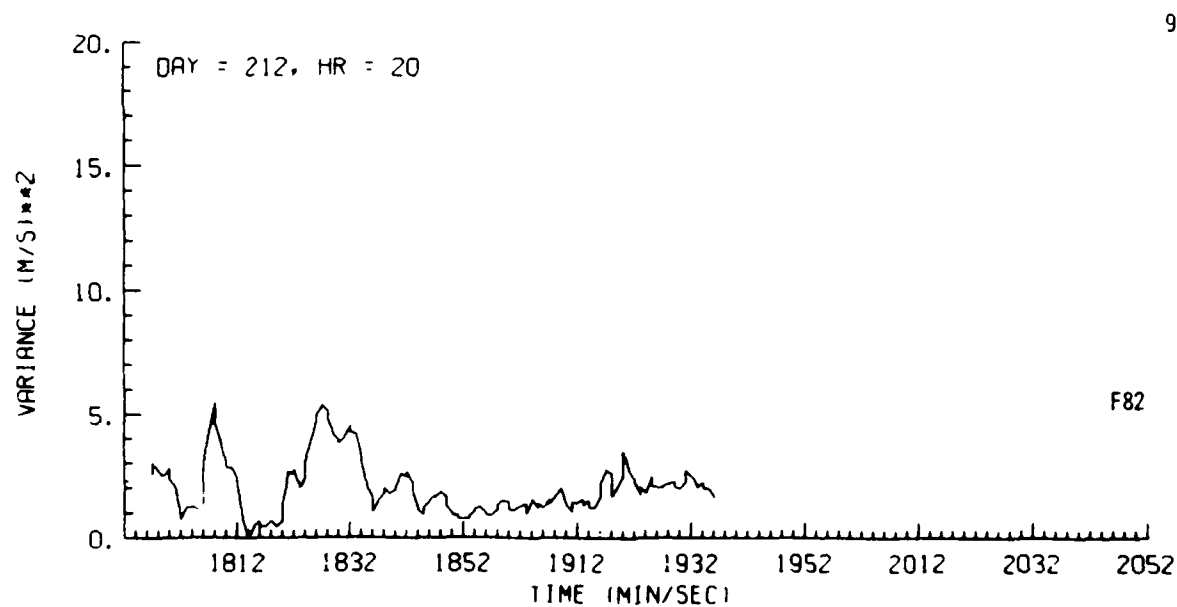


Figure F82. Tracking Gate Doppler Spectrum Variance Data, Day 212, Penetration 9

Appendix G

Estimates of Turbulence Severity Derived From Aircraft Gust Data

Data for Figures G1 through G10 were acquired in 1981 and for Figures G11 through G50, in 1982.

In all figures in Appendix G, O indicates longitudinal, A indicates transverse, and W indicates vertical directions. Ordinate units are $\text{cm}^{2/3} \text{sec}^{-1}$.

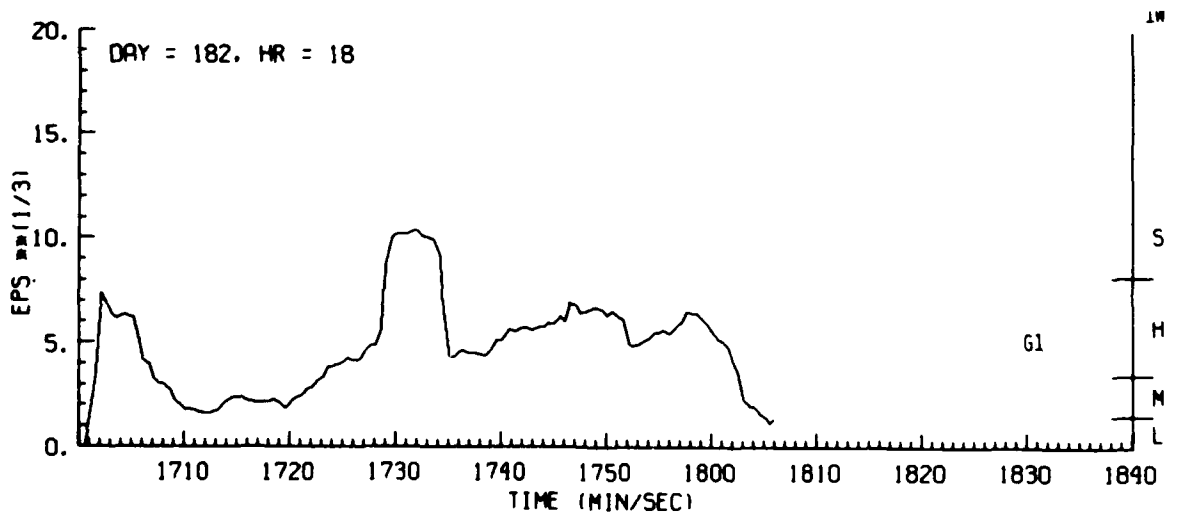
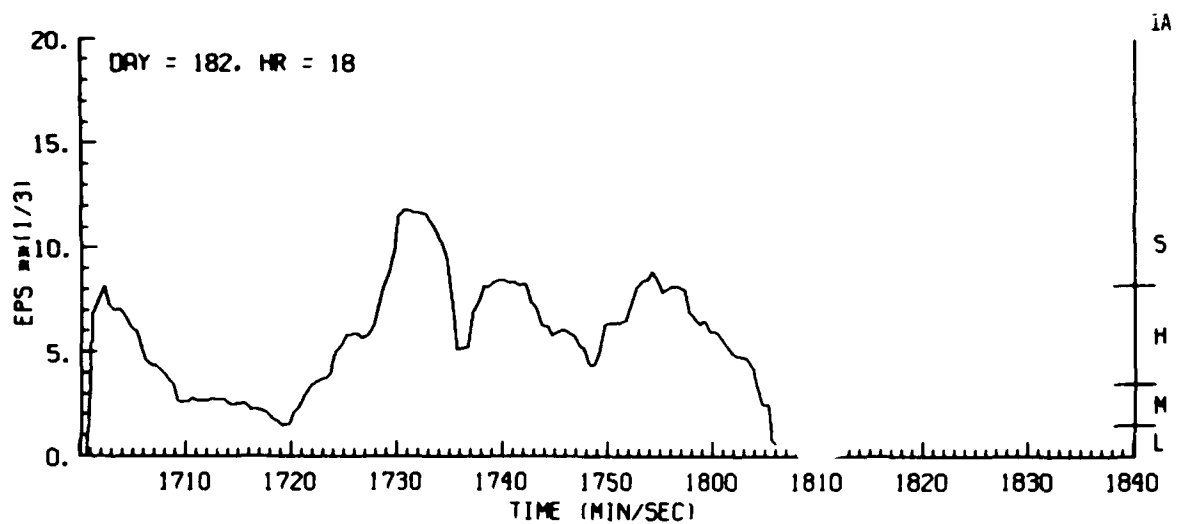
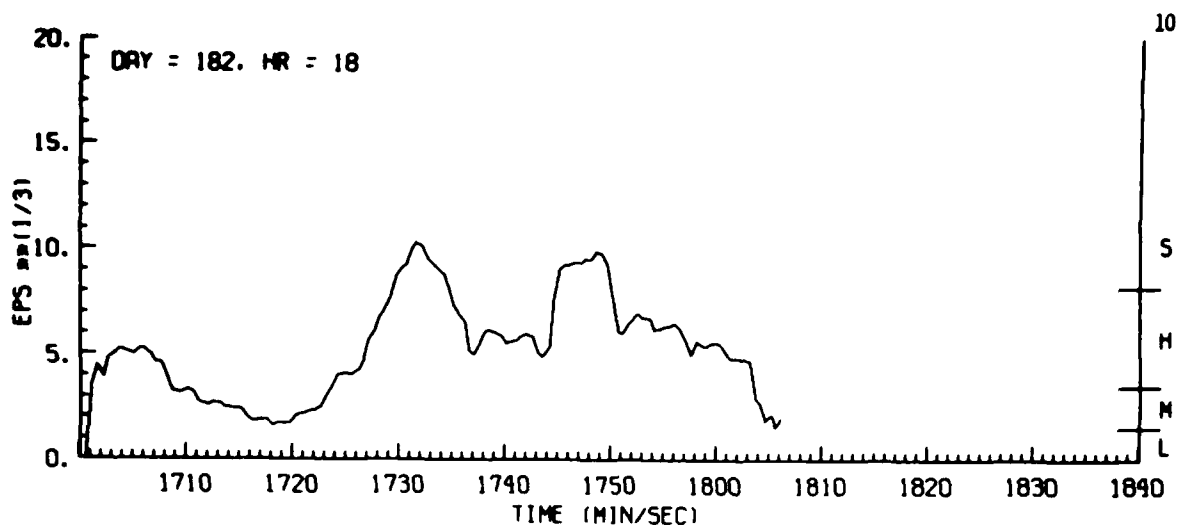


Figure G1. Estimates of Turbulence Severity Derived From Aircraft Gust Data, Day 182, Penetration 1

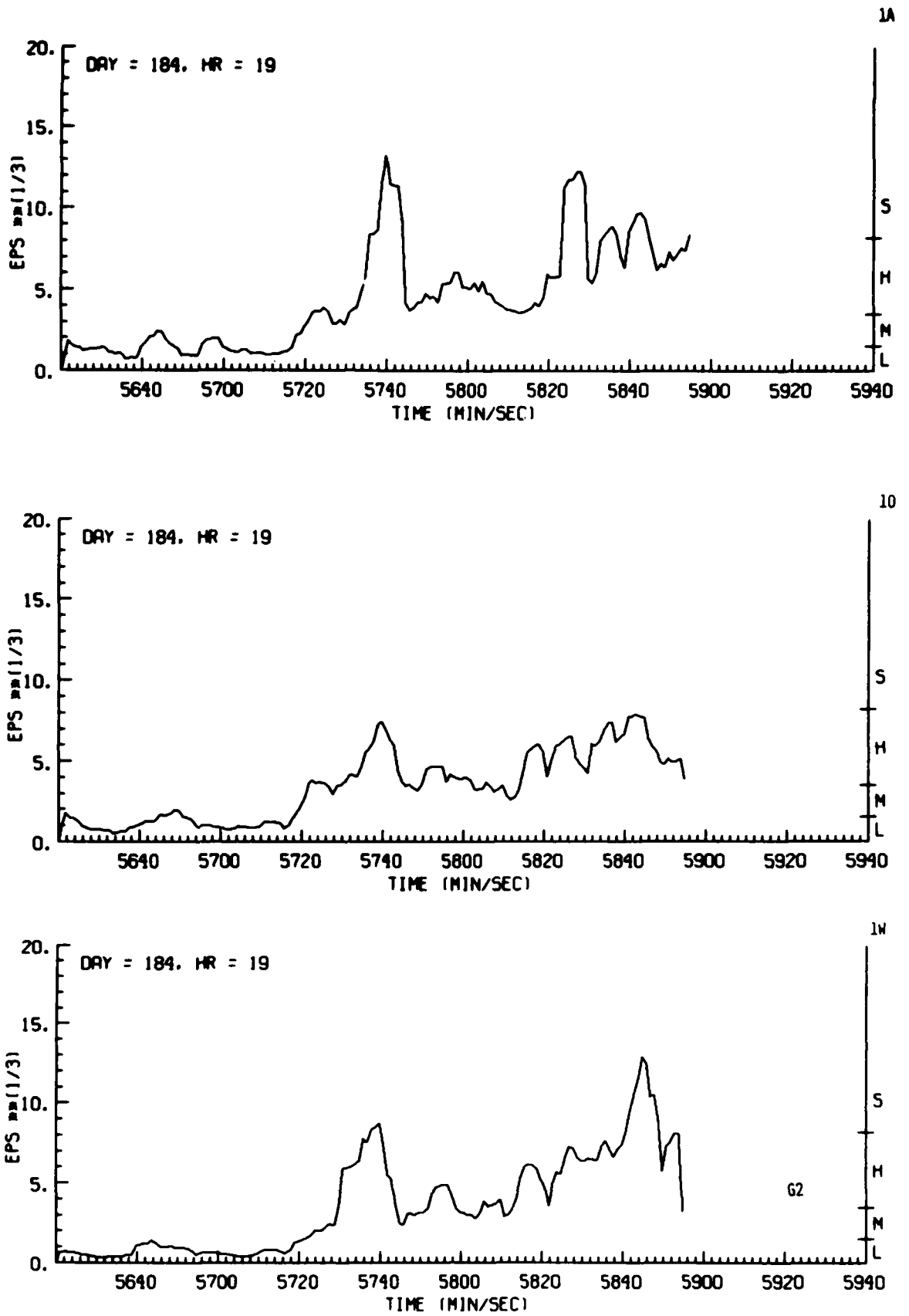


Figure G2. Estimates of Turbulence Severity Derived From Aircraft Gust Data, Day 184, Penetration 1A

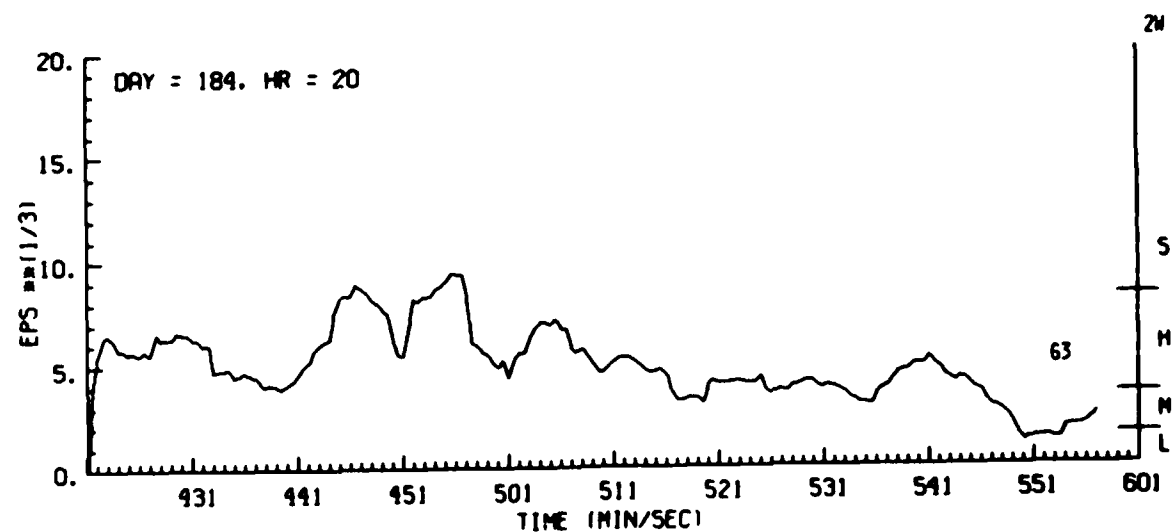
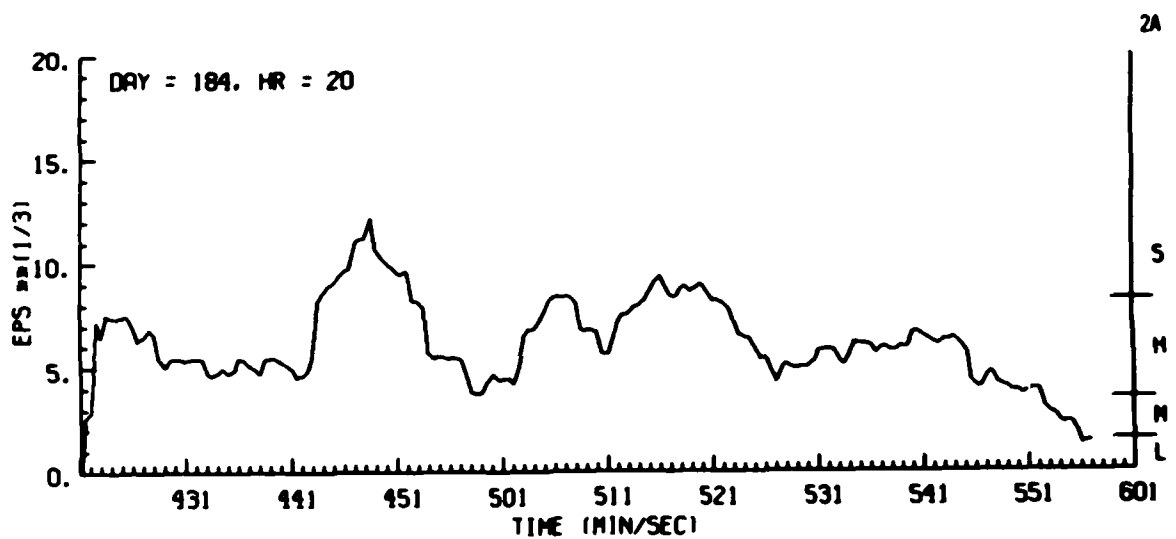
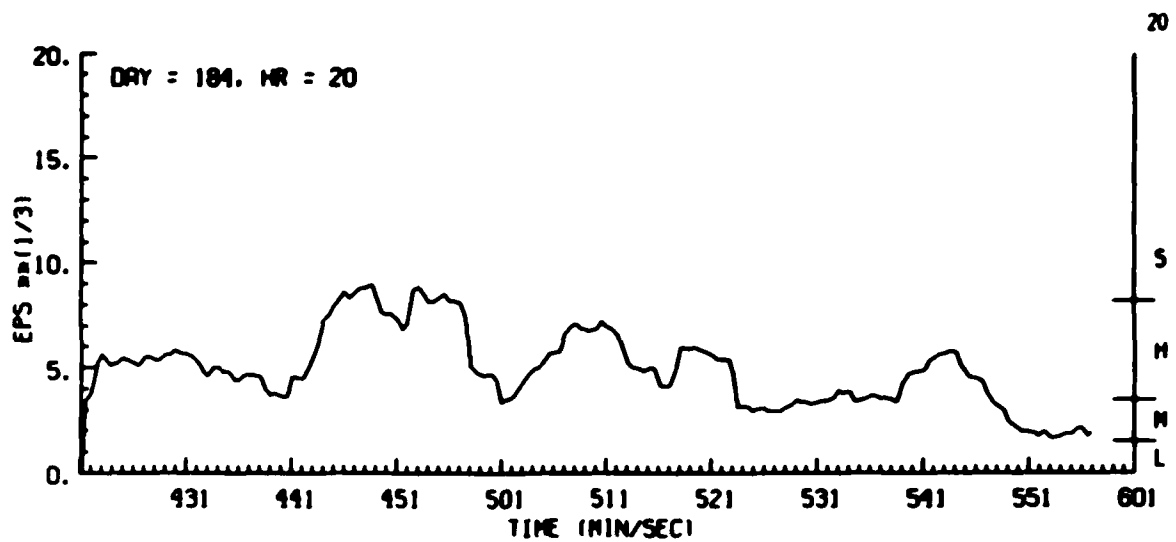


Figure G3. Estimates of Turbulence Severity Derived From Aircraft Gust Data, Day 184, Penetration 2

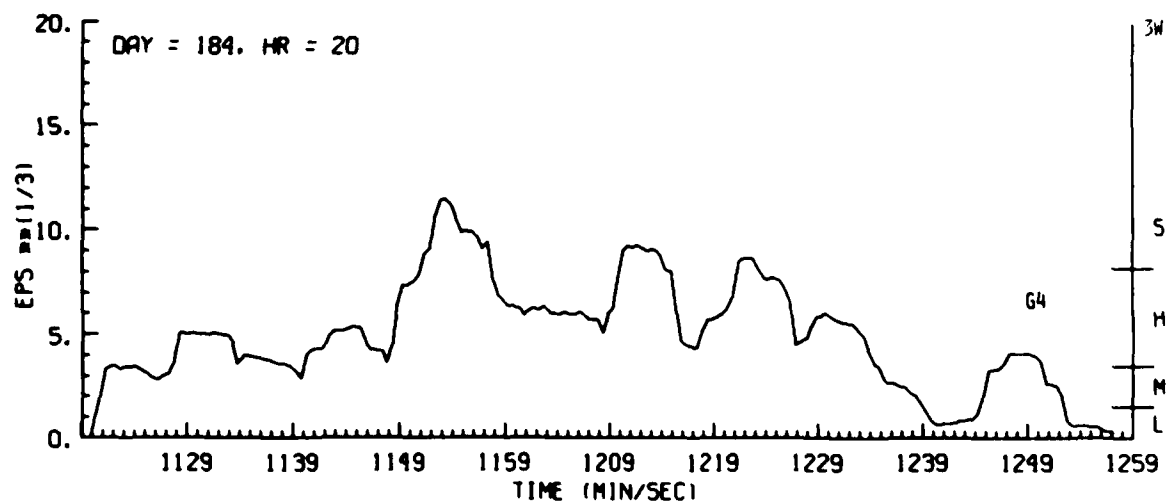
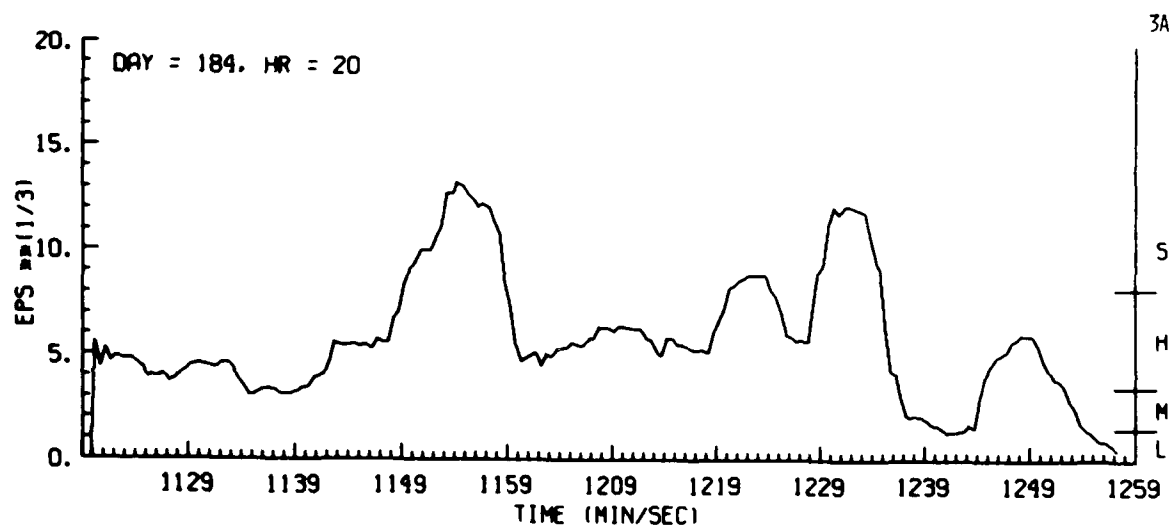
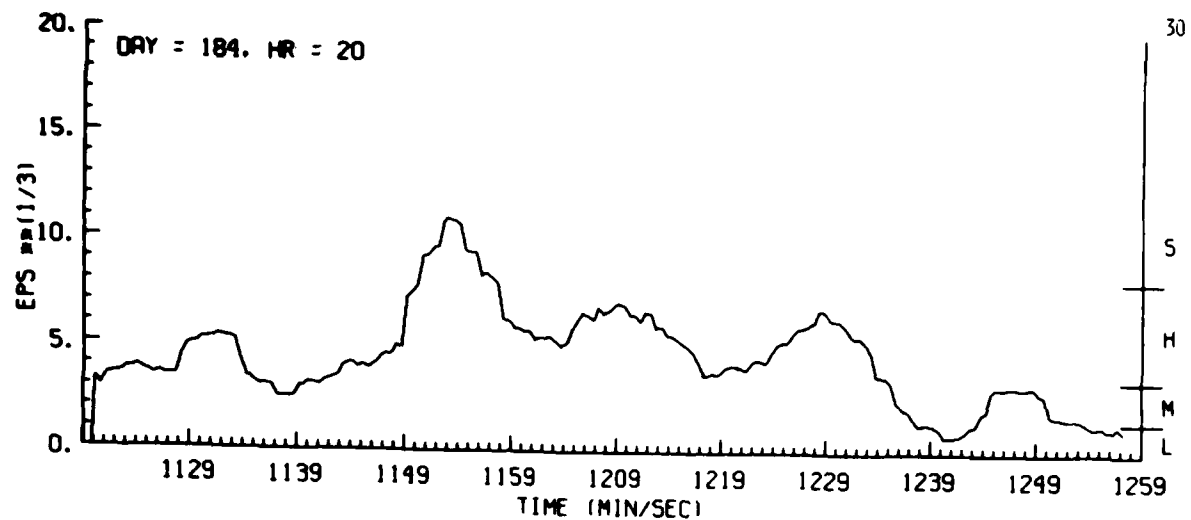


Figure G4. Estimates of Turbulence Severity Derived From Aircraft Gust Data
Day 184, Penetration 3

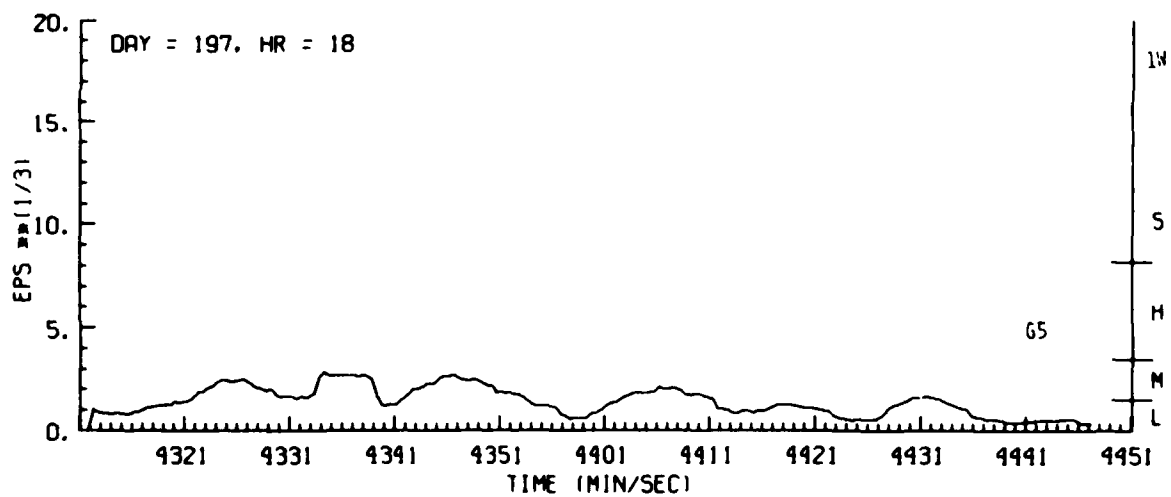
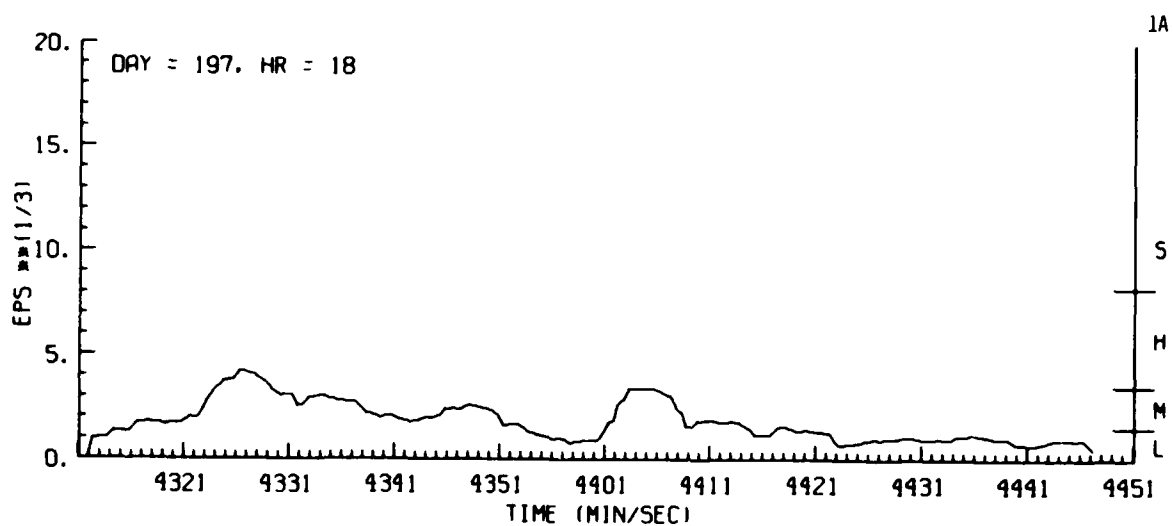
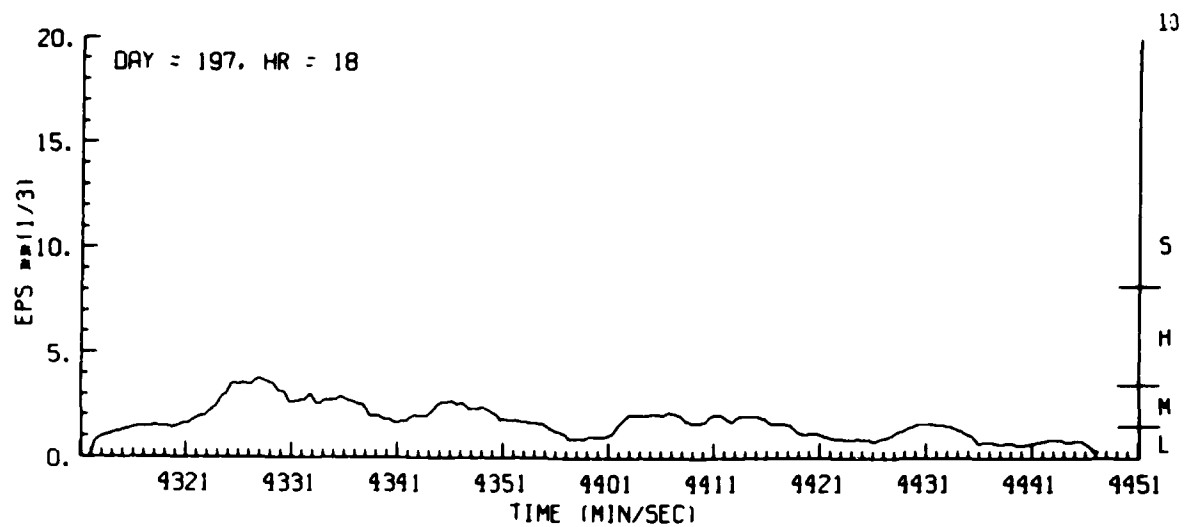


Figure G5. Estimates of Turbulence Severity Derived From Aircraft Gust Data, Day 197, Penetration 1

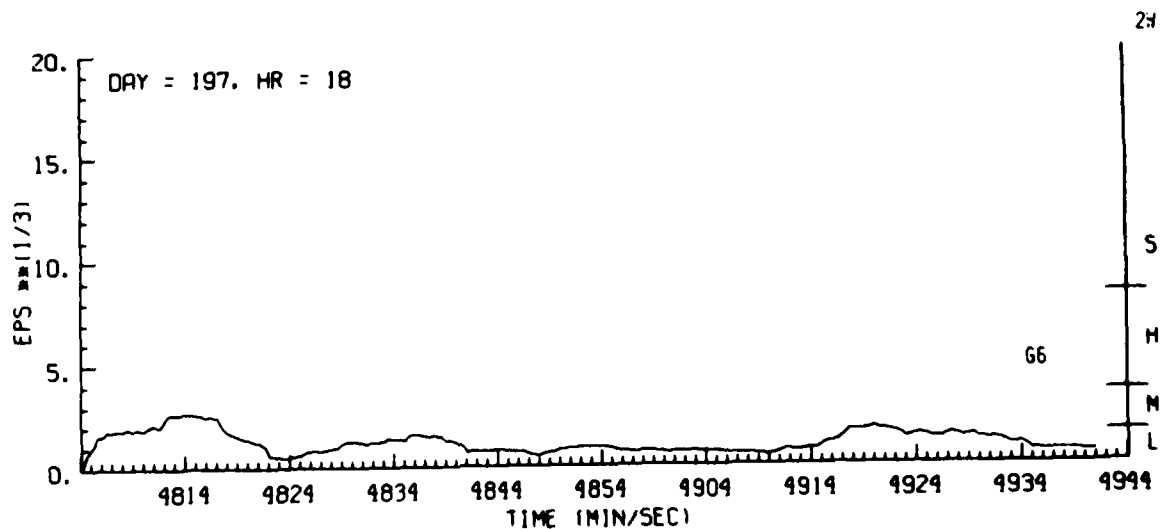
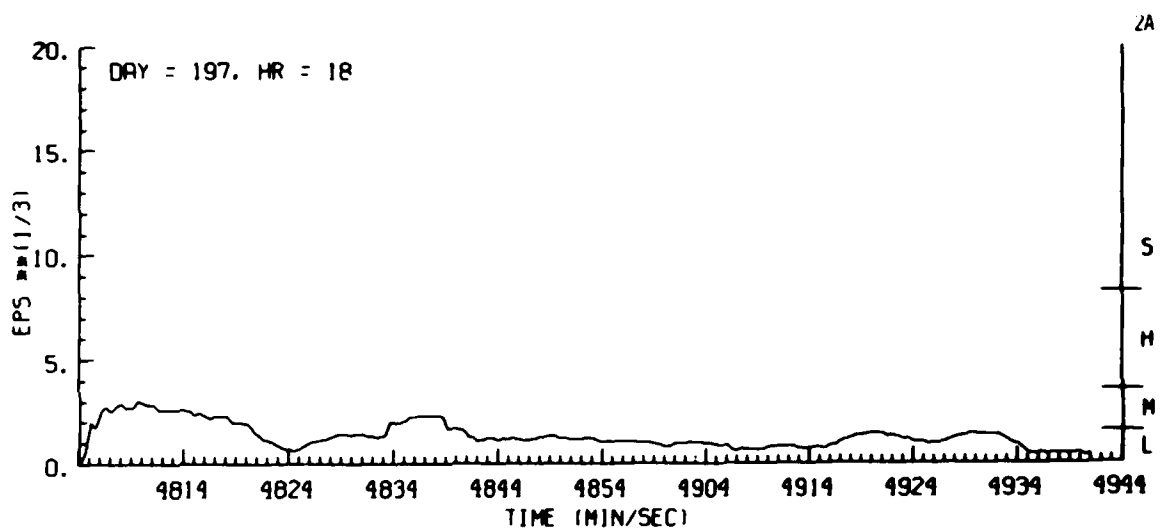
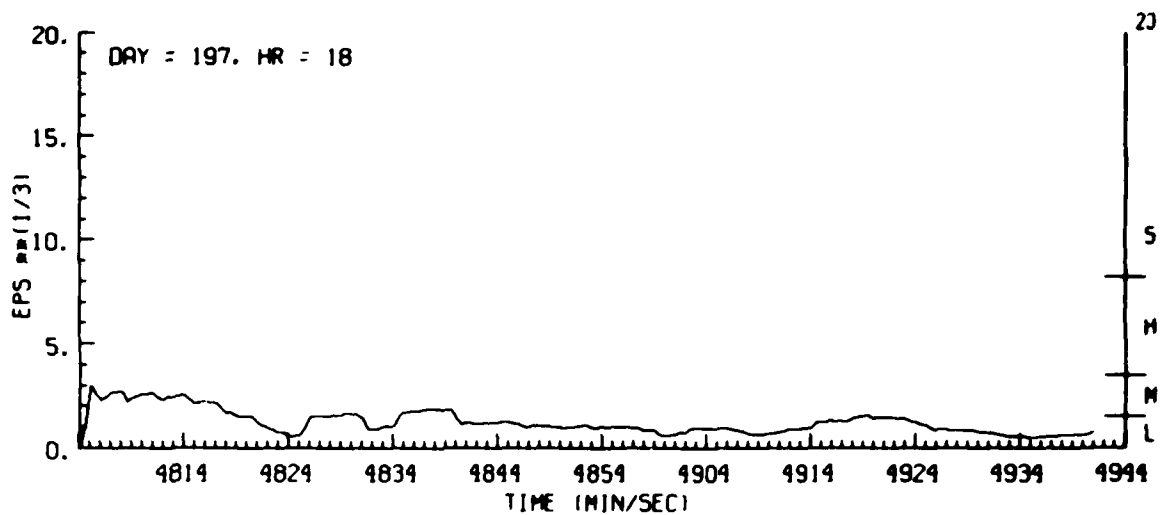


Figure G6. Estimates of Turbulence Severity Derived From Aircraft Gust Data, Day 197, Penetration 2

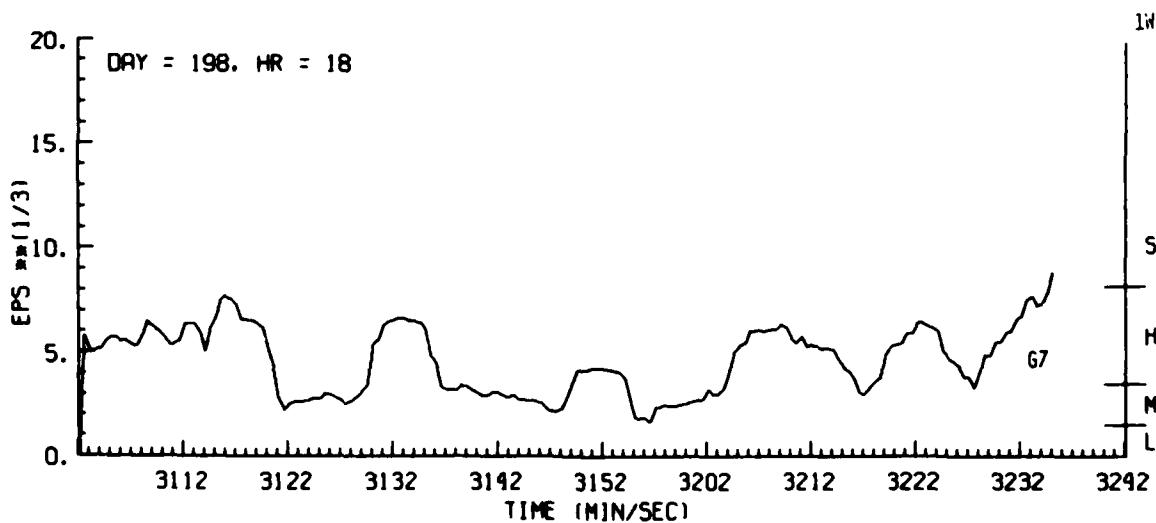
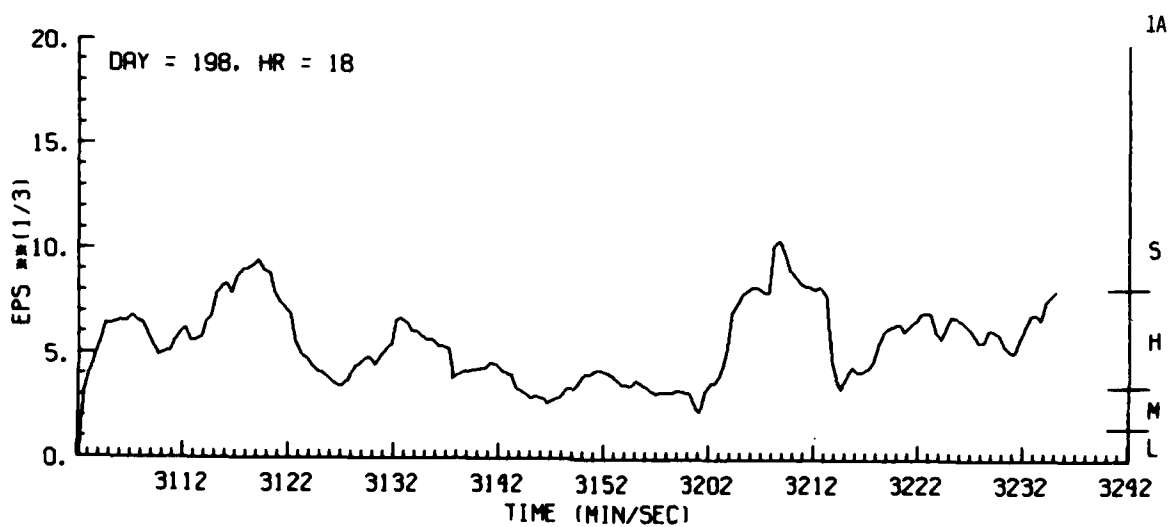
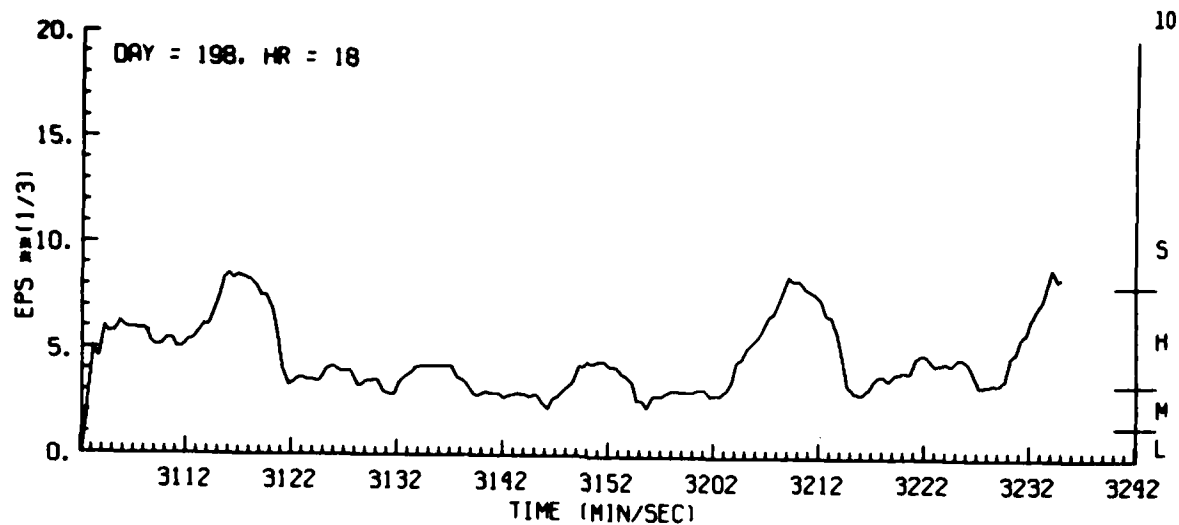


Figure G7. Estimates of Turbulence Severity Derived From Aircraft Gust Data, Day 198, Penetration 1

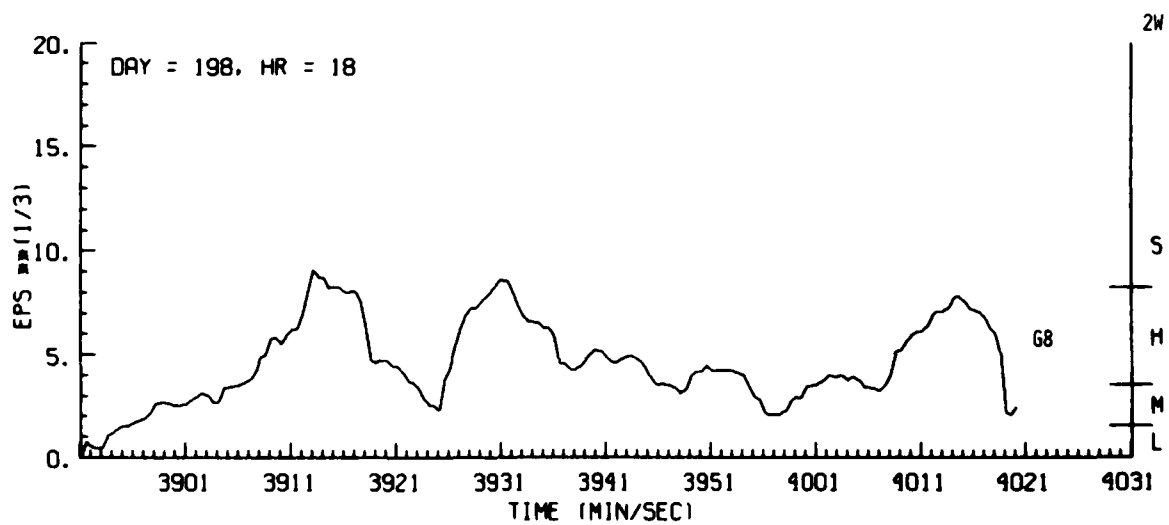
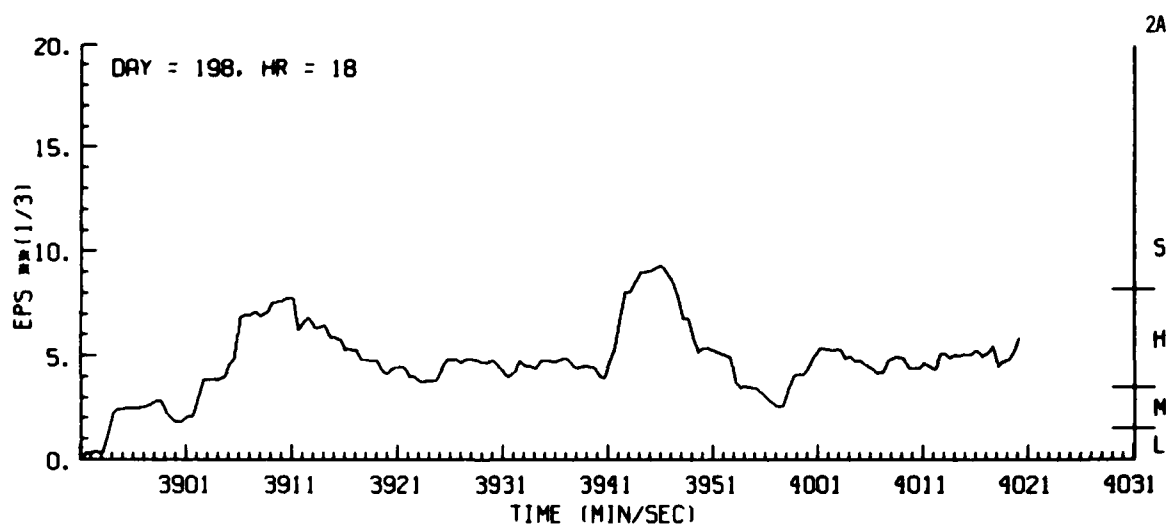
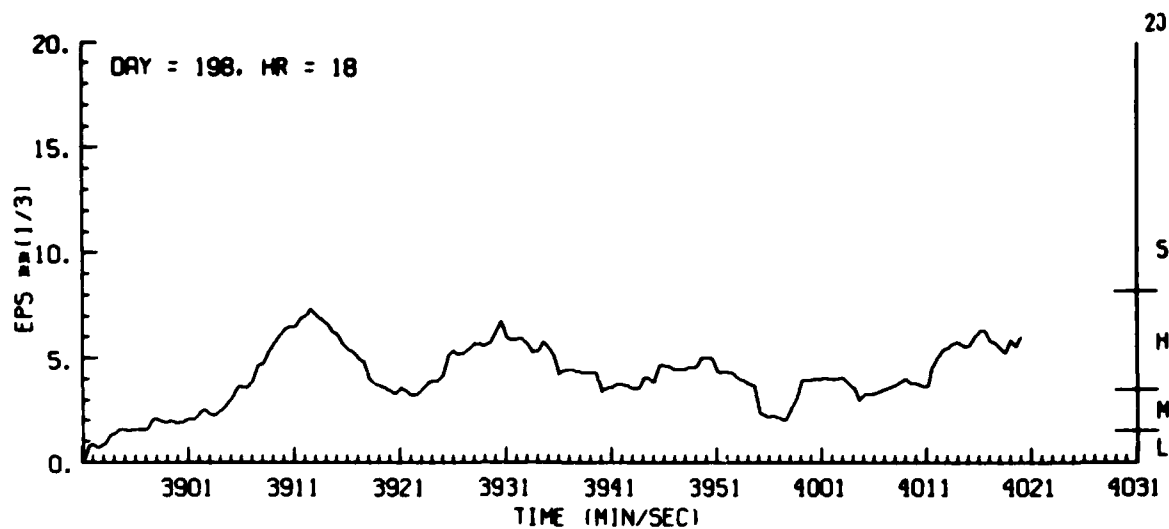


Figure G8. Estimates of Turbulence Severity Derived From Aircraft Gust Data, Day 198, Penetration 2

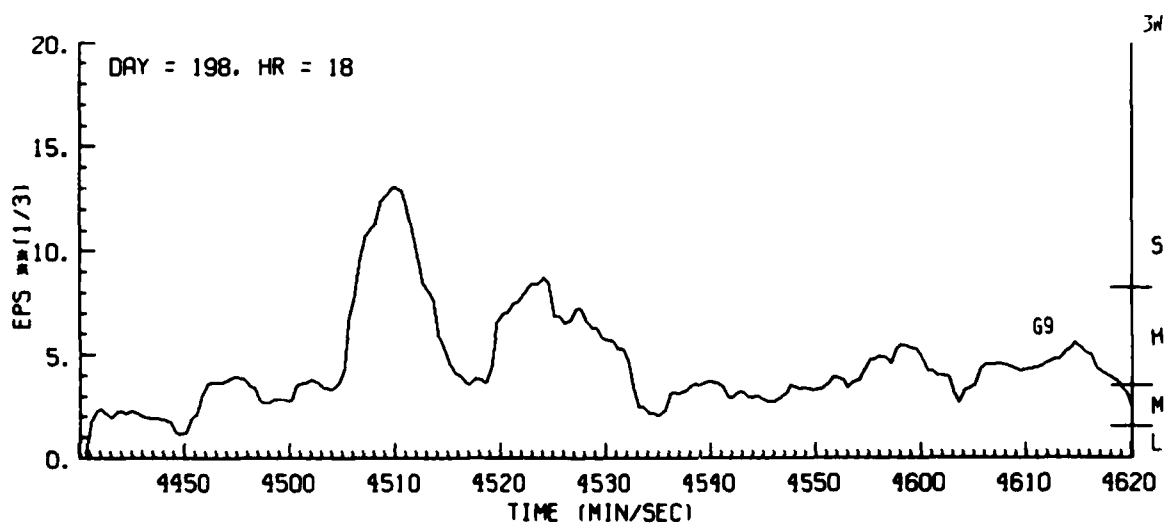
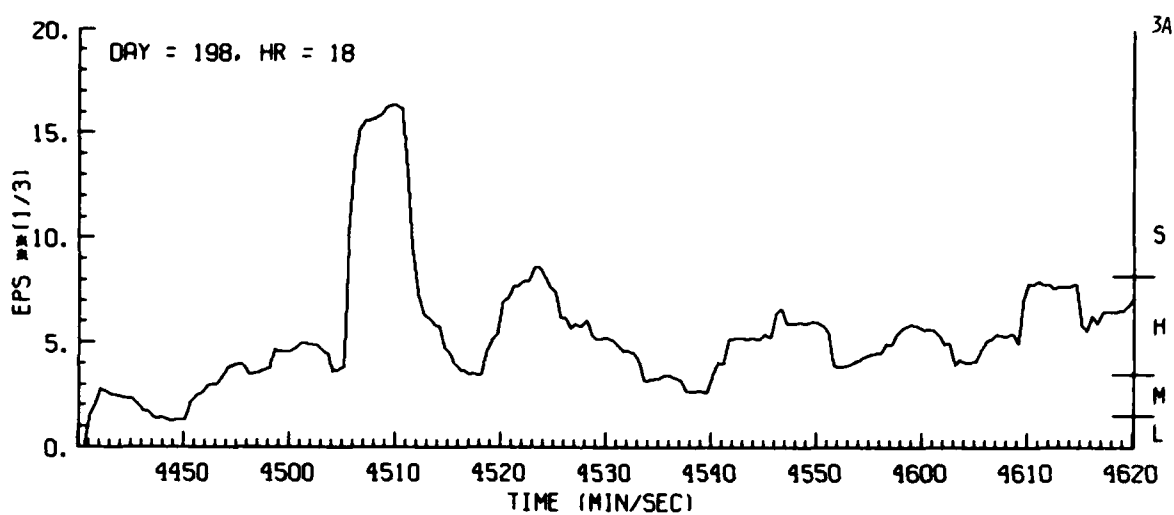
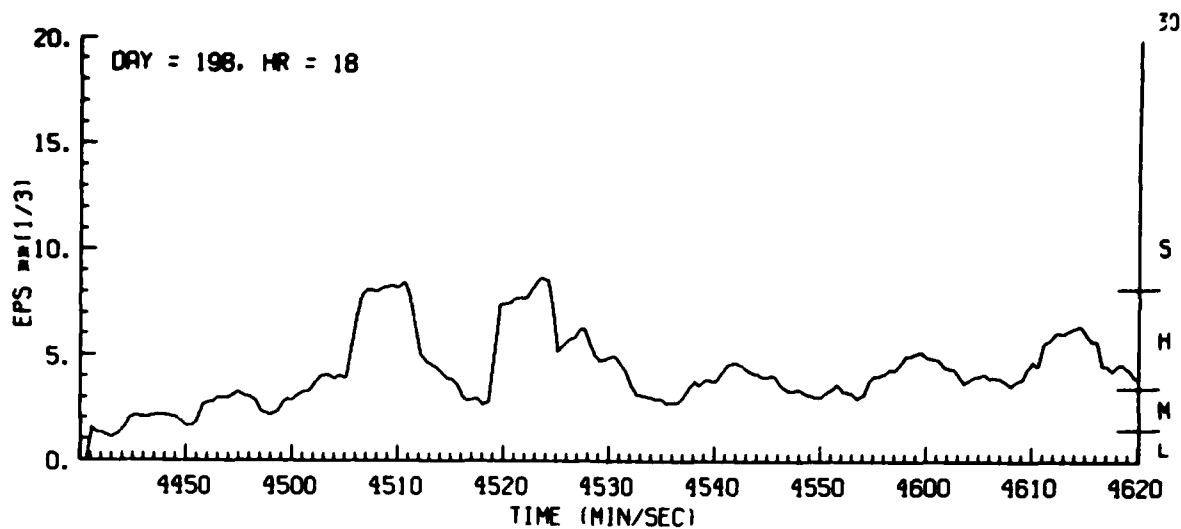


Figure G9. Estimates of Turbulence Severity Derived From Aircraft Gust Data, Day 198, Penetration 3

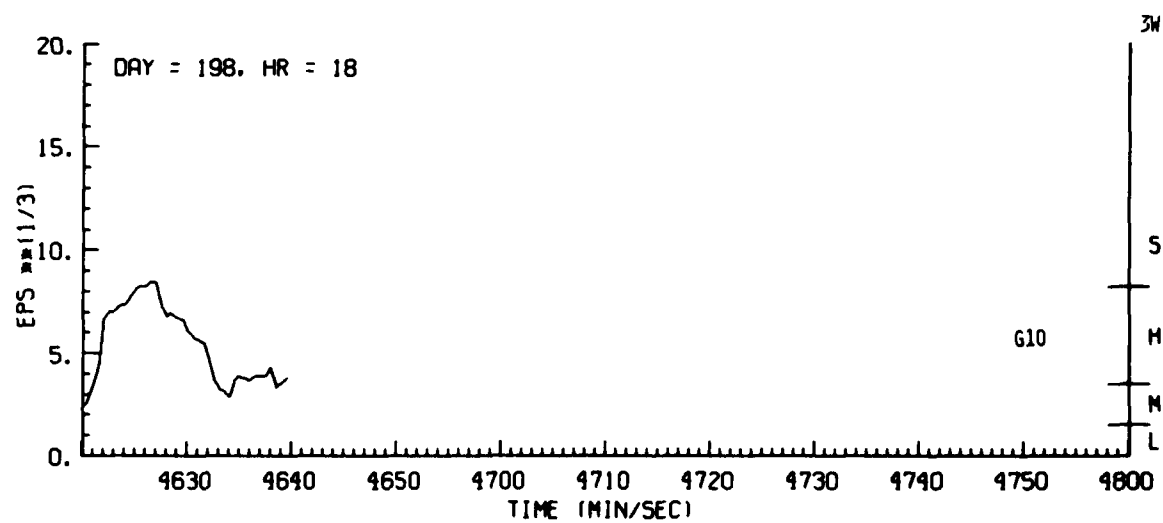
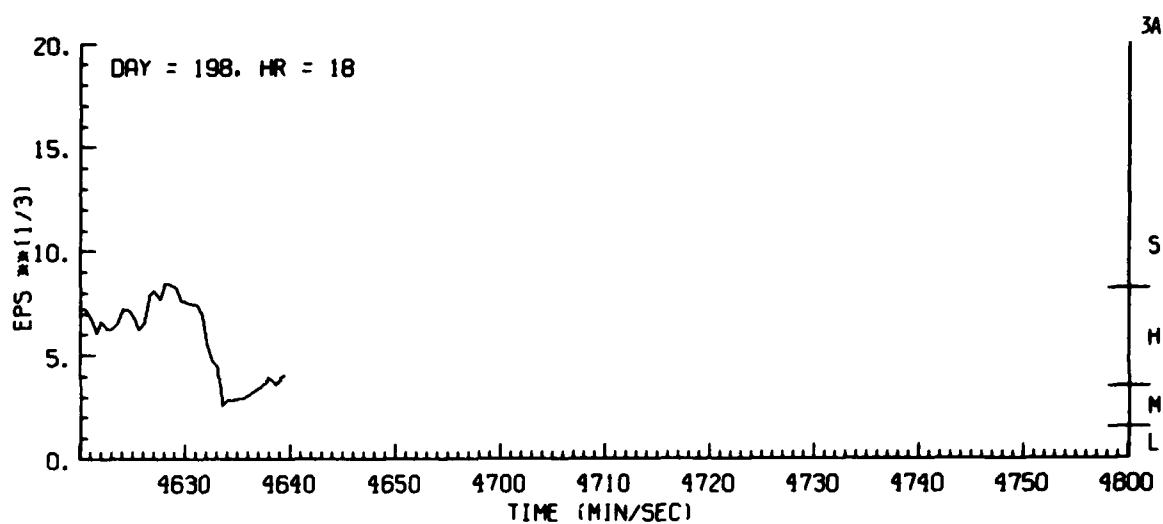
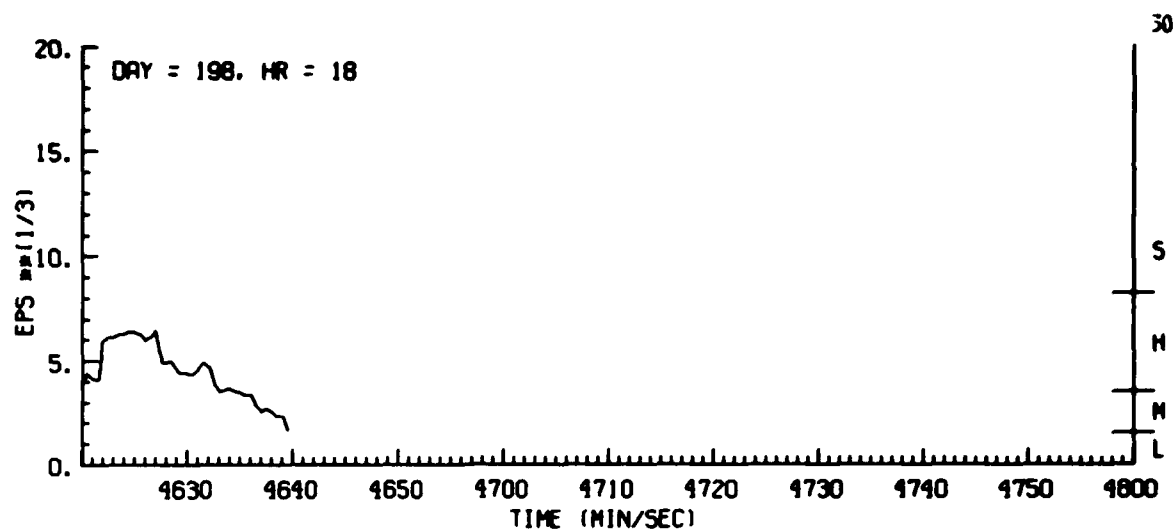


Figure G10. Estimates of Turbulence Severity Derived From Aircraft Gust Data, Day 198, Penetration 3

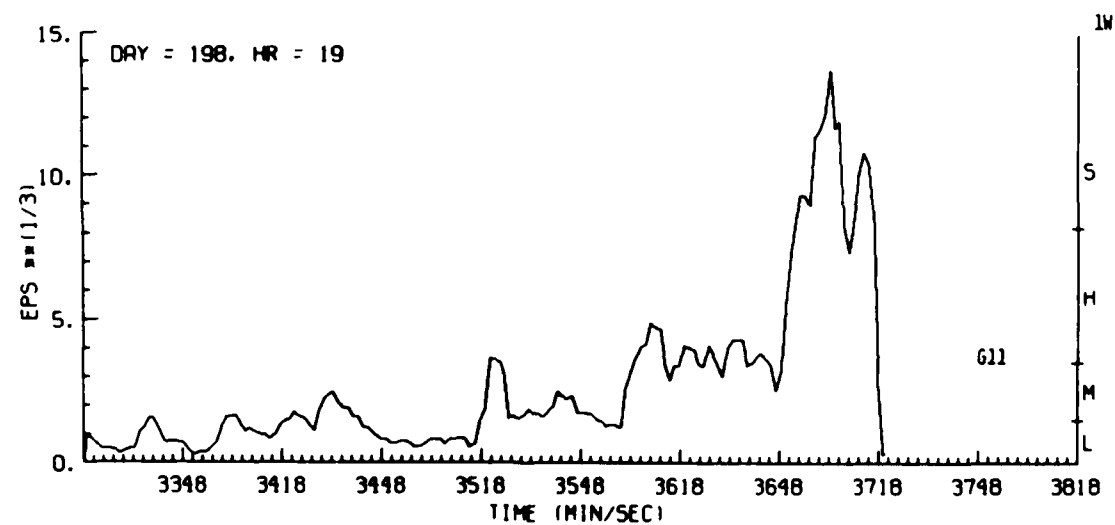
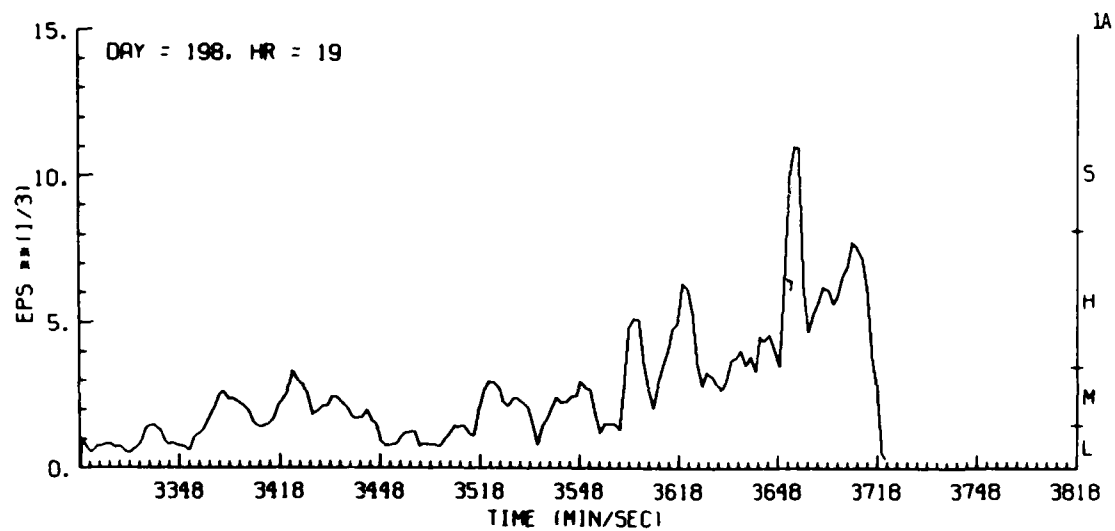
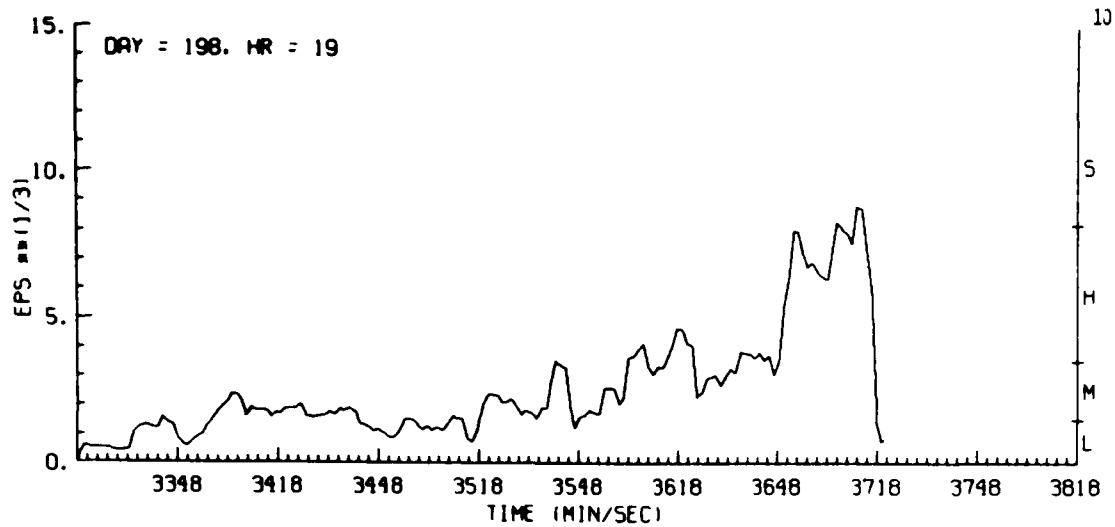


Figure G11. Estimates of Turbulence Severity Derived From Aircraft Gust Data, Day 198, Penetration 1

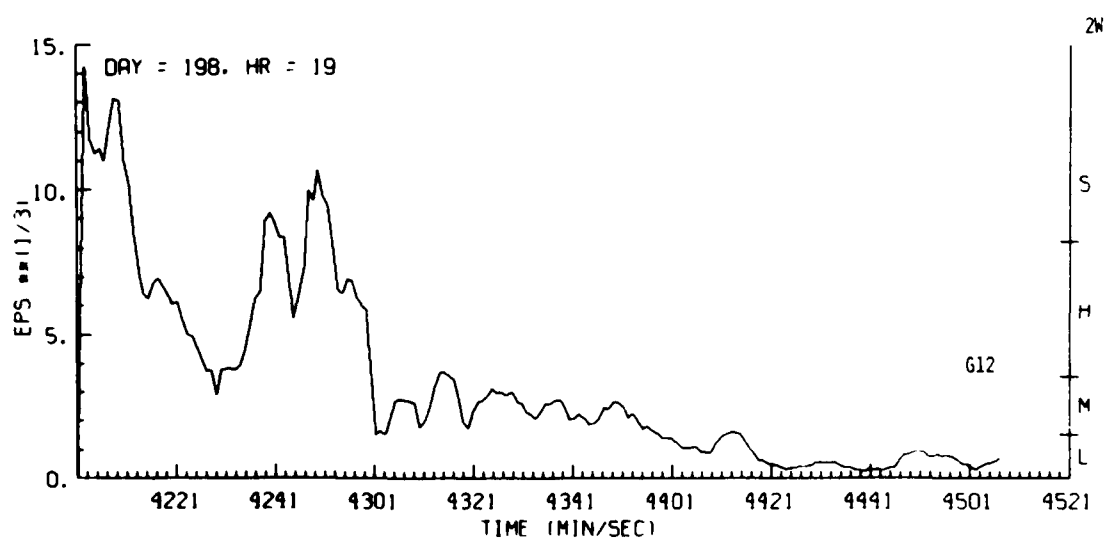
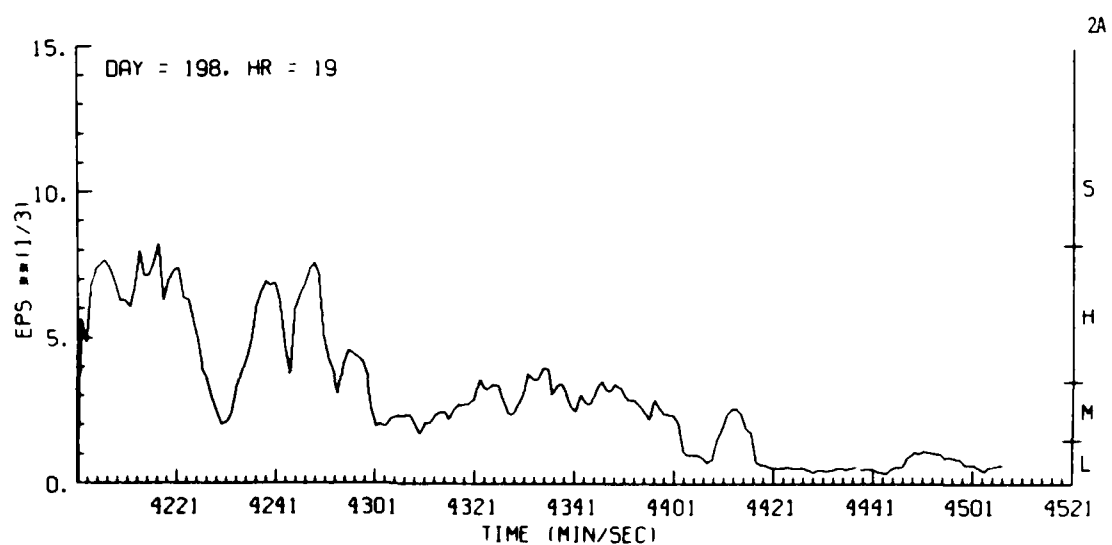
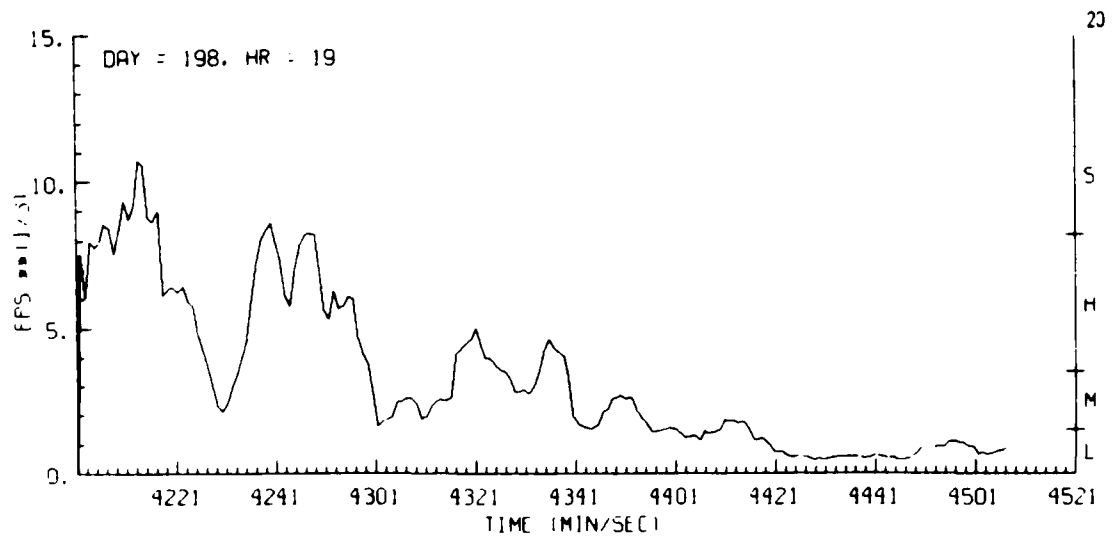


Figure G12. Estimates of Turbulence Severity Derived From Aircraft Gust Data, Day 198, Penetration 2

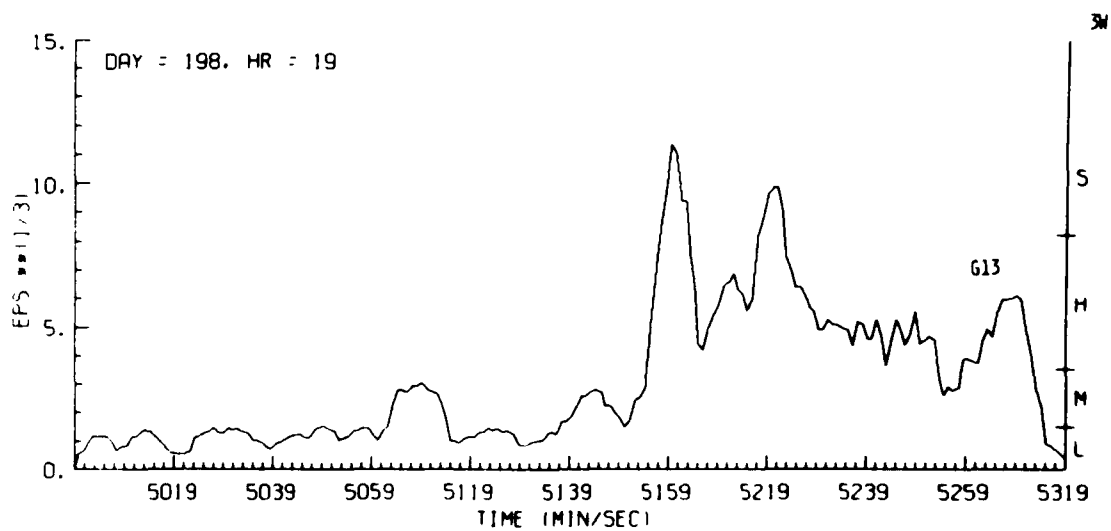
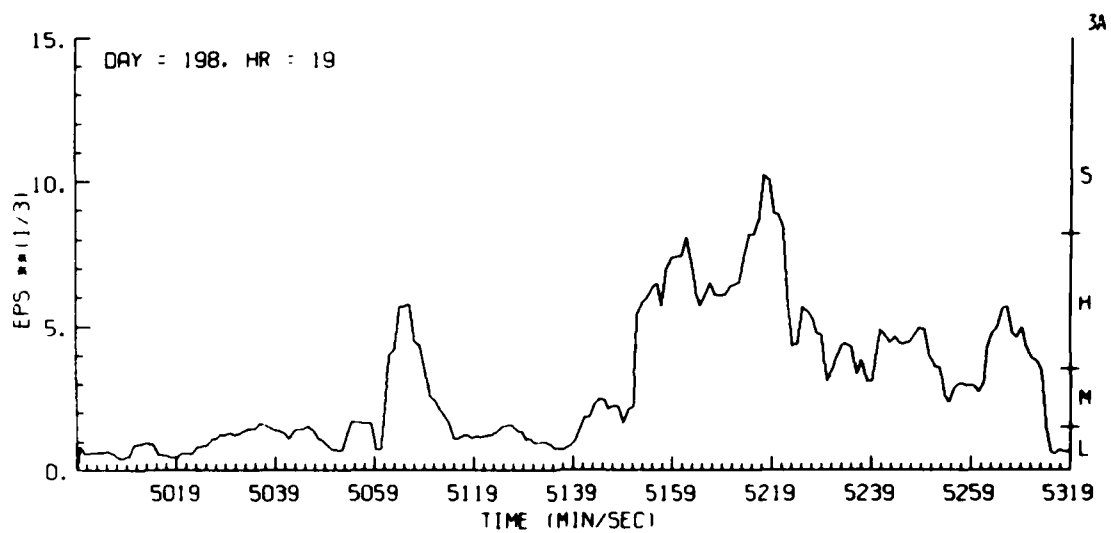
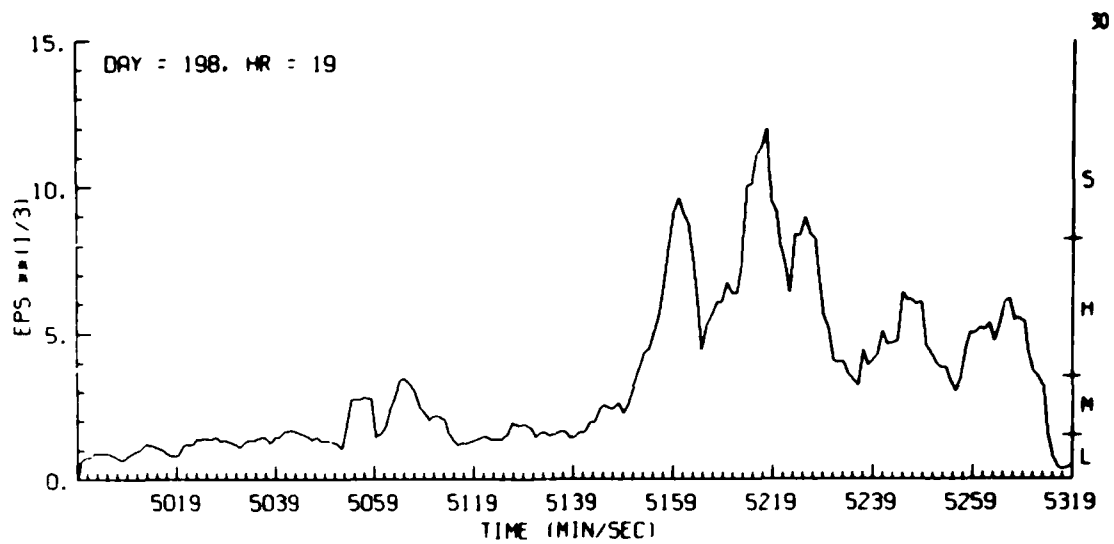


Figure G13. Estimates of Turbulence Severity Derived From Aircraft Gust Data, Day 198, Penetration 3

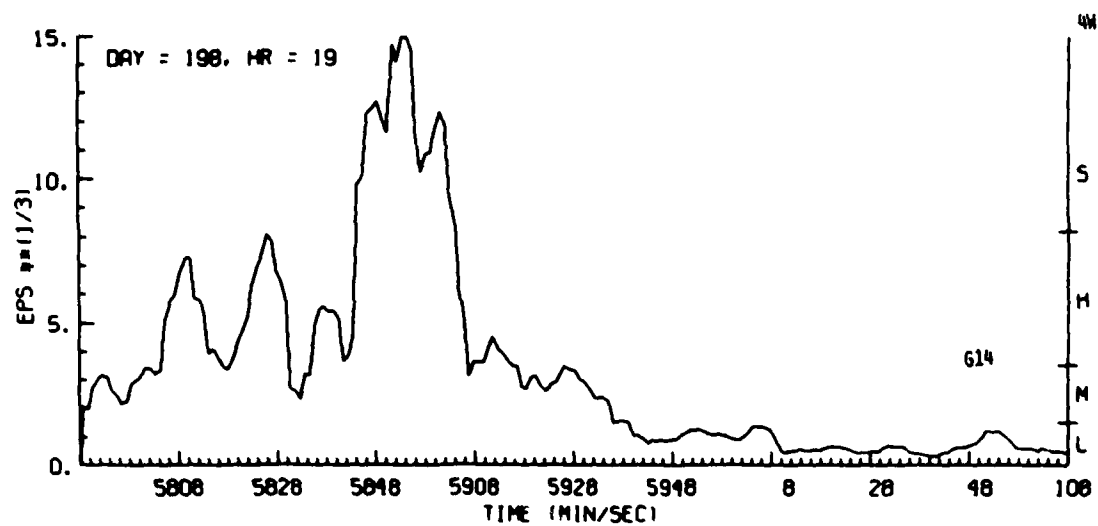
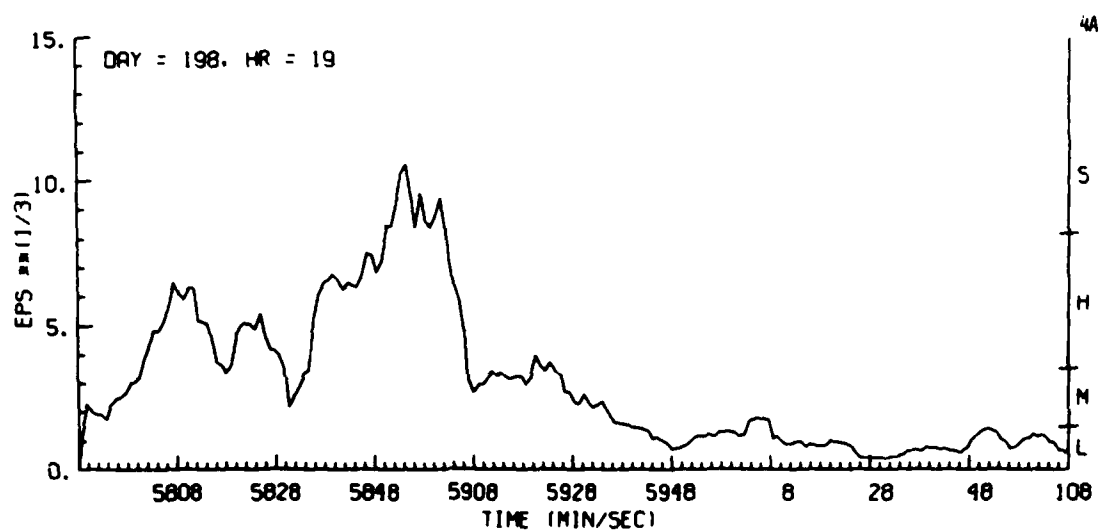
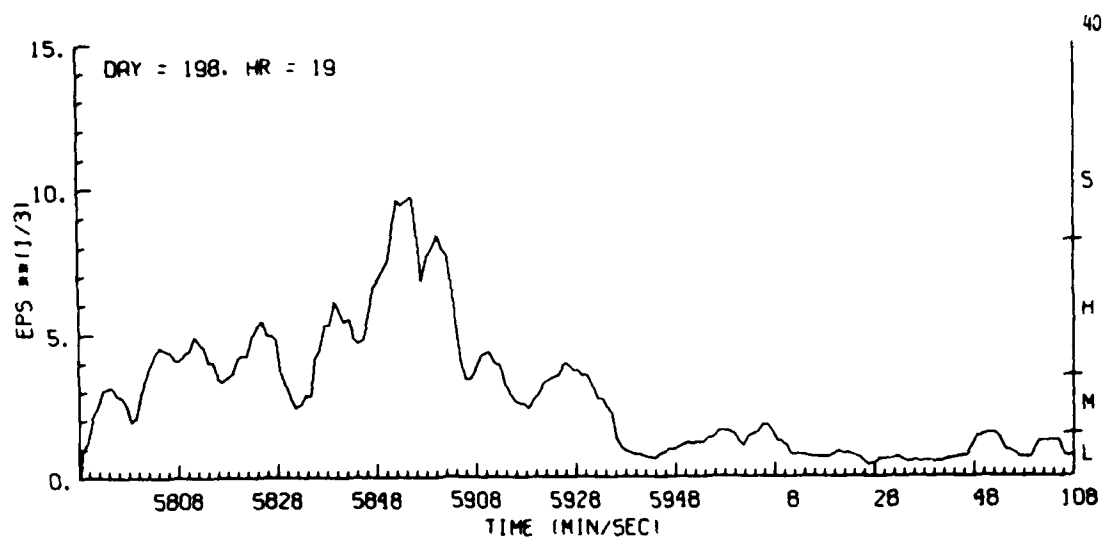


Figure G14. Estimates of Turbulence Severity Derived From Aircraft Gust Data, Day 198, Penetration 4

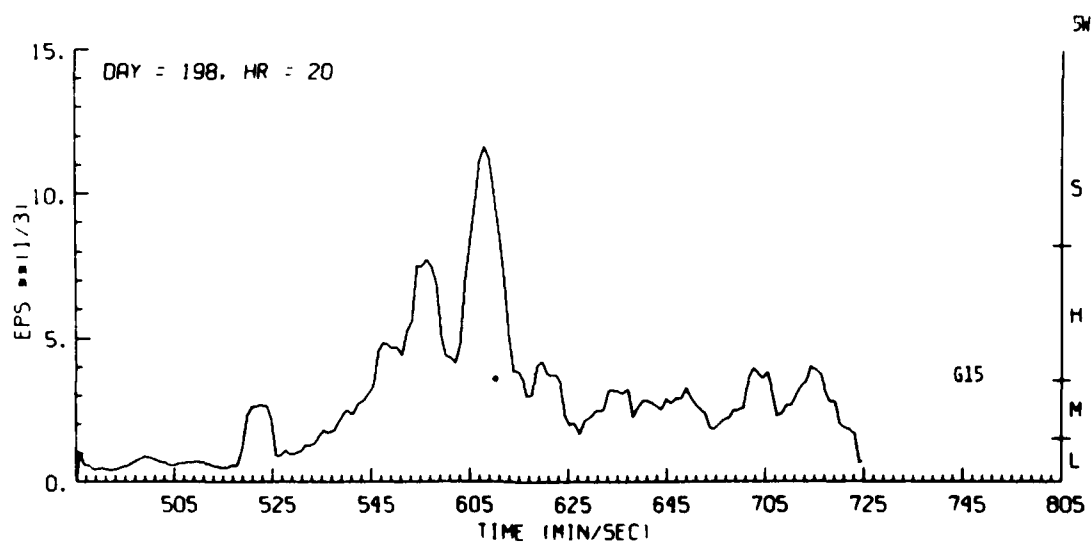
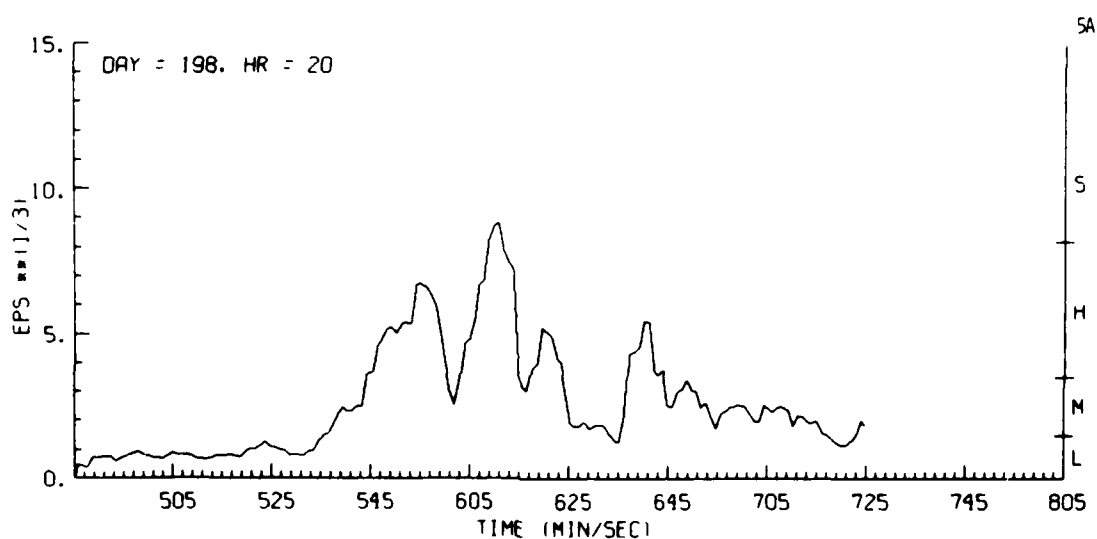
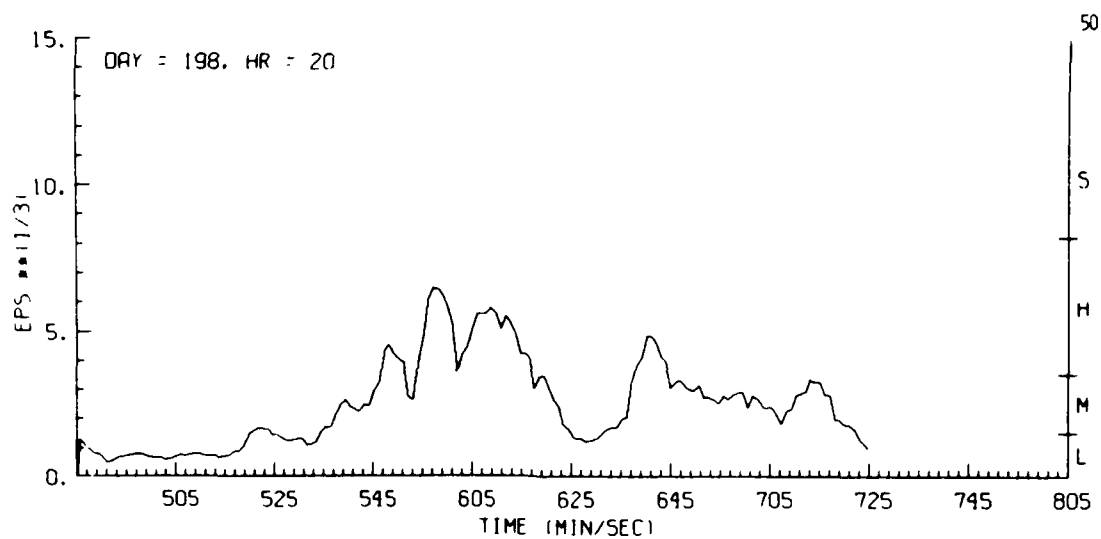


Figure G15. Estimates of Turbulence Severity Derived From Aircraft Gust Data, Day 198, Penetration 5

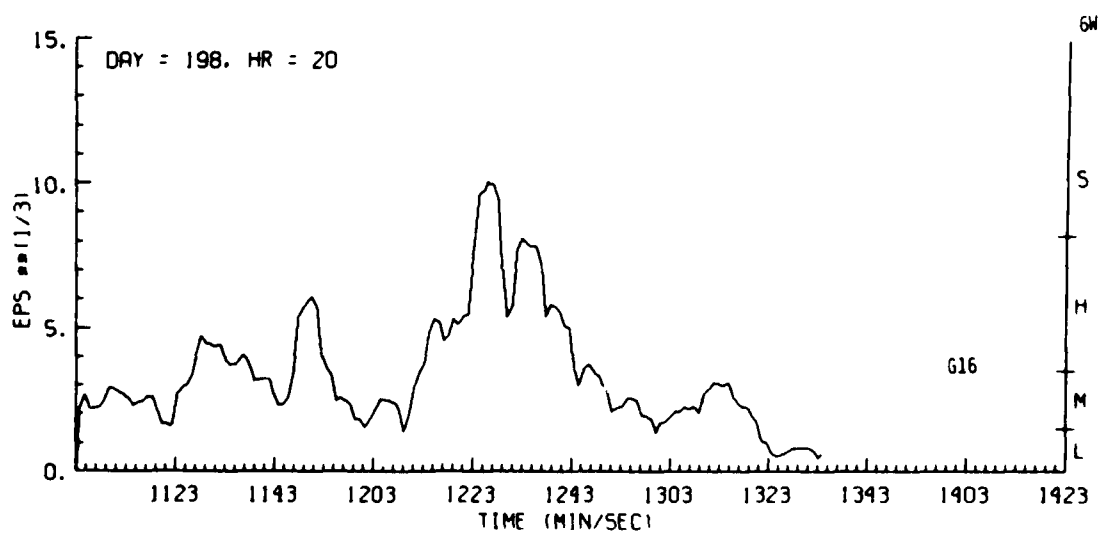
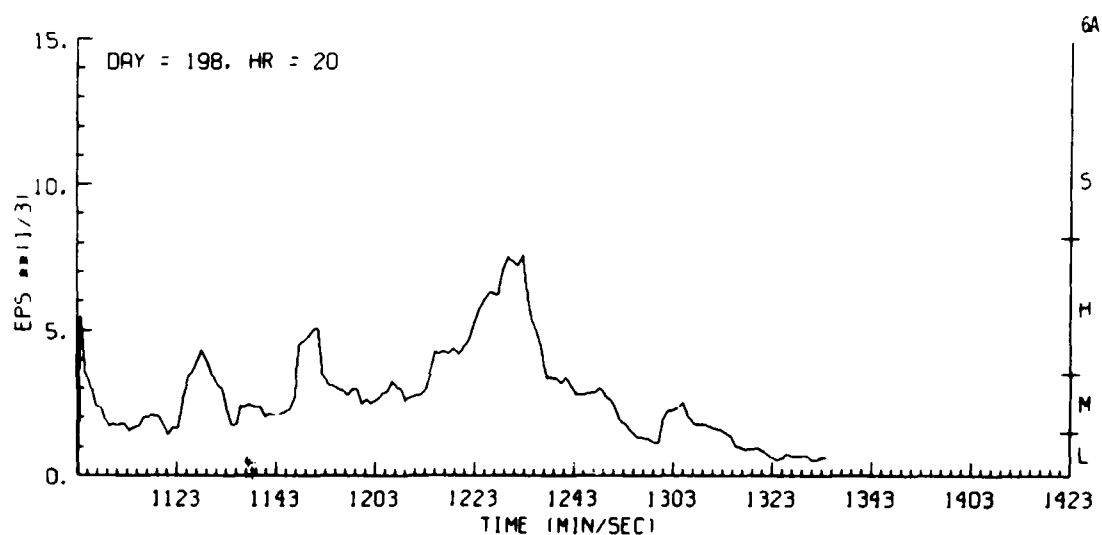
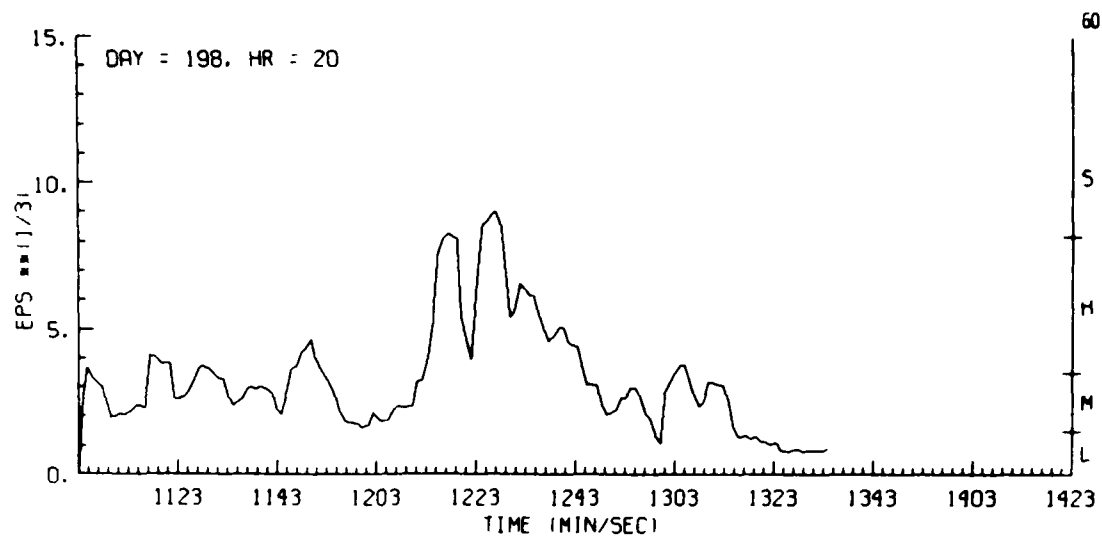


Figure G16. Estimates of Turbulence Severity Derived From Aircraft Gust Data, Day 198, Penetration 6

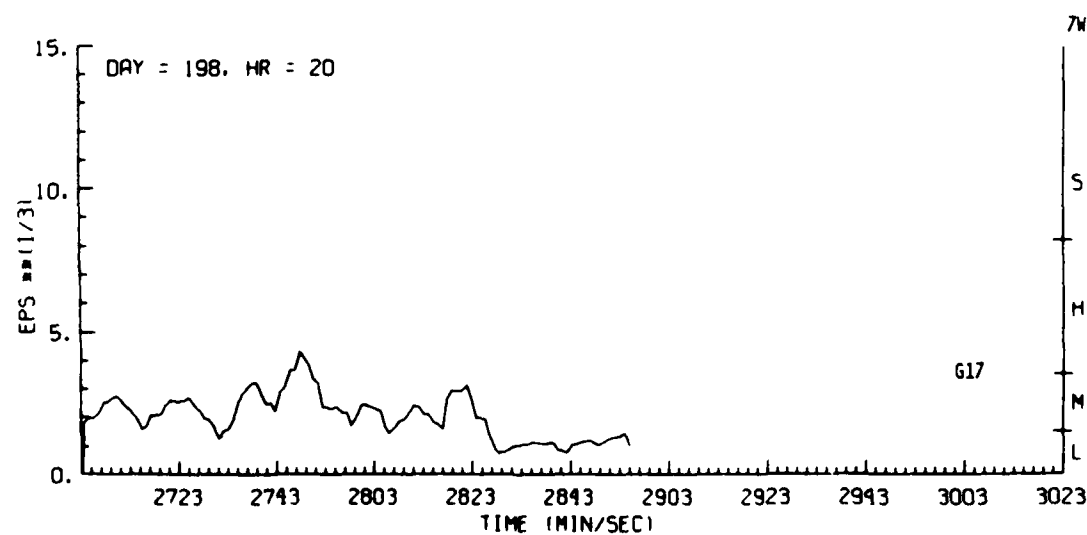
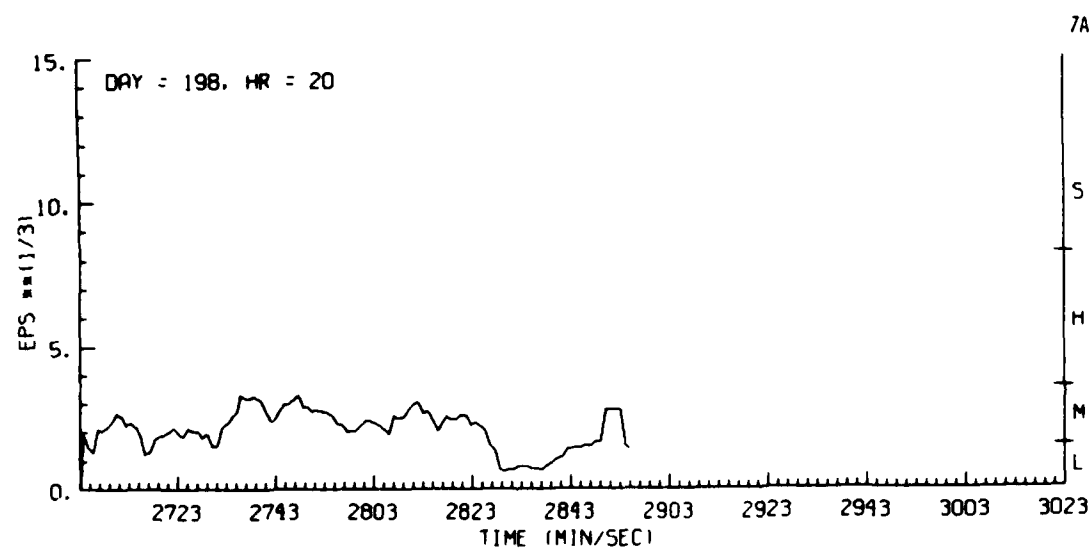
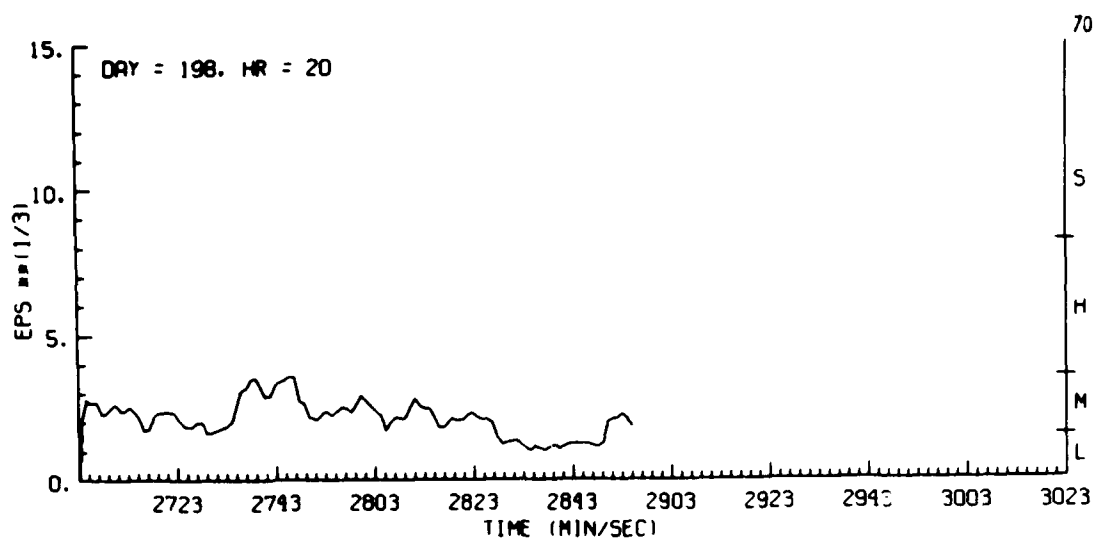


Figure G17. Estimates of Turbulence Severity Derived From Aircraft Gust Data, Day 198, Penetration 7

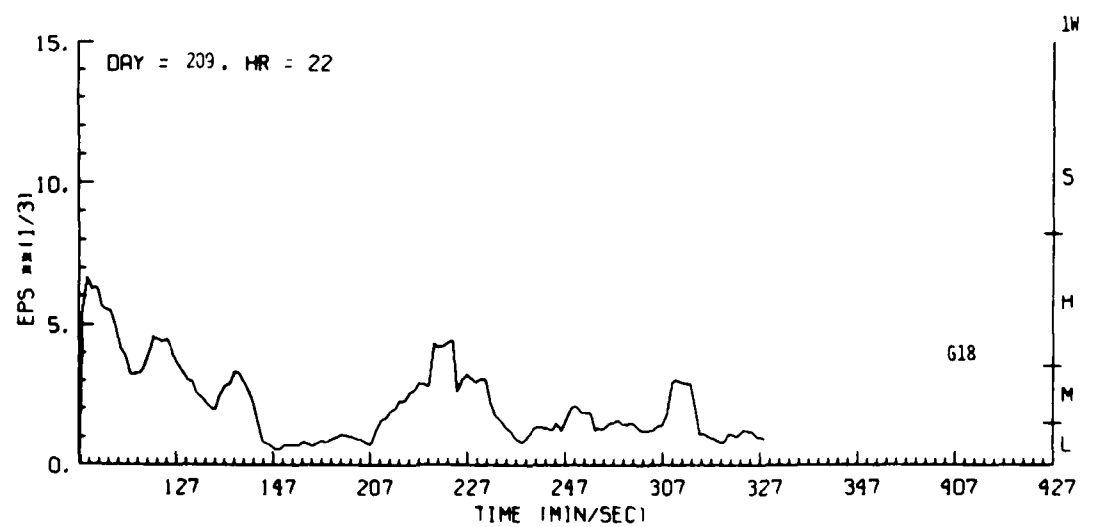
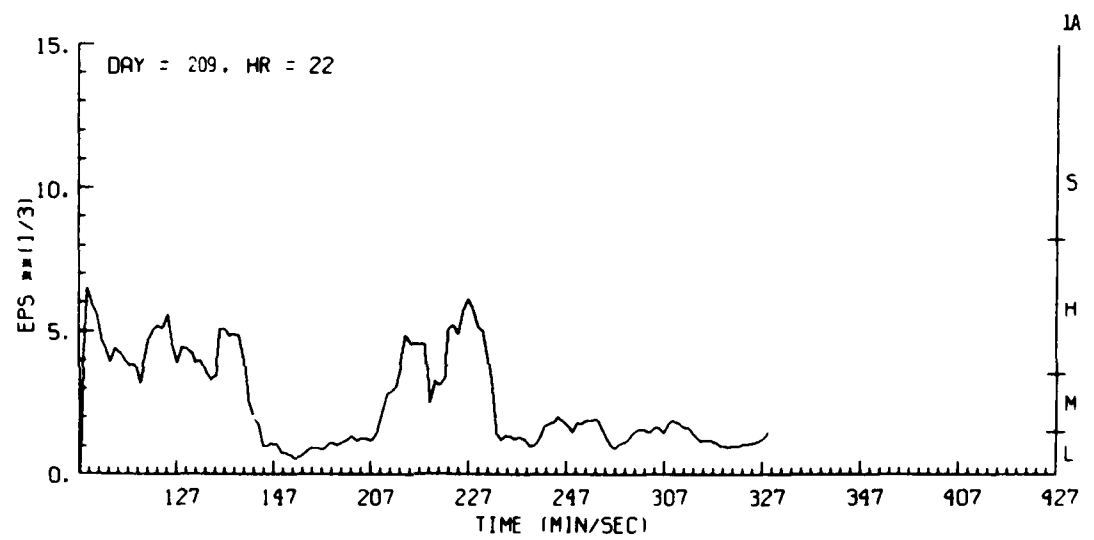
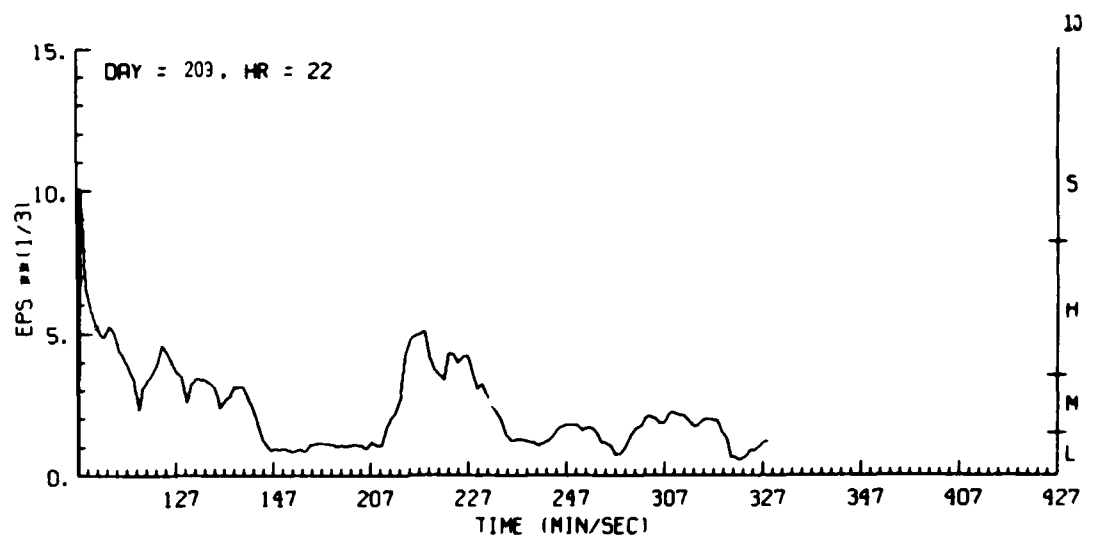


Figure G18. Estimates of Turbulence Severity Derived From Aircraft Gust Data, Day 209, Penetration 1

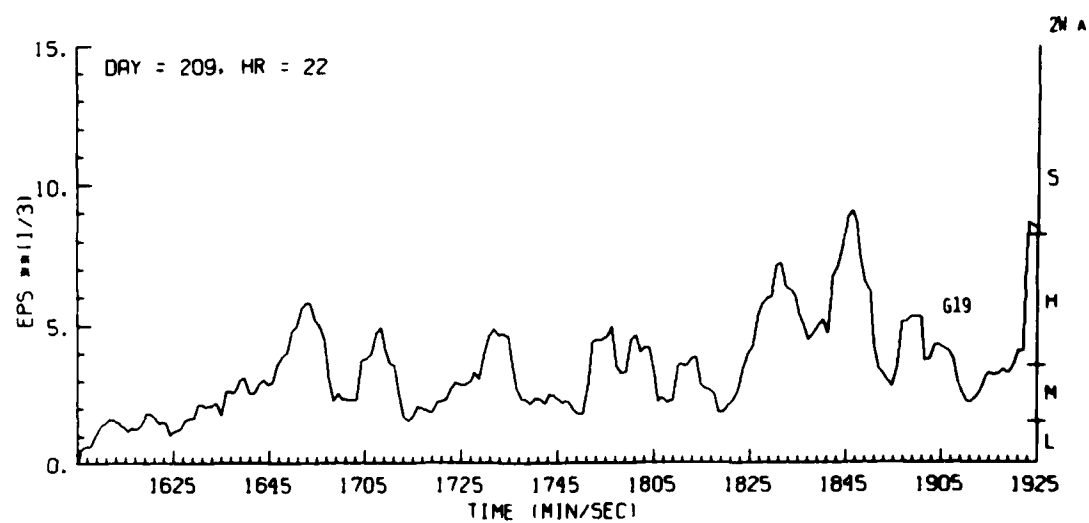
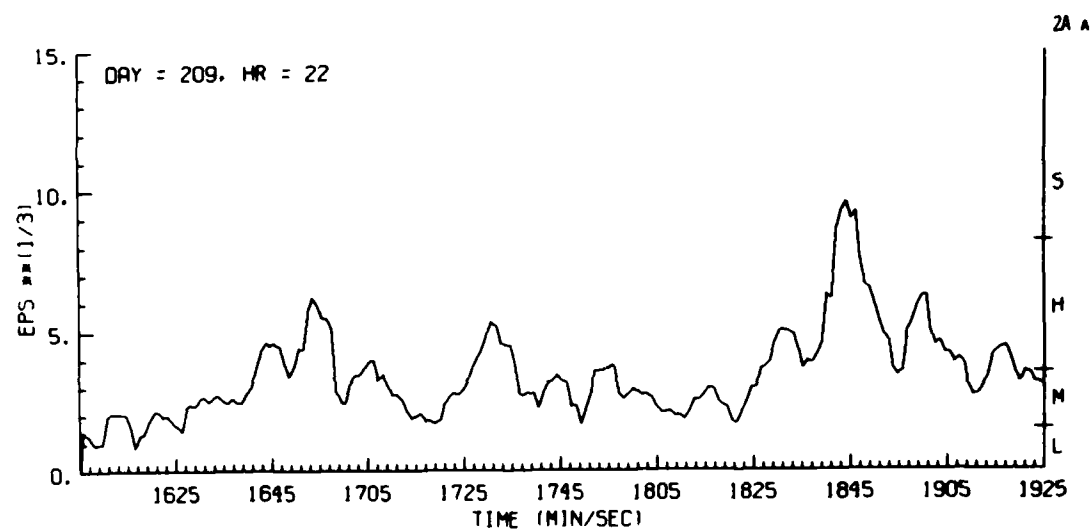
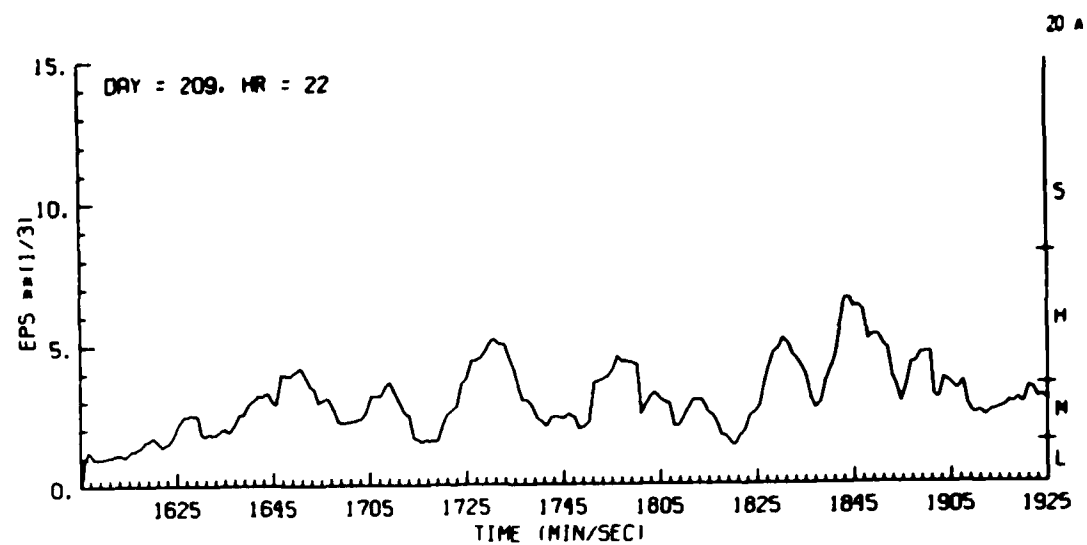


Figure G19. Estimates of Turbulence Severity Derived From Aircraft Gust Data, Day 209, Penetration 2A

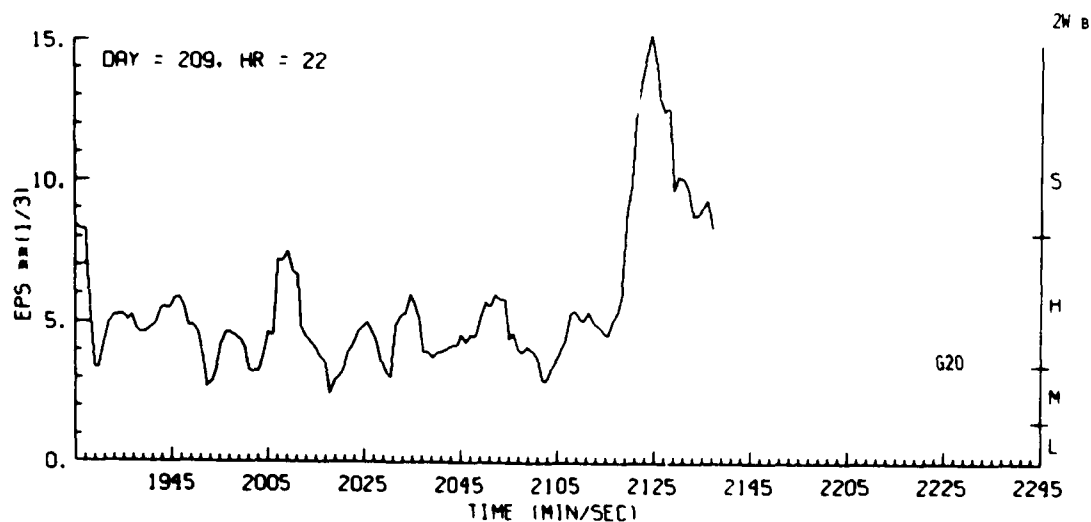
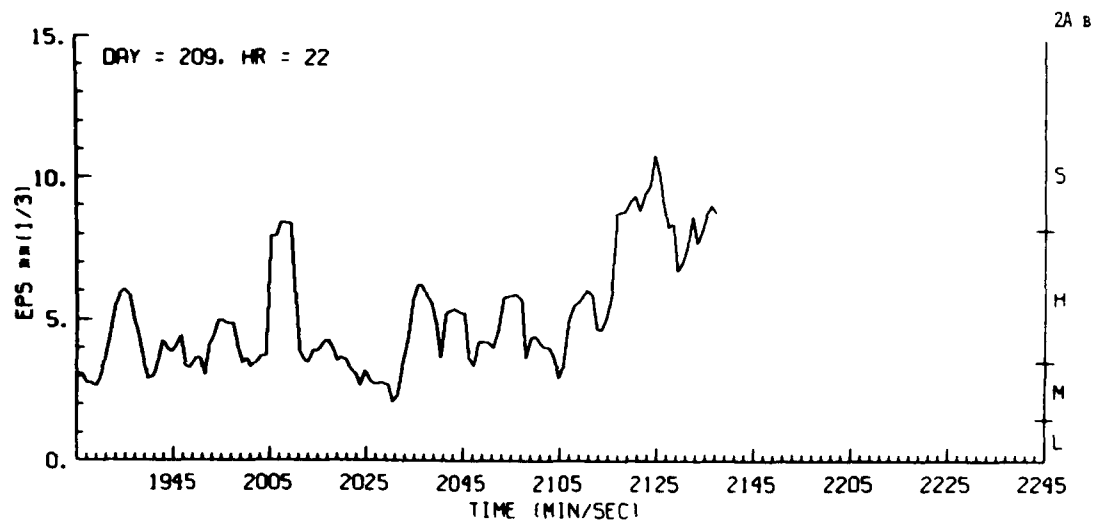
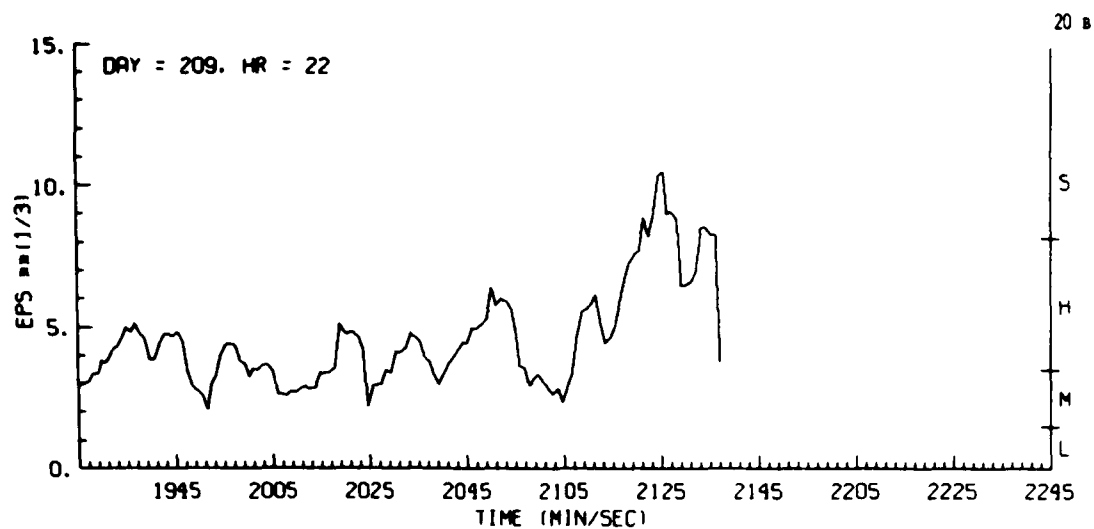


Figure G20. Estimates of Turbulence Severity Derived From Aircraft Gust Data, Day 209, Penetration 2B

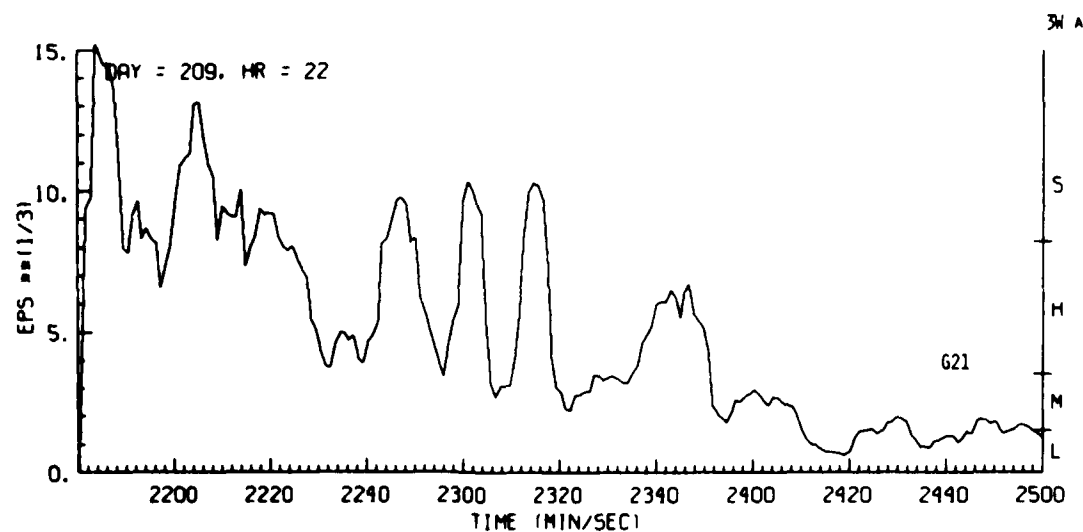
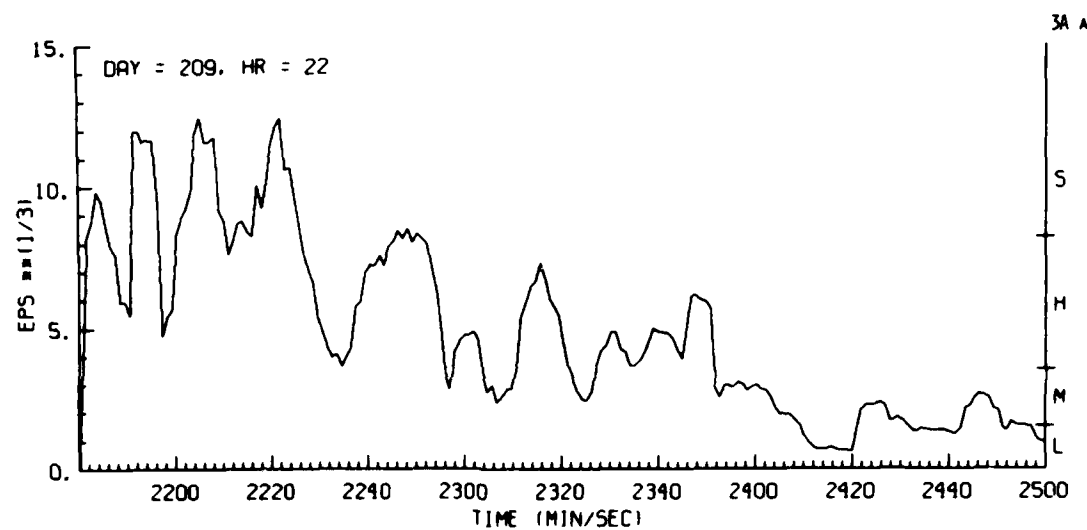
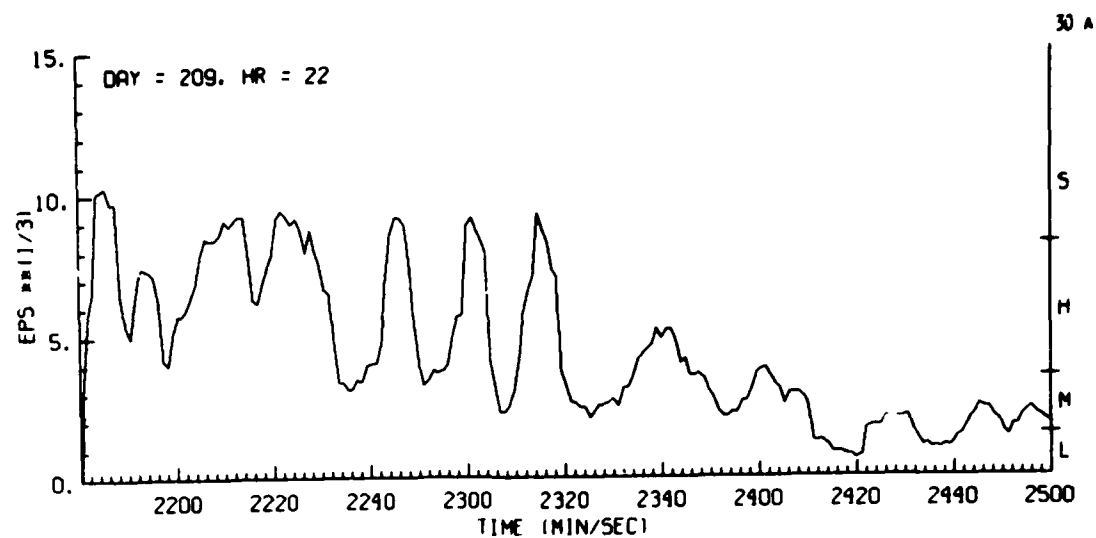


Figure G21. Estimates of Turbulence Severity Derived From Aircraft Gust Data, Day 209, Penetration 3A

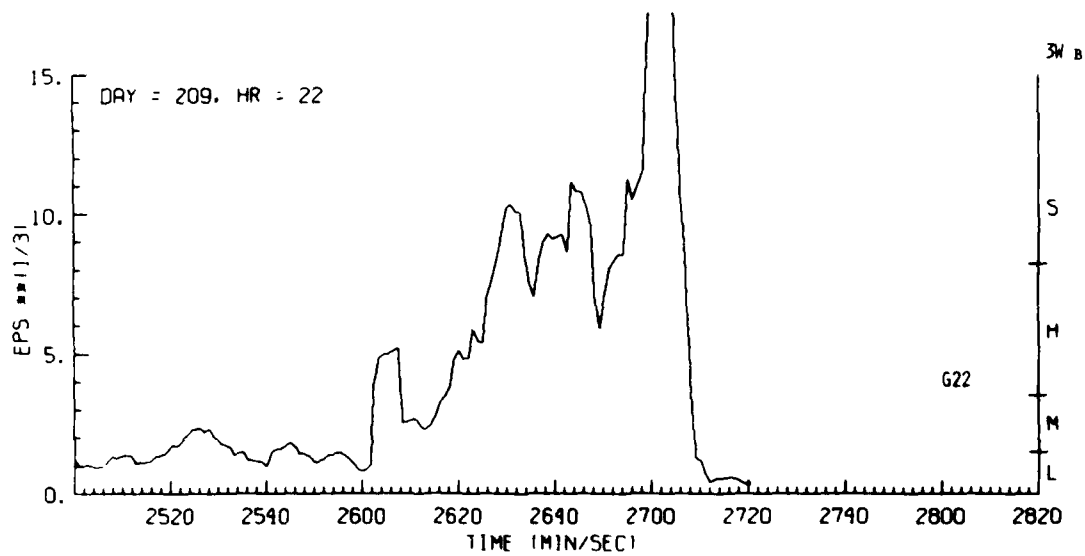
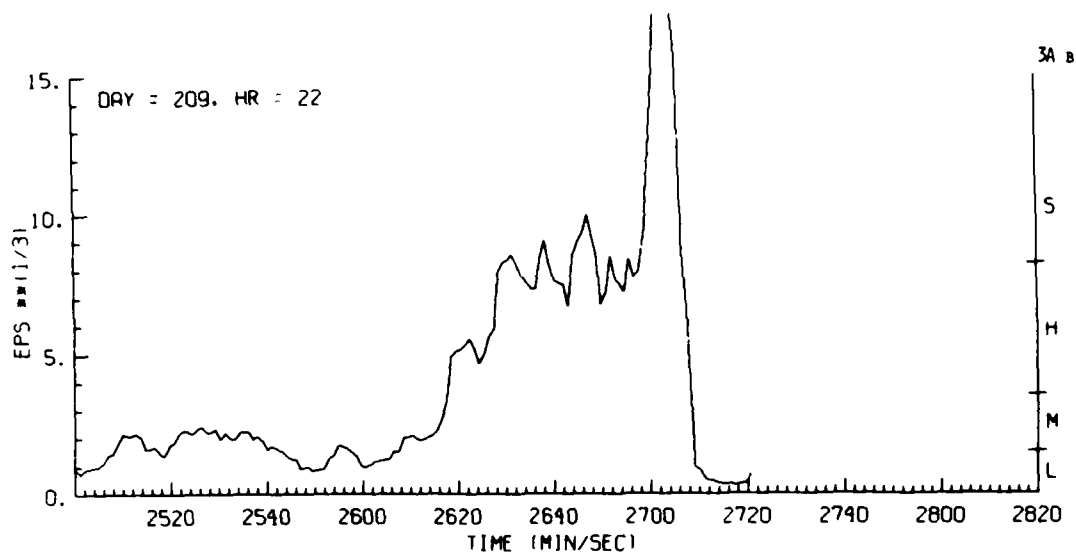
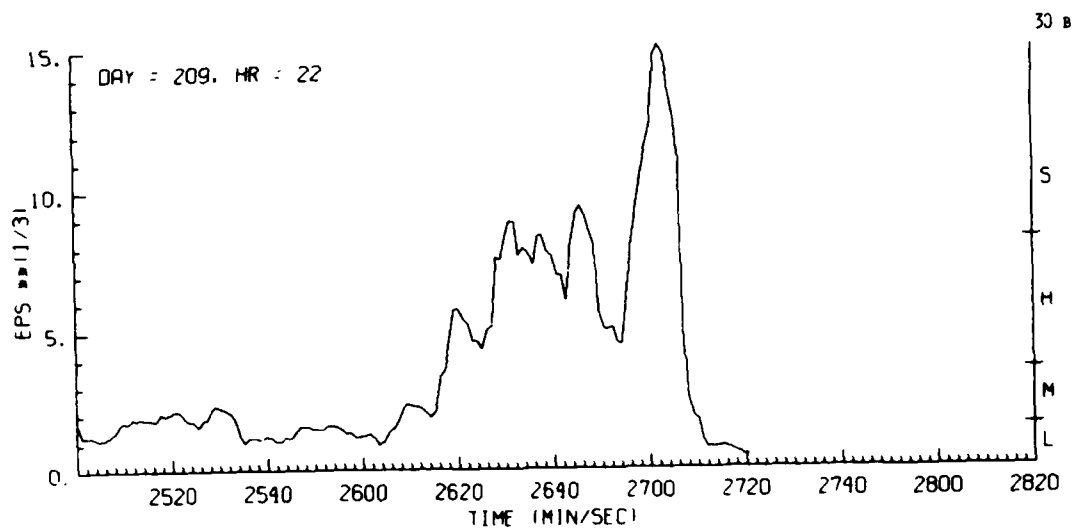


Figure G22. Estimates of Turbulence Severity Derived From Aircraft Gust Data, Day 209, Penetration 3B

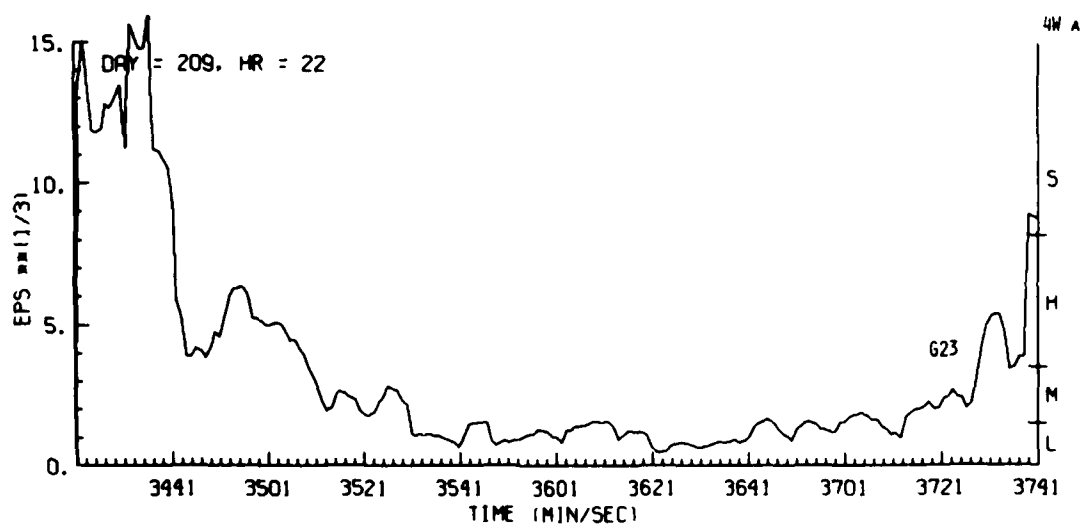
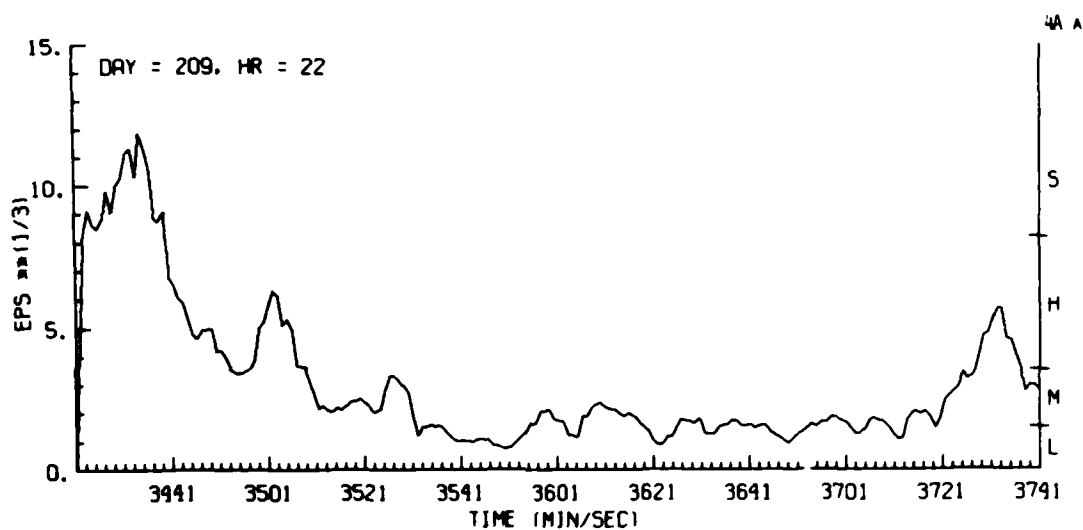
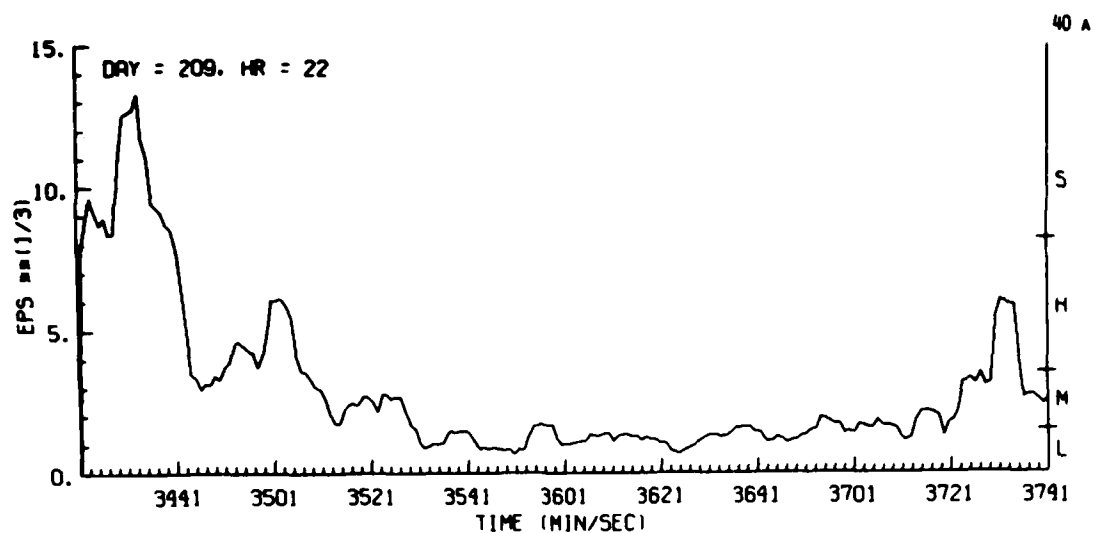


Figure G23. Estimates of Turbulence Severity Derived From Aircraft Gust Data, Day 209, Penetration 4A

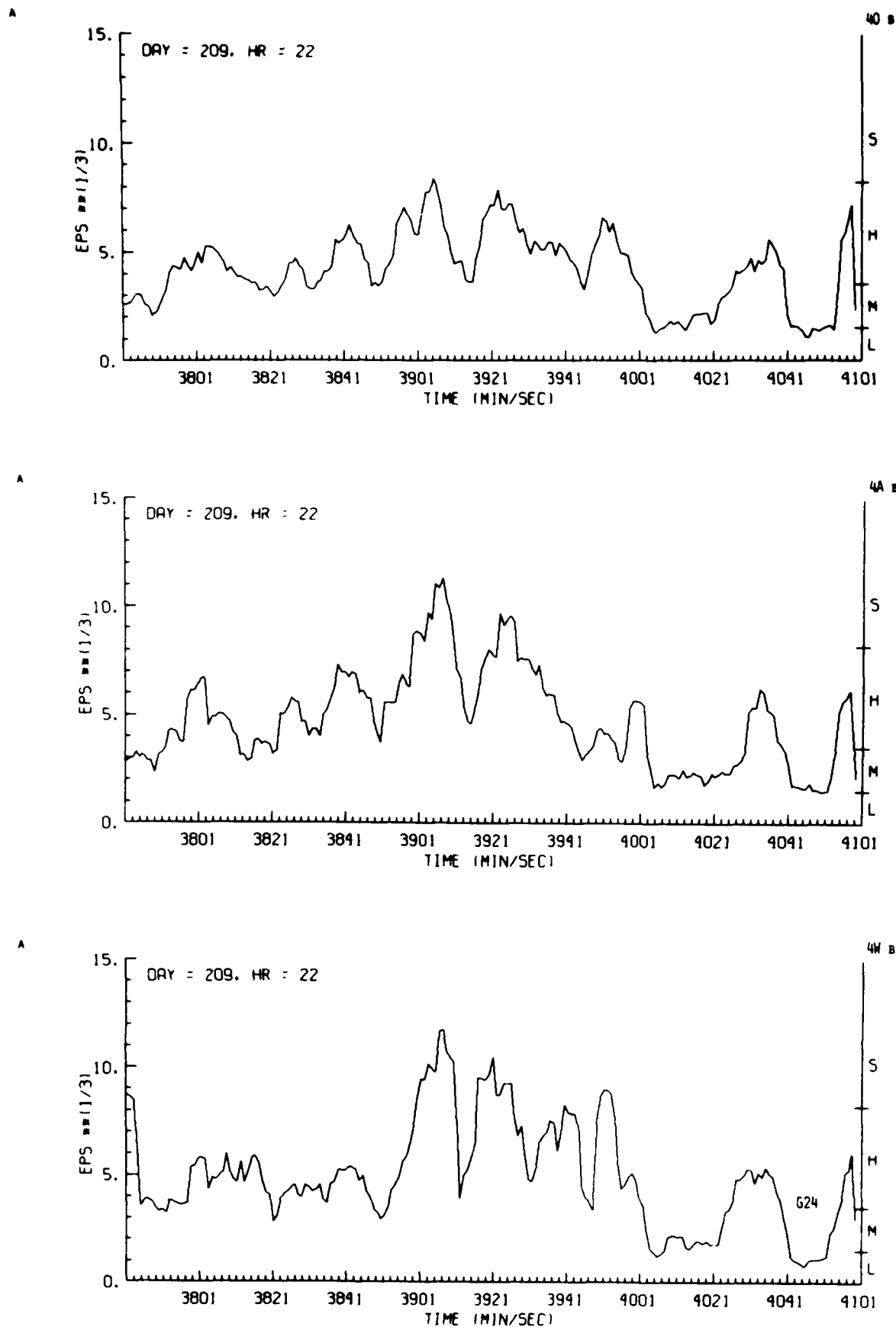


Figure G24. Estimates of Turbulence Severity Derived From Aircraft Gust Data, Day 209, Penetration 4B

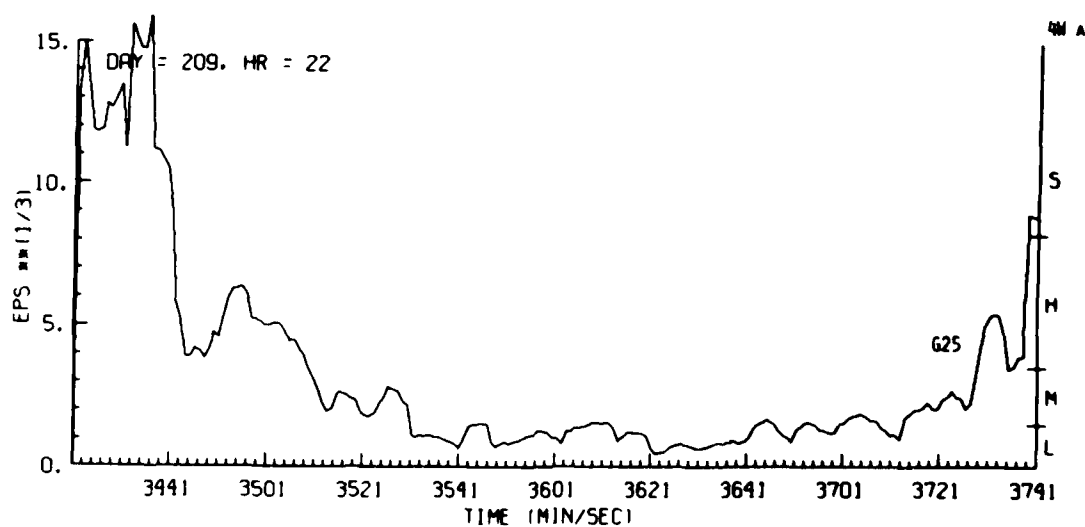
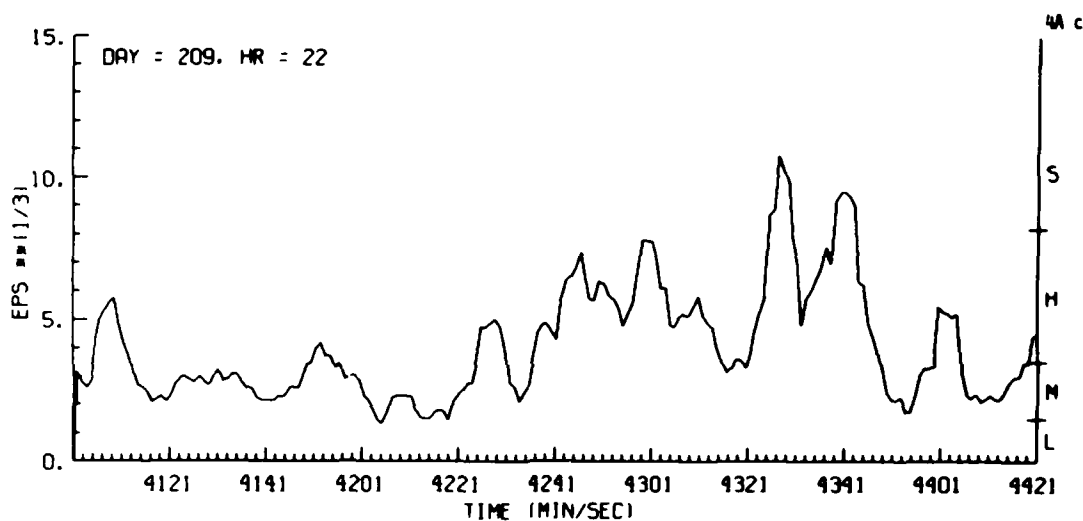
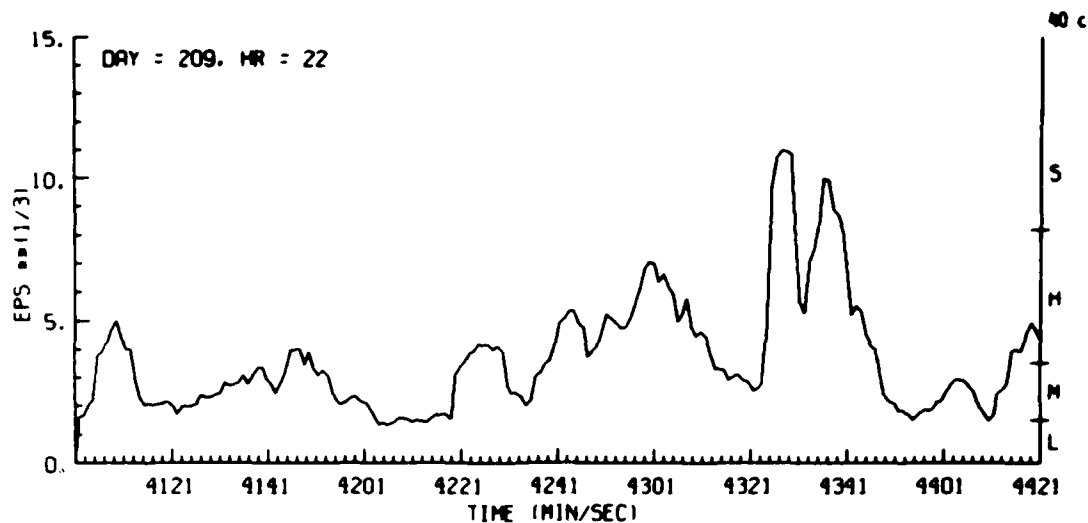


Figure G25. Estimates of Turbulence Severity Derived From Aircraft Gust Data, Day 209, Penetration 4C

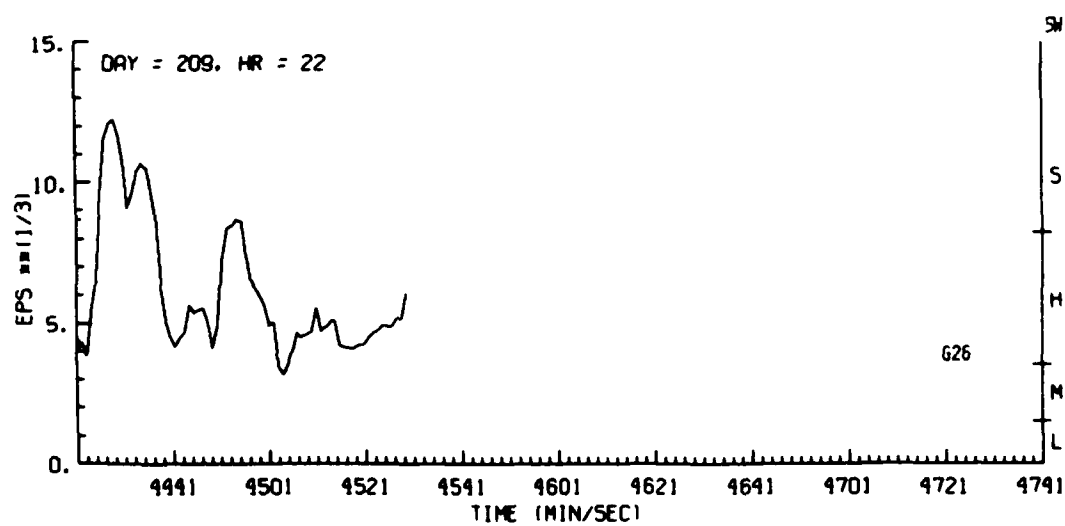
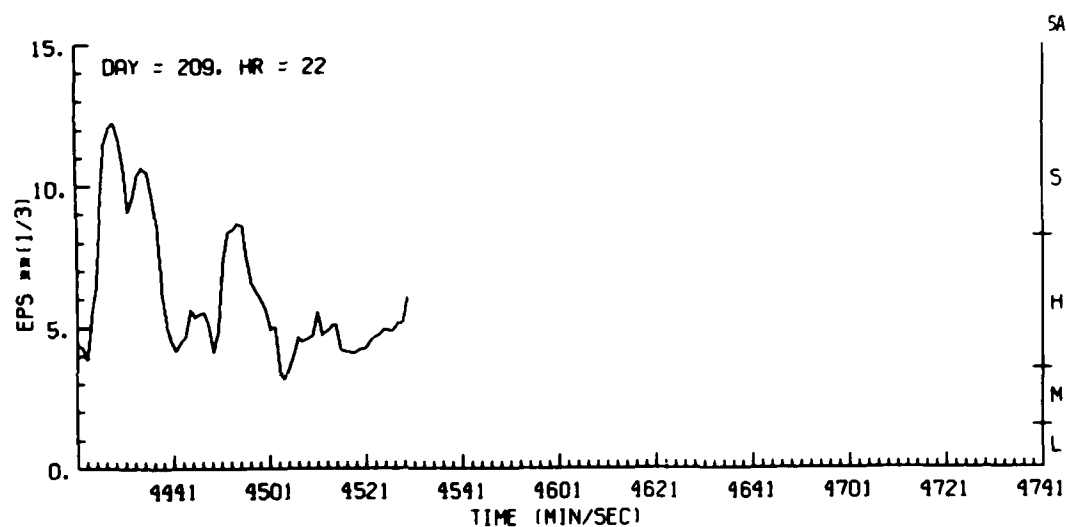
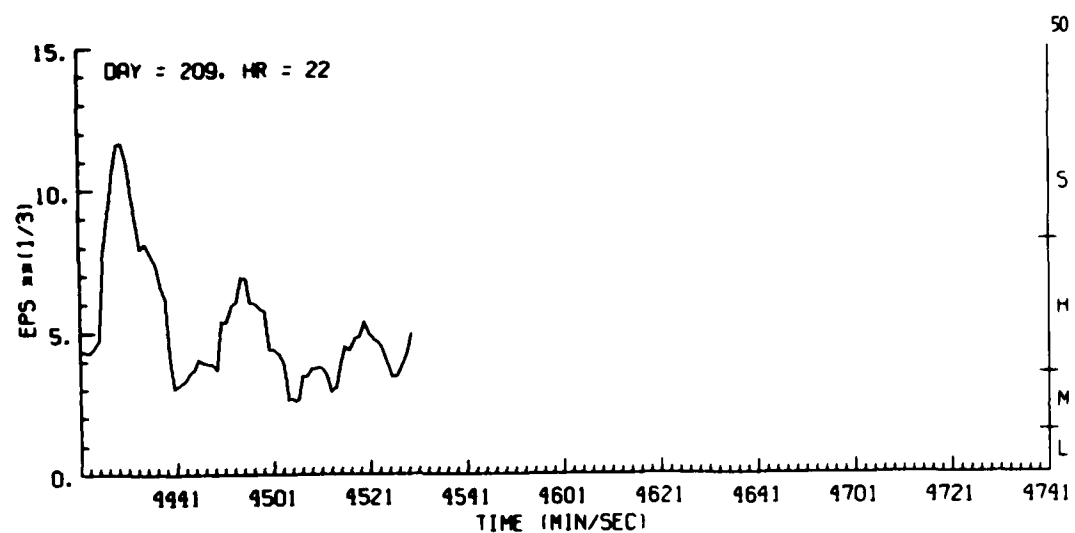


Figure G26. Estimates of Turbulence Severity Derived From Aircraft Gust Data, Day 209, Penetration 5

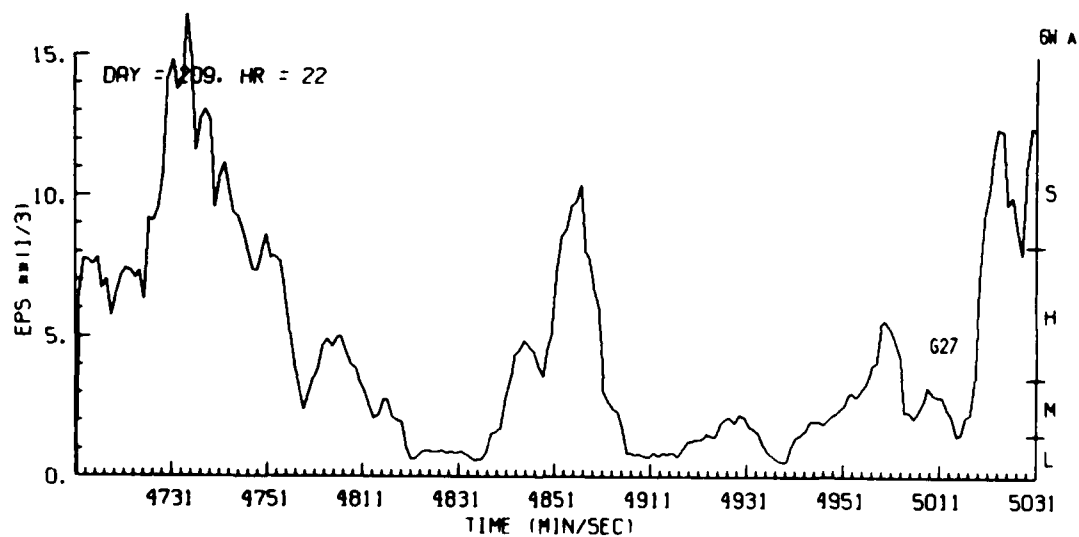
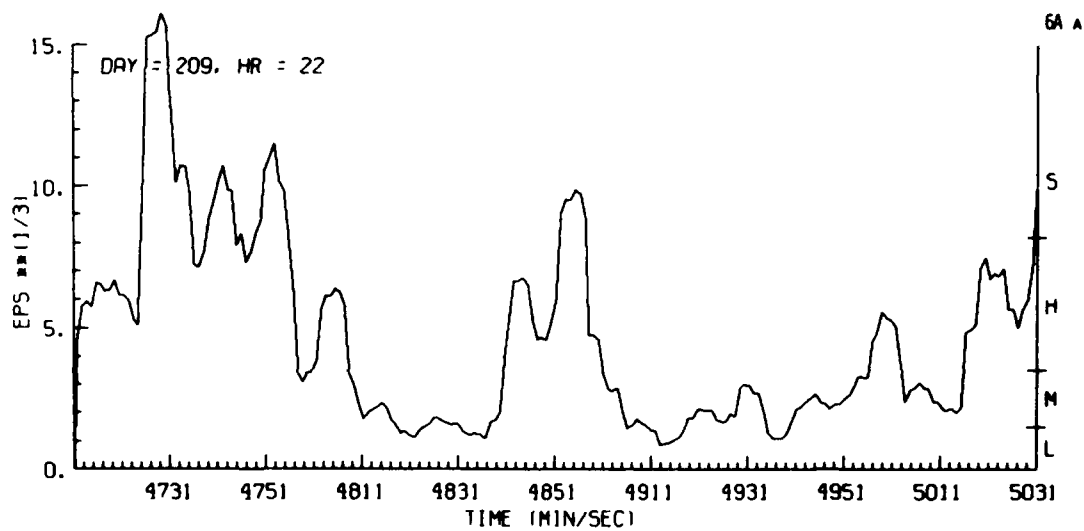
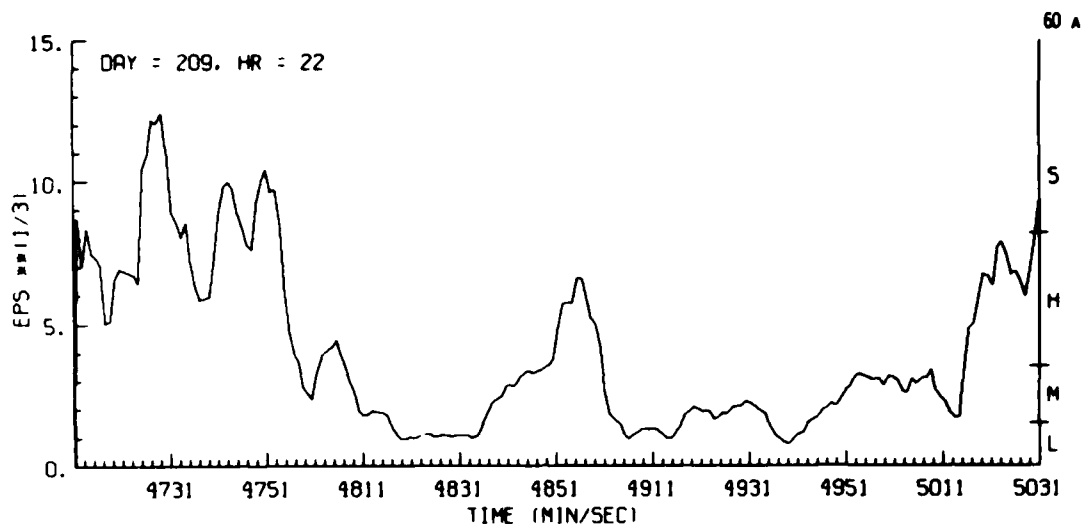


Figure G27. Estimates of Turbulence Severity Derived From Aircraft Gust Data, Day 209, Penetration 6A

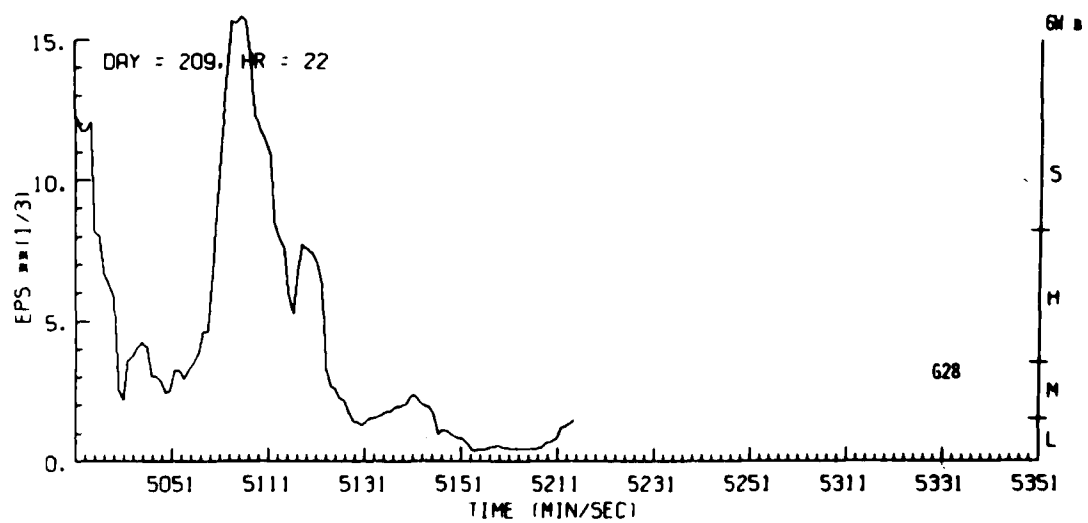
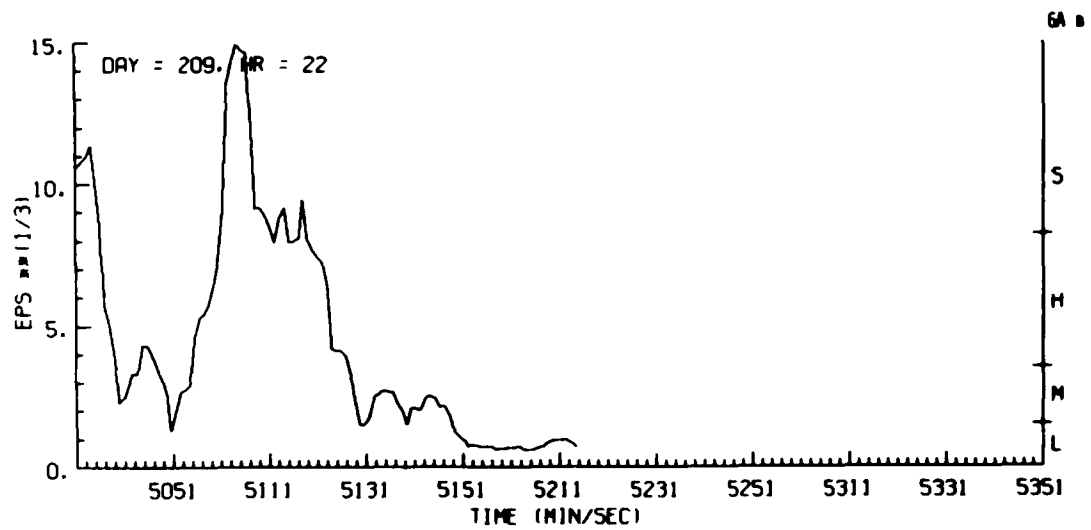
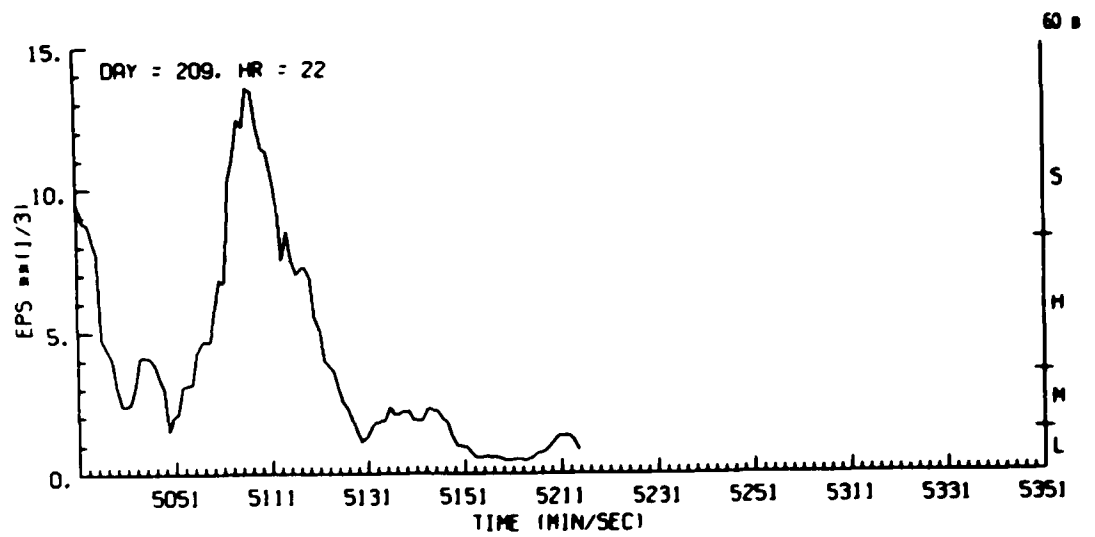


Figure G28. Estimates of Turbulence Severity Derived From Aircraft Gust Data, Day 209, Penetration 6B

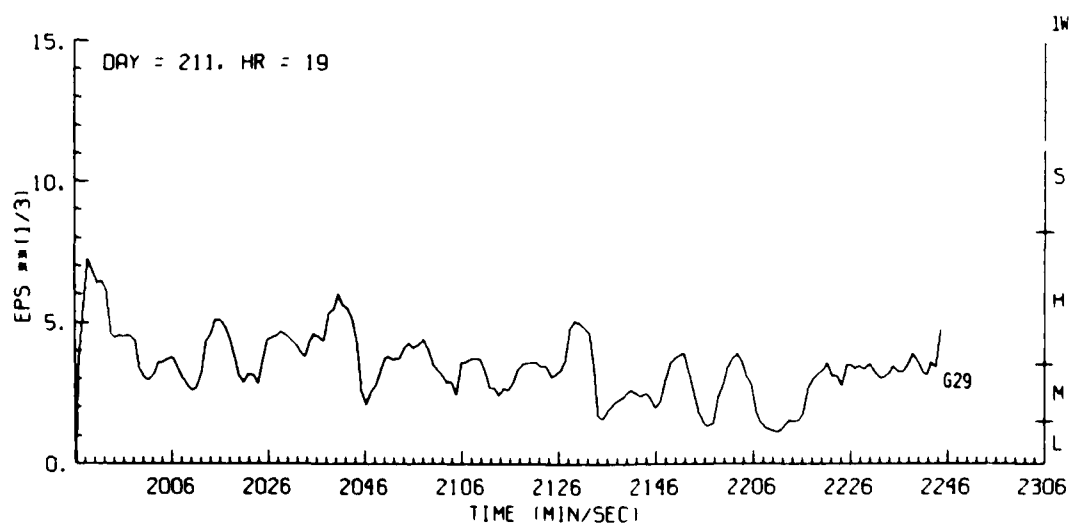
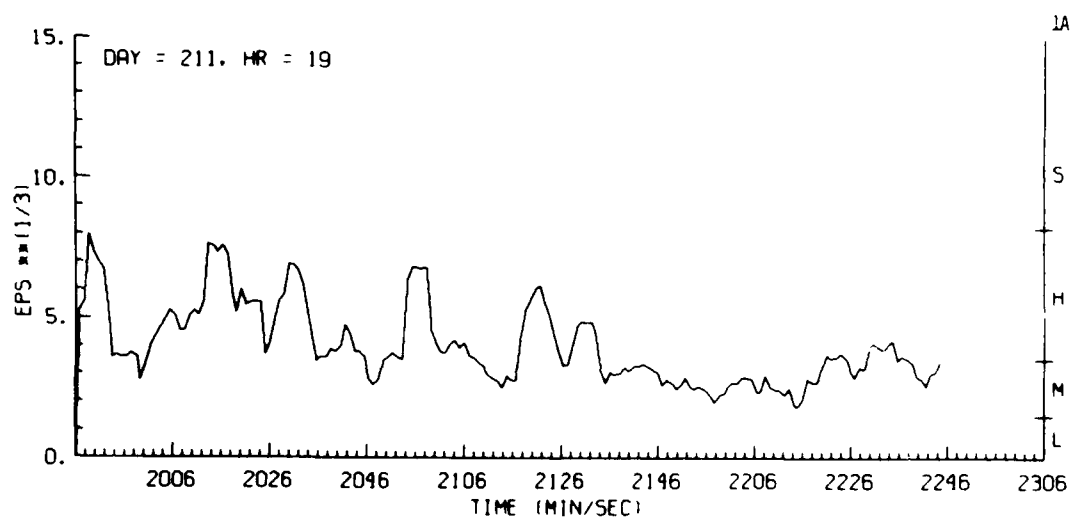
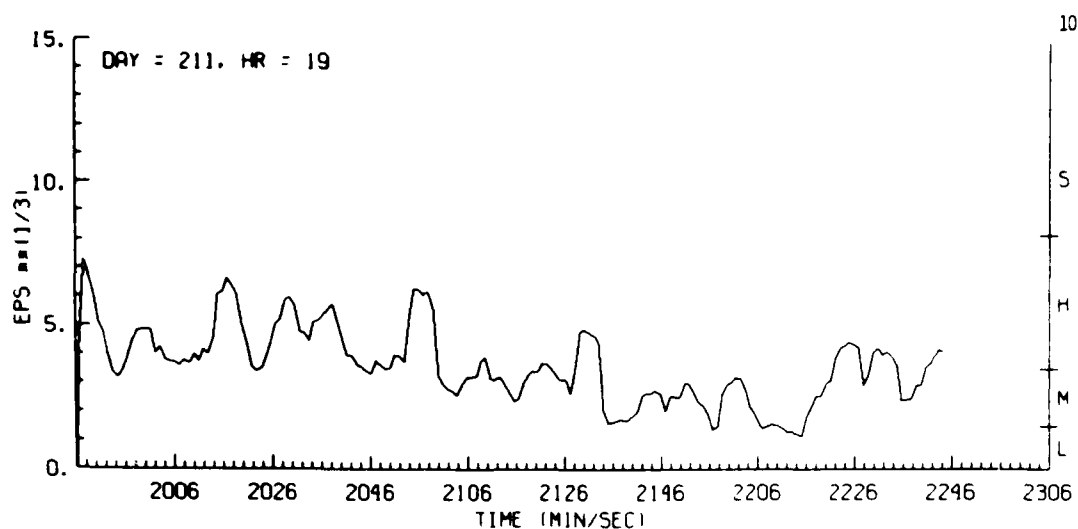


Figure G29. Estimates of Turbulence Severity Derived From Aircraft Gust Data, Day 211, Penetration 1

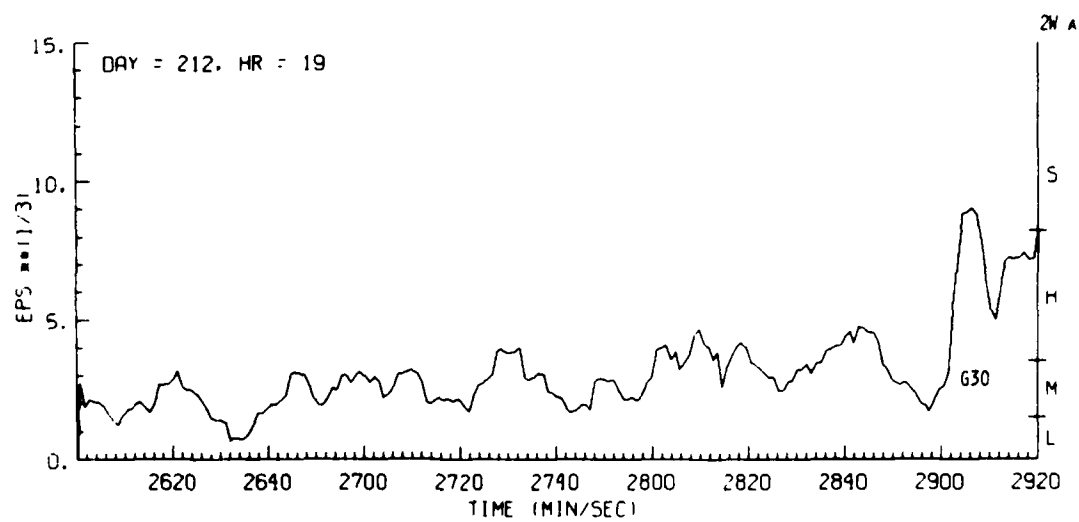
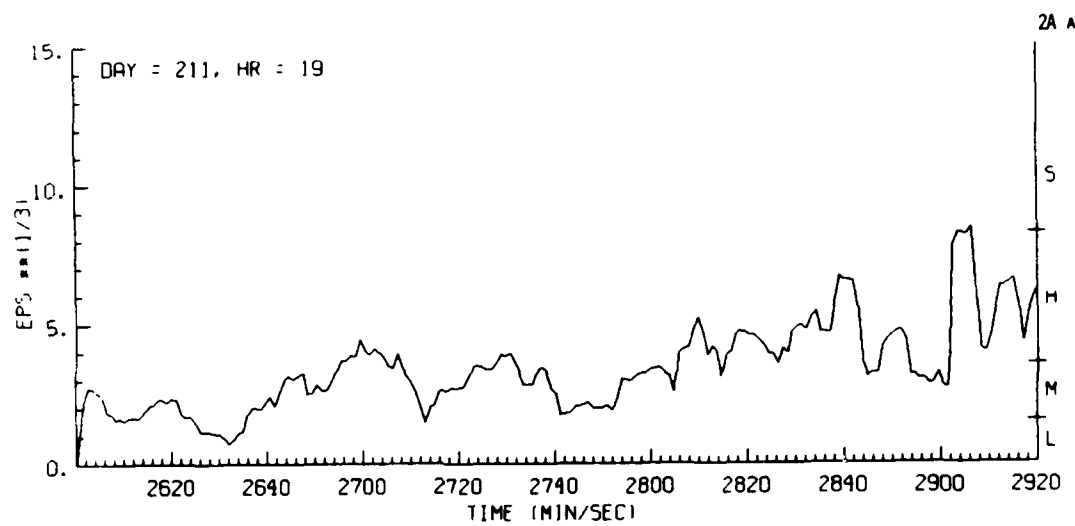
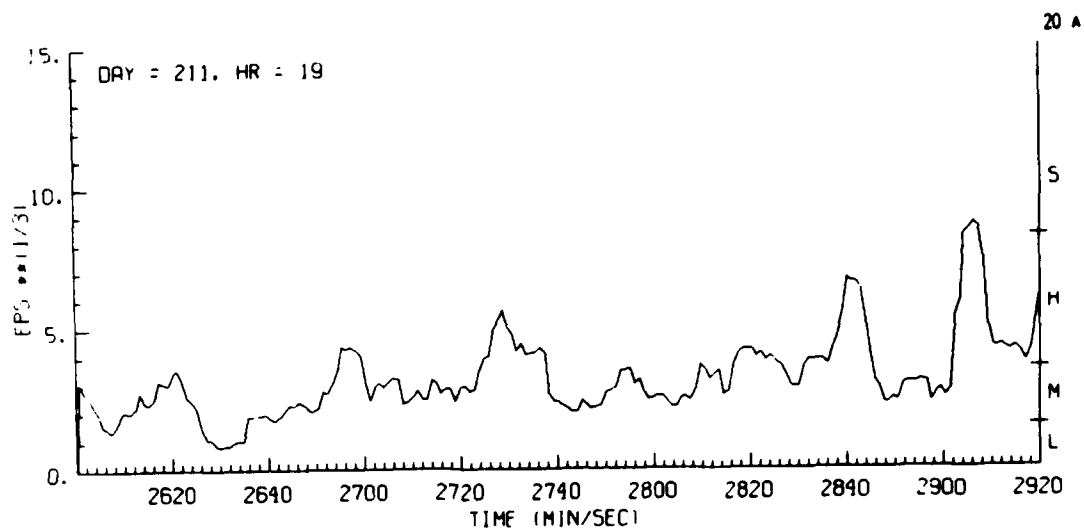


Figure G30. Estimates of Turbulence Severity Derived From Aircraft Gust Data, Day 211, Penetration 2A

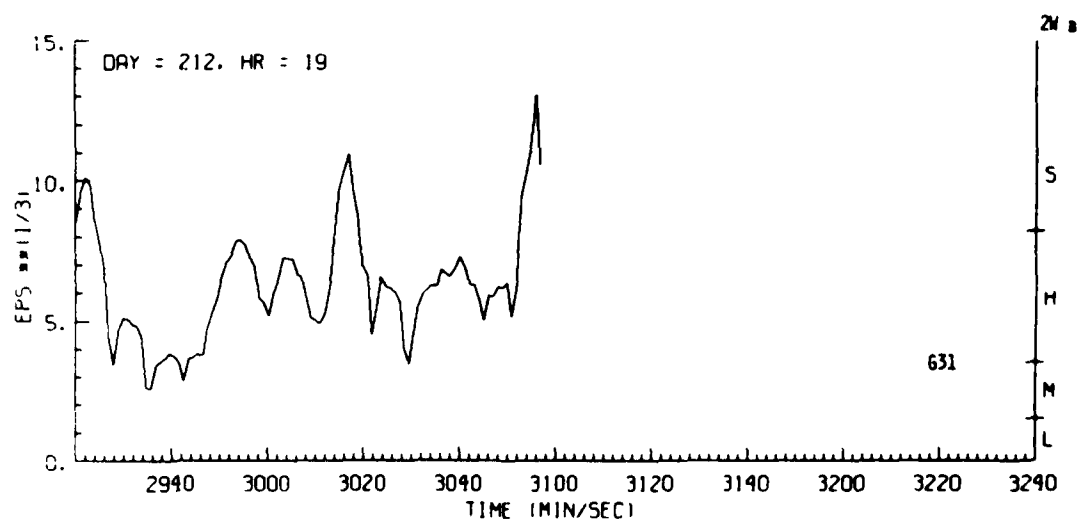
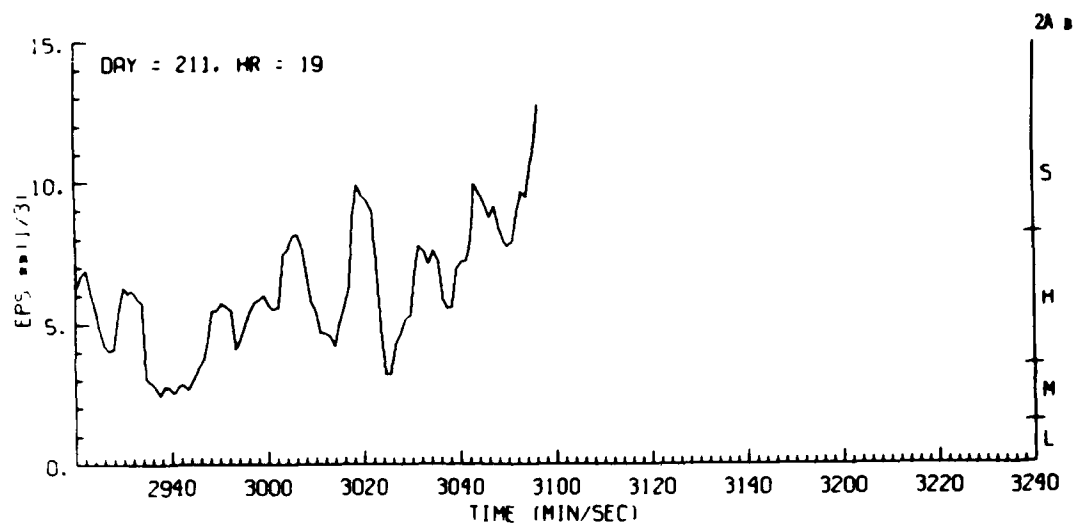
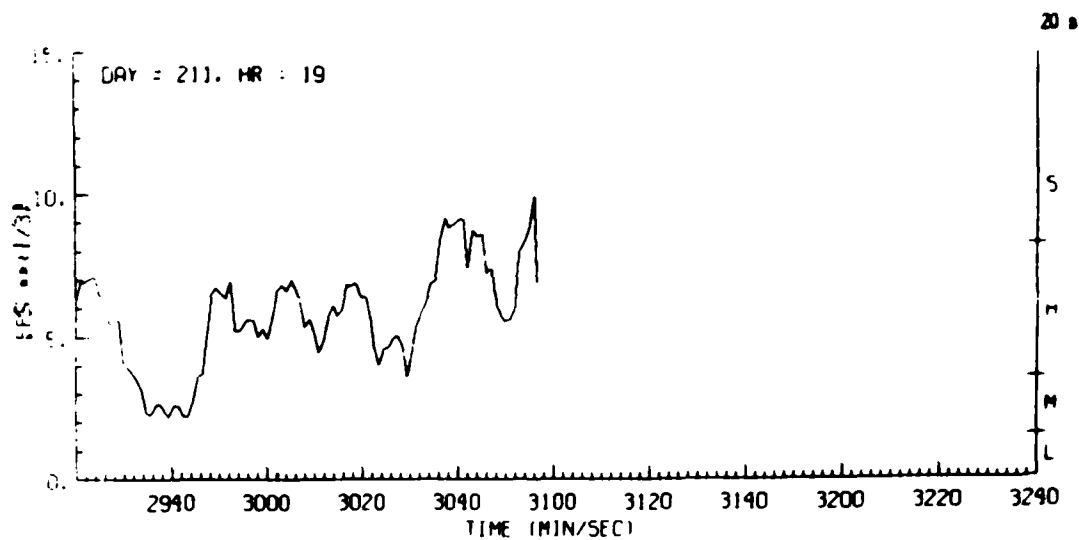


Figure G31. Estimates of Turbulence Severity Derived From Aircraft Gust Data, Day 211, Penetration 2B

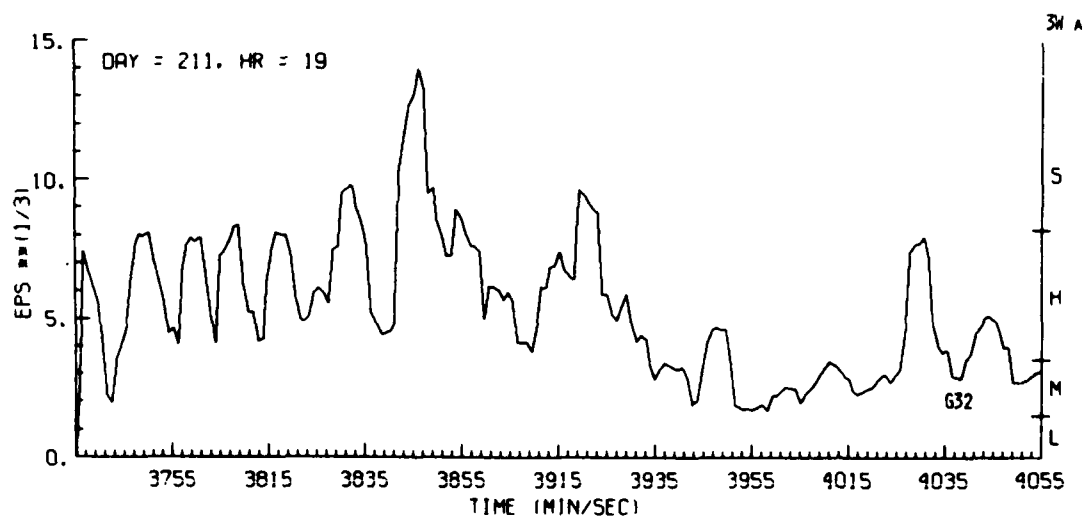
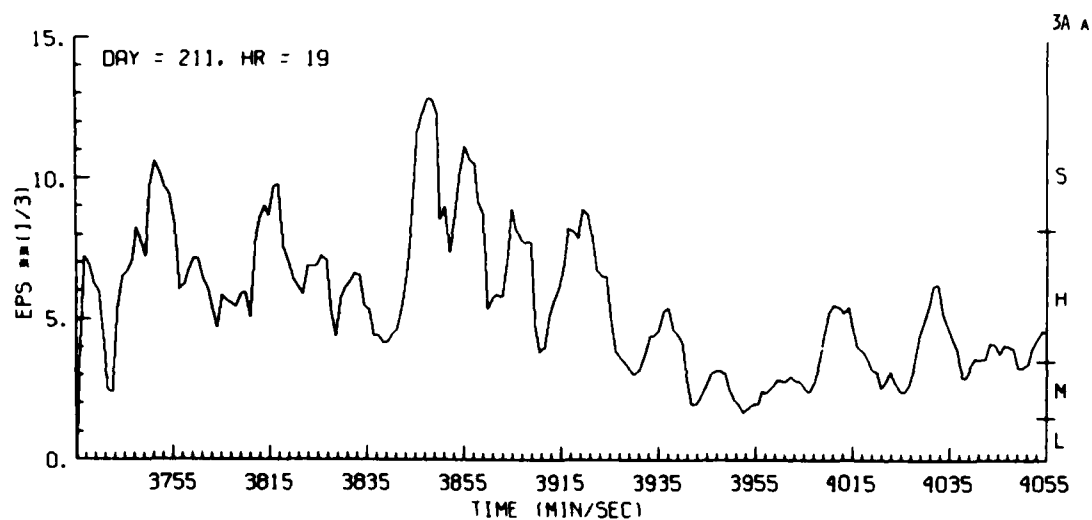
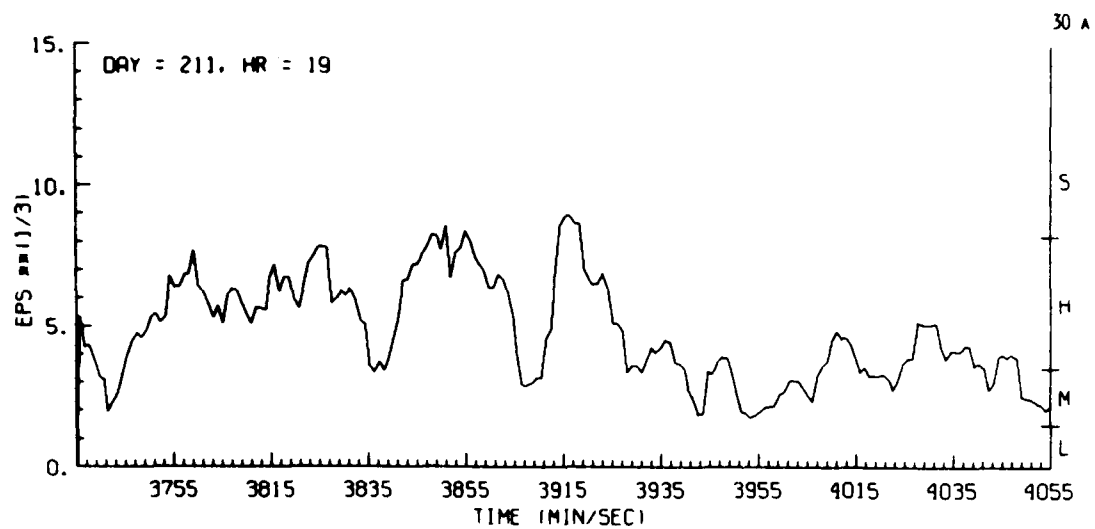


Figure G32. Estimates of Turbulence Severity Derived From Aircraft Gust Data, Day 211, Penetration 3A

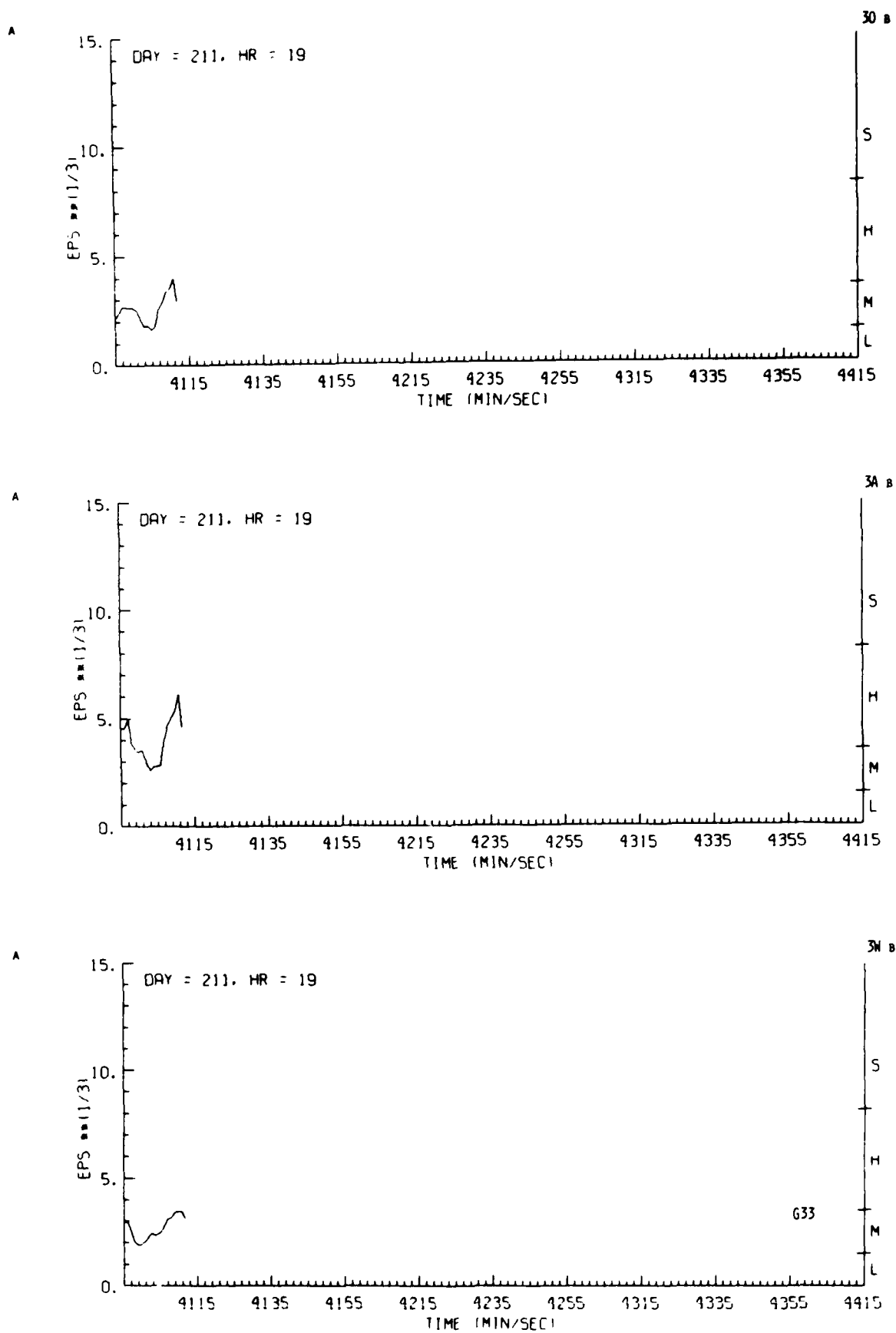


Figure G33. Estimates of Turbulence Severity Derived From Aircraft Gust Data, Day 211, Penetration 3B

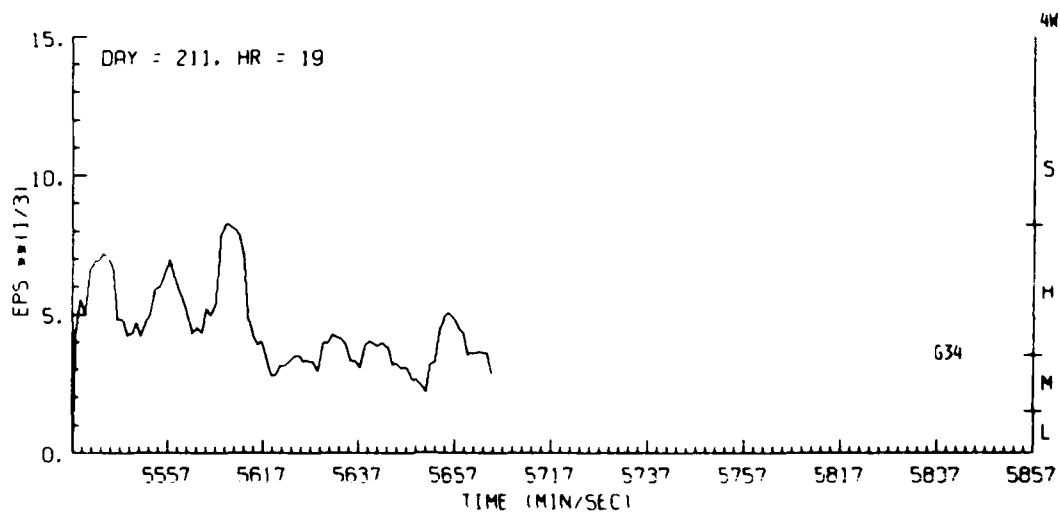
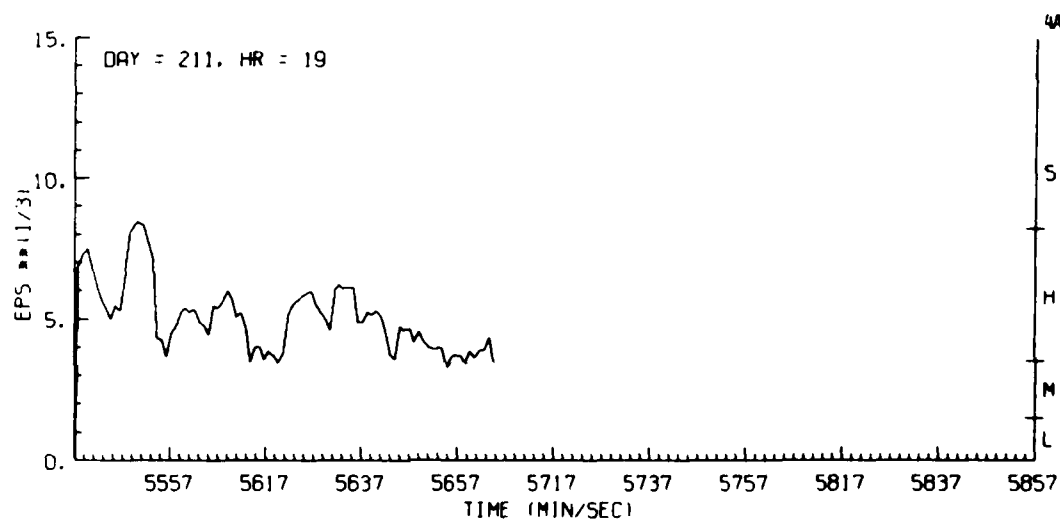
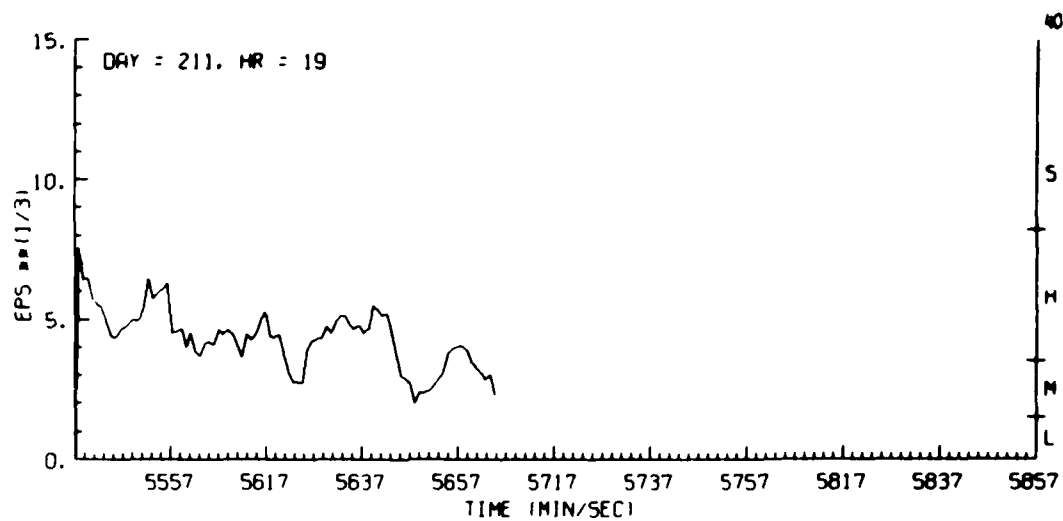


Figure G34. Estimates of Turbulence Severity Derived From Aircraft Gust Data, Day 211, Penetration 4

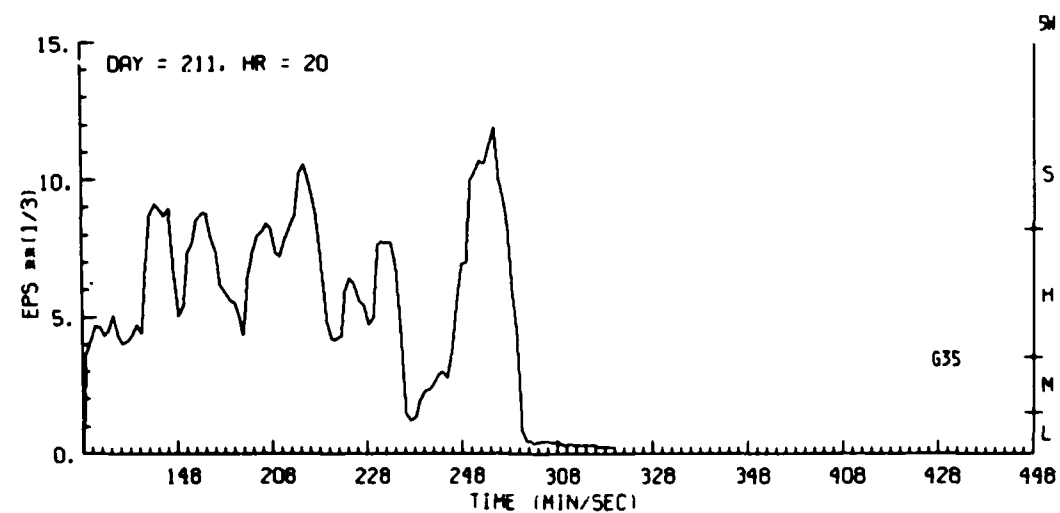
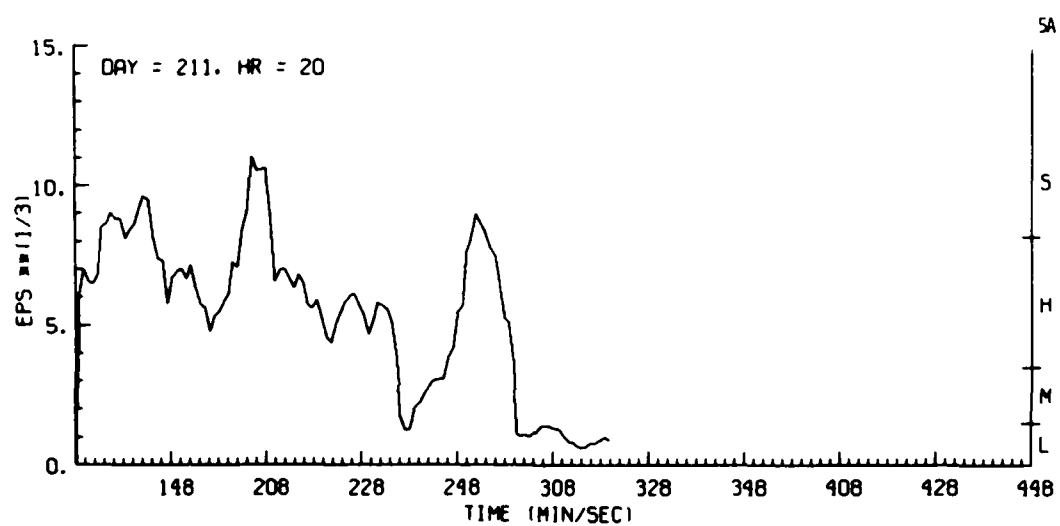
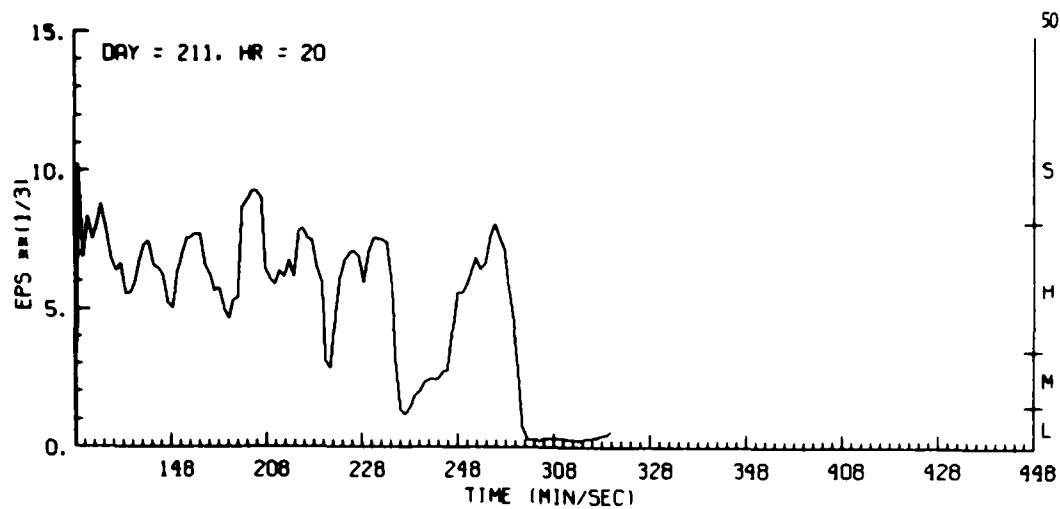


Figure G35. Estimates of Turbulence Severity Derived From Aircraft Gust Data, Day 211, Penetration 5

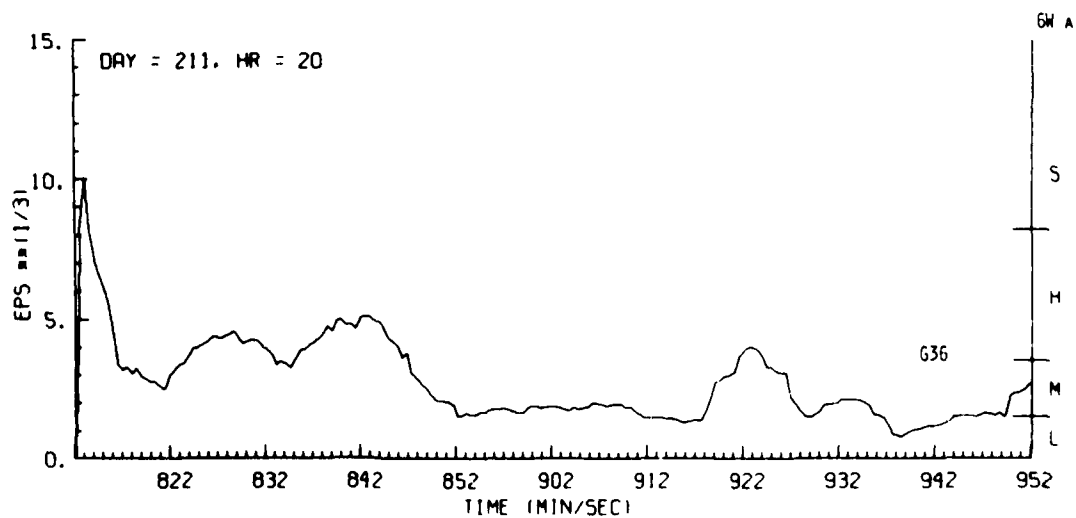
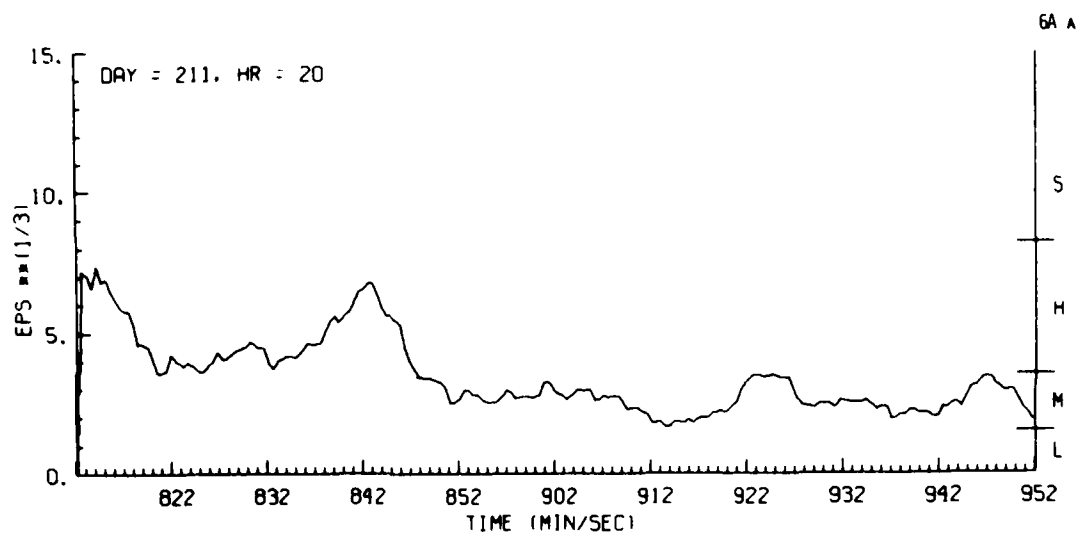
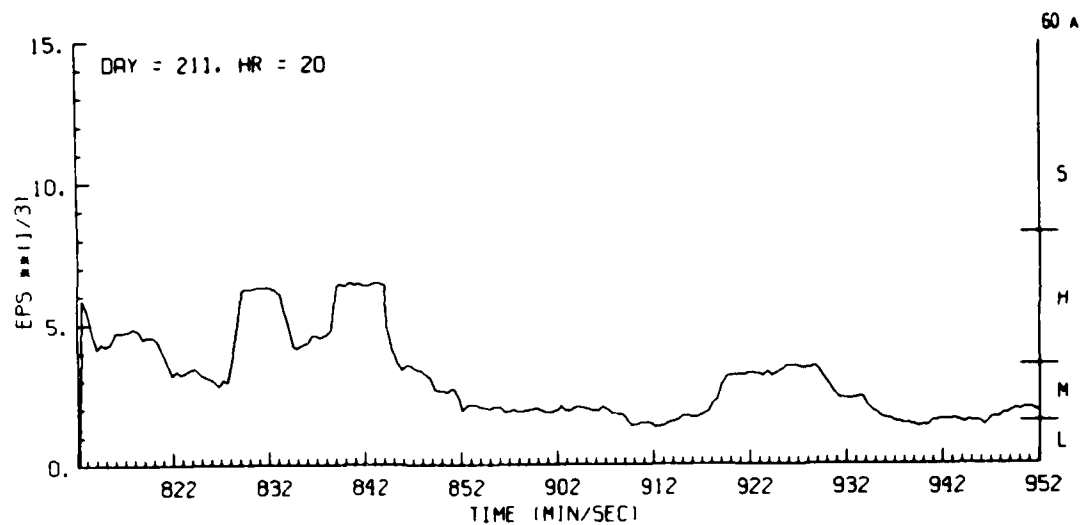


Figure G36. Estimates of Turbulence Severity Derived From Aircraft Gust Data, Day 211, Penetration 6A

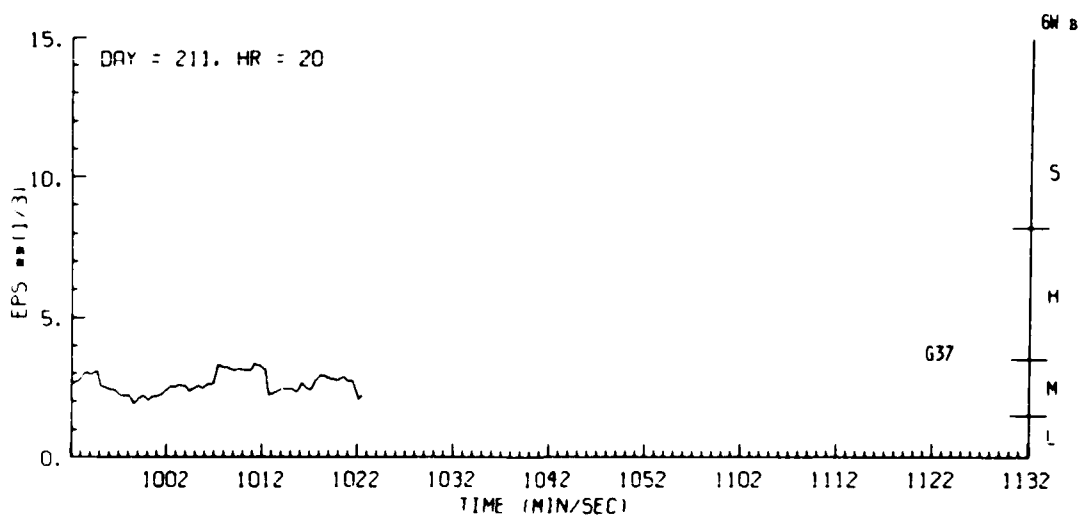
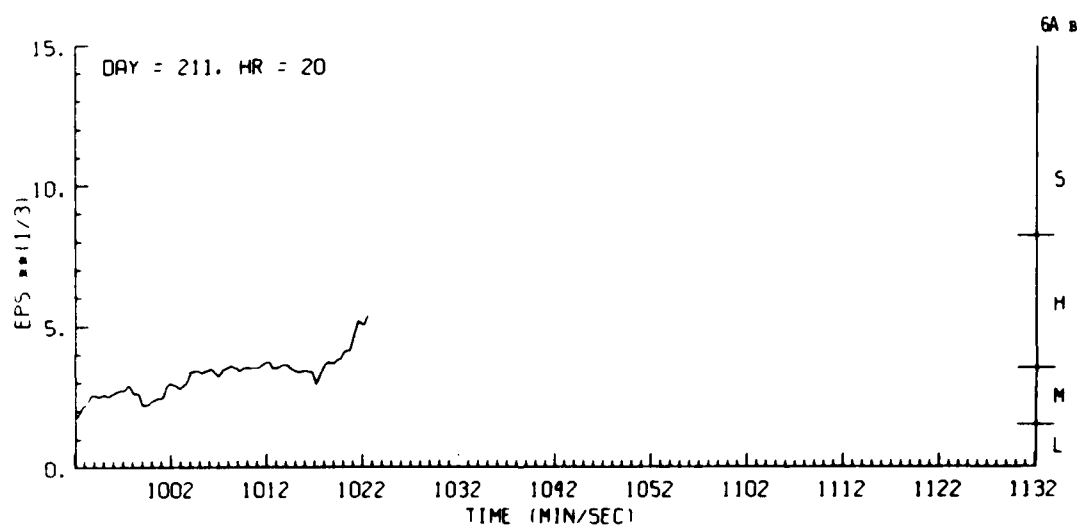
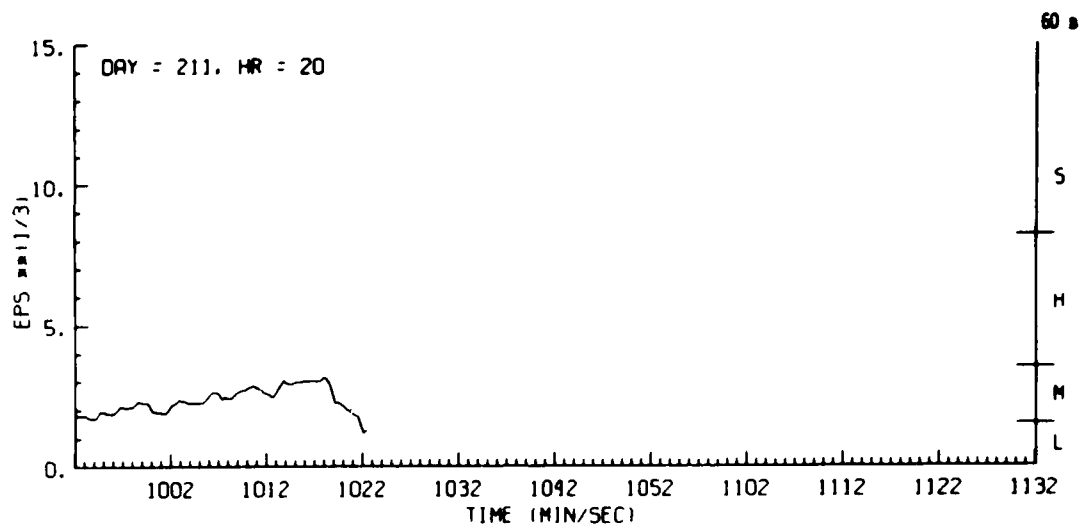


Figure G37. Estimates of Turbulence Severity Derived From Aircraft Gust Data, Day 211, Penetration 6B

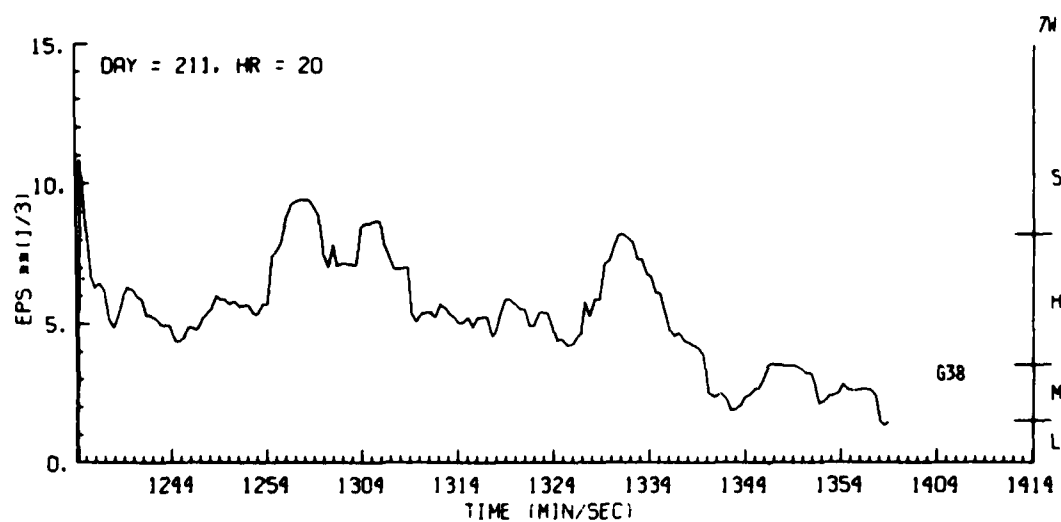
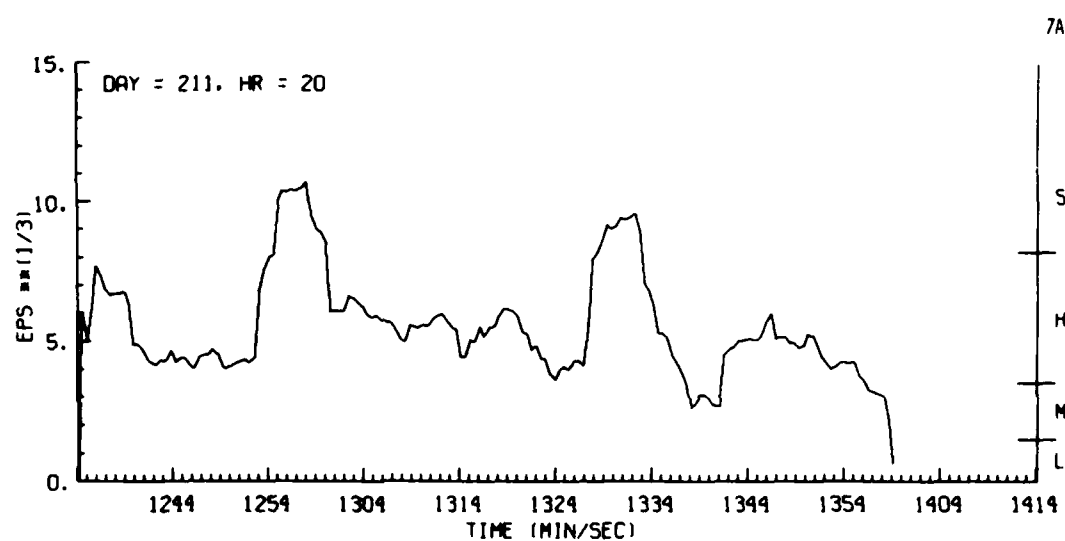
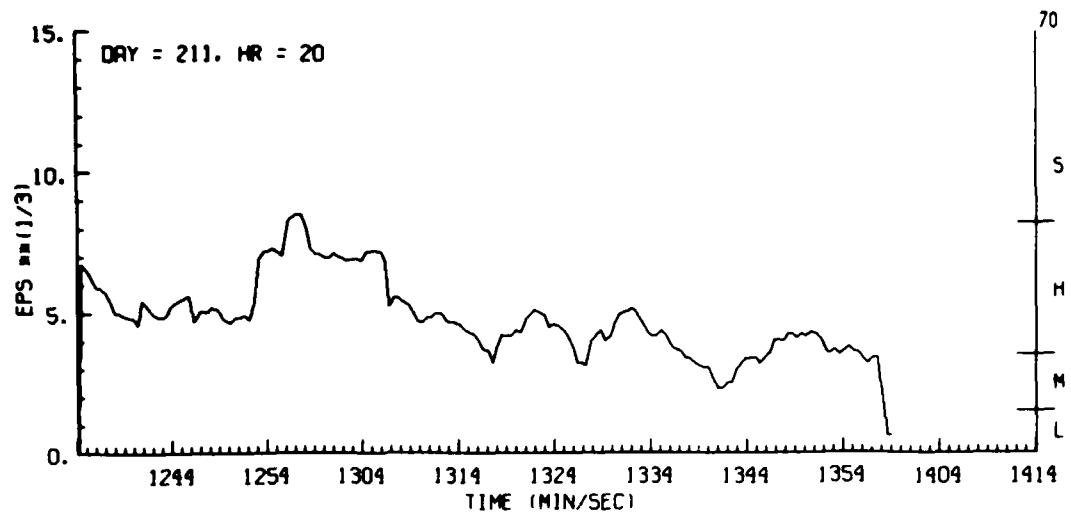


Figure G38. Estimates of Turbulence Severity Derived From Aircraft Gust Data, Day 211, Penetration 7

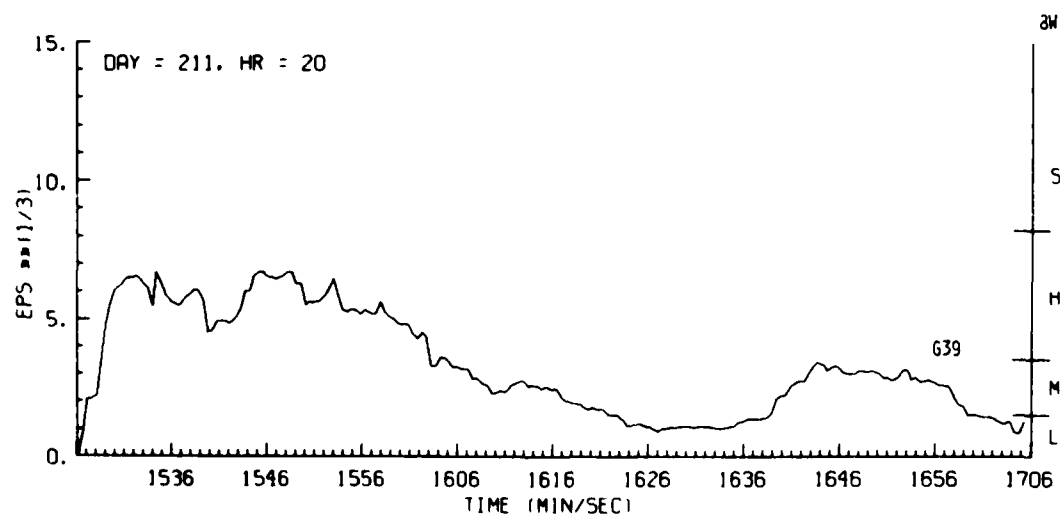
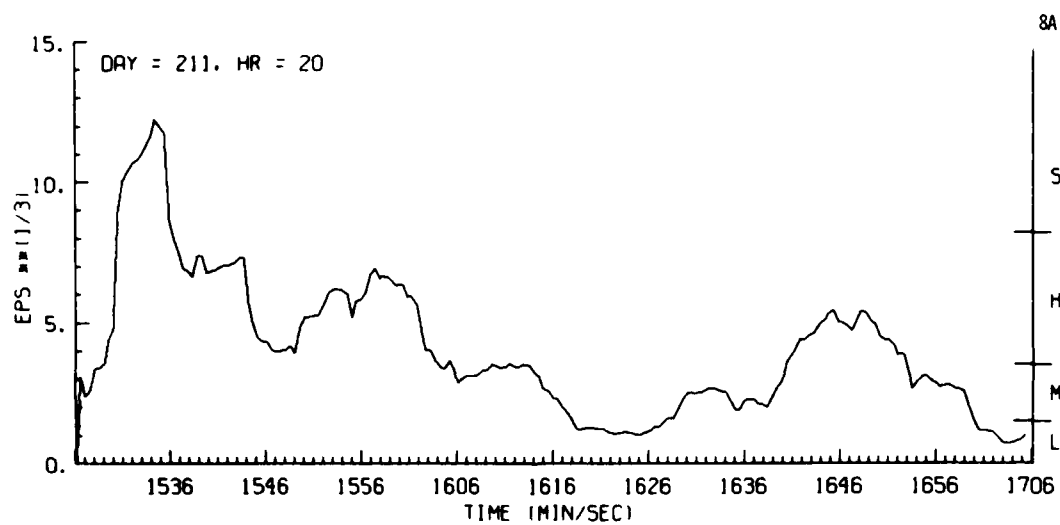
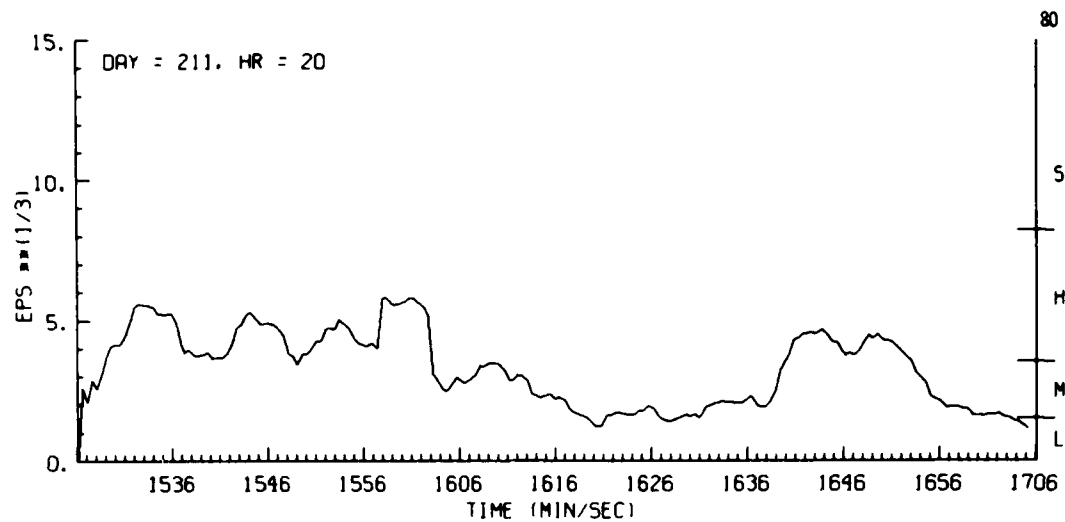


Figure G39. Estimates of Turbulence Severity Derived From Aircraft Gust Data, Day 211, Penetration 8

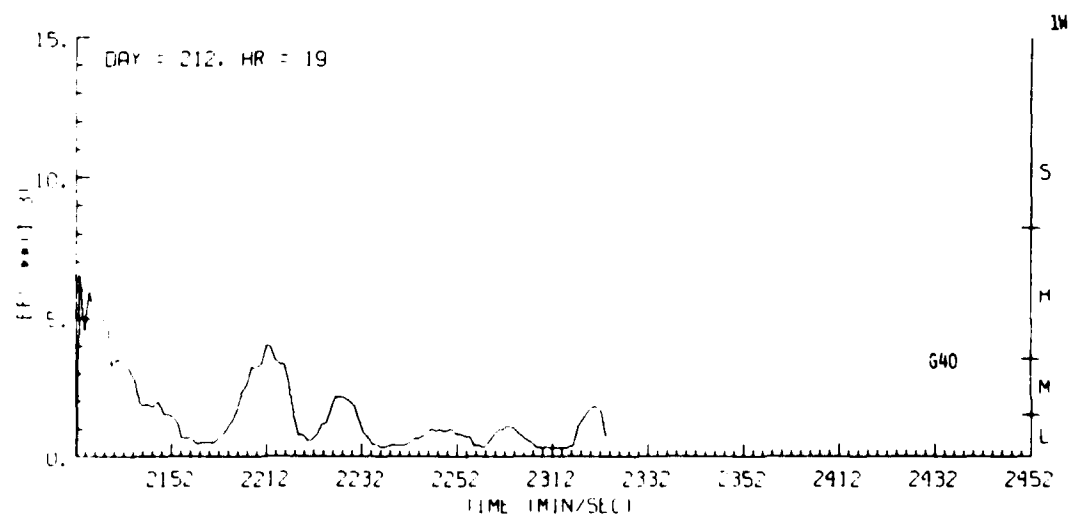
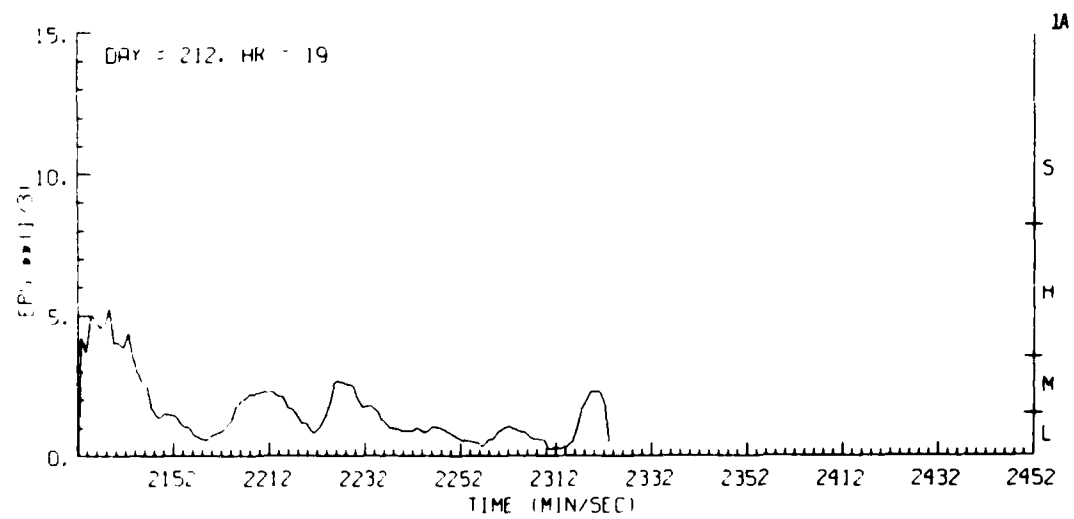
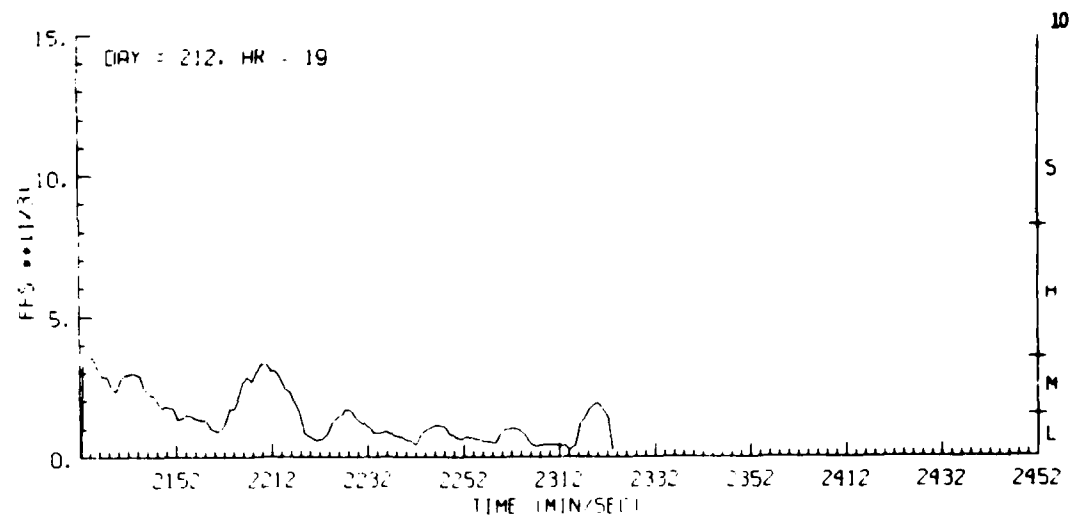


Figure G40. Estimates of Turbulence Severity Derived From Aircraft Gust Data, Day 212, Penetration 1

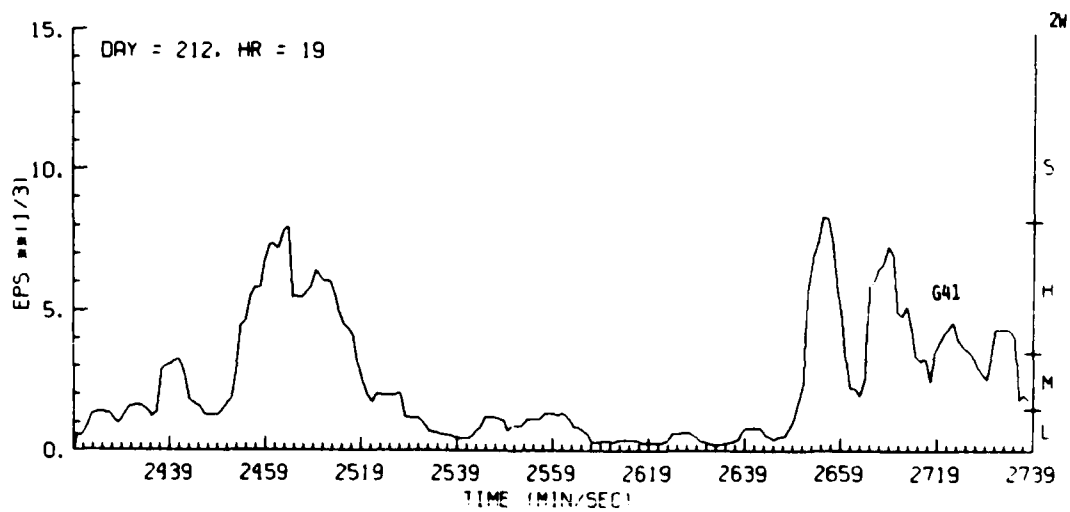
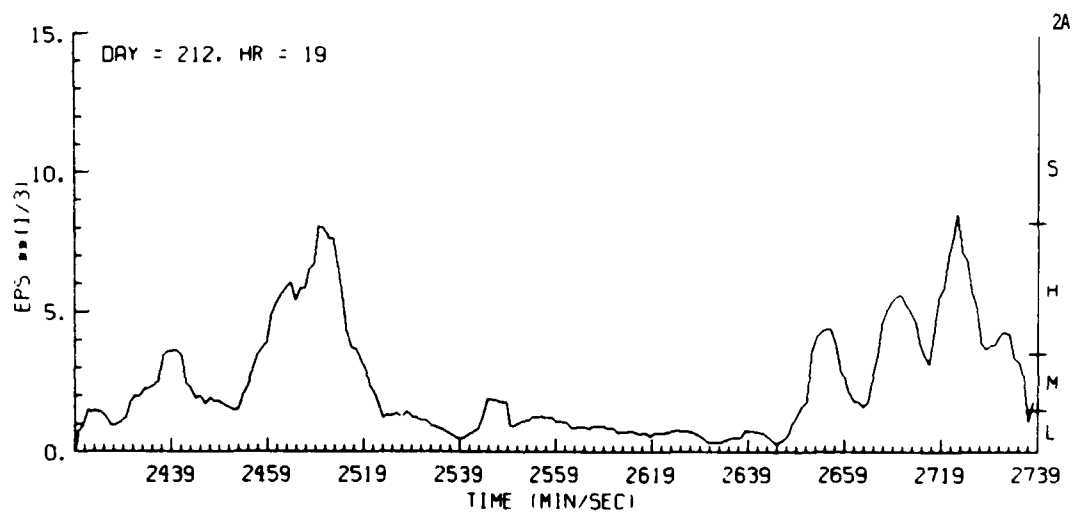
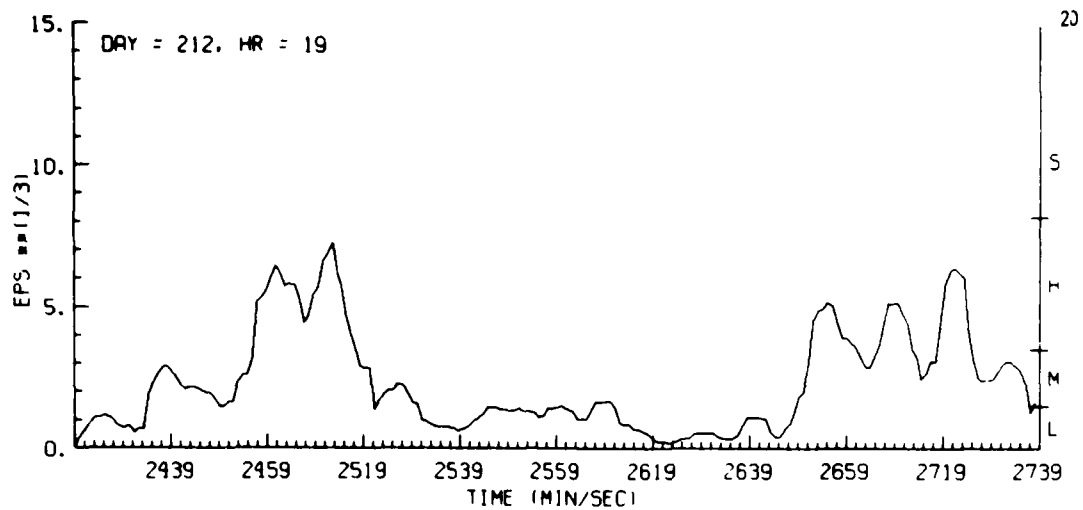


Figure G41. Estimates of Turbulence Severity Derived From Aircraft Gust Data, Day 212, Penetration 2

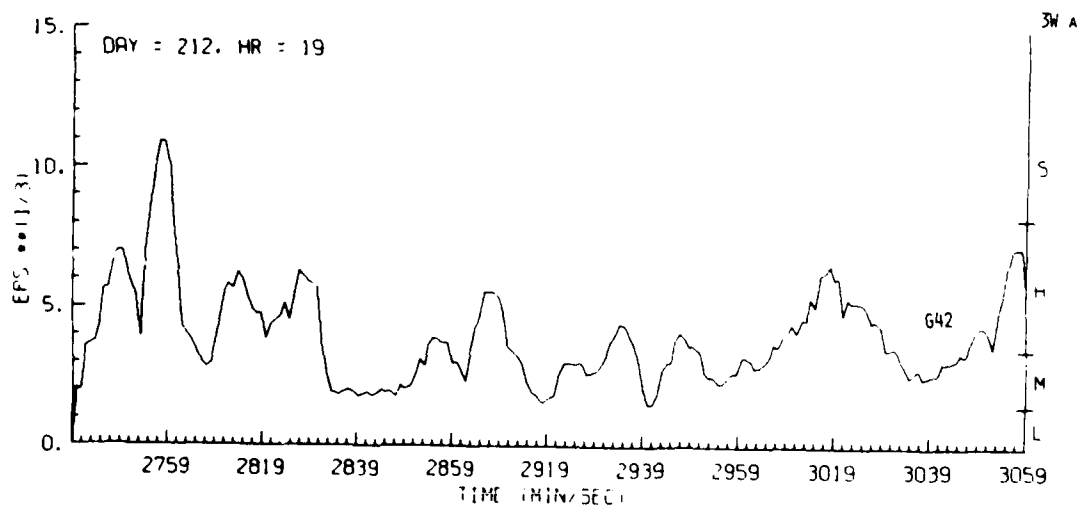
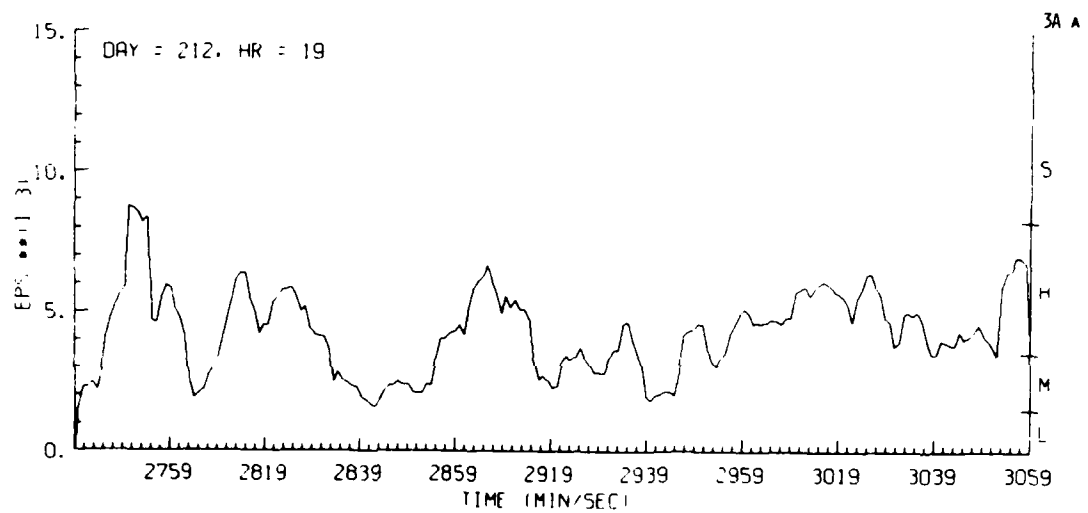
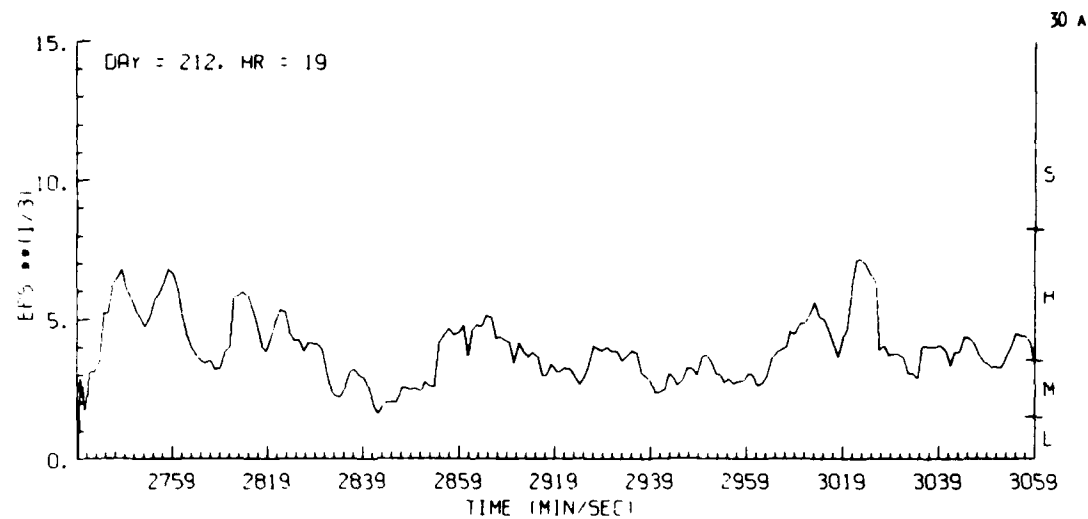


Figure G42. Estimates of Turbulence Severity Derived From Aircraft Gust Data, Day 212, Penetration 3A

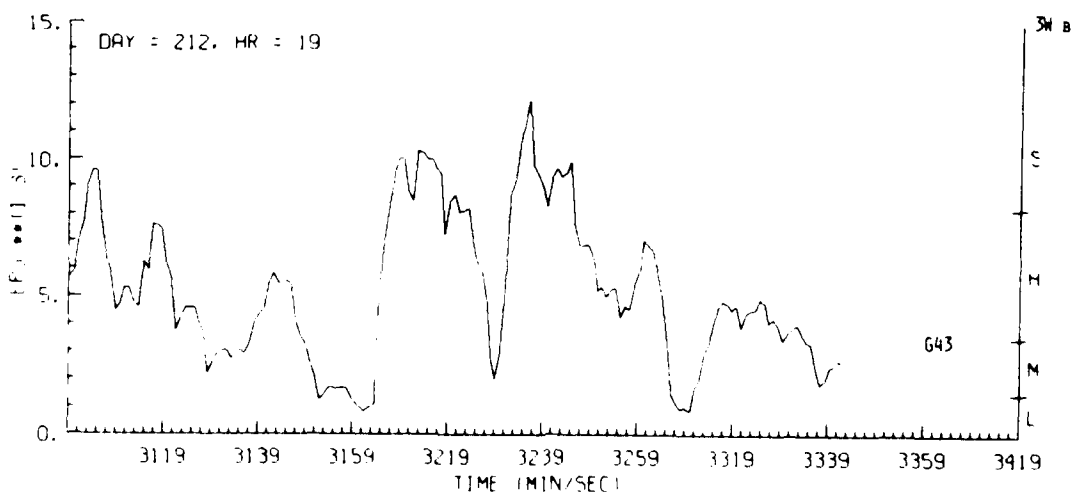
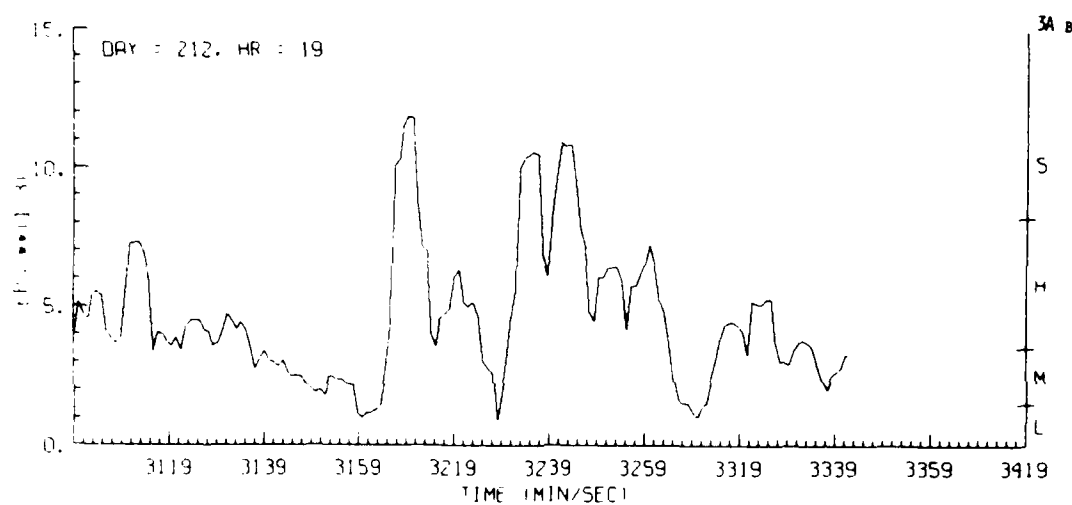
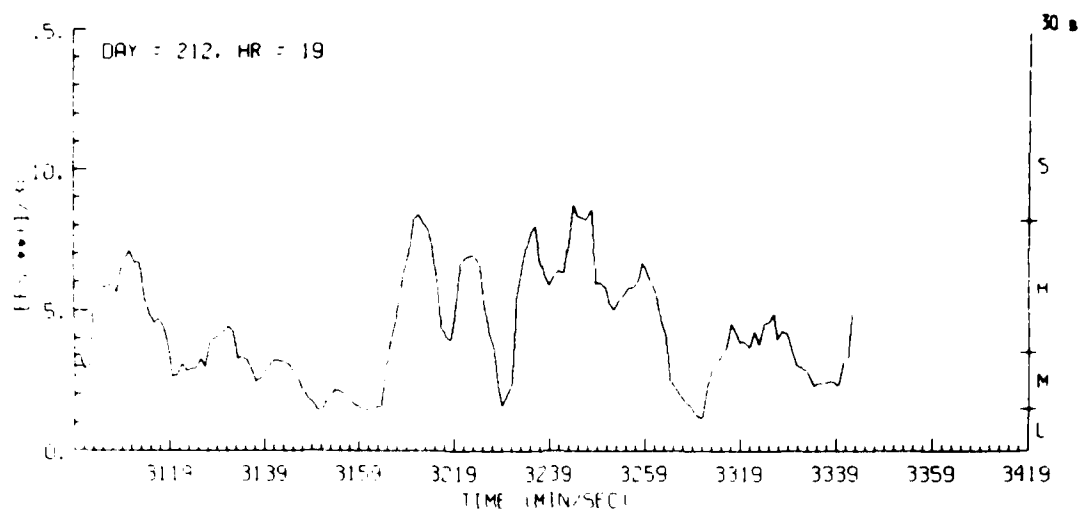


Figure G43. Estimates of Turbulence Severity Derived From Aircraft Gust Data, Day 212, Penetration 3B

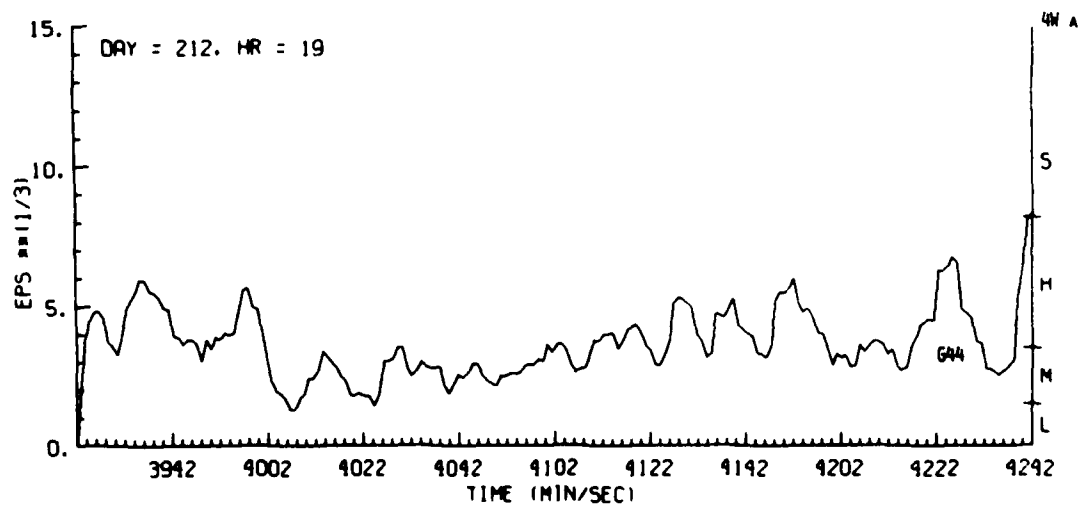
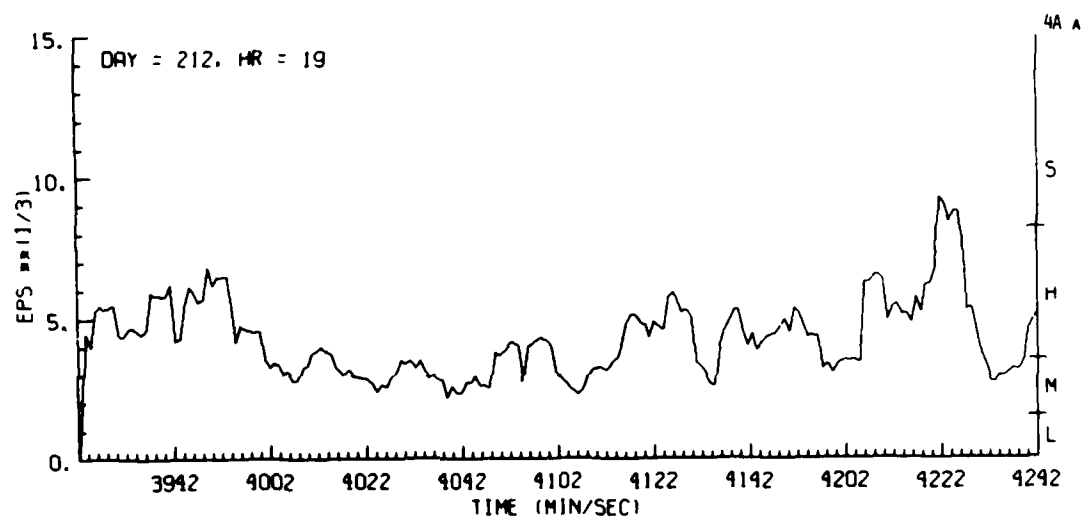
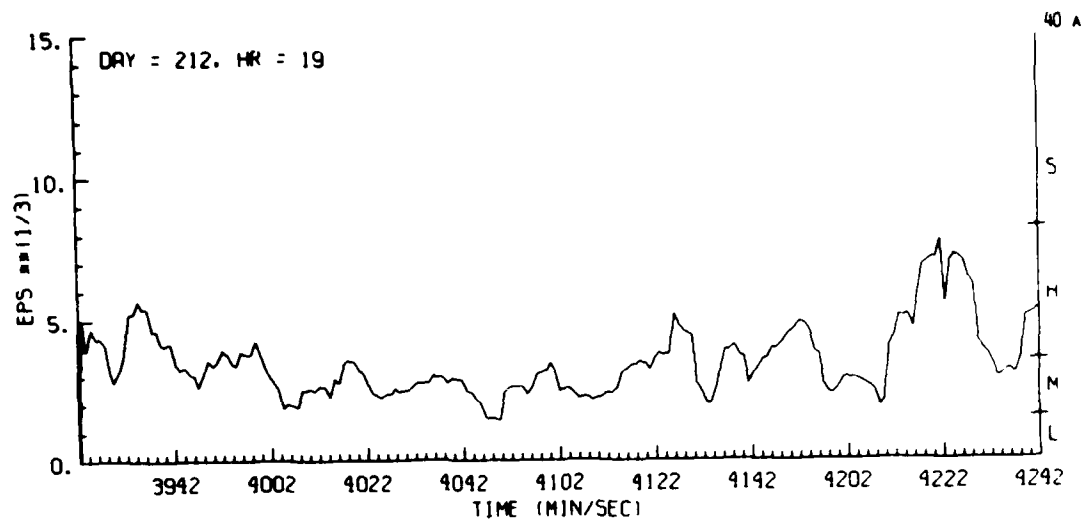


Figure G44. Estimates of Turbulence Severity Derived From Aircraft Gust Data, Day 212, Penetration 4A

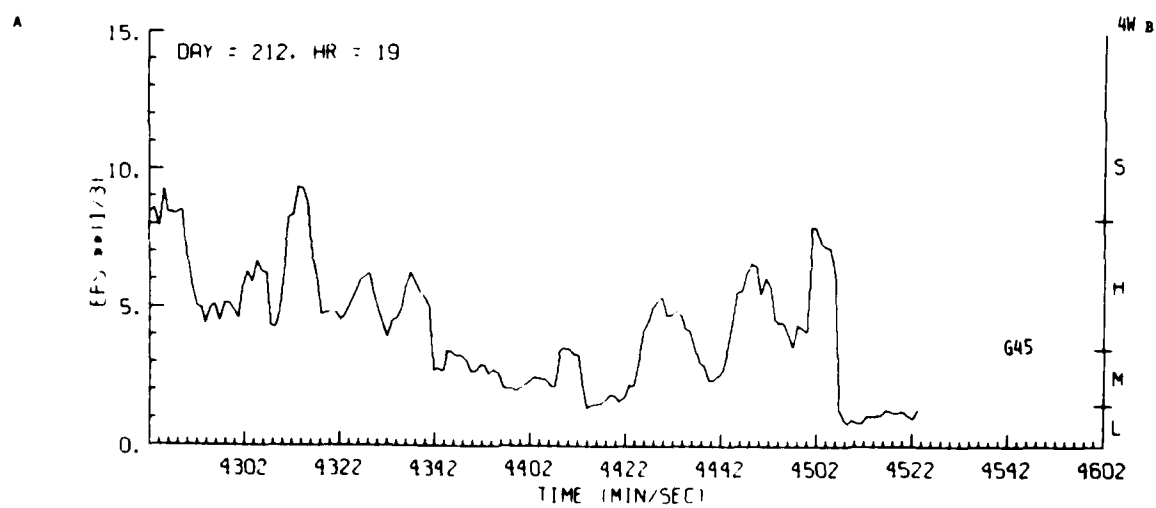
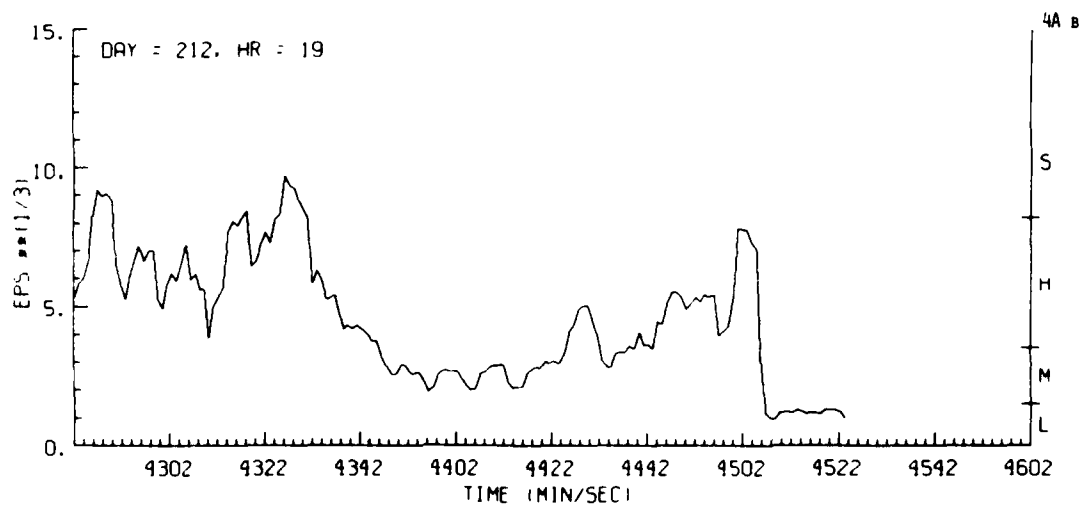
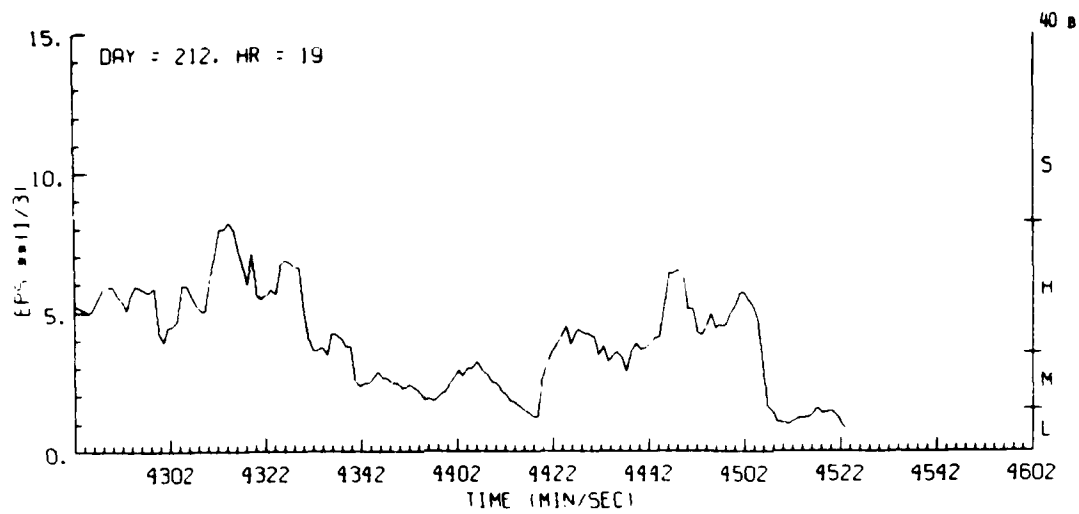


Figure G45. Estimates of Turbulence Severity Derived From Aircraft Gust Data, Day 212, Penetration 4B

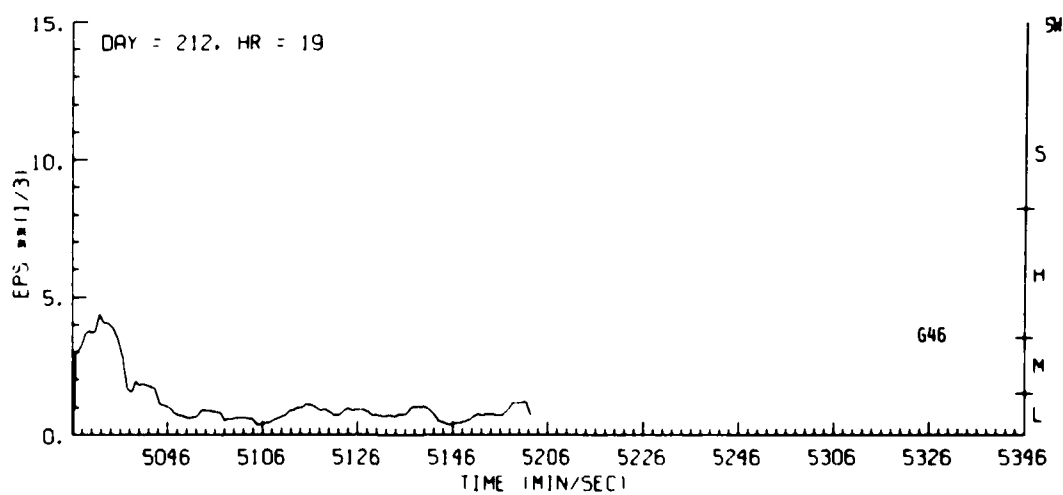
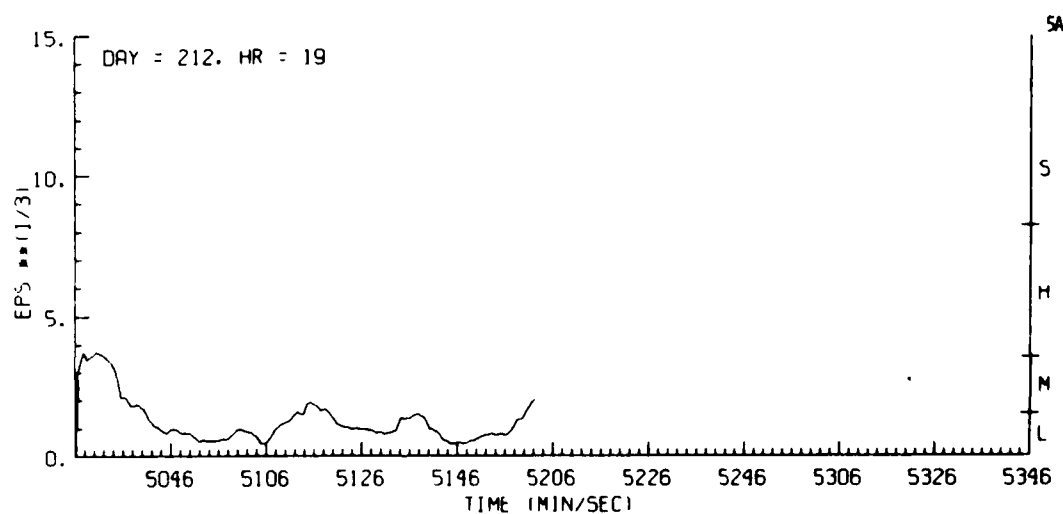
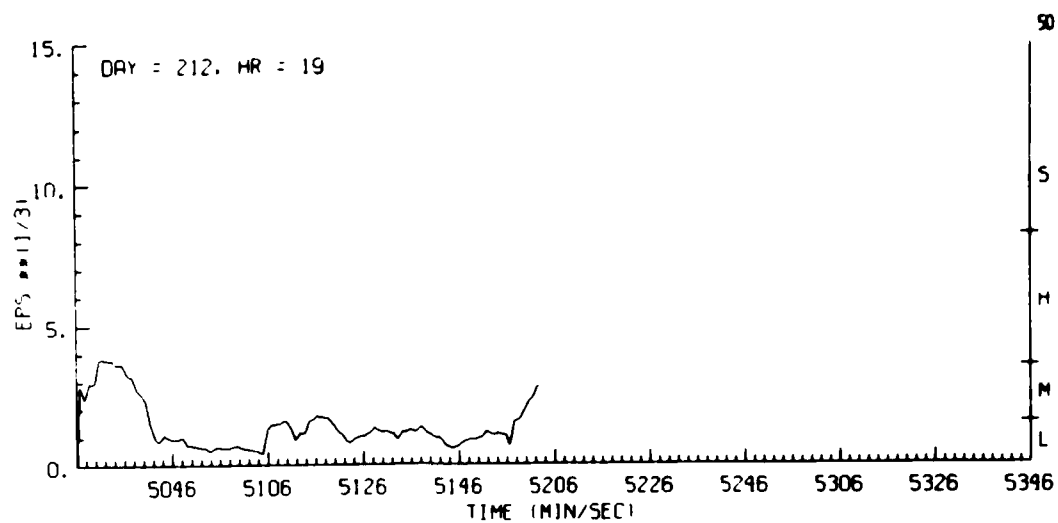


Figure G46. Estimates of Turbulence Severity Derived From Aircraft Gust Data, Day 212, Penetration 5

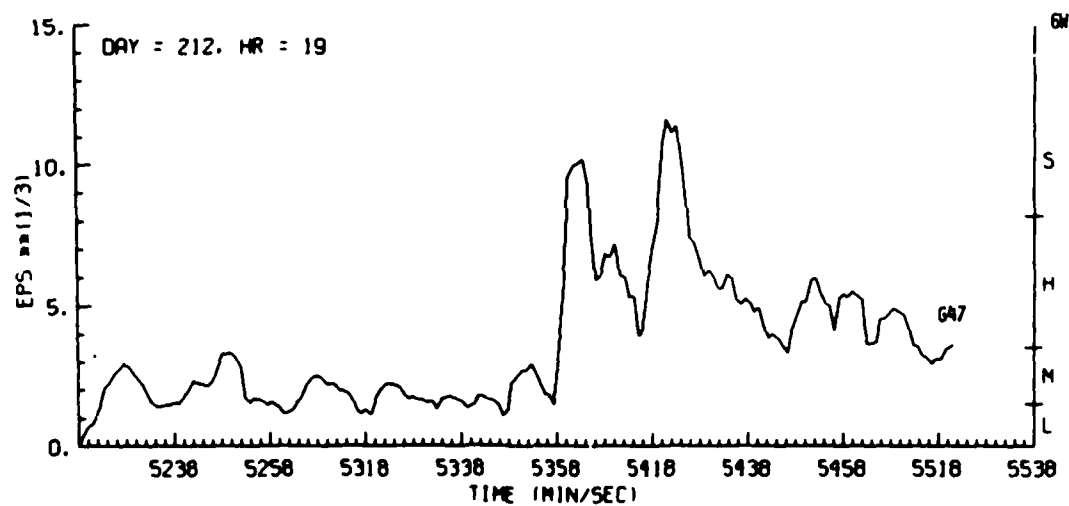
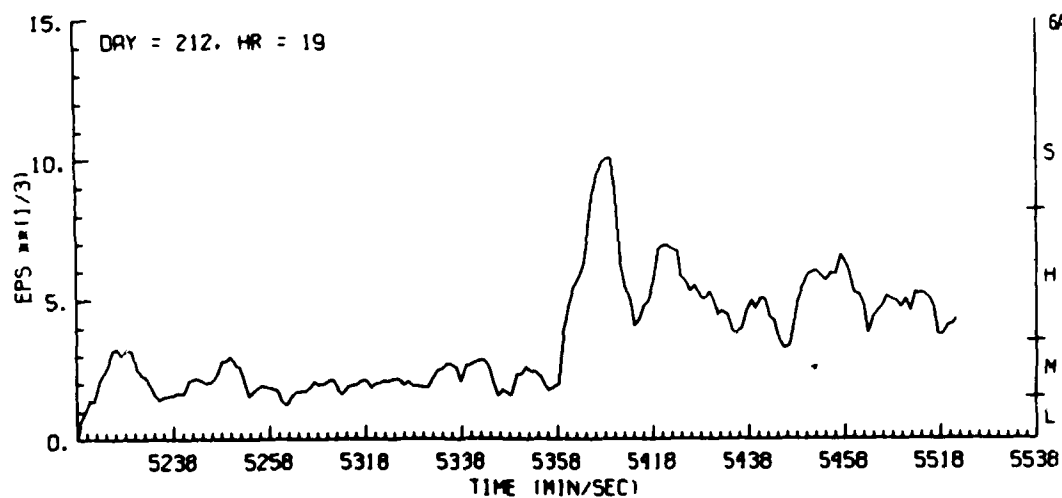
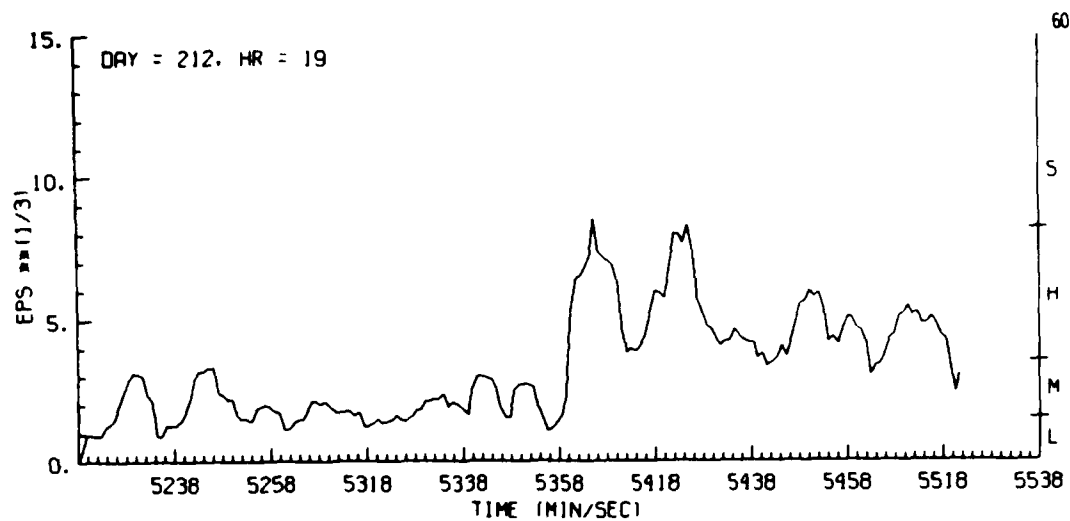


Figure G47. Estimates of Turbulence Severity Derived From Aircraft Gust Data, Day 212, Penetration 6

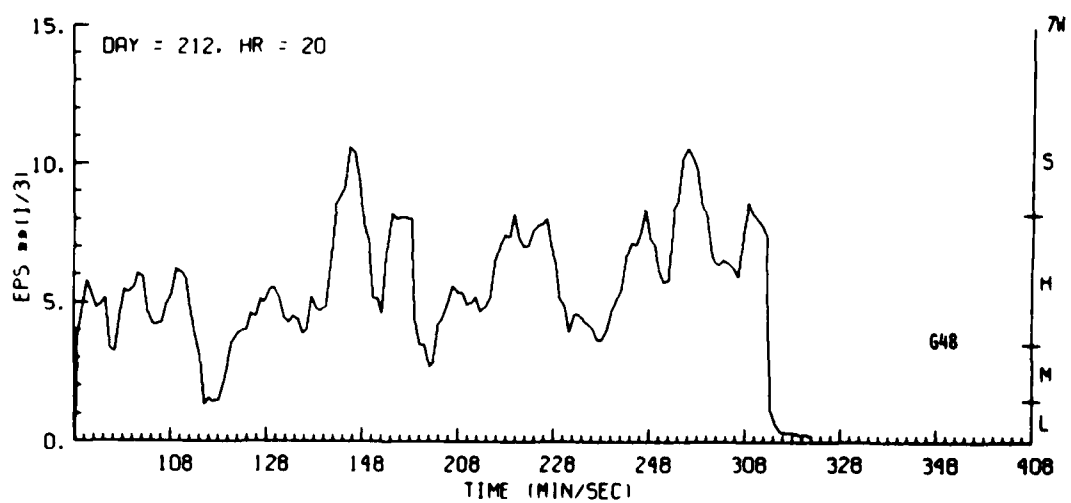
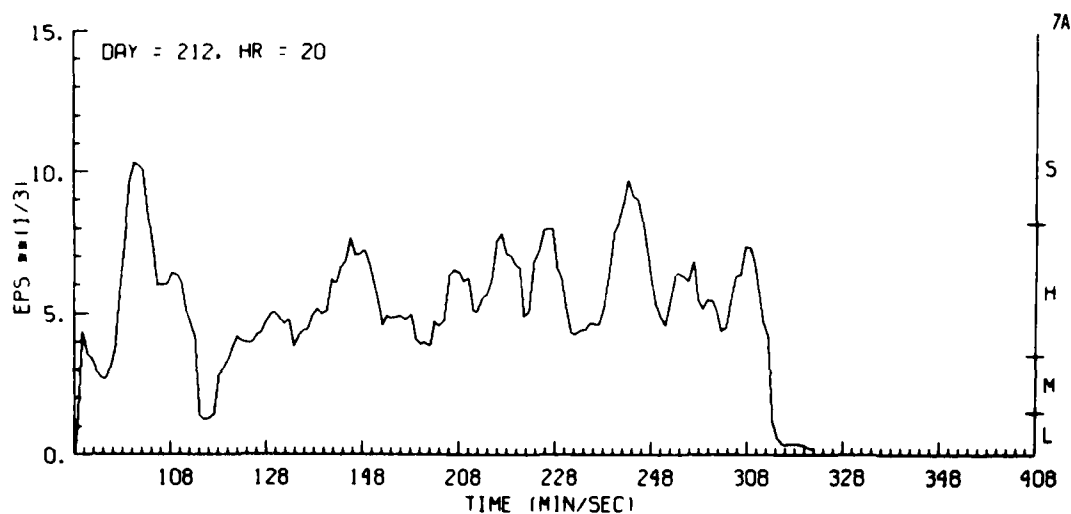
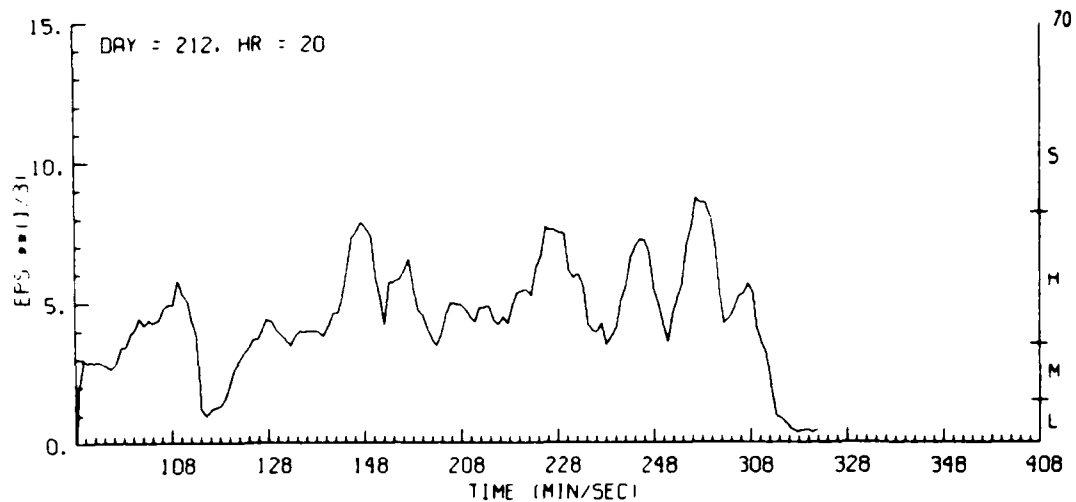


Figure G48. Estimates of Turbulence Severity Derived From Aircraft Gust Data, Day 212, Penetration 7

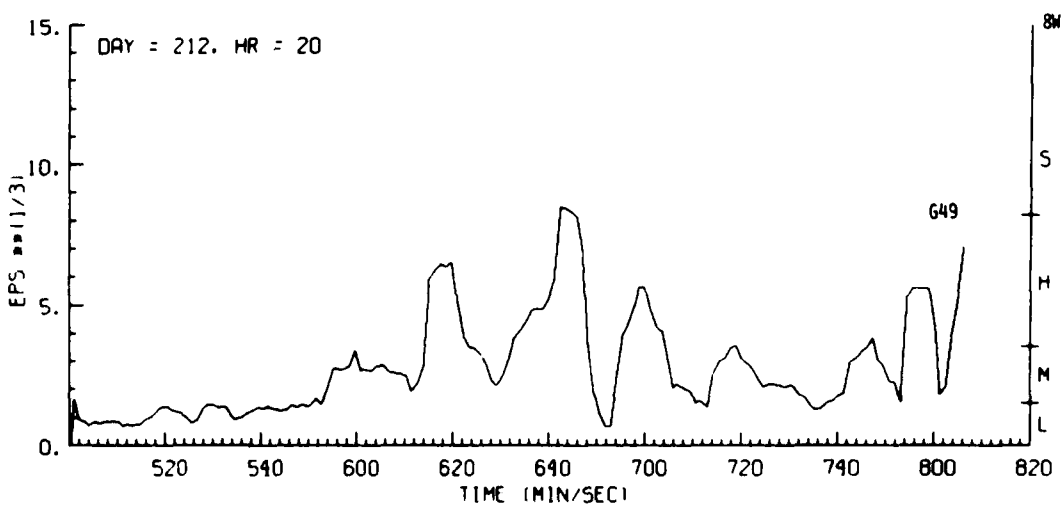
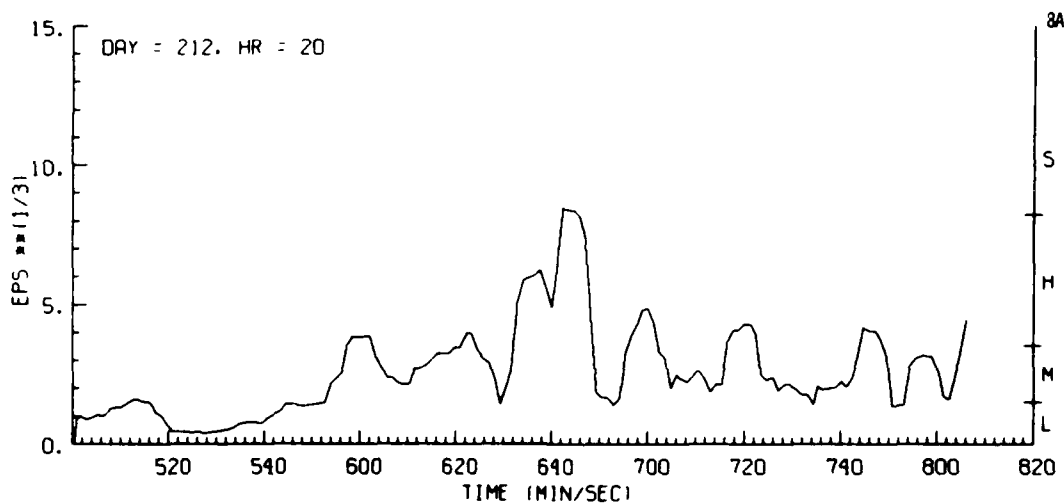
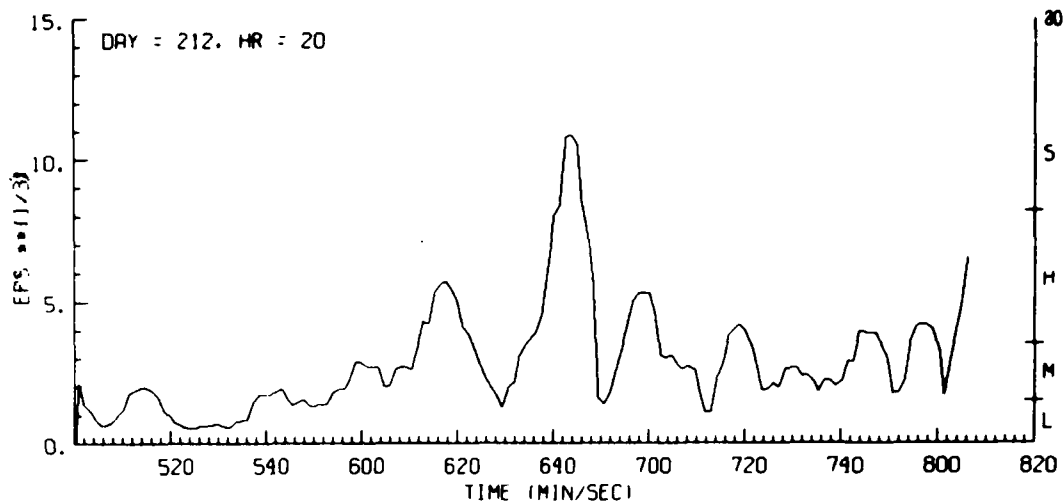


Figure G49. Estimates of Turbulence Severity Derived From Aircraft Gust Data, Day 212, Penetration 8

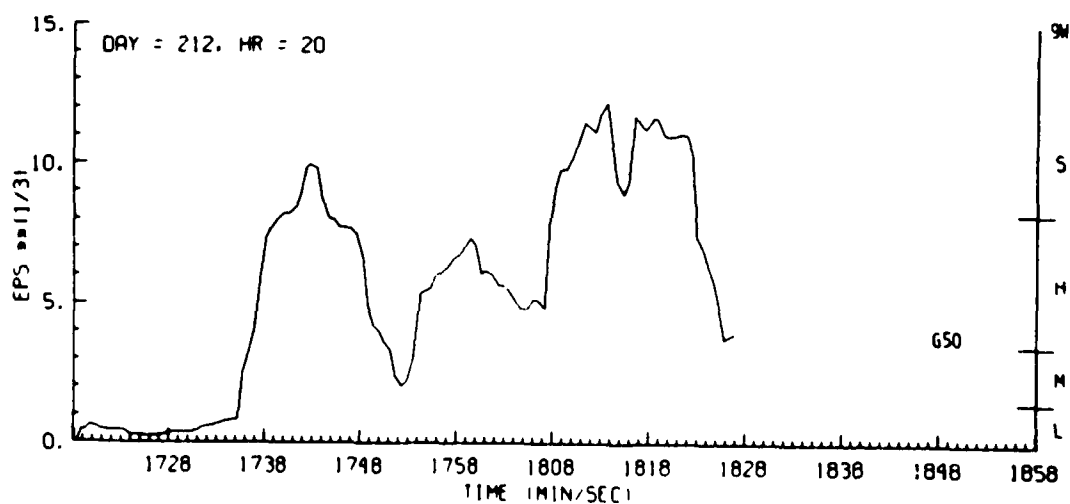
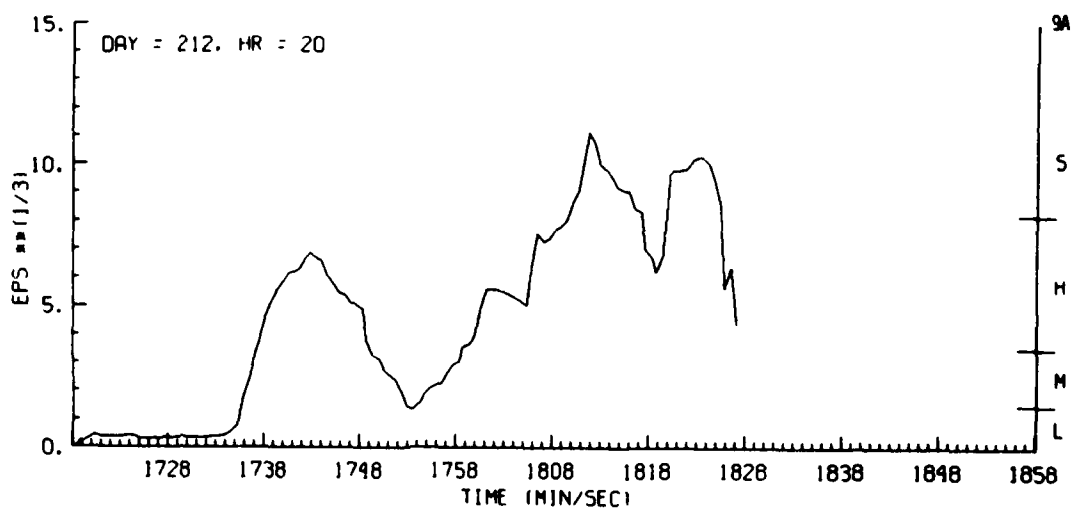
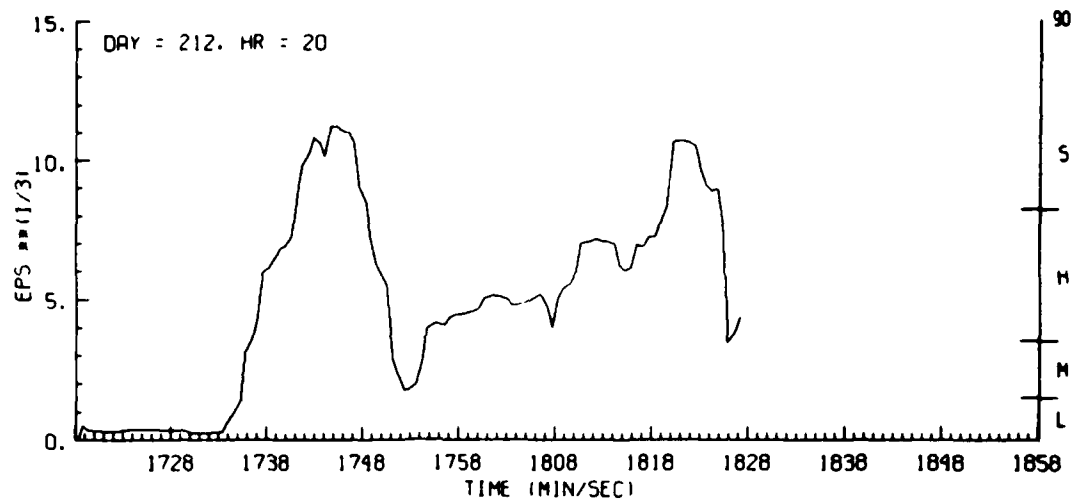


Figure G50. Estimates of Turbulence Severity Derived From Aircraft Gust Data, Day 212, Penetration 9

Appendix H

Estimates of Turbulence Severity Derived From Doppler Radar Data

Data for Figures H1 through H12 were acquired in 1981 and for Figures H13 through H55, in 1982.

Methods include structure function (lower dash), and variance with $\lambda_o = 0.5$ km (upper solid), $\lambda_o = 2.0$ km (upper dash), and $\lambda_o = \infty$ km (lower solid). Ordinate units are $\text{cm}^{2/3} \text{sec}^{-1}$.

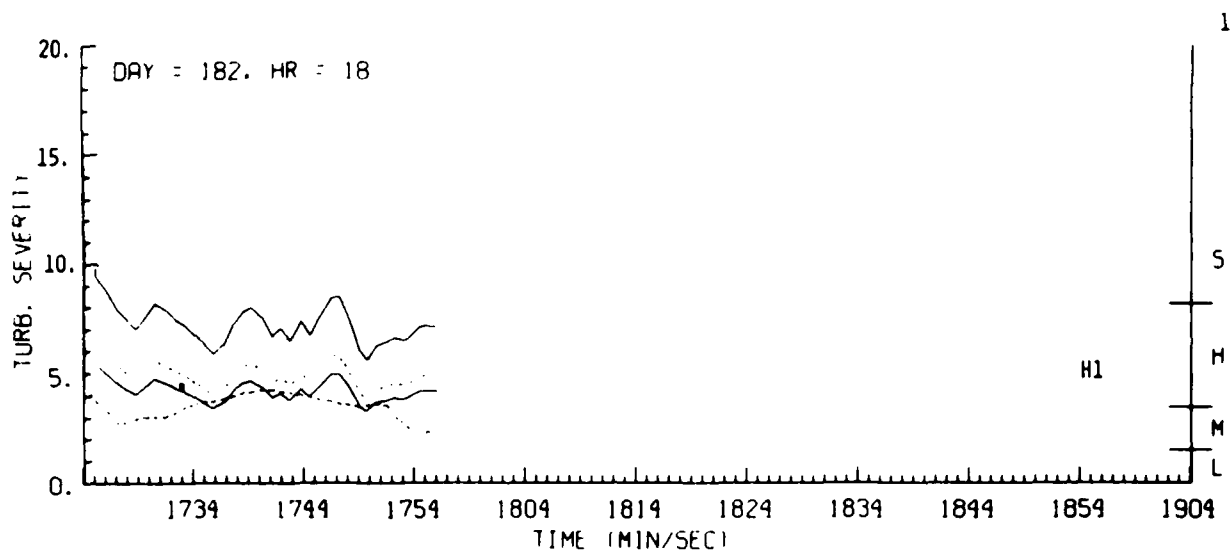


Figure H1. Estimates of Turbulence Severity Derived From Doppler Radar Data, Day 182, Penetration 1

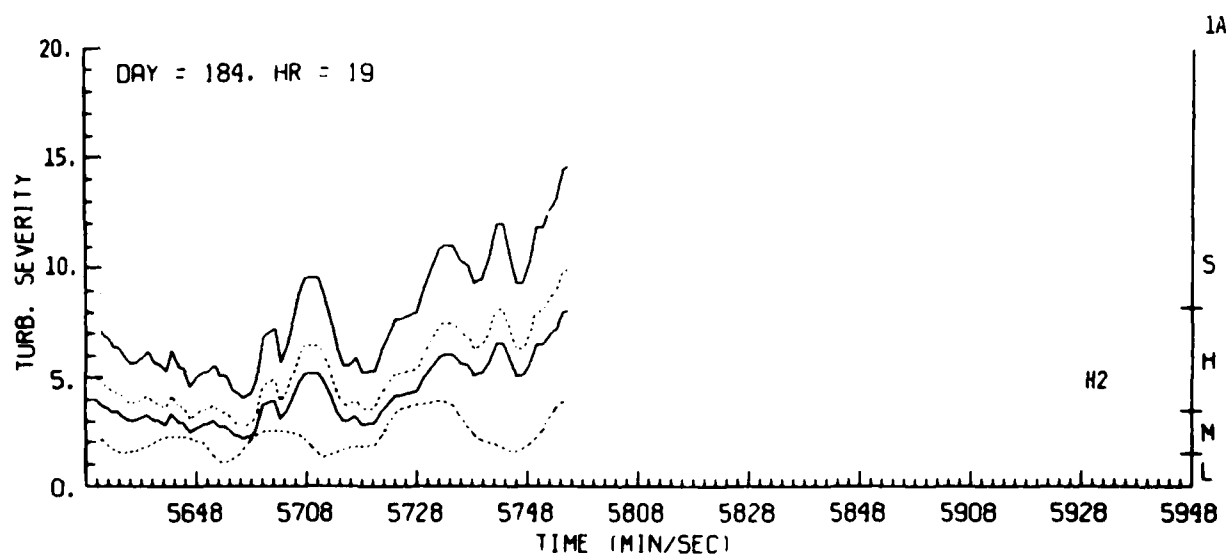


Figure H2. Estimates of Turbulence Severity Derived From Doppler Radar Data, Day 184, Penetration 1A

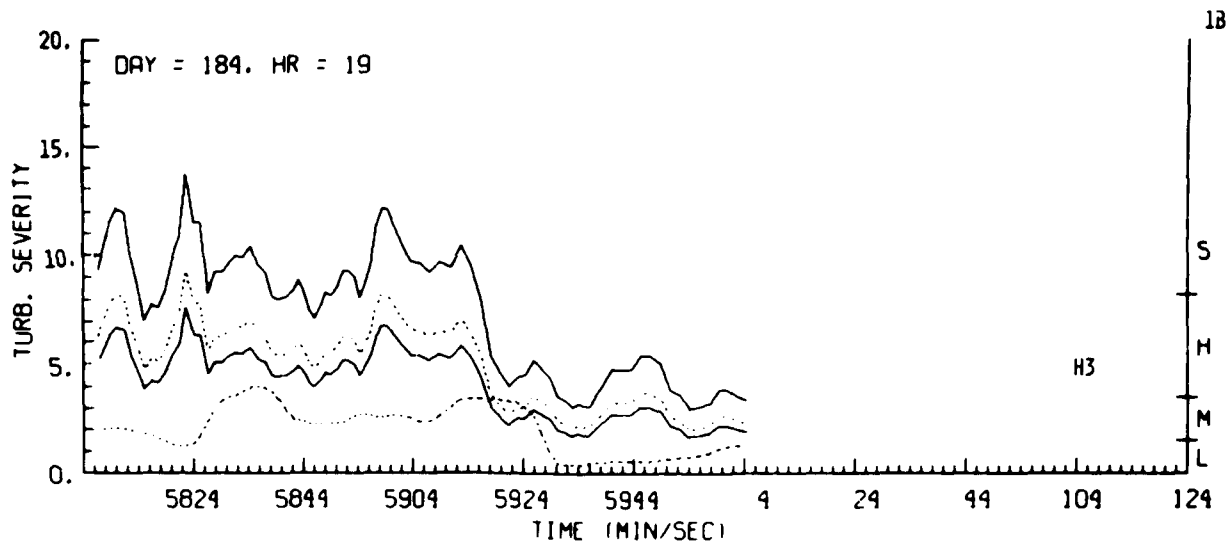


Figure H3. Estimates of Turbulence Severity Derived From Doppler Radar Data, Day 184, Penetration 1B

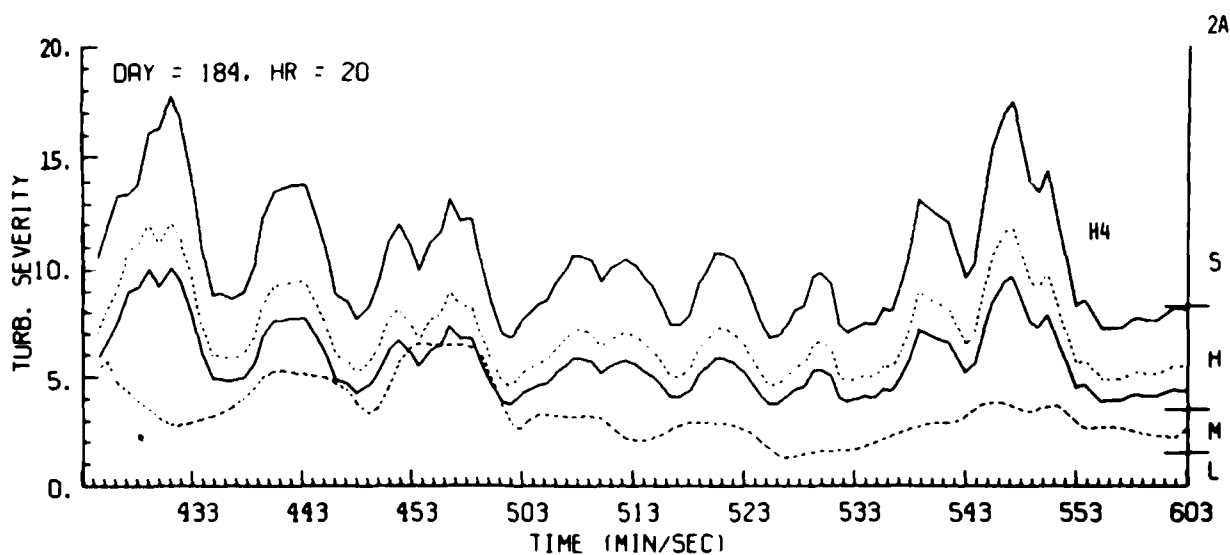


Figure H4. Estimates of Turbulence Severity Derived From Doppler Radar Data, Day 184, Penetration 2A

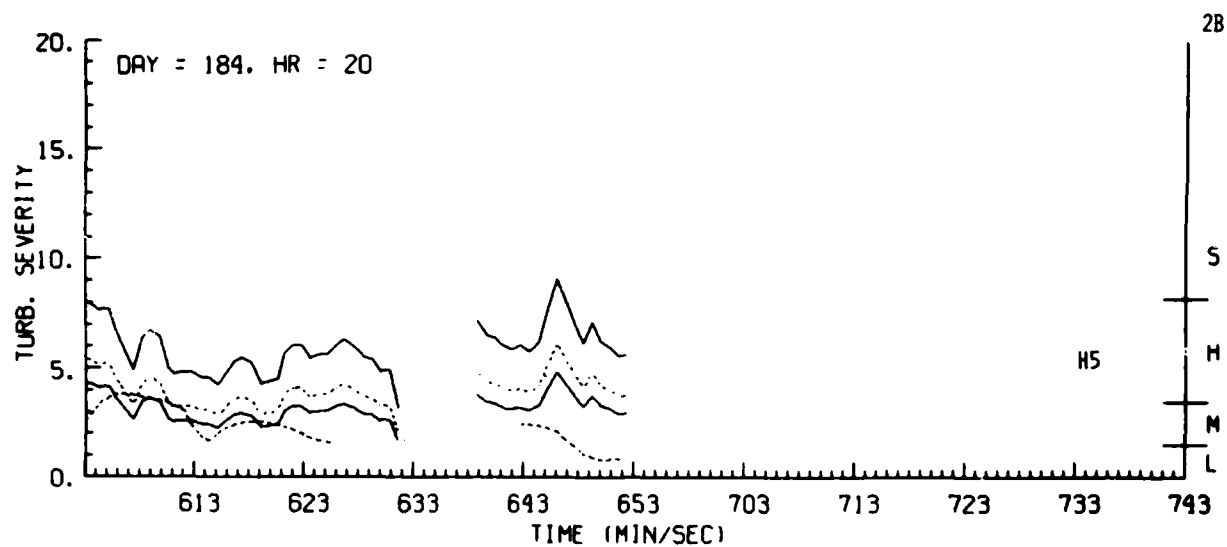


Figure H5. Estimates of Turbulence Severity Derived From Doppler Radar Data, Day 184, Penetration 2B

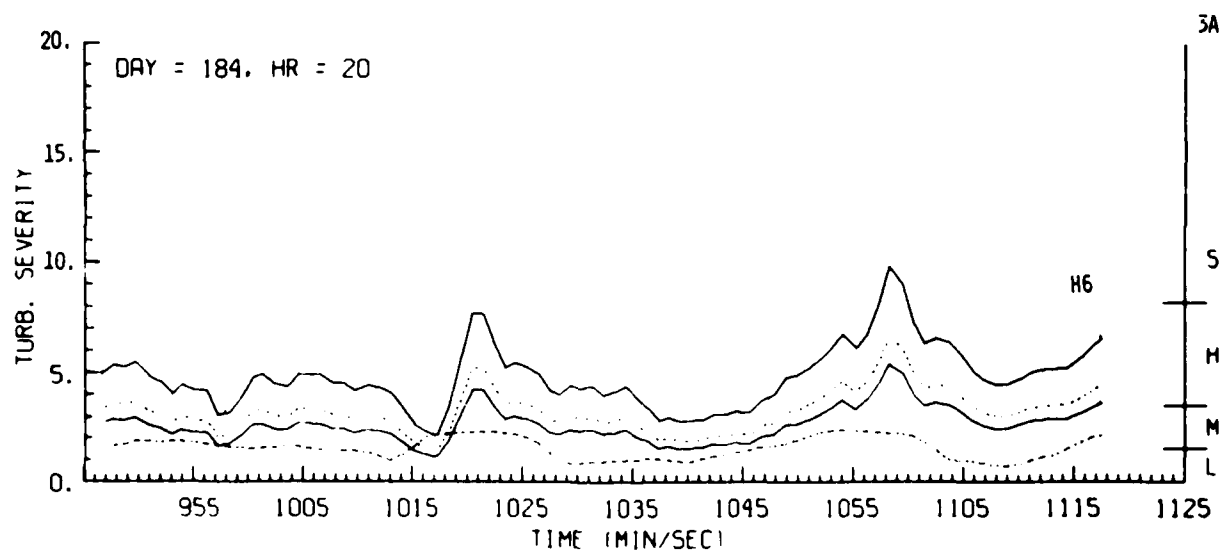


Figure H6. Estimates of Turbulence Severity Derived From Doppler Radar Data, Day 184, Penetration 3A

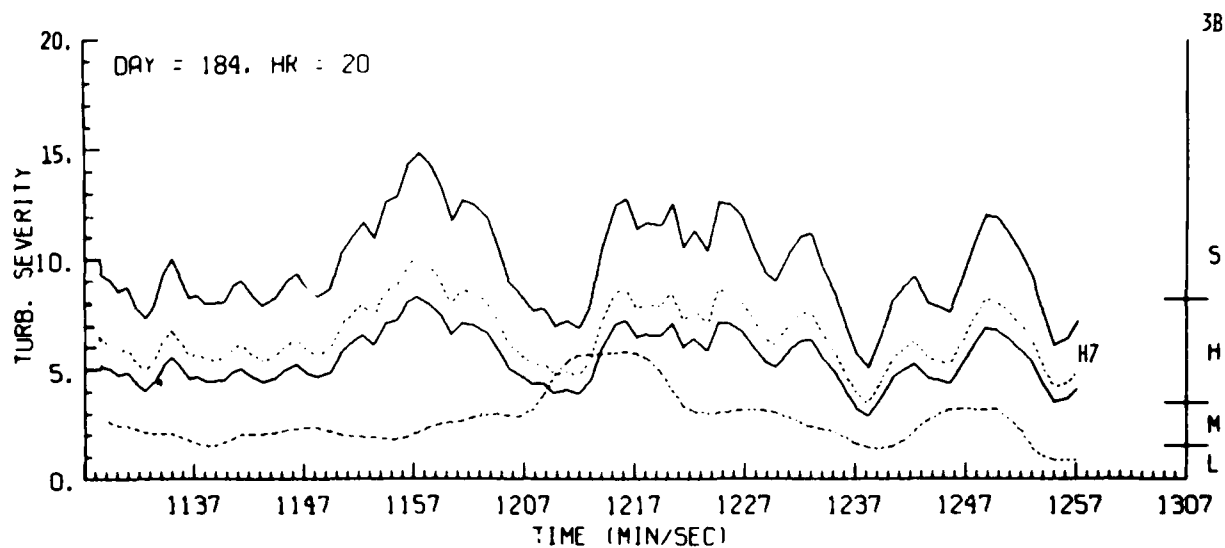


Figure H7. Estimates of Turbulence Severity Derived From Doppler Radar Data, Day 184, Penetration 3B

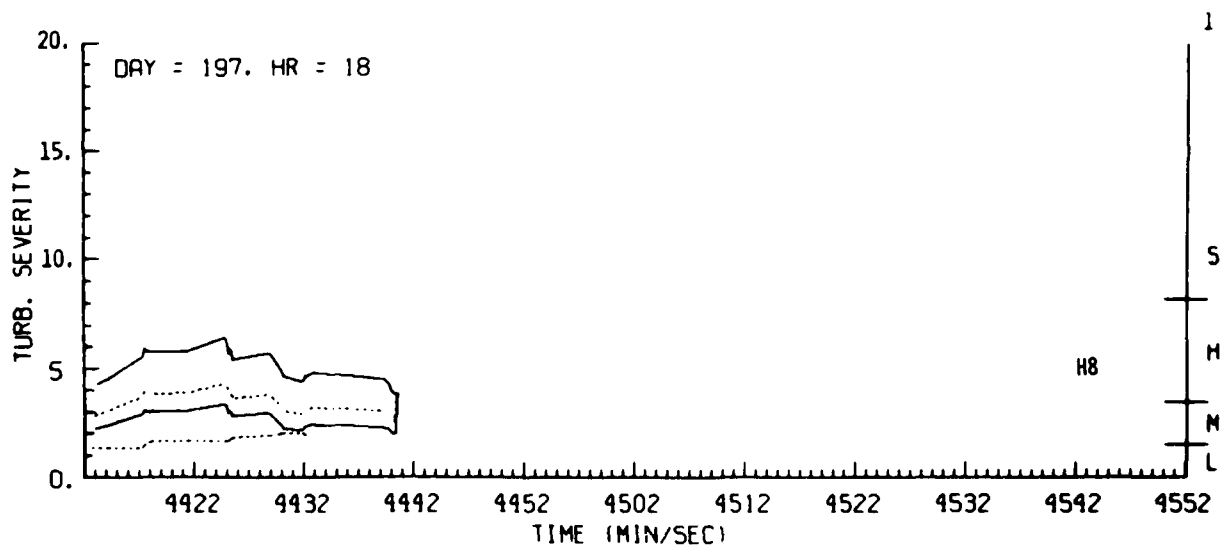


Figure H8. Estimates of Turbulence Severity Derived From Doppler Radar Data, Day 197, Penetration 1

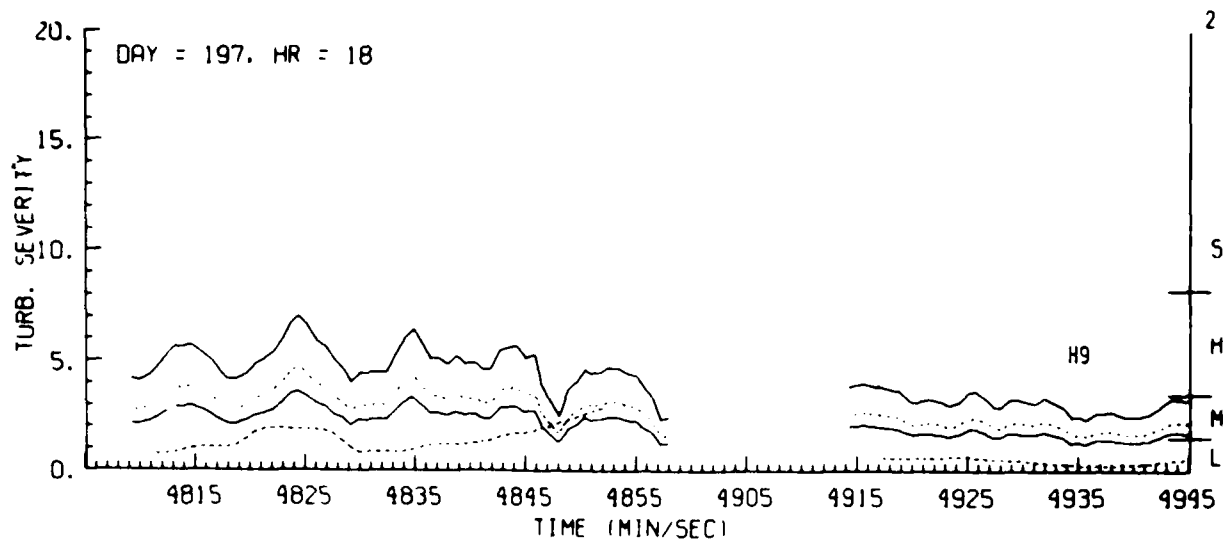


Figure H9. Estimates of Turbulence Severity Derived From Doppler Radar Data, Day 197, Penetration 2

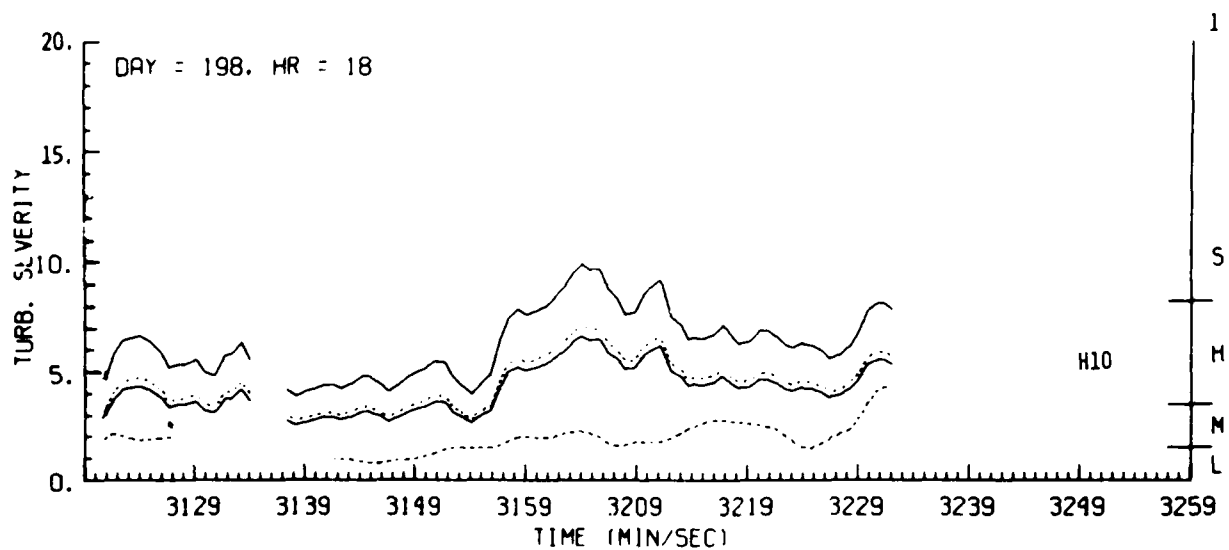


Figure H10. Estimates of Turbulence Severity Derived From Doppler Radar Data, Day 198, Penetration 1

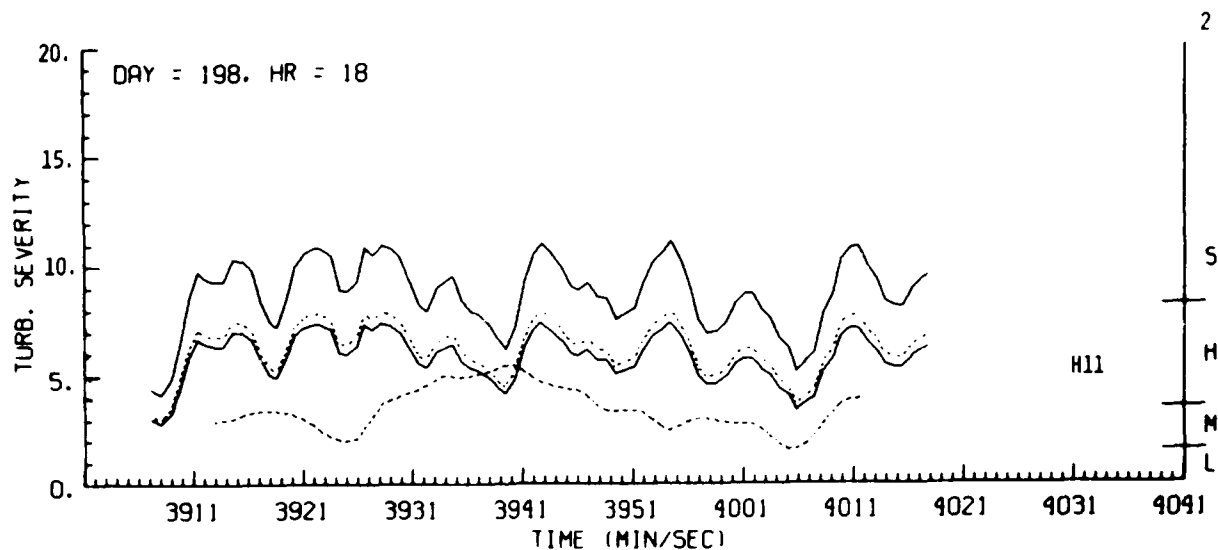


Figure H11. Estimates of Turbulence Severity Derived From Doppler Radar Data, Day 198, Penetration 2

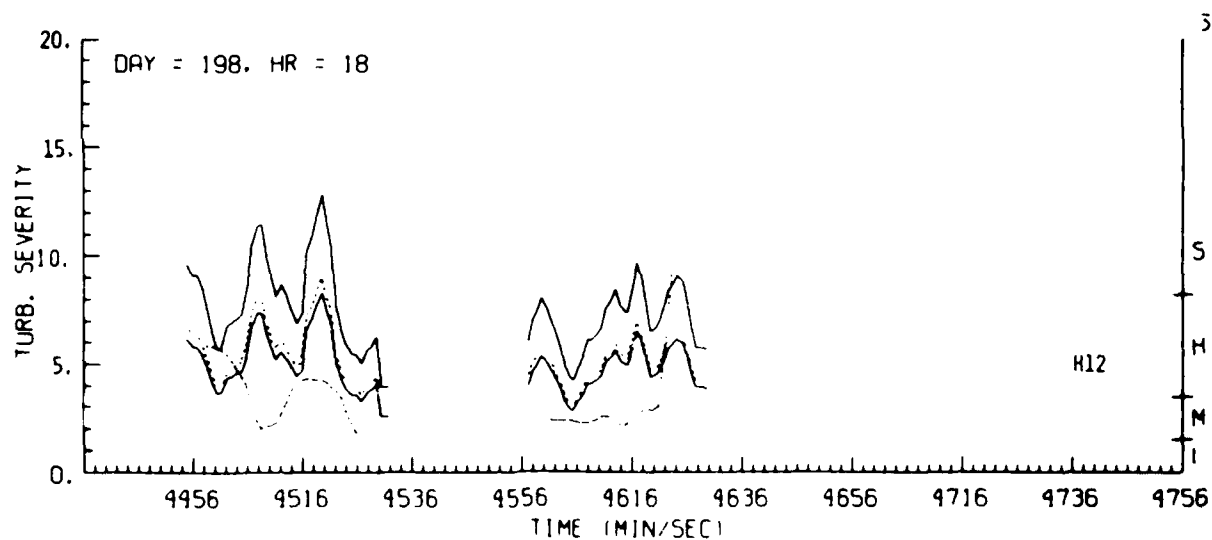


Figure H12. Estimates of Turbulence Severity Derived From Doppler Radar Data, Day 198, Penetration 3

AD-A160 420

JOINT AGENCY TURBULENCE EXPERIMENT(U) AIR FORCE
GEOPHYSICS LAB HANSCOM AFB MA A R BOHNE 21 JAN 85
AFGL-TR-85-0012

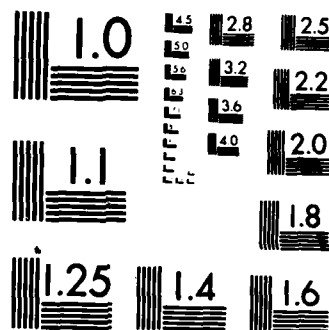
3/3

UNCLASSIFIED

F/G 17/9

NL

										END			
										FILED			
										DATE			



MICROCOPY RESOLUTION TEST CHART
NATIONAL BUREAU OF STANDARDS-1963-A

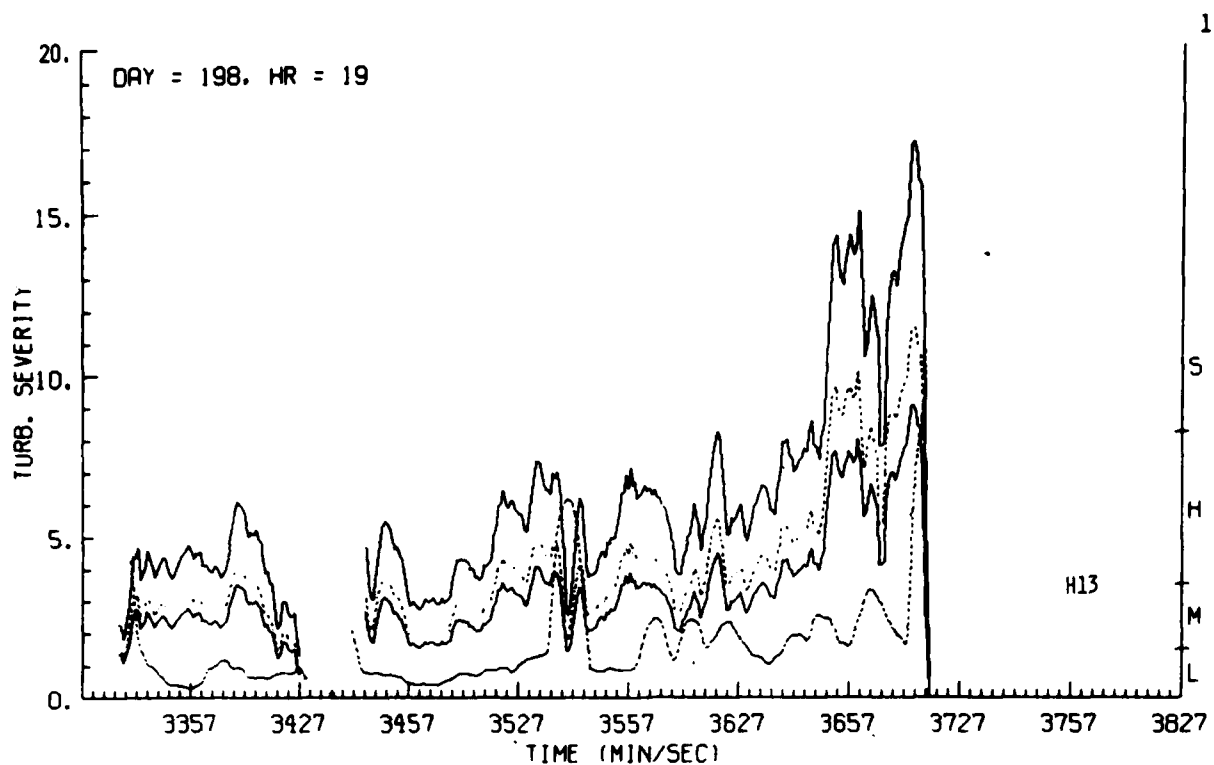


Figure H13. Estimates of Turbulence Severity Derived From Doppler Radar Data, Day 198, Penetration 1

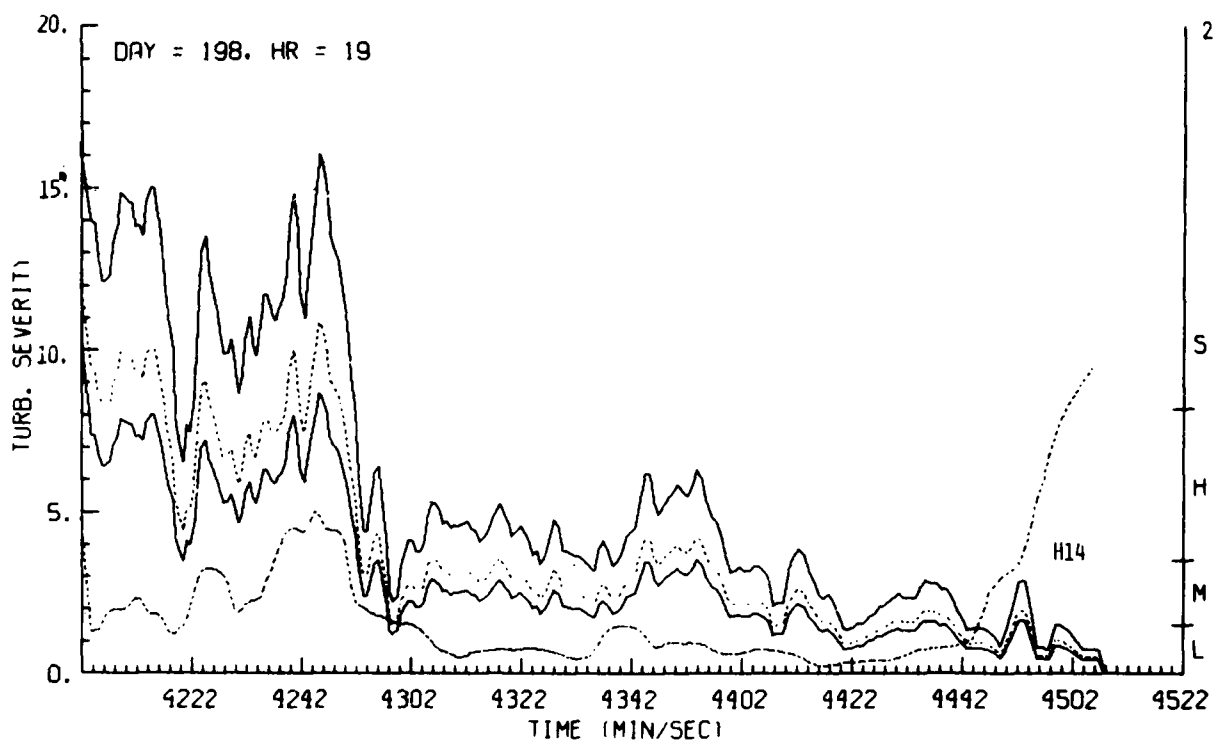


Figure H14. Estimates of Turbulence Severity Derived From Doppler Radar Data, Day 198, Penetration 2

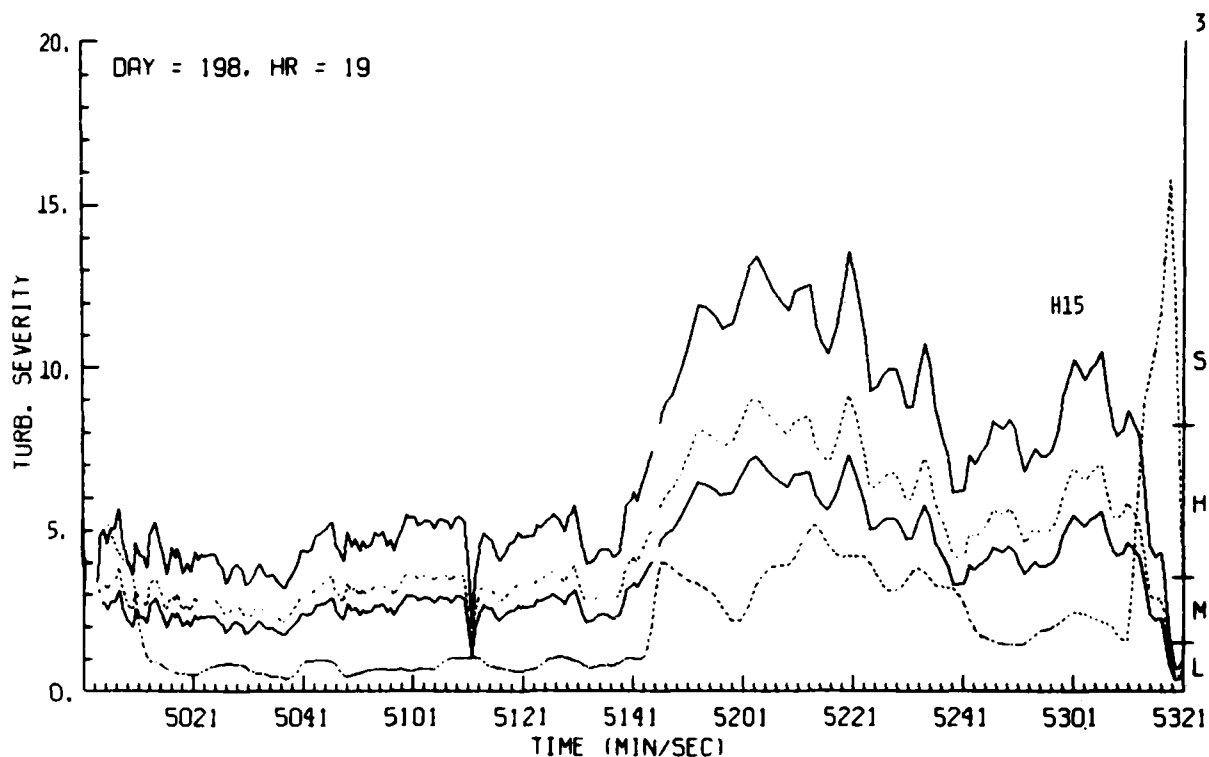


Figure H15. Estimates of Turbulence Severity Derived From Doppler Radar Data, Day 198, Penetration 3

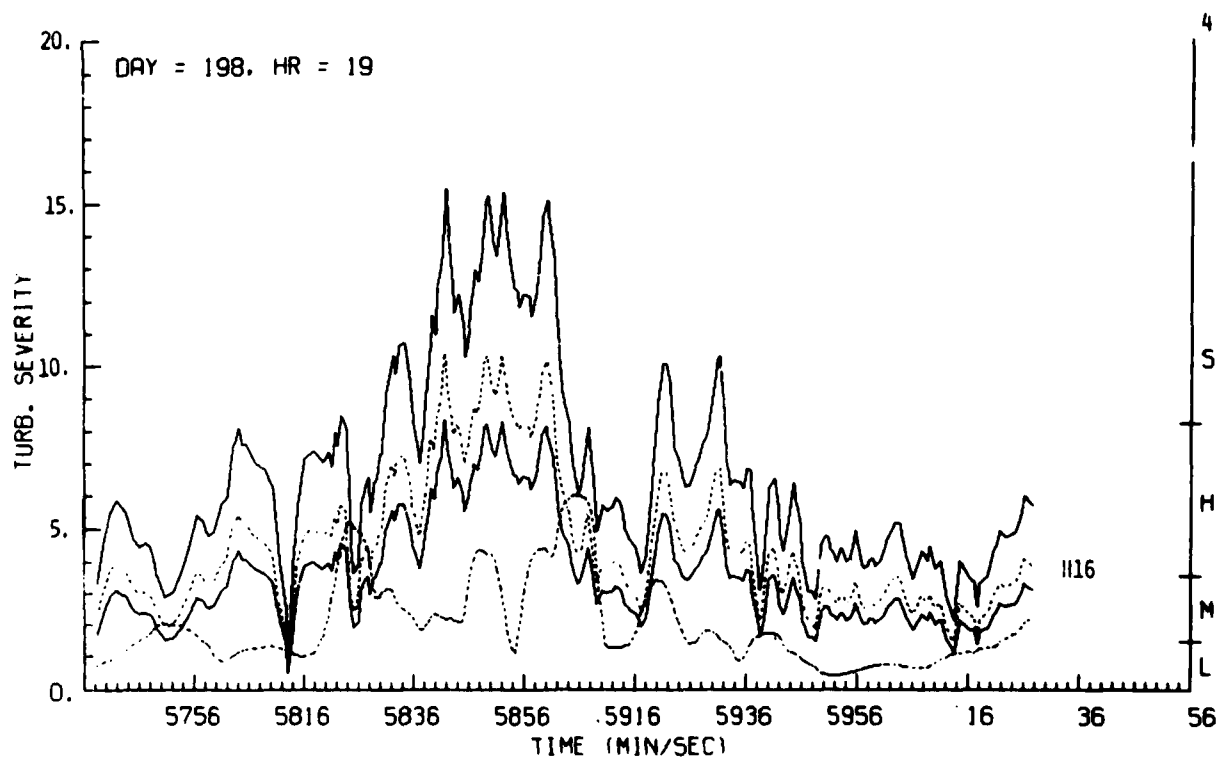


Figure H16. Estimates of Turbulence Severity Derived From Doppler Radar Data, Day 198, Penetration 4

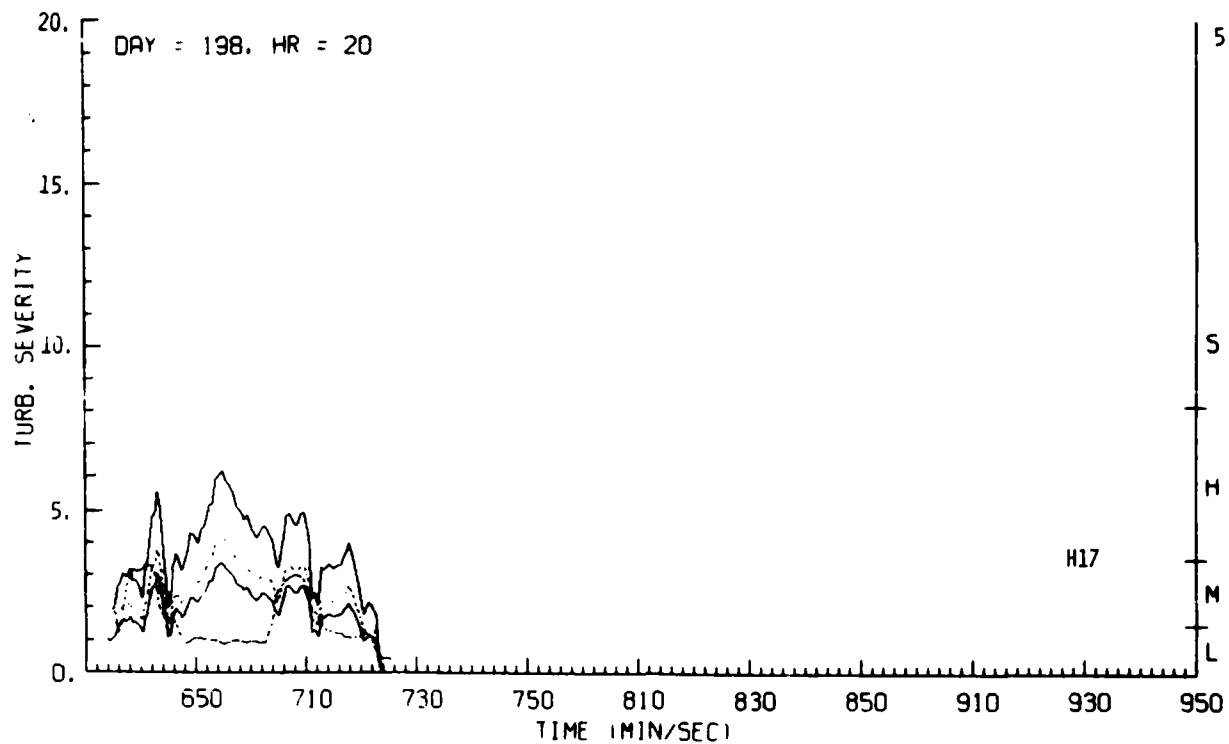


Figure H17. Estimates of Turbulence Severity Derived From Doppler Radar Data, Day 198, Penetration 5

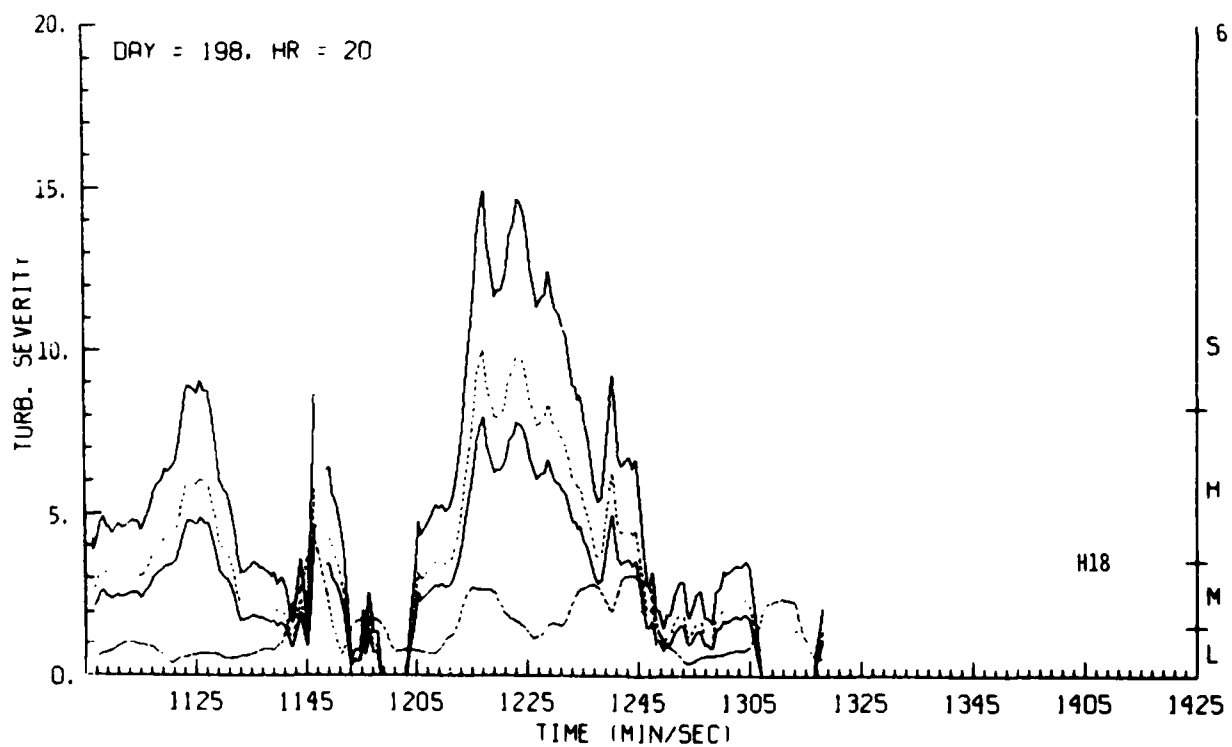


Figure H18. Estimates of Turbulence Severity Derived From Doppler Radar Data, Day 198, Penetration 6

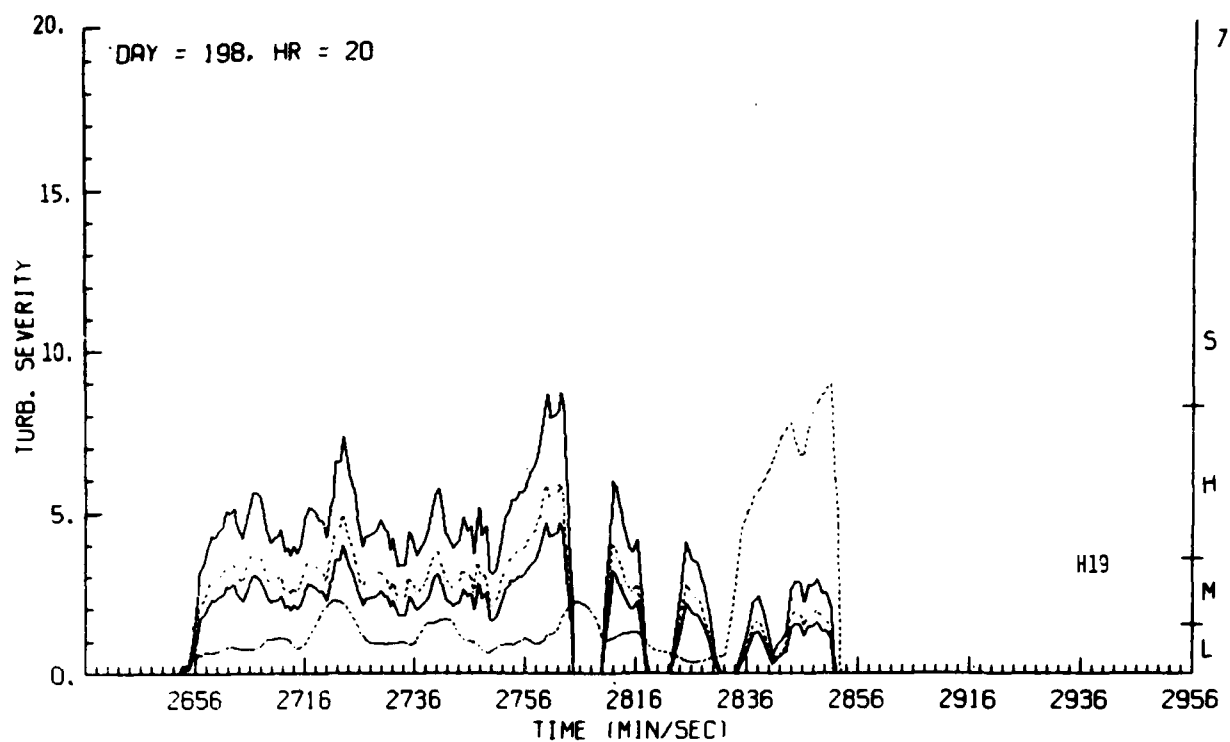


Figure H19. Estimates of Turbulence Severity Derived From Doppler Radar Data, Day 198, Penetration 7

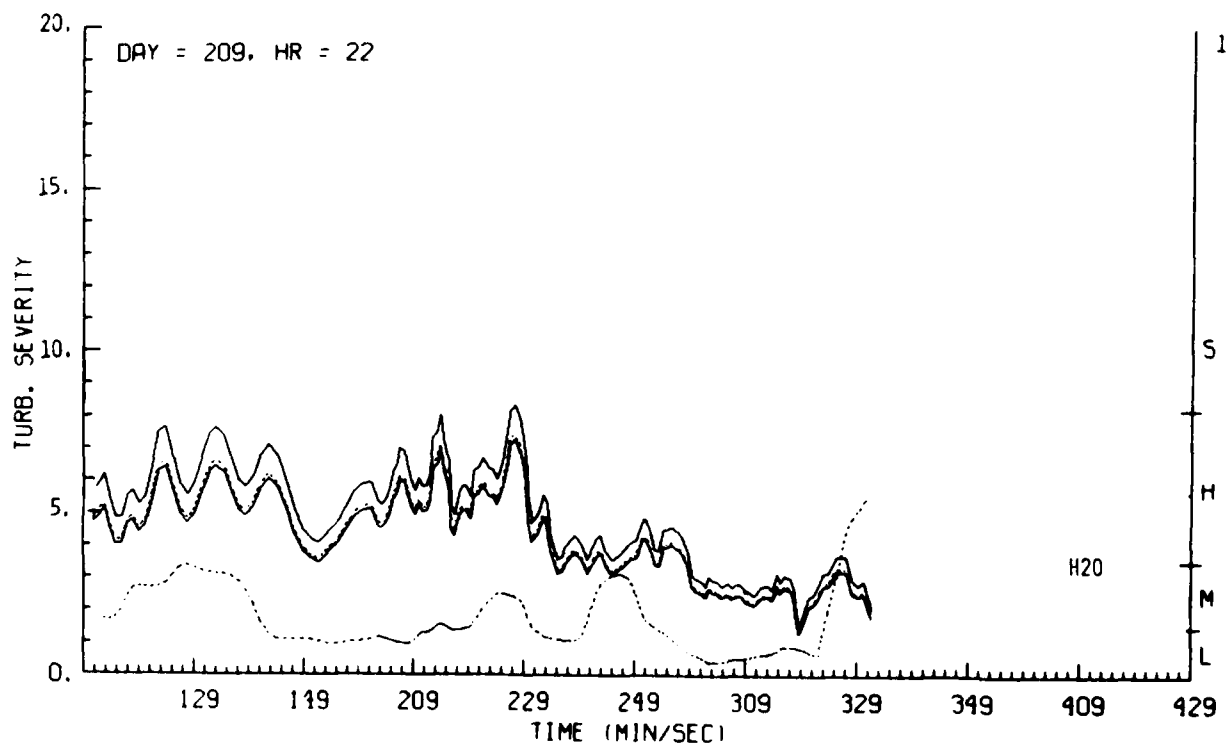


Figure H20. Estimates of Turbulence Severity Derived From Doppler Radar Data, Day 209, Penetration 1

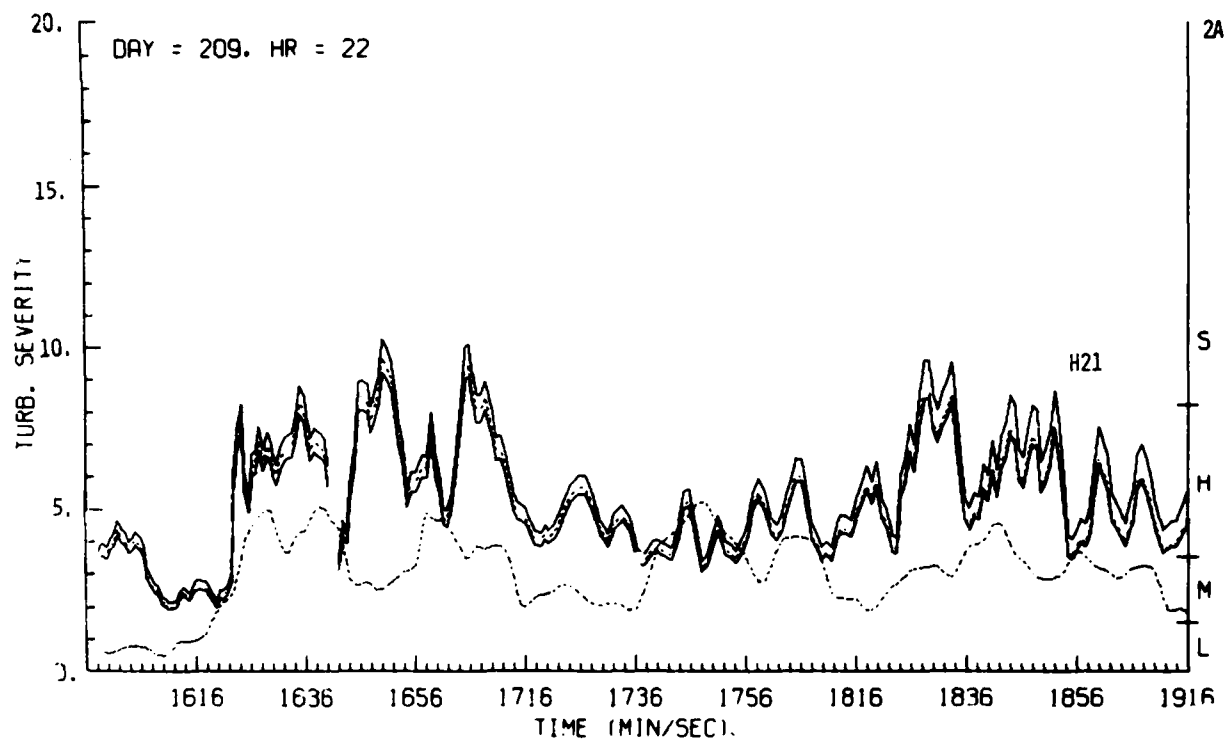


Figure H21. Estimates of Turbulence Severity Derived From Doppler Radar Data, Day 209, Penetration 2A

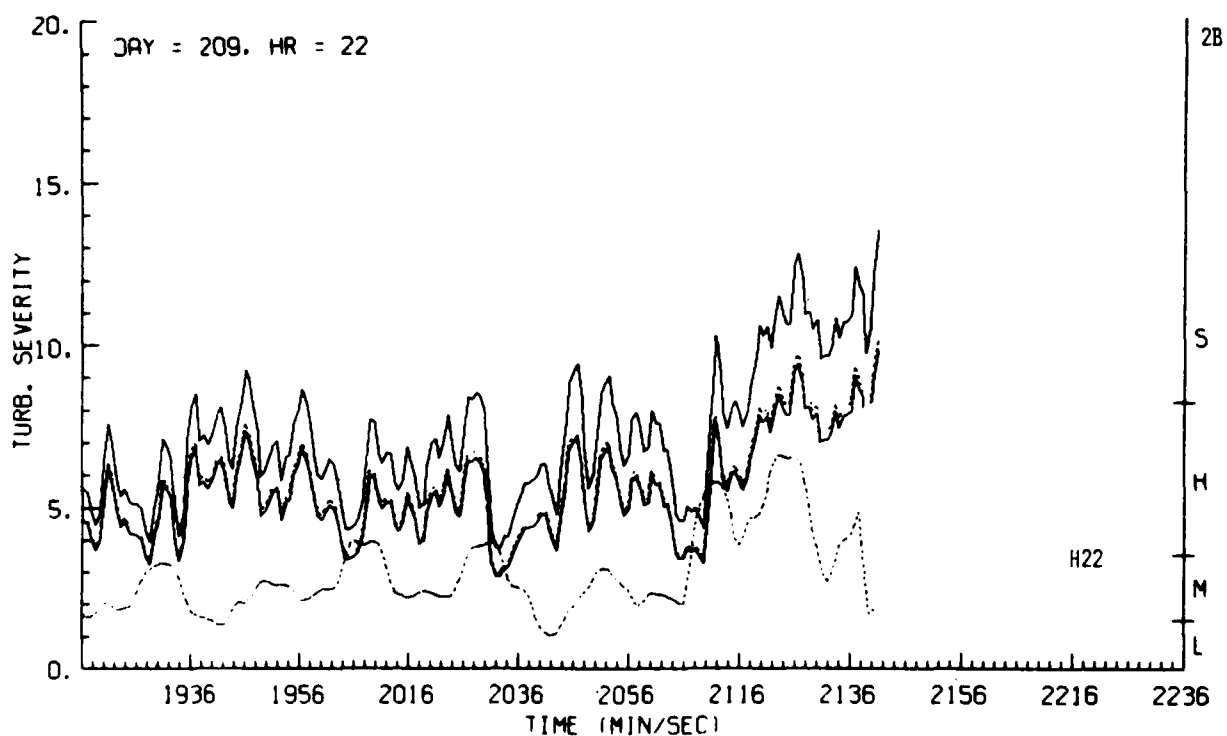


Figure H22. Estimates of Turbulence Severity Derived From Doppler Radar Data, Day 209, Penetration 2B

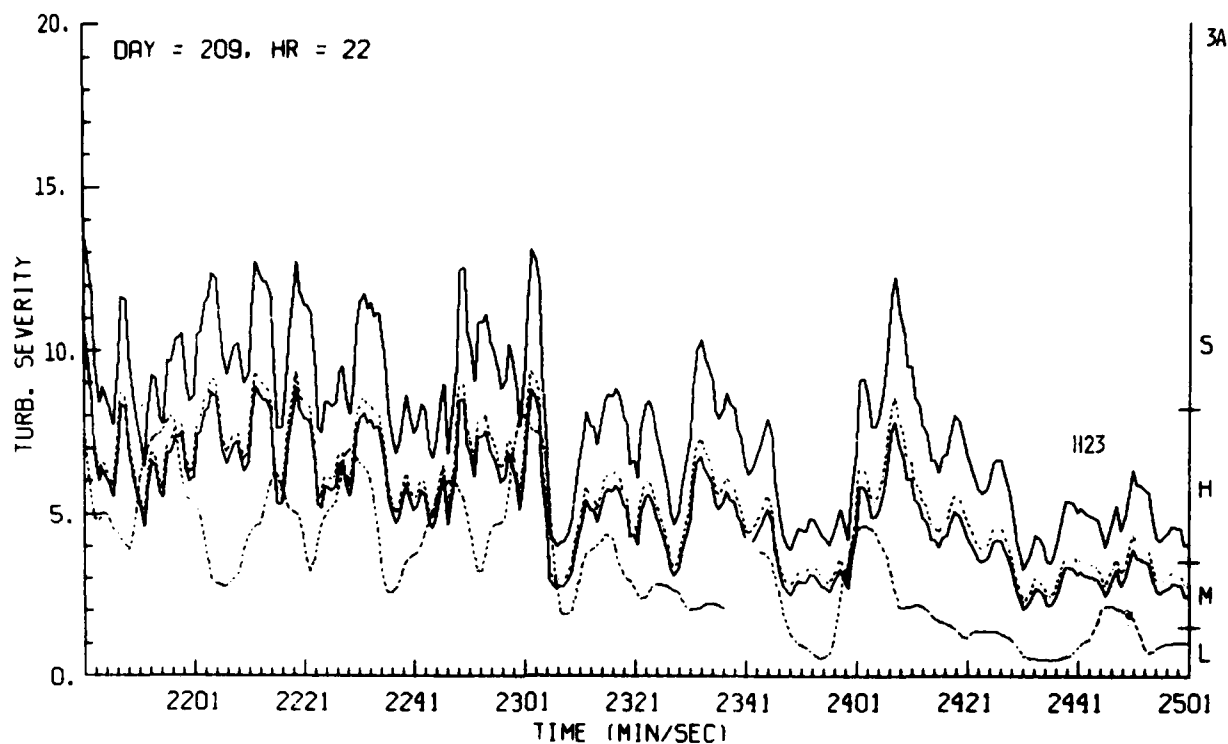


Figure H23. Estimates of Turbulence Severity Derived From Doppler Radar Data, Day 209, Penetration 3A

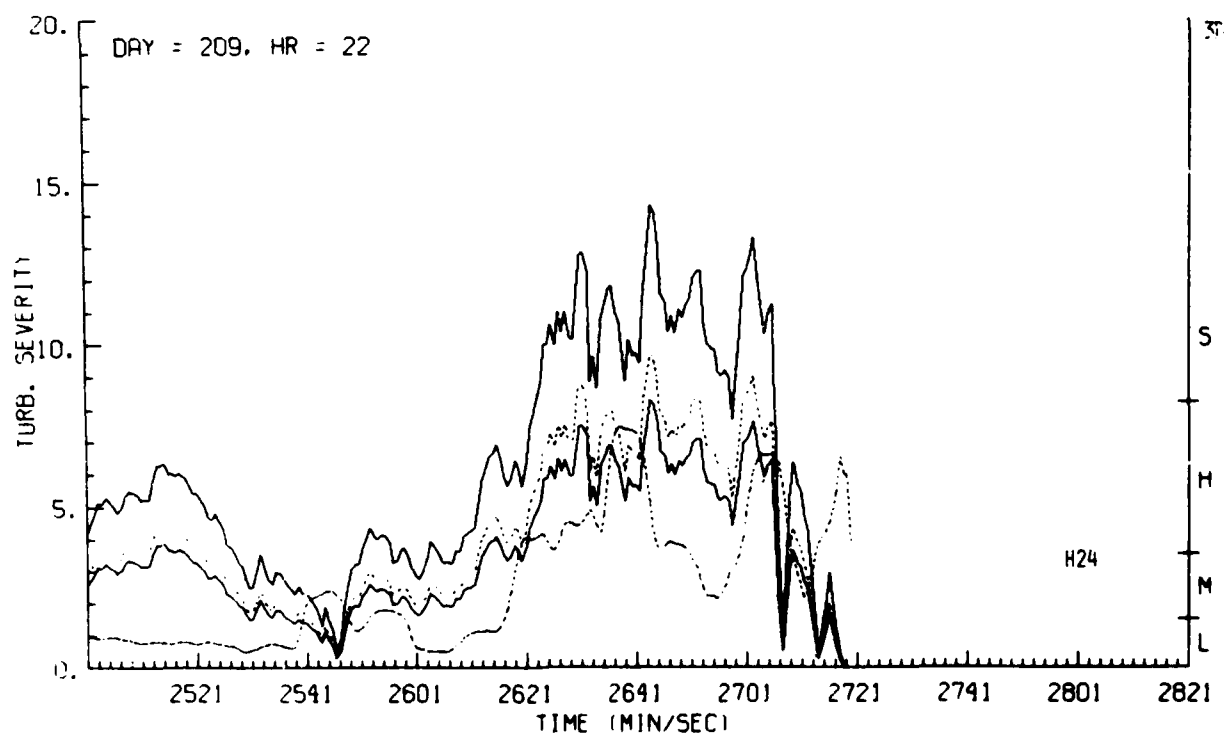


Figure H24. Estimates of Turbulence Severity Derived From Doppler Radar Data, Day 209, Penetration 3B

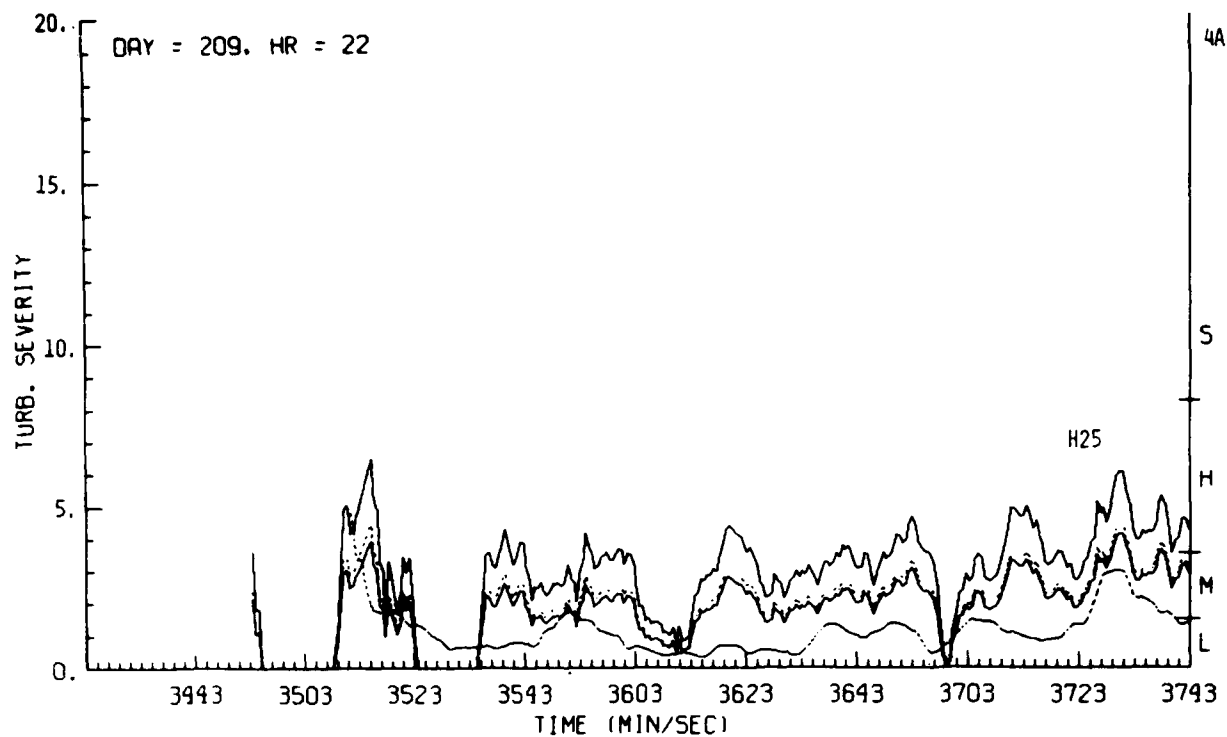


Figure H25. Estimates of Turbulence Severity Derived From Doppler Radar Data, Day 209, Penetration 4A

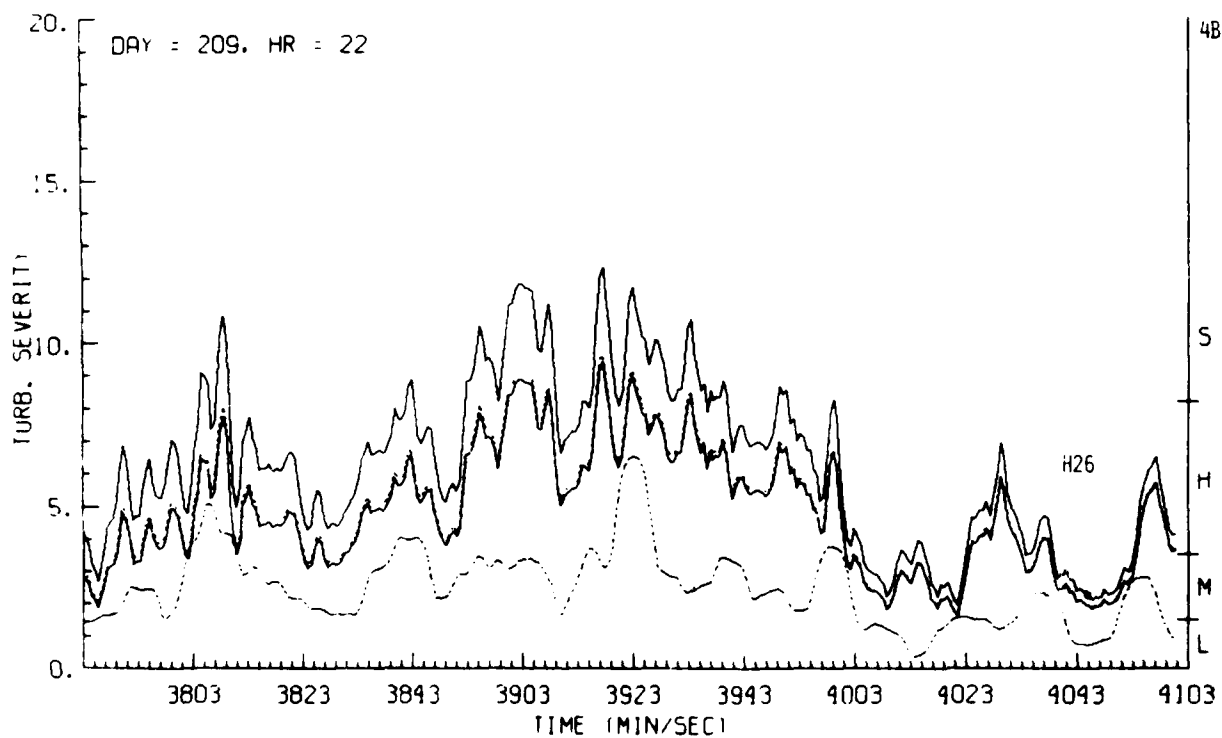


Figure H26. Estimates of Turbulence Severity Derived From Doppler Radar Data, Day 209, Penetration 4B

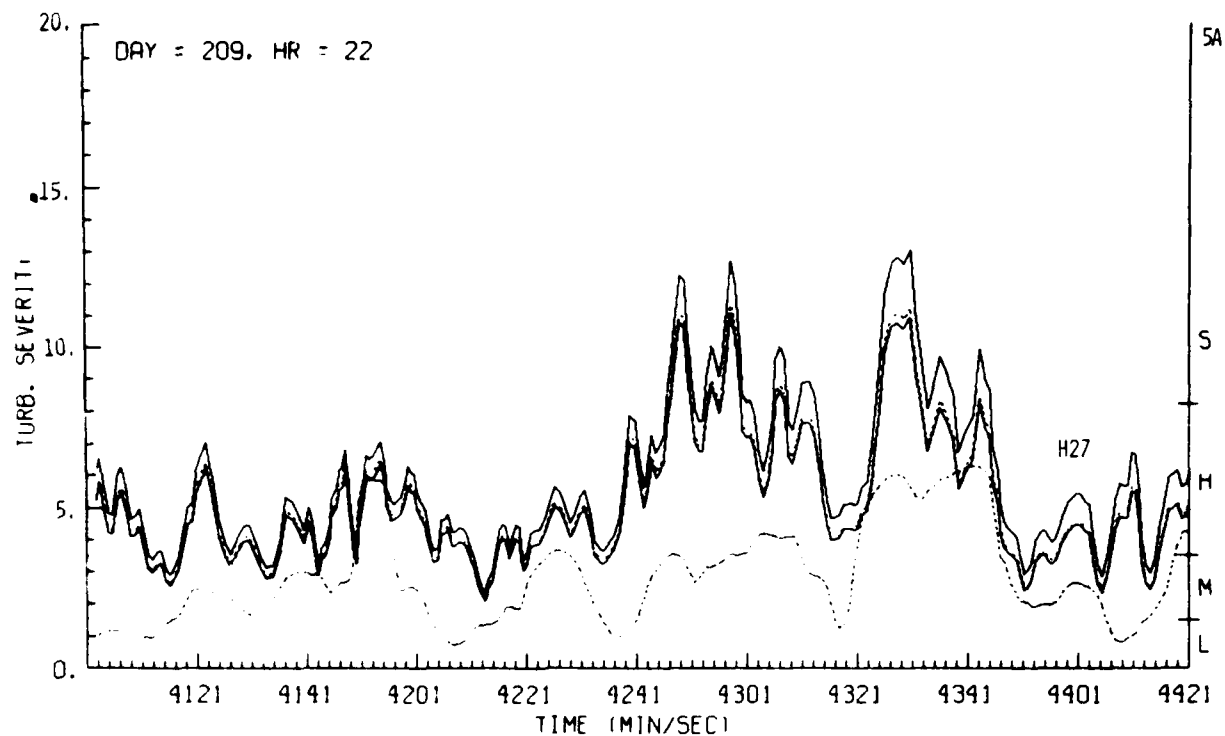


Figure H27. Estimates of Turbulence Severity Derived From Doppler Radar Data, Day 209, Penetration 5A

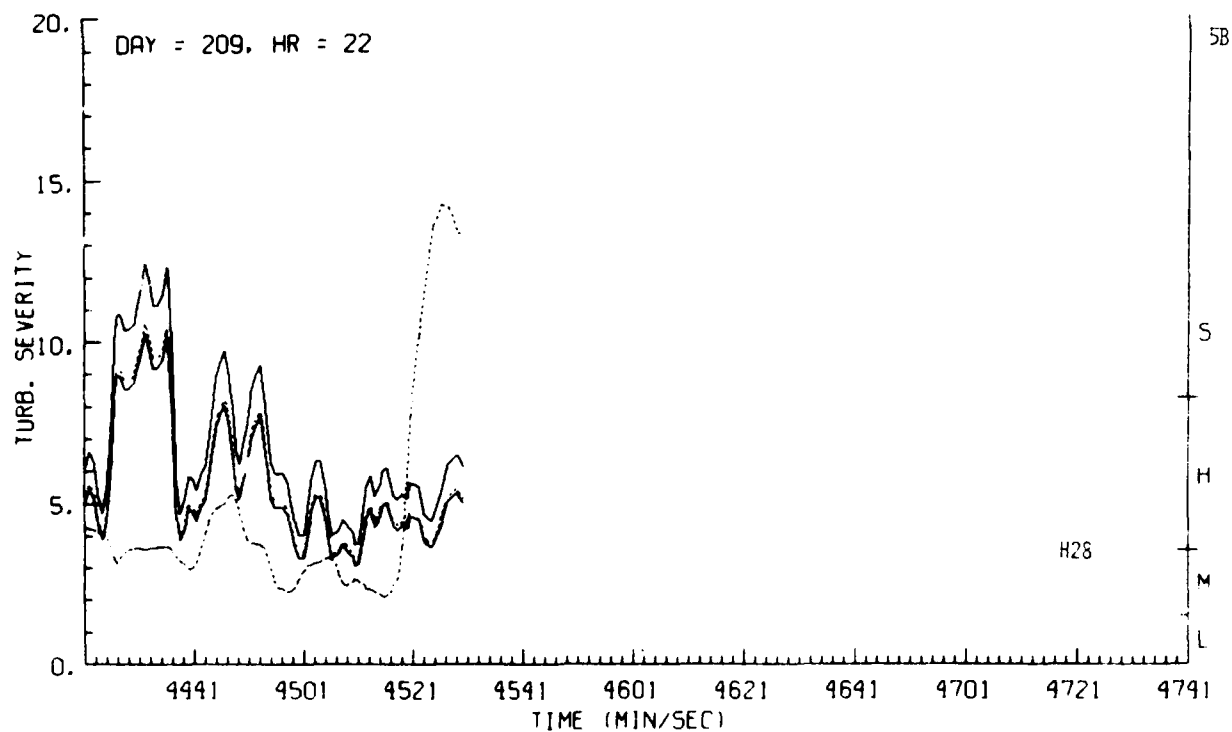


Figure H28. Estimates of Turbulence Severity Derived From Doppler Radar Data, Day 209, Penetration 5B

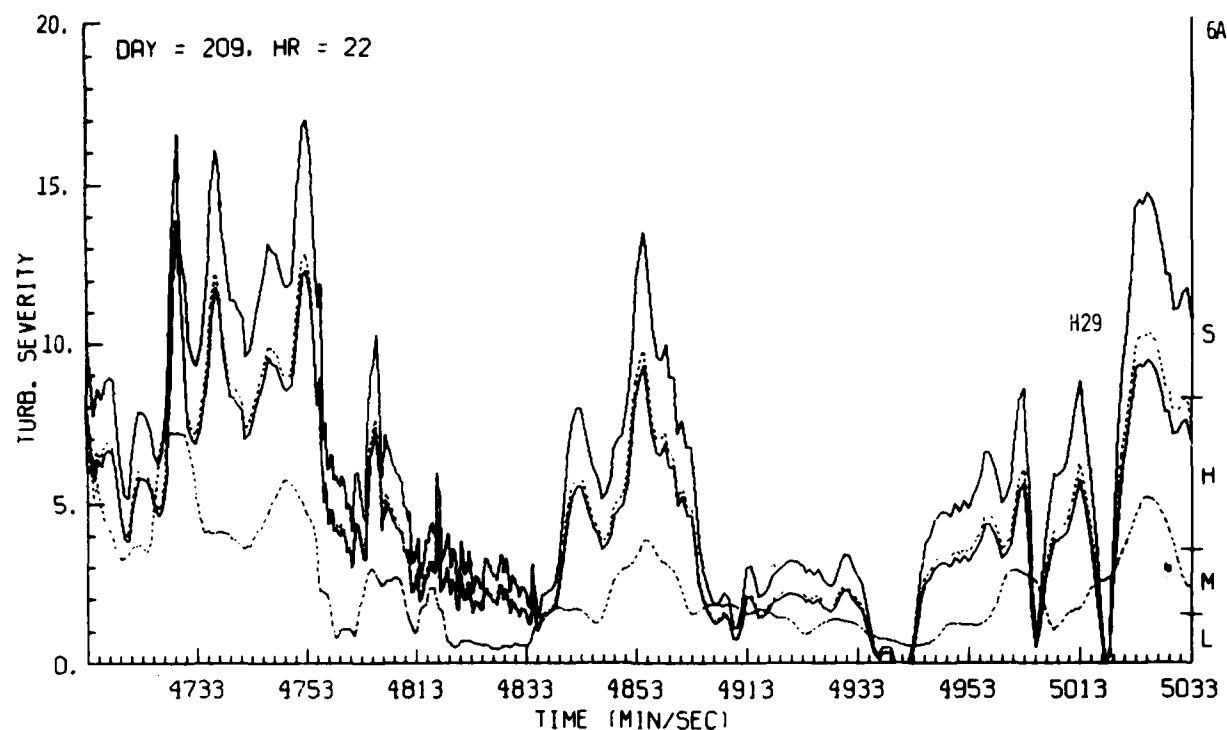


Figure H29. Estimates of Turbulence Severity Derived From Doppler Radar Data, Day 209, Penetration 6A

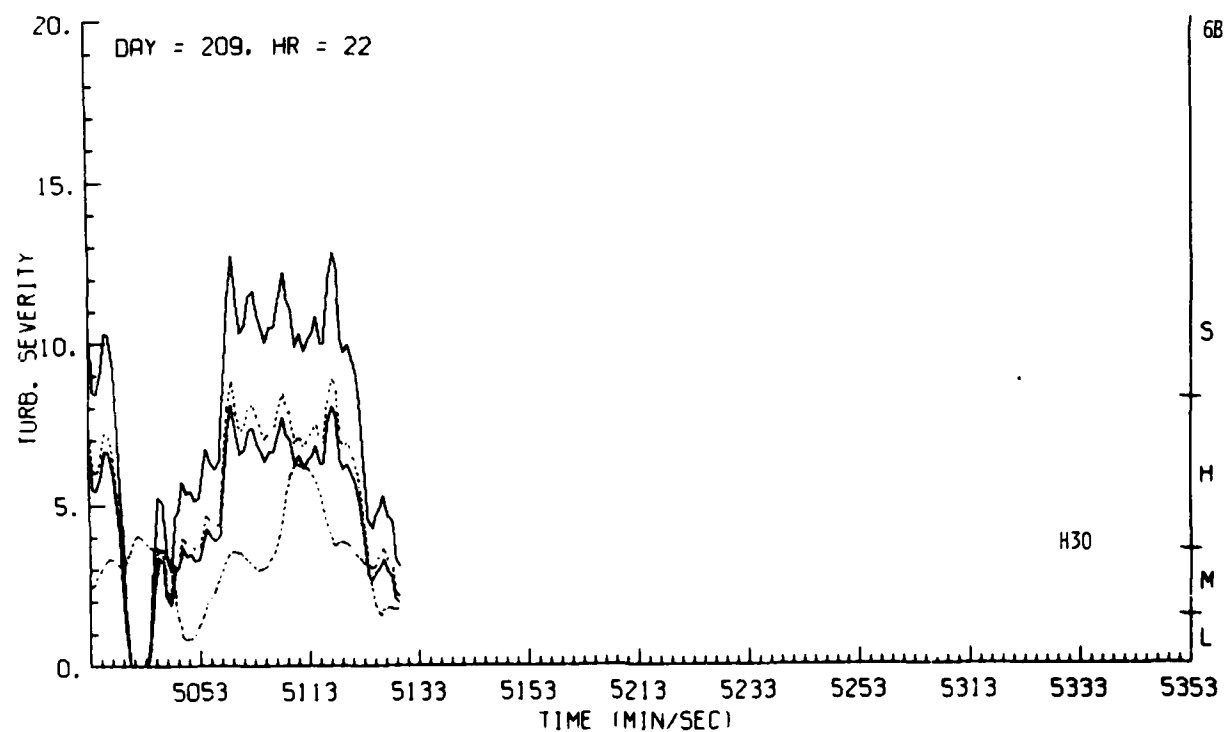


Figure H30. Estimates of Turbulence Severity Derived From Doppler Radar Data, Day 209, Penetration 6B

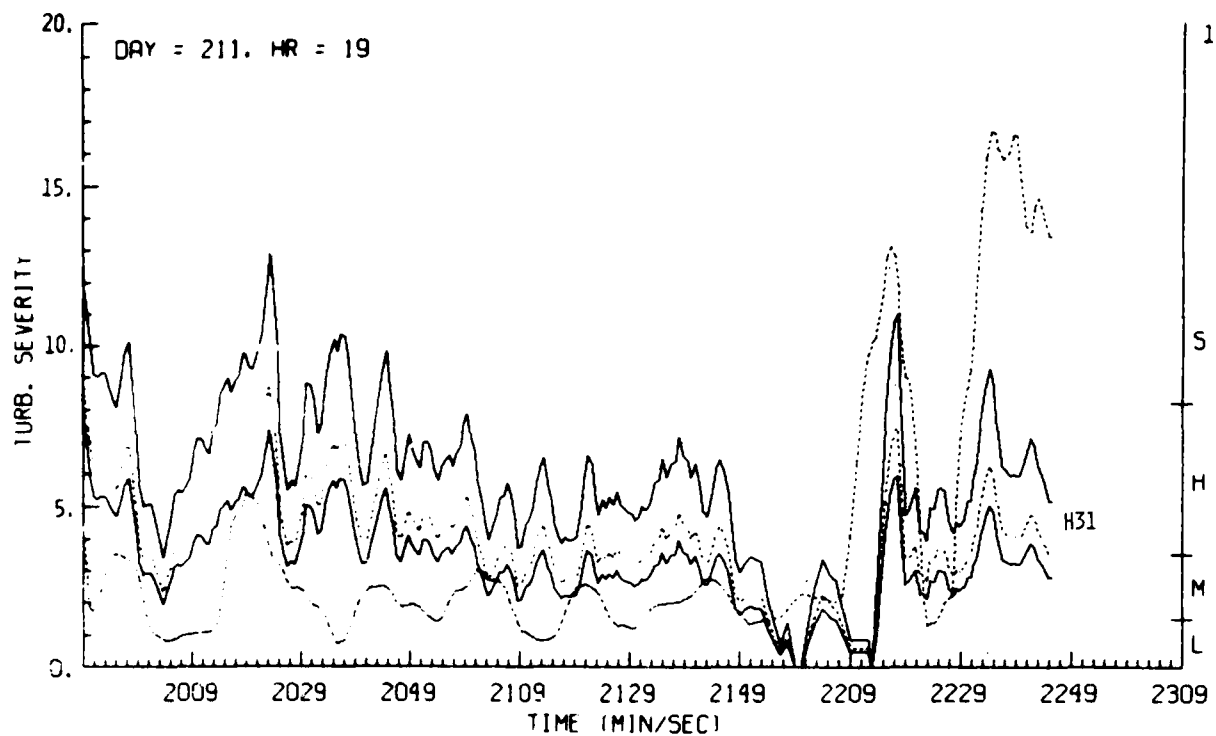


Figure H31. Estimates of Turbulence Severity Derived From Doppler Radar Data, Day 211, Penetration 1

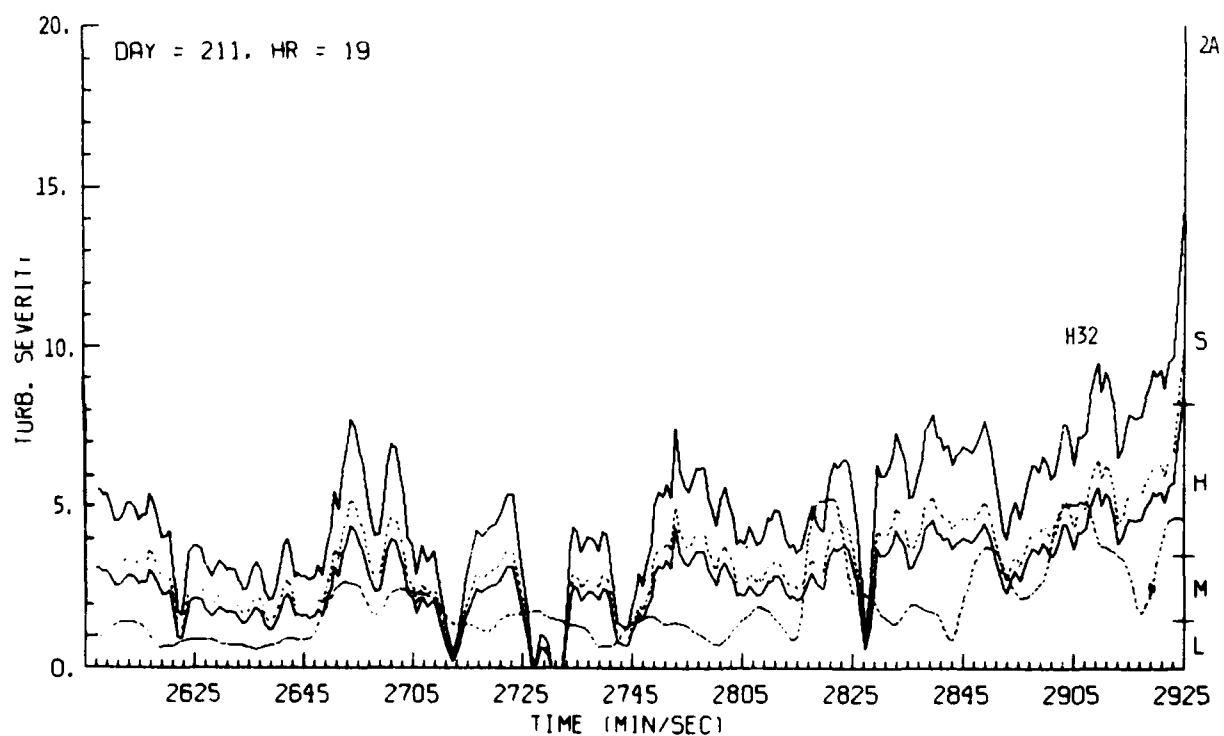


Figure H32. Estimates of Turbulence Severity Derived From Doppler Radar Data, Day 211, Penetration 2A

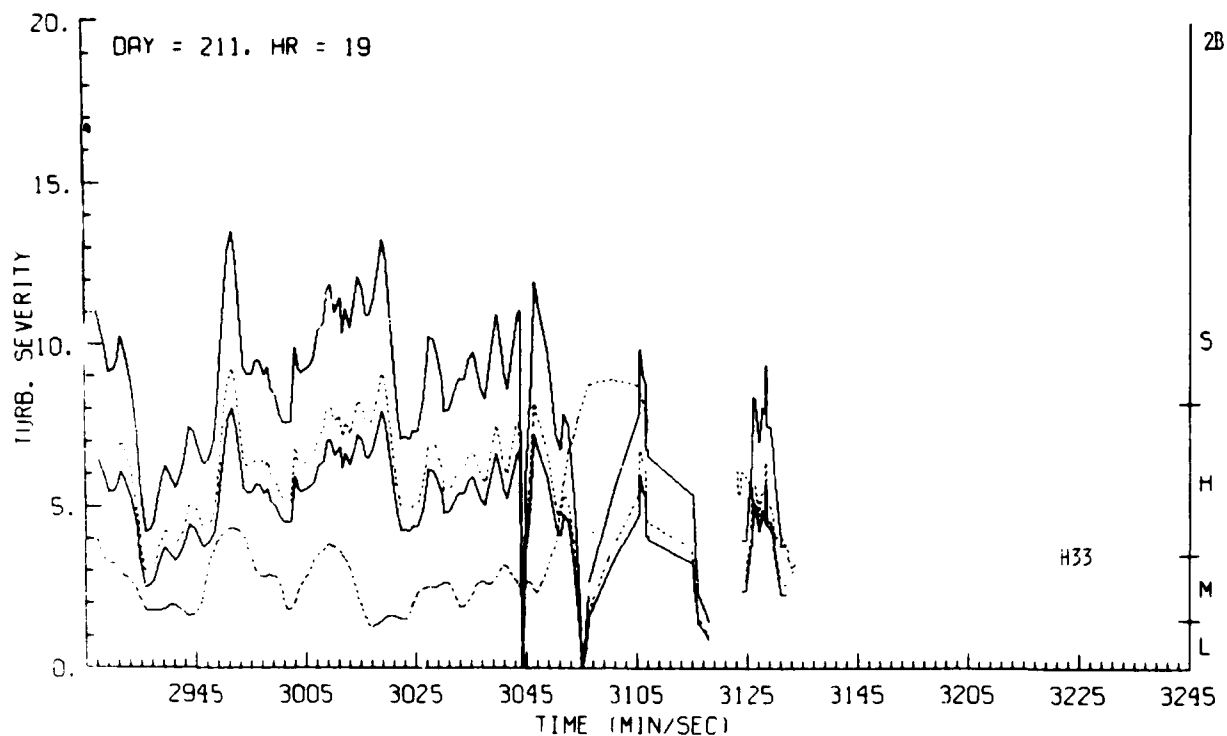


Figure H33. Estimates of Turbulence Severity Derived From Doppler Radar Data, Day 211, Penetration 2B

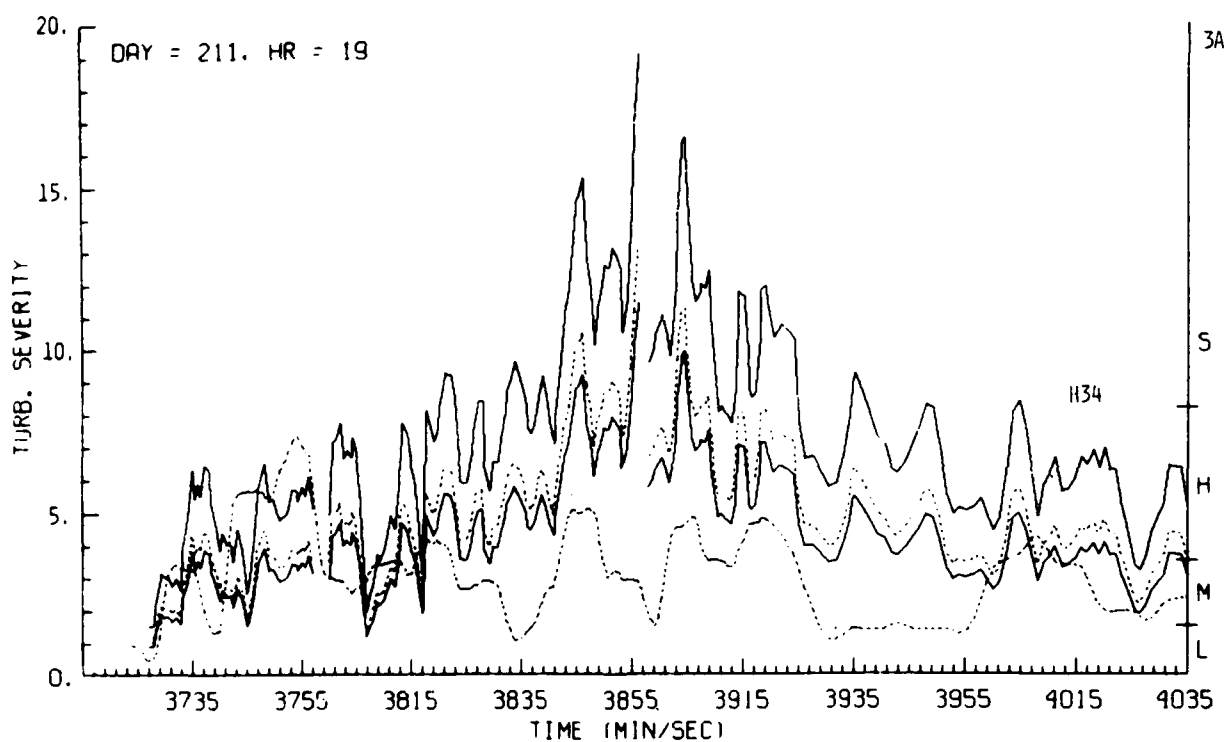


Figure H34. Estimates of Turbulence Severity Derived From Doppler Radar Data, Day 211, Penetration 3A

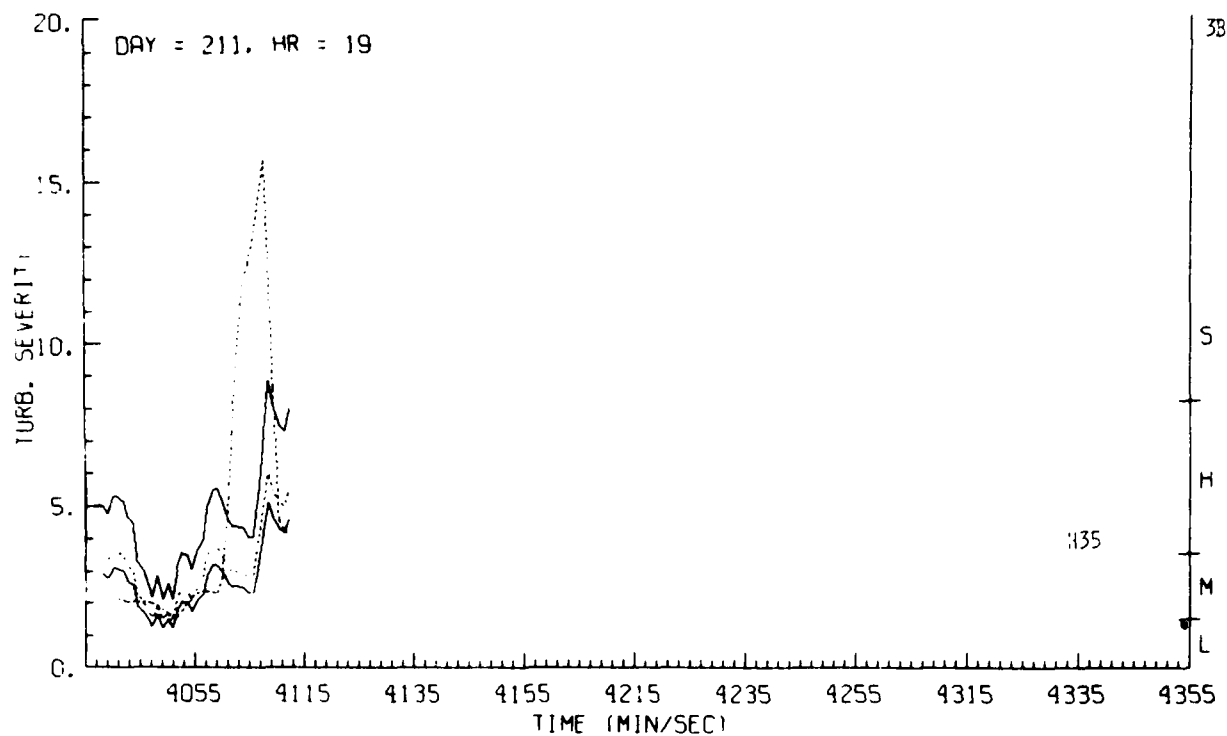


Figure H35. Estimates of Turbulence Severity Derived From Doppler Radar Data, Day 211, Penetration 3B

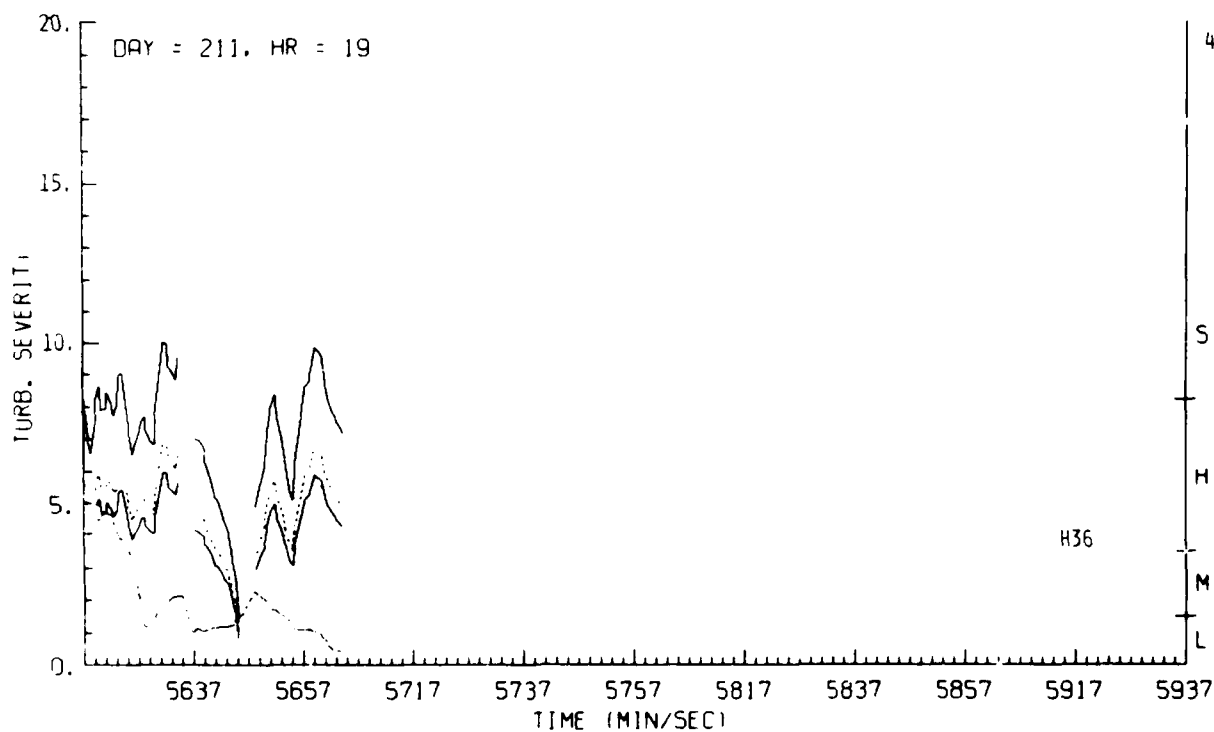


Figure H36. Estimates of Turbulence Severity Derived From Doppler Radar Data, Day 211, Penetration 4

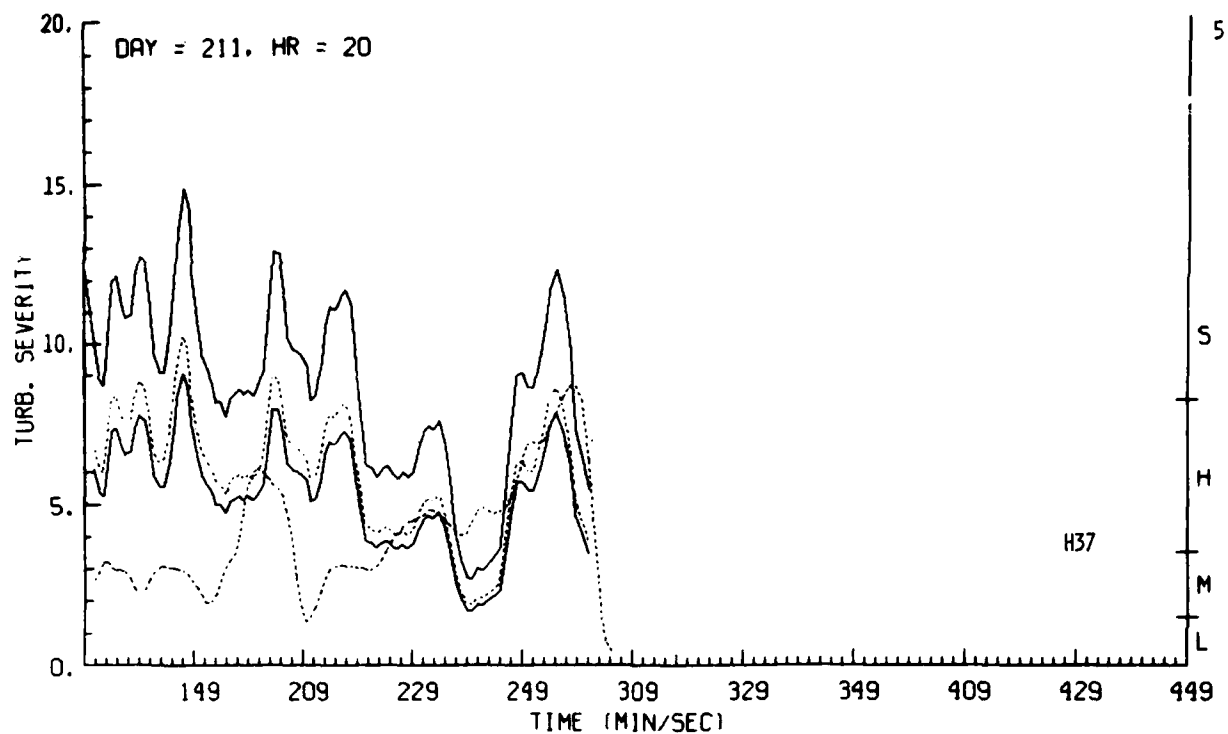


Figure H37. Estimates of Turbulence Severity Derived From Doppler Radar Data, Day 211, Penetration 5

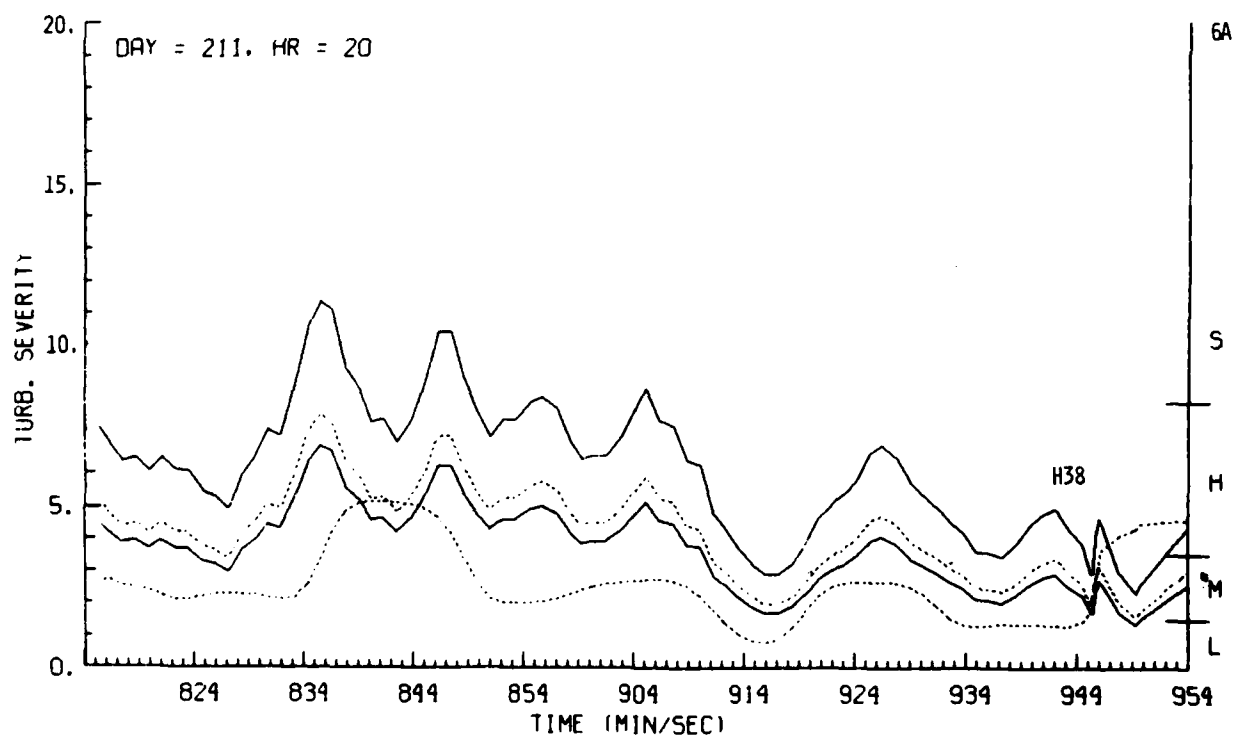


Figure H38. Estimates of Turbulence Severity Derived From Doppler Radar Data, Day 211, Penetration 6A

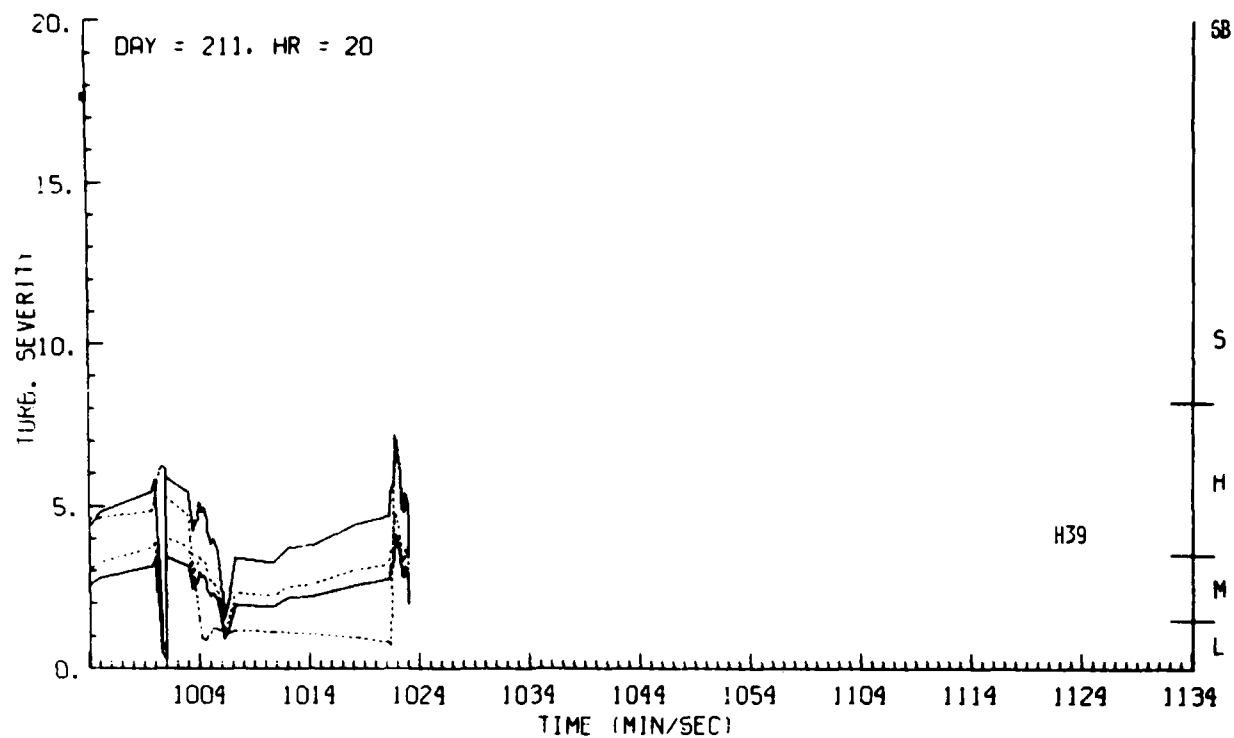


Figure H39. Estimates of Turbulence Severity Derived From Doppler Radar Data, Day 211, Penetration 6B

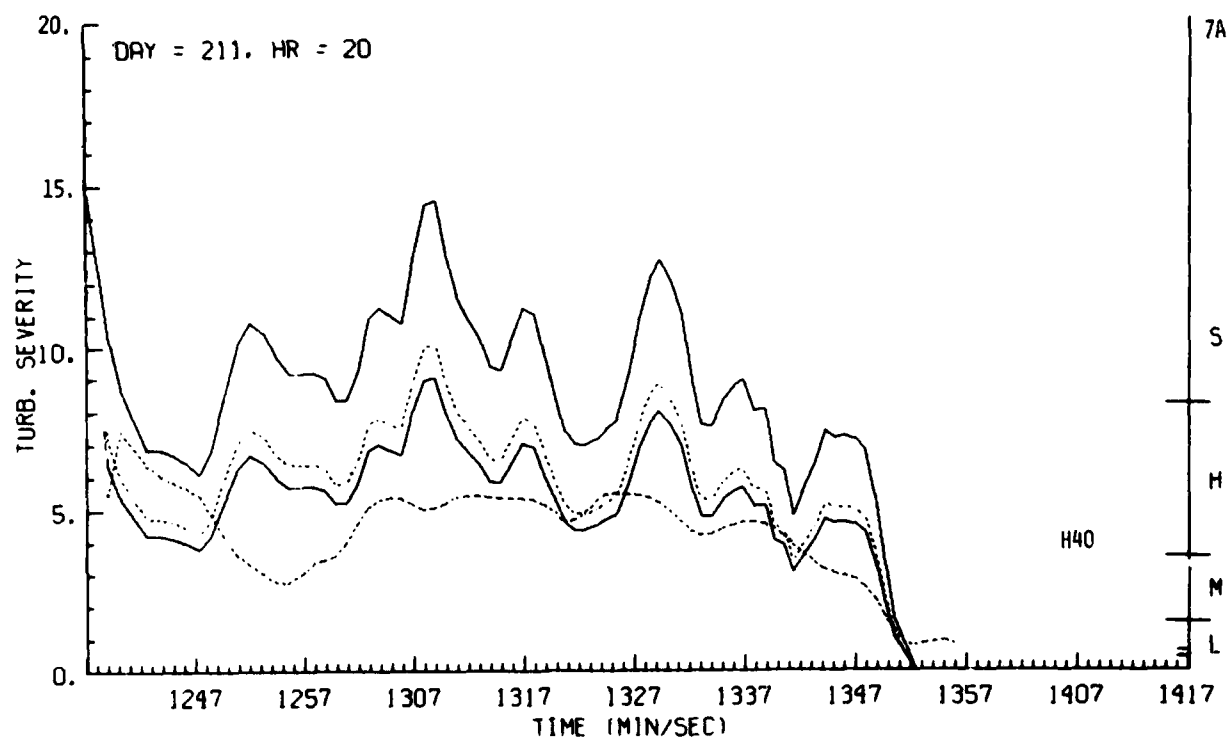


Figure H40. Estimates of Turbulence Severity Derived From Doppler Radar Data, Day 211, Penetration 7A

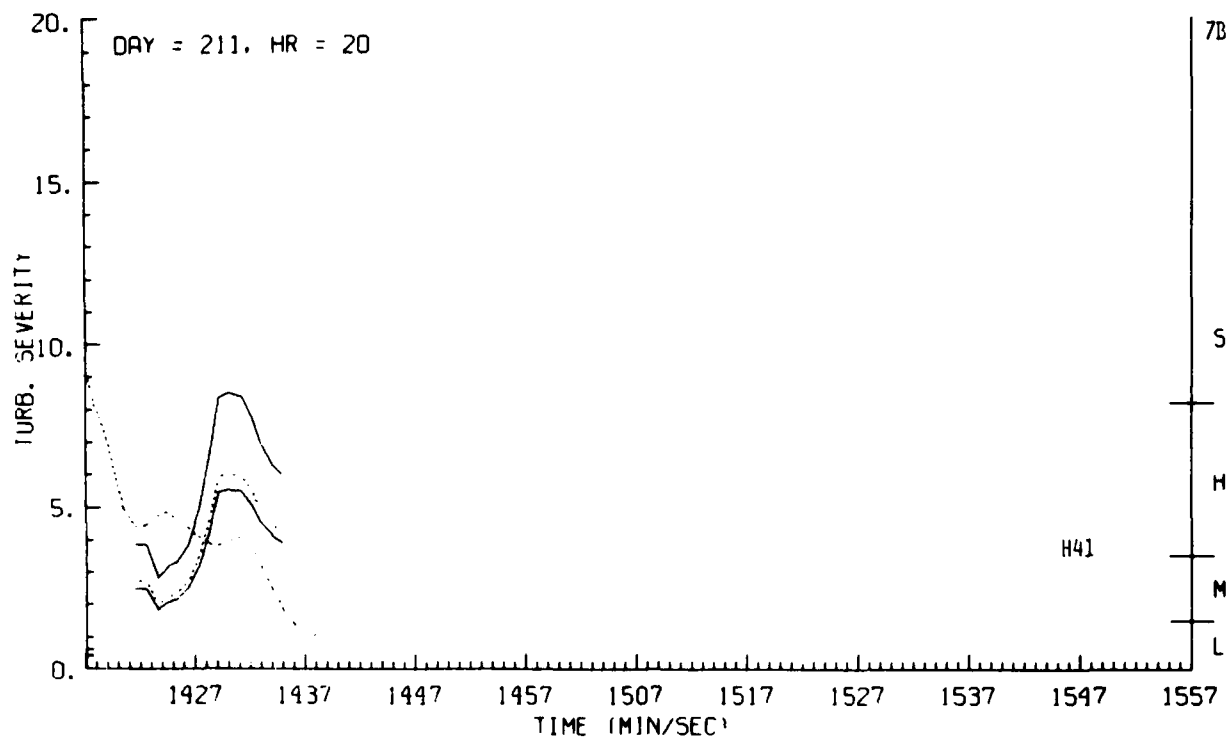


Figure H41. Estimates of Turbulence Severity Derived From Doppler Radar Data, Day 211, Penetration 7B

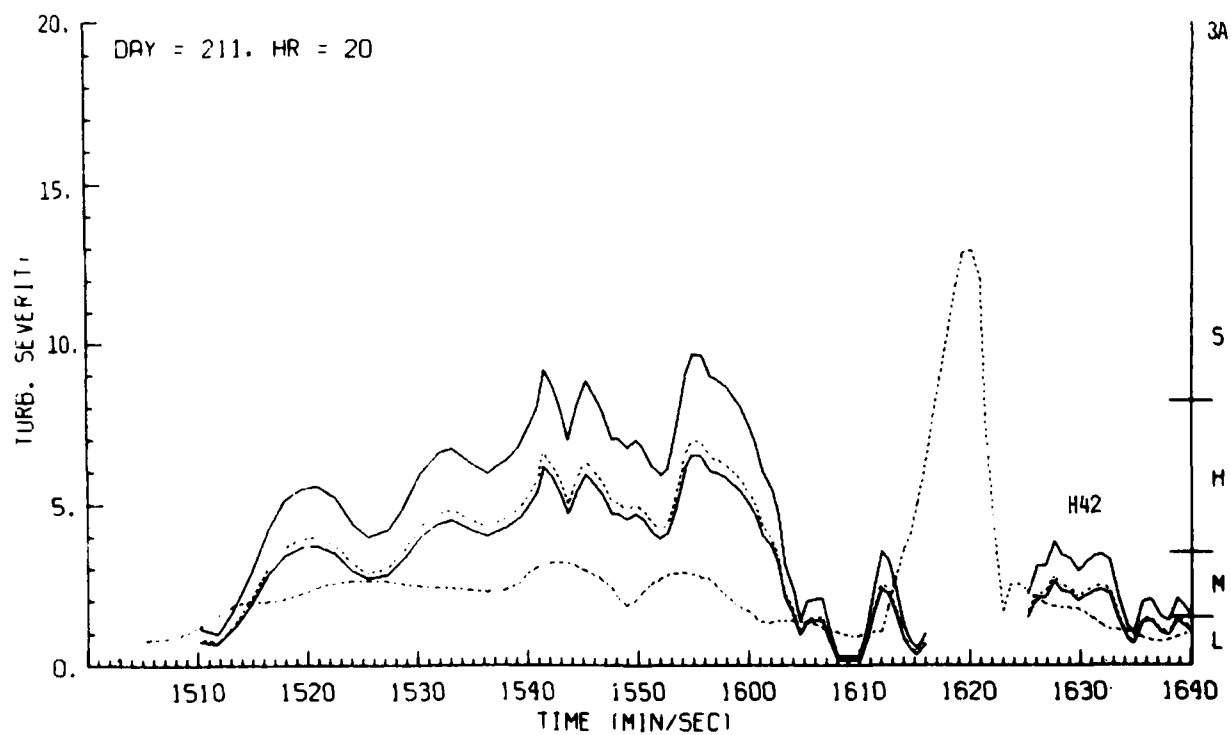


Figure H42. Estimates of Turbulence Severity Derived From Doppler Radar Data, Day 211, Penetration 8A

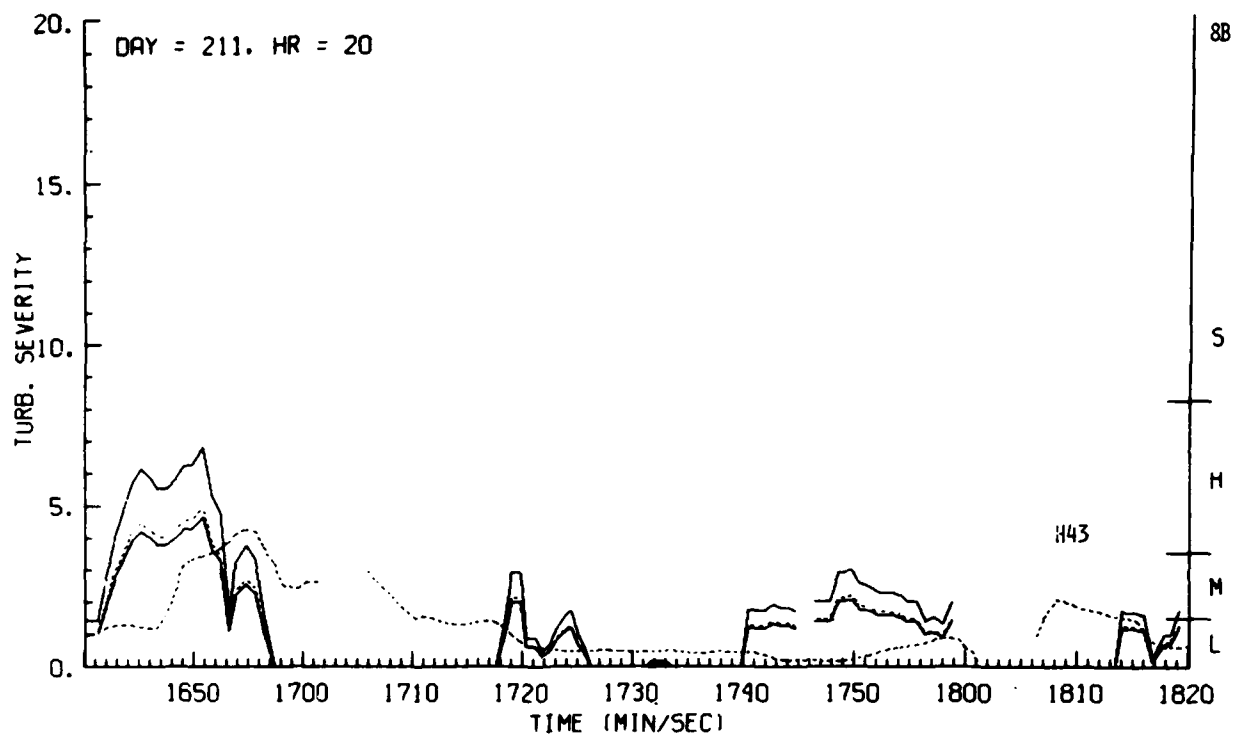


Figure H43. Estimates of Turbulence Severity Derived From Doppler Radar Data, Day 211, Penetration 8B

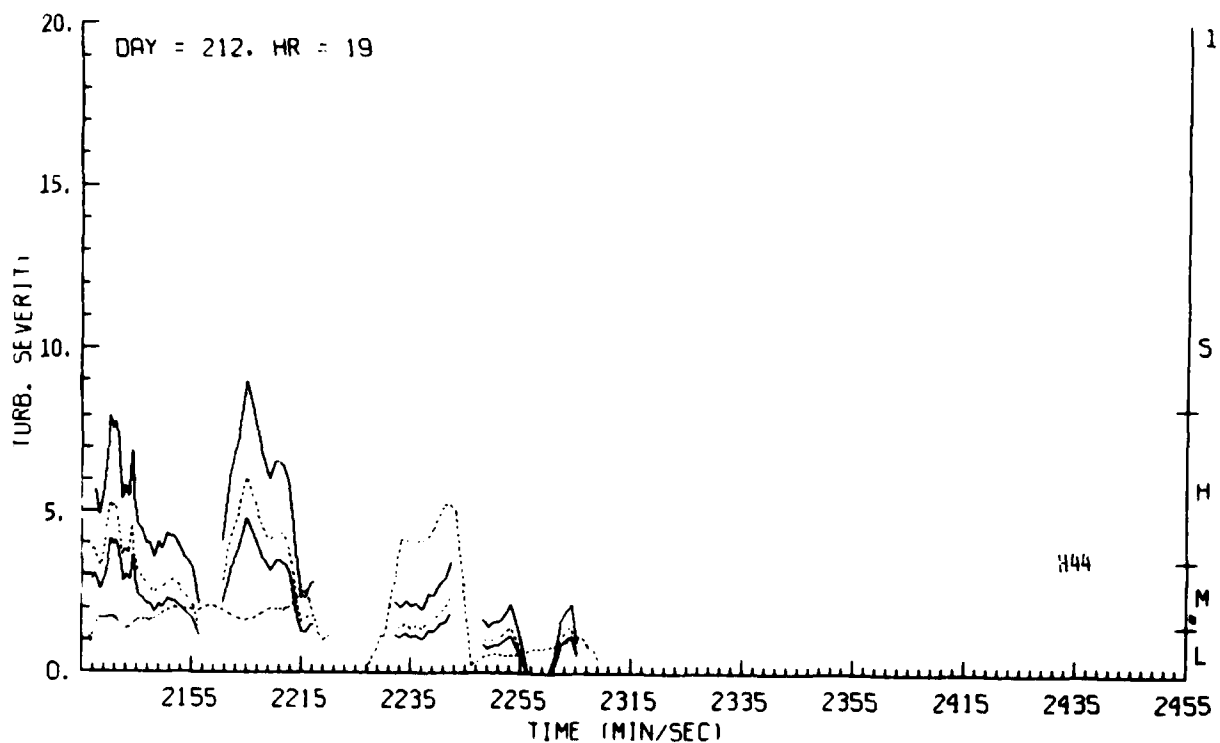


Figure H44. Estimates of Turbulence Severity Derived From Doppler Radar Data, Day 212, Penetration 1

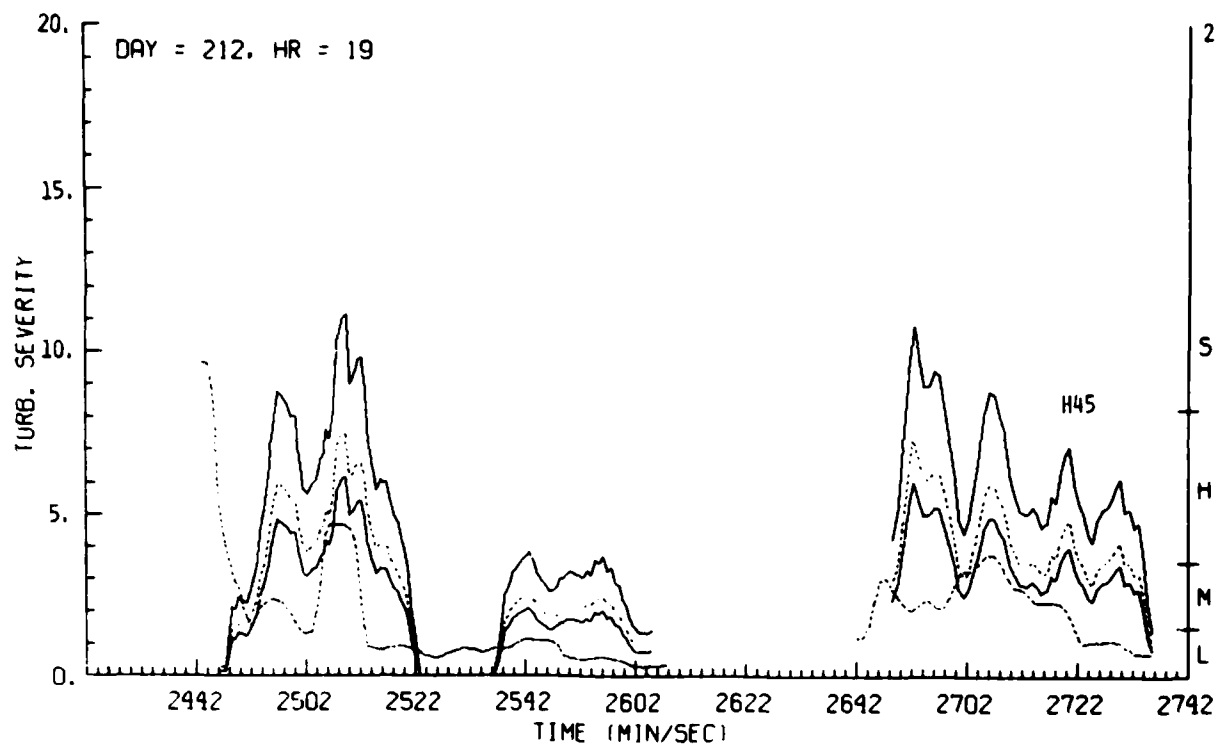


Figure H45. Estimates of Turbulence Severity Derived From Doppler Radar Data, Day 212, Penetration 2

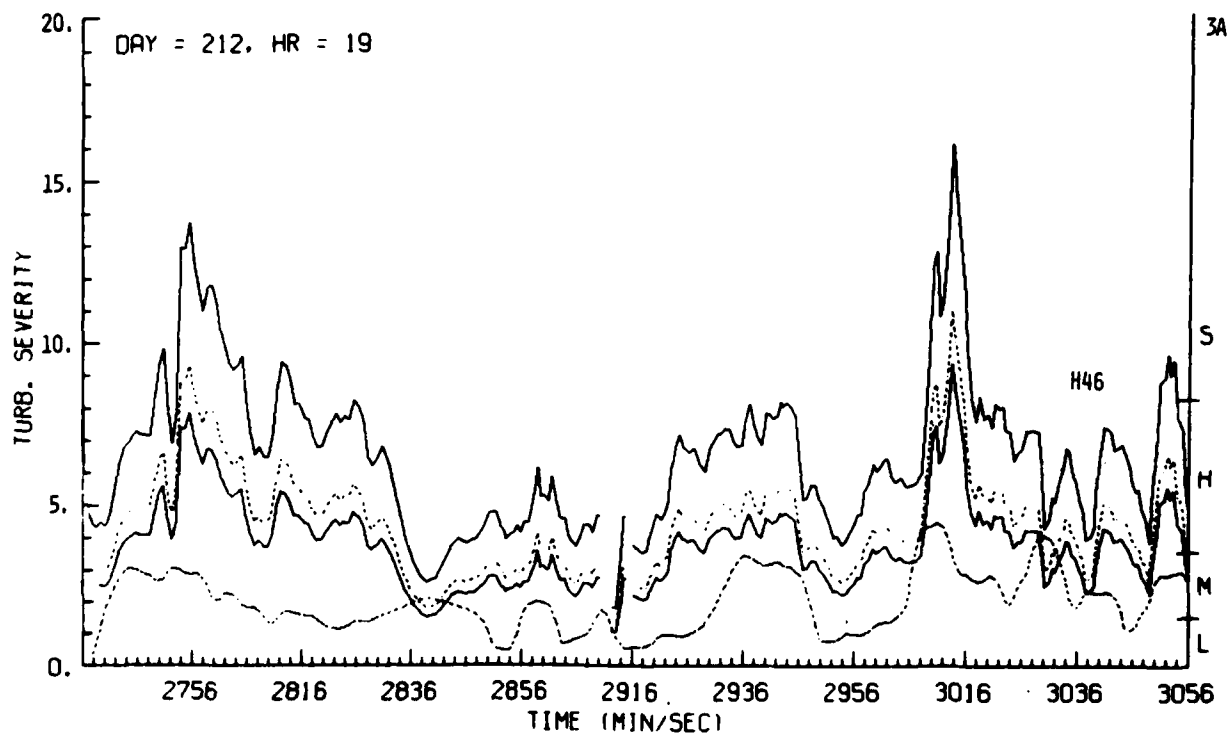


Figure H46. Estimates of Turbulence Severity Derived From Doppler Radar Data, Day 212, Penetration 3A

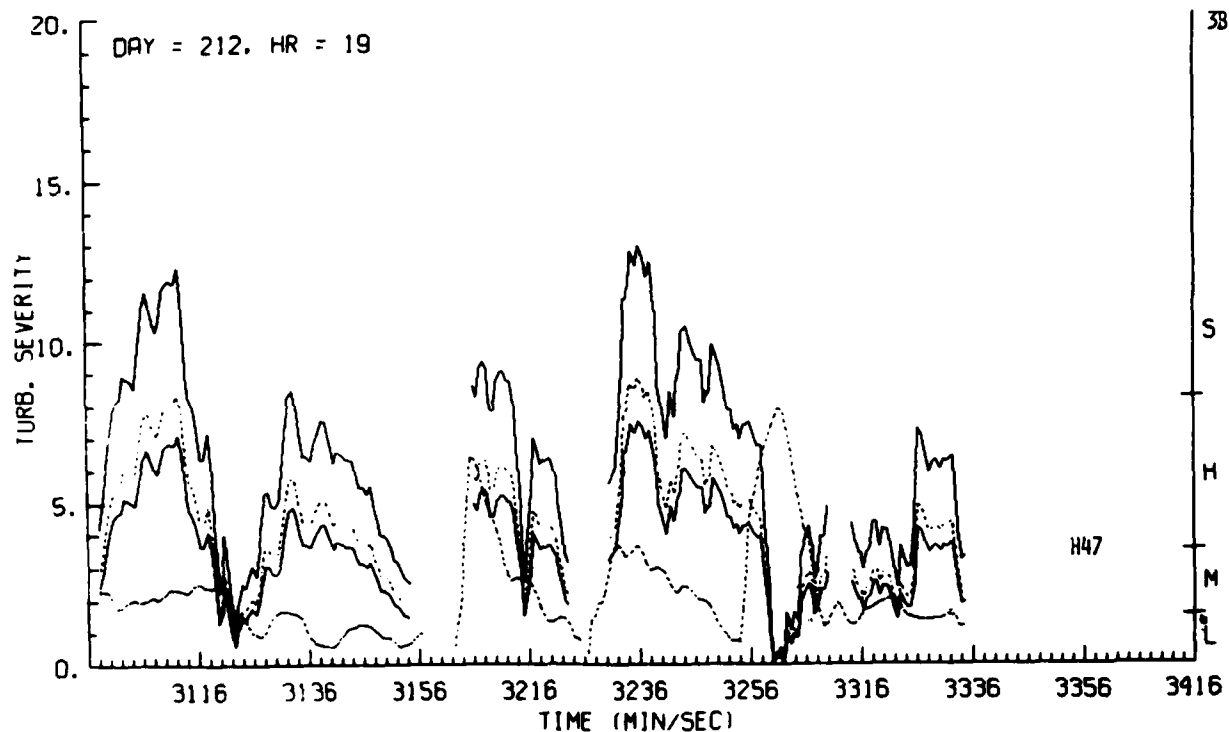


Figure H47. Estimates of Turbulence Severity Derived From Doppler Radar Data, Day 212, Penetration 3B

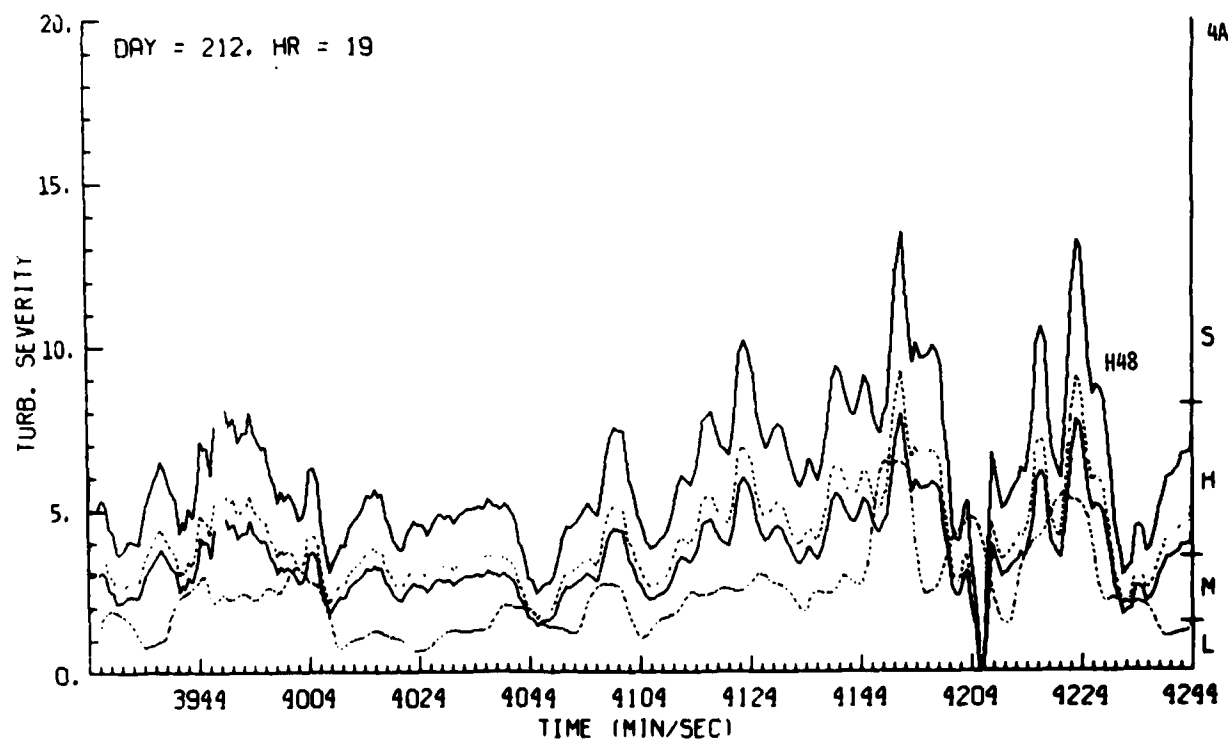


Figure H48. Estimates of Turbulence Severity Derived From Doppler Radar Data, Day 212, Penetration 4A

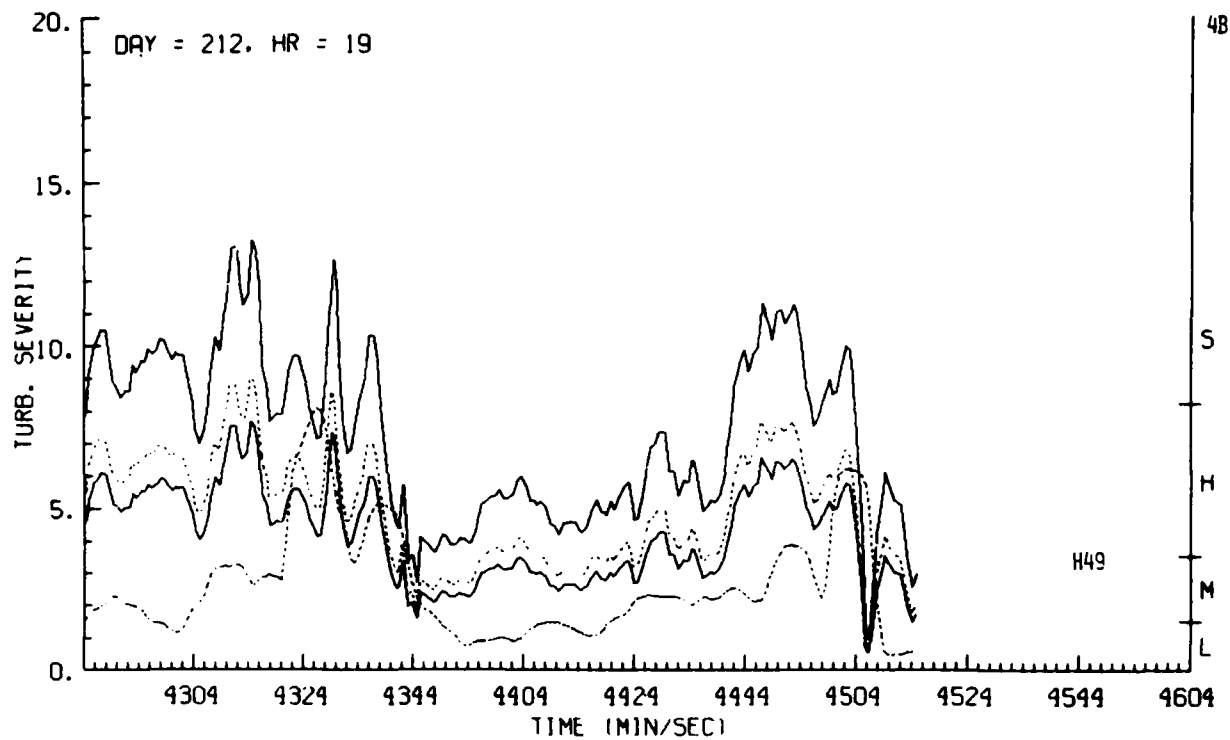


Figure H49. Estimates of Turbulence Severity Derived From Doppler Radar Data, Day 212, Penetration 4B

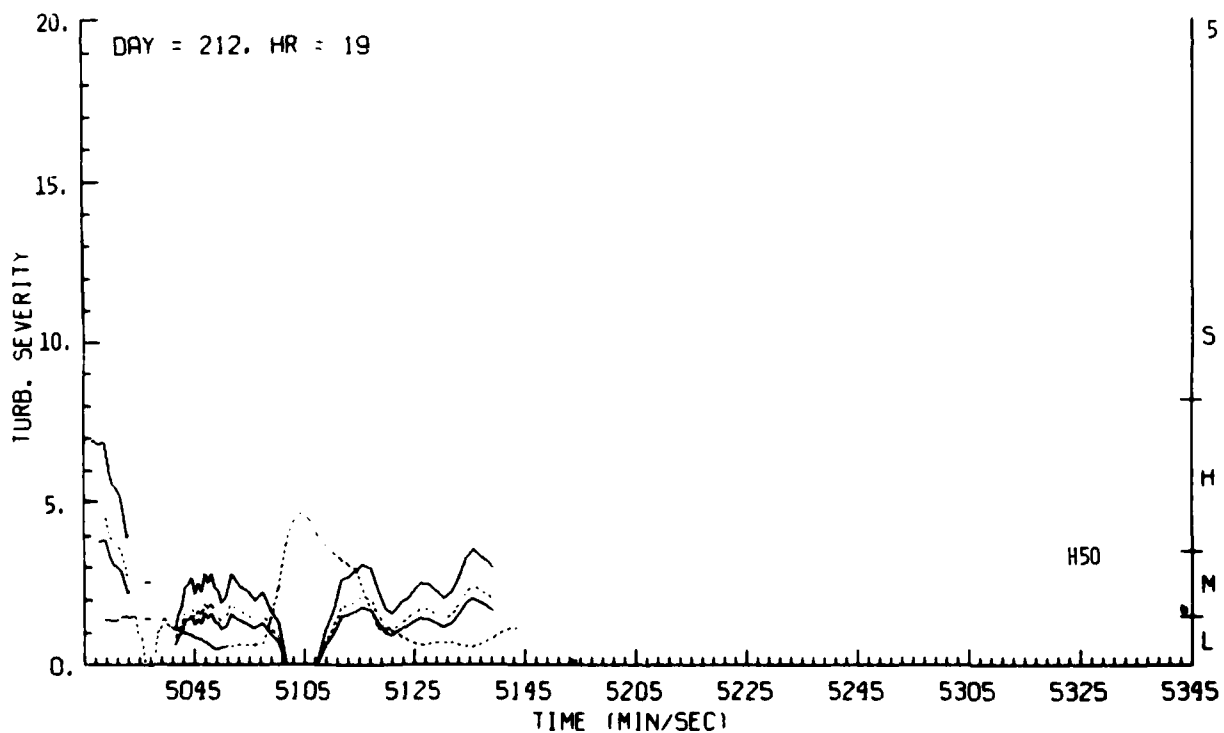


Figure H50. Estimates of Turbulence Severity Derived From Doppler Radar Data, Day 212, Penetration 5

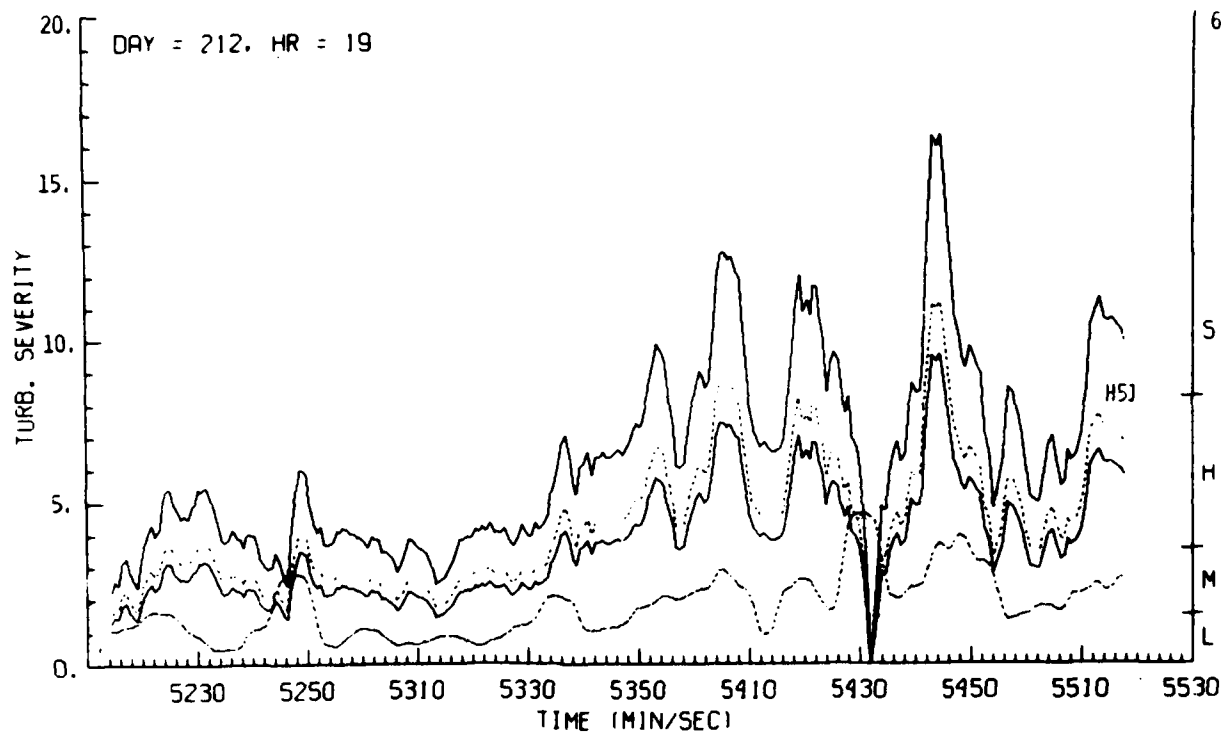


Figure H51. Estimates of Turbulence Severity Derived From Doppler Radar Data, Day 212, Penetration 6

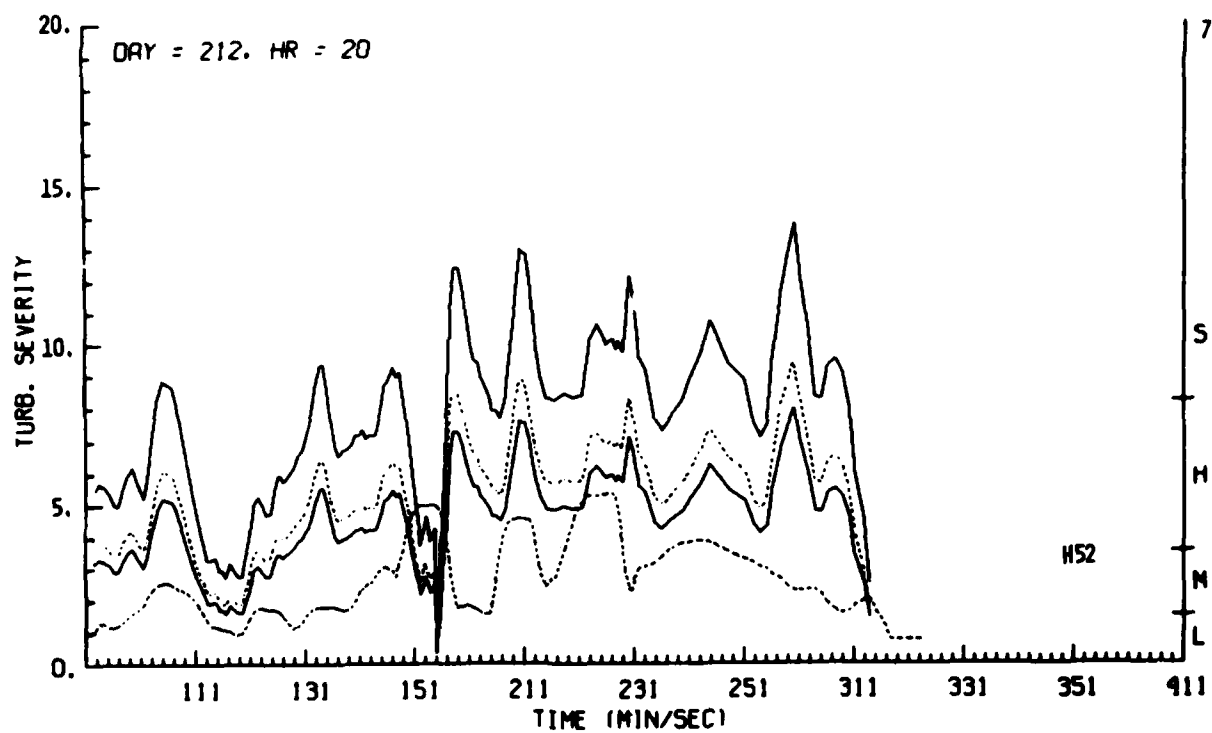


Figure H52. Estimates of Turbulence Severity Derived From Doppler Radar Data, Day 212, Penetration 7

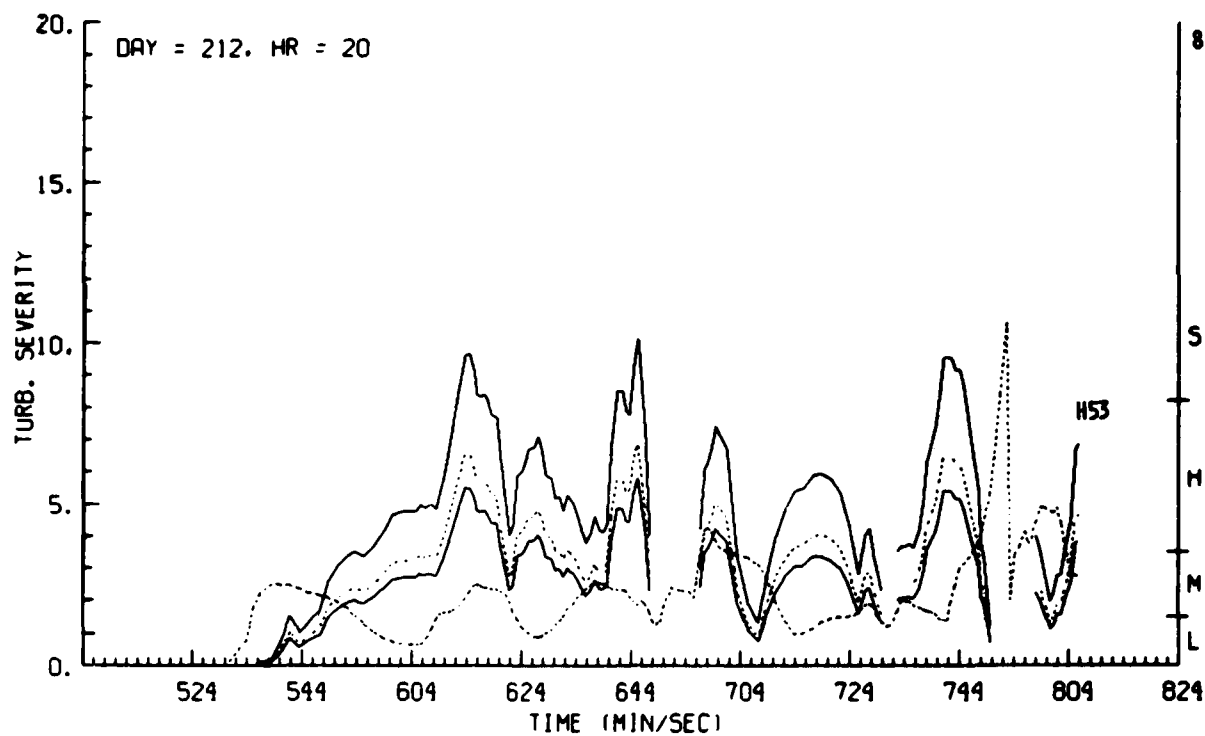


Figure H53. Estimates of Turbulence Severity Derived From Doppler Radar Data, Day 212, Penetration 8

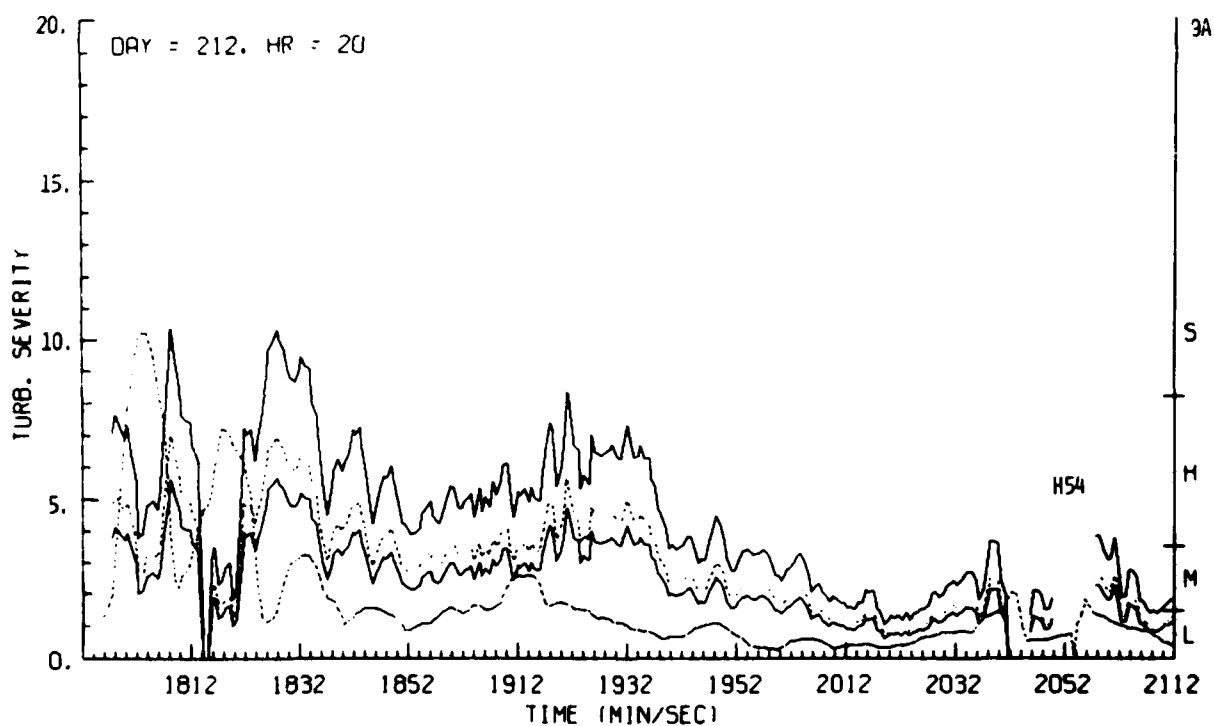


Figure H54. Estimates of Turbulence Severity Derived From Doppler Radar Data, Day 212, Penetration 9A

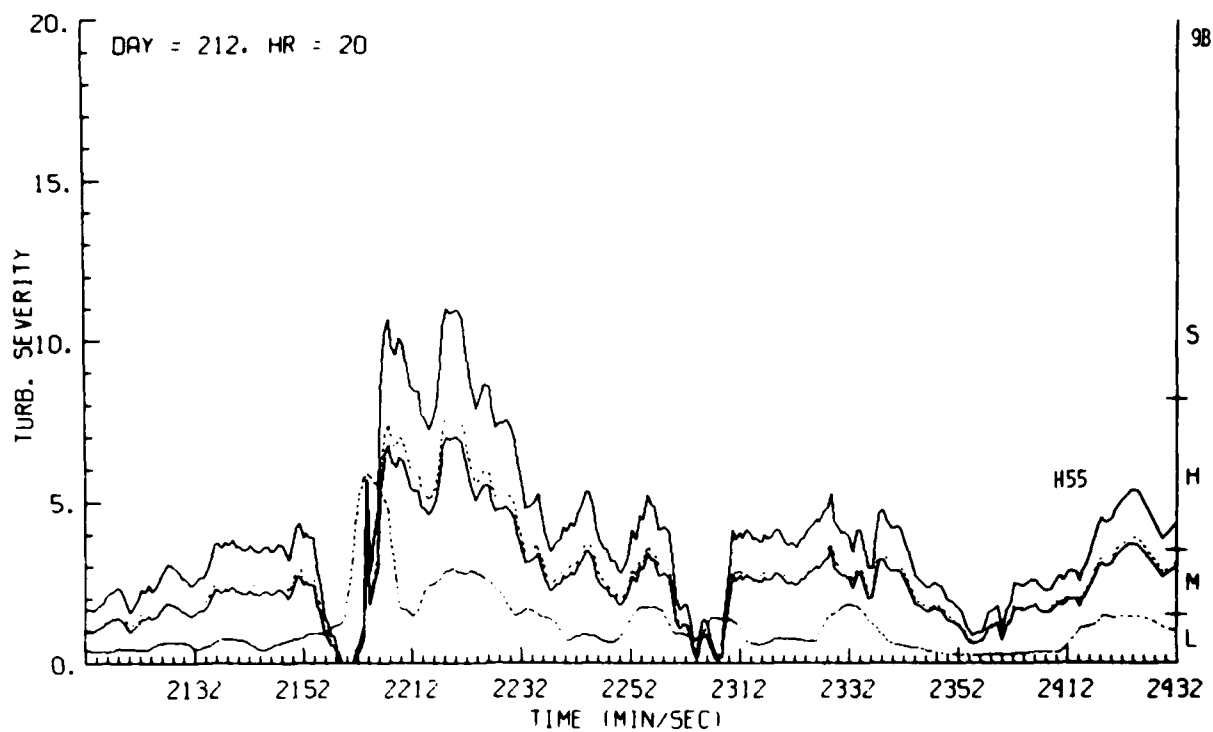


Figure H55. Estimates of Turbulence Severity Derived From Doppler Radar Data, Day 212, Penetration 9B

END

FILMED

12-85

DTIC